The Influence of Flow, Geometry, Wall Thickness and Material on Acoustic Wave Resonance in Water-Filled Piping

by

Alireza Mokhtari

A Thesis submitted to the Faculty of Graduate Studies of

The University of Manitoba

in partial fulfillment of the requirements of the degree of

DOCTOR OF PHILOSOPHY

Department of Mechanical Engineering

University of Manitoba

Winnipeg

Degree:	Doctor of Philosophy
University:	University of Manitoba
Department:	Mechanical Engineering
Title:	The Influence of Flow, Geometry, Wall Thickness and Material on Acoustic Wave Resonance in Water-Filled Piping
Author:	Alireza Mokhtari
Supervisor:	Dr. Chatoorgoon V.

Abstract

The study of acoustic resonance in fluid-filled piping systems with and without mean flow is important for the nuclear industry. For this industry, it is vital to understand the acoustic resonance in their systems; however, no comprehensive experimental benchmark data or accurate modeling tool exists for predicting such a phenomenon. The main goals of the current research are to create a new experimental data bank for the conditions not tested earlier using the configurations of straight lines and branches, and to evaluate the applicability of the linear wave solution using different damping methods and a computational fluid dynamic (CFD) code to simulate the acoustic resonance in fluid-filled piping systems.

In this experimental study, data on resonant frequencies and resonant amplitudes are collected and analyzed for a frequency range of 20–500 Hz for straight and branched tubes by varying their wall thicknesses, materials, and branch configurations at different flow rates and outlet boundary conditions. To be closer to the nuclear industry medium, water is employed in our experiments, contrasting to the fact that most of the available experiments reported were with air at a much lower sonic velocity. I consider here, in particular, measurements at the end of closed branches, upstream, downstream, and at different locations of the main line, as well as the interactions of different sonic velocities along the main pipes. A small diameter is chosen for the branched experiments since the decrease in the width of the main line and the branches has a pronounced effect on the resonant amplitudes due to an increased interaction among the unsteady shear layers forming across the side branches. The experimental results show that there is a strong

effect of turbulent flow, wall material, and wall thickness on resonant amplitudes at frequencies above ~250 Hz.

Numerical investigations are performed solving the one-dimensional (1D) linear wave equation with constant and frequency-dependent damping terms and a CFD code. Employing frequency-dependent damping methodologies shows improvement in terms of resonant amplitude prediction over constant volumetric drag method. Comparing the 1D and CFD results shows that the CFD solution yields better predictions of both resonant frequency and resonant amplitude rather than the 1D solution. This finding is valid especially for frequencies higher than ~300 Hz. For a lighter material (aluminum), even the CFD code is unable to predict results accurately when the frequency is more than 300 Hz. Further investigations assume that fluid structure interactions are necessary for such a material.

Acknowledgements

I would like to express my sincere gratitude to my advisor Dr. Vijay Chatoorgoon for his supportive and inspirational supervision through my Ph.D. study. He has encouraged me to become an independent researcher and helped me to grasp the supremacy of critical reasoning. My special acknowledges goes to Vijay for his understanding, wisdom, patience and support during all the years of my research work. He is a great thinker and has always helped me to remain focused on achieving my goal.

My thanks go to my committee members Dr. Bing-Chen Wang and Dr. Puyan Mojabi whom I got their assistance and comments for completing my research.

Most importantly, I have saved my deepest appreciation and gratitude for my loving, supportive, inspiring and tolerant wife, Shabnam, whose faithful support throughout the difficult steps of this Ph.D. is so valued for me. I would love to thank her for patiently help me to edit my dissertation, for always supporting me in all aspects of my life and for the brilliant life that we share together. Her financial and emotional support and patience of my unstable moods during my student life is a tribute in itself of her unyielding devotion and love. To compensate very little part of Shabnams' unwavering love, I dedicate this dissertation to her. I am truly thankful for having her in my life.

At the end, I would like to appreciate my parents for their effort and love in bringing me up to be a better individual. They have remotely supported me during all the years of my Ph.D. study. Also, I have to thank my sisters and friends for their encouragements.

Table of Contents

List of Tables

List of Figures

Nomenclature

C= speed of sound in the line, m/s

C_0= speed of sound in water, m/s

E= line Young's Modulus of Elasticity, GPa

f_s= sampling rate, sample/s

Δf = frequency resolution, Hz

f_{rm}= maximum amplification frequency, Hz

f_{nm}= minimum amplification frequency, Hz

K= water Bulk Modulus of Elasticity, GPa

L= length of the test line, m

m= mean value of the measurement

n_s= number of samples per data set

$P_{0,1,2,3,4}$= acoustic pressure at different locations, Pa

P= acoustic pressure, MPa

r= inside radius of the pipe, m)

R= outside radius of the pipe, m

Re= Reynold's number

$R(t)$= pressure loss due to fluid friction per length

s= Fourier variable

t= time, s

T= record length, s

V= fluid particle velocity, m/s

$w(\tau)$= weighting function

$\boldsymbol{Z(s)}$= characteristic impedance

Greek Letters

$\boldsymbol{\beta_e}$= effective bandwidth of the spectral window

$\boldsymbol{\beta_s}$= compressibility of water

$\boldsymbol{\lambda}$= wave length, m

$\boldsymbol{\sigma}$= Standard Deviation

$\boldsymbol{\rho}$= fluid density, m3/s

$\boldsymbol{\nu}$= line Poisson's Ratio

$\boldsymbol{\upsilon}$= water viscosity, $m^2/s \times 10^{-6}$

$\boldsymbol{\omega}$= angular frequency, rad/s

Ψ= non-dimensional parameter

$\boldsymbol{\Gamma(s)}$= propagation factor

Abbreviations

Al= Aluminum

I.D= inner diameter

O.D= outer diameter

LWS= linear wave solution

UVK= damping methodologies of Urbanowicz & Zarzycki, Vitkovsky et al. and Kagawa et al.

RMSE= residual mean square error

SS= Stainless Steel

SST= shear stress transport turbulence model

VD= Volumetric Drag

Chapter 1 Introduction

1.1 Background

An acoustic wave resonance phenomenon in fluid-filled pipes is important because of its relevance to several industrial applications. Some examples of these applications include the main steam lines and fuel channels of the nuclear power plants, the re-heat steam lines of the boilers, and the combustion processes in jet engines. In the nuclear industry application, with the flow entering the header and exiting through the complex branched geometries, it is important to know the acoustic pressure at the mainline and the branched sections because of the need to preserve structural integrity of piping systems exposed to acoustic resonances. Gorter et al. (1989), Docquier and Candel (2002), and the NRC Information Notice (2004) discussed about the integrity of the nuclear power plants encountered by the acoustic resonance.

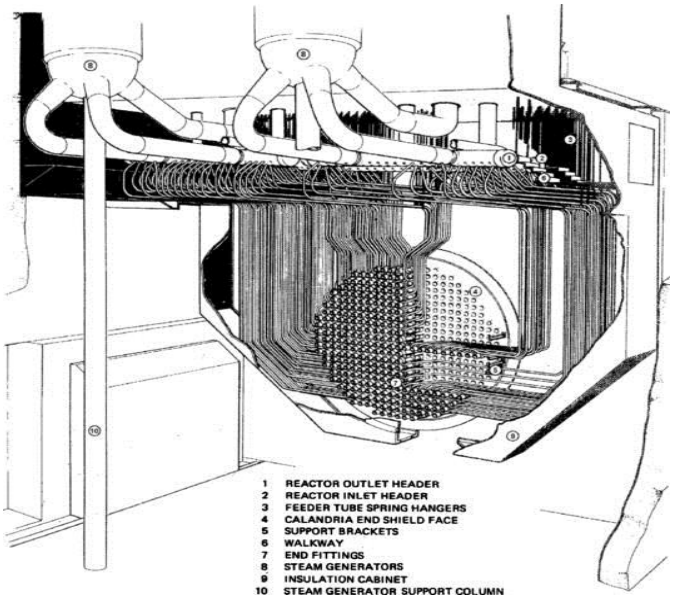

Figure 1.1: Primary Heat Transport Ssystem- Typical Fedder Arrangement

In a typical Canadian Deuterium and Uranium (CANDU) reactor, there is a complex branched geometry between the pump and the fuel channels. This complex configuration includes feeder take-off from the header, emergency cooling injections, shutdown cooling lines, and pump discharge lines. Indeed, an accurate prediction of acoustic resonance in such a complex geometry is necessary to design a system free of any potential damage to the fuel channels. Figure 1.1 shows a picture of the primary heat transport system of a CANDU reactor. It depicts the complexity involved in the system.

Acoustic resonance was recognized as the reason for cracks and fretting wear in the fuel bundles end plates of the Darlington and Bruce reactors (Janzen et al., 1999). This finding led to investigations of the acoustic impulses initiated from the primary heat transport system pumps. The investigations, which included both experimental and numerical studies, were undertaken at Stern Laboratories Inc. and the Ontario Hydro Research Division (OHRD). The acoustic wave resonance in the Darlington reactor was also investigated numerically at the OHRD (Misra et al., 1994) using the ABAQUS code, which solves linear wave equations with a constant damping term. A constant volumetric drag (VD), estimated from the loop tests, was used in the ABAQUS simulations. Their focus was on modelling the acoustic resonance in reactor piping. Misra et al. (1994) also pointed out that to define the acoustic pulsation amplitudes in the header, the region between the pump and the header was required to be modelled accurately. This region consists of a mainline pipe with some closed and open-ended branches from where the flow enters and exits through the system. The pipe sizes are small (0.04 to 0.08 m) compared to the header (~ 0.5 m). If high amplitude acoustic resonance occurs between the pump and the inlet header, it could be concluded that the pulsation amplitude at the header and the fuel channels will also be high and

therefore detrimental. Thus, it is very important to figure out the acoustic resonance through this region accurately.

The experimental results from both STERN and OHRD labs and simulations with ABAQUS demonstrated that significant levels of acoustic pressure were generated at 150 Hz and pressure pulses were generated via a 5 vane impeller pump. This problem was solved by replacing the 5 vane impeller pump to a 7 vane impeller one. The 7 vane pump shifted the resonant frequency to 209 Hz with a lower level of pulsation magnitude. Although the problem was solved by changing the pump vanes, their results showed that an agreement between the complex geometry experimental results and the acoustic resonance predictions was not always good and, therefore, further research was required.

Other than the nuclear industry, some experimental and numerical studies were carried out to provide better insight into the acoustic resonance in the fluid-filled piping system. The focus of those experimental studies was on water hammer, aero-acoustic, or frequencies less than 100 Hz (D'Souza & Oldenburger, 1964), which was considerably below the frequencies of 100–300 Hz encountered in a typical CANDU reactor. In order to deal with the aero-acoustic problems, the focuses of most studies were on the vortices generated by a flowing air over a sharp-edged corner. They assumed those vortices as a source of acoustic resonance (Graf & Ziada, 2010; Ziada & Buhlmann, 1992). Since those studies were based on air flow rather than liquid flow, it is unknown how those can be applied directly to liquid flow.

In terms of the numerical study, several numerical approaches using the transfer function method, the method of characteristics, and the finite element/difference solution of the governing equations were proposed for an acoustic resonance analysis. Some of the numerical studies showed significant discrepancies in the attenuation and the phase shift of pressure traces in

comparison to the experimental studies (Chatoorgoon et al., 2006; Martinez-Lera et al., 2009; Misra, et al., 1994; Rzentkowski et al., 1993). The strength and the weakness of these methods need to be studied.

1.2 Motivations and Objectives of the Current Study

At the complex region of the pump to the inlet header of a CANDU reactor, several parameters, such as branch arrangements, area changes, entrance to volumes, inflow velocity, etc. might influence the resonant frequency and amplitude. These influences would make resonance predictions very difficult. Therefore, studies with more simplified geometries than the ones in the region between the pump and the inlet header need to be carried out to obtain better understanding of the phenomena involved.

Furthermore, based on the previous experimental studies, acoustic resonance at frequencies less than 100 Hz in the fluid-filled pipes has been studied. However, the acoustic resonance phenomena at higher frequencies for different wall materials and thicknesses in zero and non-zero mean flows have not been studied experimentally. It is also hard to find an experimental data bank in the frequency range of 20–500 Hz, and the scarcity of comprehensive experimental data is evident. Besides, the acoustic wave damping in flowing fluid tubes is still unfolding, particularly for turbulent flows. Experiments with zero and turbulent flows are necessary to evaluate developed damping methodologies.

In fact, in order to understand the dominant parameters that may influence acoustic resonance, it is necessary to conduct acoustic wave propagation experiments in laminar and turbulent pipe flows with low levels of uncertainty.

Since the nuclear industry uses ABAQUS, which solves the linear wave equations and employs a constant VD to simulate resonant amplitude, the same condition is considered in the present study. Also, to assess the frequency dependency of the acoustic resonance predictions, ABAQUS is chosen here to employ some developed frequency-dependent damping methodologies (Kagawa et al., 1983; Schohl, 1993; Trikha, 1975; Urbanowicz & Zarzycki, 2012; Vardy & Brown, 2004; Vitkovsky et al., 2004). Using linear wave solution (LWS) is a common practice of making a number of conservative assumptions in performing an acoustic resonance data analysis of fluid-filled piping systems. These assumptions need to be assessed for more accurate predictions of the actual amplitudes.

Several CFD software packages for solving fluid mechanic problems are available; however, none of the available software has yet been proven to predict the acoustic resonance at the frequency range of 20–500 Hz accurately. Understanding the capabilities of commercial software in predicting acoustic resonance in fluid-filled tubes will benefit not only the nuclear industry, but also other industrial application involving an acoustic resonance problem.

ANSYS-CFX, a commercial CFD software, is also employed for the current study to examine the effect of flow conditions (laminar and turbulent) on resonant frequencies and resonant amplitudes. The $k-\varepsilon$ turbulent model provides mostly accurate resolution for many freestream conditions and the $k-\omega$ turbulence model models near-wall effects (like separation) effectively. The Shear Stress Transport Model (SST) turbulence model uses the freestream resolution of the $k-\varepsilon$ model and the near-wall effects of the $k-\omega$ model. To capture the near-wall effect, SST model is employed to predict the resonant frequencies and amplitudes for a turbulent flow in a straight line tube. By solving the full Navier–Stokes equations (using ANSYS-CFX 14.5), nonlinearities effects, if any, can be properly modeled. Also, rather than approximating the

amplitude strength using a semi-empirical method (Graf & Ziada, 1992/2010) or using different developed damping terms (Kagawa et al., 1983; Schohl, 1993; Trikha, 1975; Urbanowicz & Zarzycki, 2012; Vardy & Brown, 2004; Vitkovsky et al., 2004; Zeilke, 1967), the CFD approach inherently models the resonant amplitude. Indeed, by introducing a reliable model for an unsteady flow friction and taking the flow conditions into account, the prediction of the acoustic waves becomes more physically accurate.

In order to further understanding of the acoustic wave resonance and evaluate the capabilities of the LWS and CFD in modeling this phenomenon, the objectives of this study are to:

1. Understand and document the current state of the art of research on acoustic resonance for zero, laminar, and turbulent flows in piping systems by performing a comprehensive literature review.
2. Experimentally investigate acoustic wave propagation in fluid-filled tubes by conducting simple experiments with very low levels of uncertainty for a frequency range relevant to the nuclear industry application.
3. Study—experimentally and numerically—the effect of an explicit excitation source and a flowing fluid on the resonant frequency and amplitude of straight and branched piping.
4. Determine—experimentally and numerically—the influence of wall thickness, material, and different branched geometries on the resonant frequency and amplitude of a fluid-filled tube for zero and non-zero flows with different boundary conditions.
5. Assess LWS using constant VD, and using frequency-dependent damping methods and the more general non-linear Navier–Stokes equations predictions by comparing them with each other and against the conducted experiments.
6. Determine the effect of the SST turbulence model on the acoustic resonance predictions.

7. Make some recommendations on the most accurate approach to determine the acoustic wave resonance in the reactor piping systems.

1.3 Contributions and Publications

The experimental tests are designed and implemented to investigate the effects of geometry, wall material and thickness for stagnant and moving flow on the acoustic resonance with reliable and conclusive results. The current experimental data benchmark has some potential to be used for assessing the existing fluid transport systems of reactors and also designing new plants. The literature is comprehensively reviewed and the potentials in other researches for the current investigation are addressed. For the first time different resonant-frequency methods is applied on ABAQUS to investigate acoustic resonance in the frequency range which is important for nuclear industry. Also, applying CFD method in the broad frequency range for the laminar and turbulent flow is investigated with the first time conclusive results. The strengths and weaknesses of the 1D linear wave solution and CFD results in predicting acoustic resonances are addresses which are useful for nuclear industry. The outcomes of this research have been published as a journal and two conference papers listed below.

1.3.1 Journal Papers

Mokhtari A., Chatoorgoon V., A Study of Acoustic Wave Resonance in Water-Filled Tubes with Different Wall Thicknesses and Materials, ASME J of Nuclear Rad Sci 2(3), 031011

Mokhtari A., Chatoorgoon V., Investigation of Acoustic Wave Resonance in Water-Filled Tubes with Different Branch Configurations, In preparation

1.3.2 Conference Papers

Mokhtari A., Chatoorgoon V., Study of Wall Thickness and Material Effect on Acoustic Wave Propagation in Water-Filled Piping, Internoise ASME NCAD Conference, August 19-22, 2012, New York City, NY, USA

Mokhtari A., Chatoorgoon V., THE INFLUENCE OF GEOMETRY, WALL THICKNESS, AND MATERIAL ON THE ACOUSTIC RESONANCE PREDICTIONS IN CLOSED-ENDED WATER-FILLED PIPING, ASME 2013 International Mechanical Engineering Congress & Exposition, November 14-21, 2013, San Diego, California, USA

1.4 Thesis Outline

This thesis consists of seven chapters: introduction, literature review, experimental strategy, LWS model description, ANSYS-CFX model description, results and discussions, and conclusions and recommendations. Chapter 2 covers the literature review, which includes previous experimental studies about acoustic waves, developed laminar and turbulent flow damping models for unsteady flows, numerical simulations, and aero-acoustic.

Chapter 3 reports test facilities, data acquisition systems, and instrumentations employed in this research. Also, the measurements and the data processing methods employed for the tests are presented. Also, ABAQUS using a constant VD and some selected frequency-dependent damping methodologies are discussed in Chapter 4.

Chapter 5 explains the simulations with ANSYS-CFX 14.5. Fluid properties, boundary conditions, meshing choices, analysis type, and solver controls are outlined and discussed.

The focus in Chapter 6 is on explaining the acoustic resonance measurements for some straight and branched tubes. Also, predictions are compared against the attained experimental data.

The last chapter, Chapter 7, provides a summary of findings and concludes the achievements of the research. Finally, some recommendations for future research are provided.

Chapter 2 Literature Review

2.1 Introduction

While looking at the literature to review acoustic wave propagation in fluid-filled pipes, it becomes noticeable that several authors report experimental and numerical studies of acoustic waves in many applications, such as acoustic resonance, water hammers, and aero-acoustic. This literature review is divided into four main sections. The first section focuses on reviewing the previous work on experimental studies in acoustic wave propagation; the second section focuses on the literature about the different developed damping methods in pulsating/oscillating flows; the third section focuses on reviewing the literature on different numerical methods in acoustic wave modeling; and the fourth section focuses on the literature about aero-acoustic simulation.

2.2 Review of Experiments

Several studies were performed to experimentally investigate the acoustic wave propagation in fluid-filled lines. The damping effects in unsteady pipe flows were investigated experimentally by Brown et al. (1969), Daily et al. (1956), Hino et al. (1977), Iguchi et al. (1985), Kirmse (1979), Margolis and Brown (1976), Mizushina et al. (1973/1975), Ohmi et al. (1980), Sauer (1969), Tu and Ramaprian (1983), and Wood and Funk (1970). They measured the pressure loss and the velocity profile in laminar and turbulent flows for various frequencies. Numerous experiments were conducted on water hammer application by Bergant et al. (1999b/2002b), Brunone et al. (2000), Budny (1991), Carstens and Rooler (1959), Elansary et al. (1994),

Holmboe and Rouleau (1967), and Safwat and Polder (1973). They studied water hammer waves that were caused by the opening and closing valves of the laminar and turbulent flows. Also, the closure times of the valves were investigated. Other studies were performed by Morgentroh and Weaver (1993/1998), Rzentkowski and Zbroja (2000), Stirnemann et al. (1987), and Zielke et al. (1969) to assess the acoustic waves generated by pumps.

Chatoorgoon and Li (2006), D'Souza and Oldenburger (1964), and Rzentkowski et al. (1993) measured the frequency responses of a single straight line filled with stagnant water.

The problem with the acoustic resonance in the piping networks with close-ended branches were investigated and reported by Baldwin and Simmons (1986), Chen and Florjancic (1975), and Chen and Sturchler (1977). The flow passing the side branches in the main pipe excites the standing sound waves of each branch in single and multiple branch systems. The acoustic resonance in the piping system with the branches was further studied by several researchers (Bruggeman et al., 1991; Kriesels et al., 1995; Dequand et al., 2003; Ziada & Buhlmann, 1992; Ziada, 1994; Ziada & Shine, 1999). They found that excited pressure amplitudes could be higher than the main line pressure head. Thus, the reliable operation of the piping systems with closed side-branches could be severely restricted. An example of the destructive consequences of acoustic fatigue happened in the Quad-Cities nuclear power plant in the USA and the steam dryer of a boiling water reactor (Deboo et al., 2007).

The response mechanism between the instability of the free shear layer at the entrance of the branch and the acoustic particle velocity generated by the branch's resonance modes create acoustic resonance in closed side-branches. The concept of unstable instabilities in the shear layer relative to the disturbances for a range of frequencies was shown by Michalke (1965). Ziada (1994) studied a feedback mechanism based on the acoustic particle velocity provided by

acoustic standing waves. Because of the vorticity field created in a system with closed side-branches, this type of excitation is associated with the shear layer coinciding with the location of the maximum acoustic particle velocity. Well-tuned coaxial branches are especially capable of generating very intense acoustic resonances over wide ranges of flow velocity. This was demonstrated by Graf and Ziada (1992), who found that only 2% of the acoustic power of the coaxial branches was radiated into the main pipe. Geveci et al. (2003) and Rockwell and Schachenmann (1983) considered the problem of coupling of the shear layer of a cylindrical cavity and the longitudinal resonance modes of the associated piping system. Lafon et al. (2003) and Ziada et al. (2003) experimentally demonstrated the excitation of the two-dimensional (2D) duct cross-modes by the shear layer of a branch attached to one sidewall of the duct.

Some of the performed experimental setups and conditions are selected and briefly listed in Table 2.1.

Table 2.1: List of Previous Experiments

Authors & subject	*Remarks*
D'Souza et al. (1964) Dynamic Response of Fluid Lines	• **Acoustic Source: Laminar flow** • **Frequency Range: 0-100 Hz** • **Horizontal line** • **Hydraulic oil Mil-0-5606**
Bruggemen (1987)	• **Acoustic sources: Air flow 16-40 m/s & Loudspeaker** • **Frequency range: 50-200 Hz** • **Demonstrated inlet & outlet of main pipe had main effect on the acoustic pressure amplitude**

	produced during flow acoustic coupling • **Investigated the effect of diameter ratio on Strouhal number (St) and amplitude**
Jungowski et al. (1989) Cylindrical side branch as tone generator	• **Acoustic source: Air flow** • **Frequency range: 0-2000 Hz** • **Re = (0.1-16)*10^6**
Ziada and Bulhlmann (1992) Resonances of two side branches in close proximity	• **Acoustic source: Air flow (10 to 86 m/s)** • **Frequency range: 0-1000 Hz** • **Showed increasing branch diameter (d) over main line Diameter (D) for a single branch reduced resonant amplitude** • **Orifice plates (D/2) before upstream branches were reduced pulsation of tandem and coaxial branches** • **Author didn't know why amplitude was 10% less in downstream branch for the tandem case.** • **Higher velocity created higher resonant frequency** • **No measurement on turbulence level were carried out** • **Orifice reduced amplitude**
Rzentkowski (1993) Estimation of pump generated pressure pulsation	• **Stagnant water used for the experiment** • **Acoustic source: Shaker** • **Frequency range: 20-500 Hz** • **Found more discrepancy between prediction & experiments for higher resonant frequency modes**

Ziada (1994) A flow visualization study of flow acoustic coupling at the mouth of a resonance side- branch	• **Acoustic source: Air flow and loudspeaker** • **All experiments were forced at first resonance frequency of the side branches at 86 Hz**
Ziada and Shine (1999) Strouhal numbers of acoustic resonance of closed side branches	• **Acoustic source: Air flow & elbow at upstream** • **Designed the chart to predict velocity at the onset of resonance. (critical St)** • **Designed chart for elbow distance and diameter ratio effect on St** • **Coaxial branch had larger amplitude** • **Coaxial with larger length had lower amplitude** • **Higher static pressure created higher amplitude** • **Higher branch over main line diameter created larger amplitude**
Dequand et al. (2003) Self-Sustained Oscillations in a Closed Side Branch System	• **Acoustic Source: Air Flow 10-150 m/s** • **Frequency range: 400-2000 Hz** • **Improved the prediction of the maximum pulsation amplitude to within 40% of the experimental results** • **oscillation frequency within 2%**
Takahashi (2008) Experimental study of acoustic and flow induced vibration in BWR	• **Acoustic source: Air flow** • **Fluctuating pressure was normalized by averaged main steam line fluctuating pressure**
Arthurs and Ziada (2009) Flow-excited acoustic resonances of coaxial side-branches in an	• **Acoustic source: Air flow 17 to 112 m/s (turbulent)** • **Frequency range: 0-2000 Hz**

annular duct	
Graf and Ziada (2010) Excitation source of a side-branch shear layer	• **Acoustic source: Air flow and loud speaker** • **Tandem & coaxial branch** • **All experiments were forced at first resonance frequency of side branches at 113 Hz** • **Vortex acoustic source depended on St & acoustic particle velocity**
Tonon et al. (2011) Oscillations in pipe systems with multiple deep side branches: Prediction and reduction by detuning	• **Acoustic source: Air flow up to 70 m/s.** • **Six side branches** • **Frequency range 0-600 Hz**
Okuyama et al. (2012) Acoustic resonance at the mouth of one or two side branches	• **Acoustic source: Air flow 5 to 80 m/s** • **Investigated single, tandem & coaxial branches** • **Studied the effect of distance between side branches and cross section ratio on amplitude** • **0.3 <St<0.5 generated higher fluctuating pressure**

D'Souza and Oldenburger (1964) experimentally studied the laminar flow in a pipe with hydraulic oil in the frequency range 0–100 Hz. The oil was discharged into the atmosphere through an orifice at the outlet. Their experiment was reasonably well-performed with a low level of uncertainty.

Bruggeman (1987) studied the acoustic damping caused by friction loss and found that static pressure had an important role on acoustic damping. For high pressure, the friction loss became insignificant. He found that a single branch with the same diameter of the main line and under

certain boundary conditions could be regarded as harmless with respect to vibrations, although a two-branch system with the same diameter ratio and under the same boundary conditions could cause serious vibration problems. Jungowski et al. (1989) investigated the effect of the branch diameter on the pulsation strength and reported a substantial reduction in the pulsation amplitude when the diameter ratio of the branch diameter over the main line diameter was increased. Ziada and Bulhlmann (1992) studied the influence of the distance between the branches, the branch length, the static pressure, the upstream turbulence level, and the angle between the branches on the general acoustic response of a piping system with single and double branches. They found that in tandem branches, there was a 10% reduction in downstream branch pressure pulsation in comparison to the upstream branch. The reason of this small but steady difference is not known, and has not been explored to date. In their experiments, the overall system response of co-axial branches and tandem branches were almost the same, although for the coaxial branches the dimensionless amplitude was higher and the lock-in range was wider. Due to an increase in the static pressure, the pulsation amplitude was increased. They believed that higher static pressure reduced the fluid density that decreased the acoustic damping due to friction losses at the pipe wall. Ziada and Bulhlmann (1992) reported that the resonant frequencies of the branches can be detuned by rearranging the length of the branches. To study higher levels of turbulence for tandem and coaxial branches, they used an orifice plate upstream. Their results showed that by increasing the level of turbulence, the critical flow velocity at the onset of resonance did not change.

Rzentkowski et al. (1993) measured the frequency responses of a single straight fluid-filled line at the frequency range of 20–500 Hz and found that damping increases with increasing

frequency. Their experiments were limited to a closed-end tube with zero mean flow and a single wall thickness.

Instead of changing the turbulent intensity with orifice at the downstream end of the branch pipes, Ziada and Shine (1999) used an elbow to lead it to the upstream end of the closed-ended branches. They investigated the effect of the diameter ratio of the branches to the main pipe diameter, the distance of the branches, and the effect of an added elbow on the critical St. They stated that there were pulsation amplitude increments for the cases with added elbow at the outer side of the branches. Based on the experimental results, they created a chart that could predict the mainline flow velocity, which caused the initiation of the branch resonances.

Takahashi et al. (2008) studied a 1/10 scale of the boiling water reactor to scrutinize the propagation of fluctuating pressure from the safety valve relief (SVR) to the dryer through the main steam lines. They showed that the amplitudes of the pressure perturbations were much higher for a number of stub tubes because of the interaction between them. Single SRV pressure perturbation exposed resonating when the St was less than 0.44.

The effects of diameter ratio, branch length ratio, and thickness of the annular flow on the resonant frequency and amplitude of the first acoustic mode were experimentally investigated by Arthurs and Ziada (2009). Indeed, their experiments were innovative as the branches in their case were connected to an annular duct. Flow velocities in the main duct were adequate to excite the three lowest acoustic modes of the branches. The lowest flow velocity in the duct that initiated the first resonant mode was about 21m/s and continued until it was approximately 50 m/s. The first resonant frequency was about 304 Hz, and its amplitude was the highest of all the acoustic modes found during the experiment.

Graf and Ziada (2010) performed some experiments to investigate the acoustic resonances in

closed side-branches that were excited by the turbulent flow in the main line. Their experimental results for the flowing air that excited acoustic resonances of branches represented an important occurrence, and this was that vortex damping led to nonlinear saturation at large amplitudes. The acoustic resonances were initiated when the Reynolds number (Re) was less than 2.6×10^5. In all the experiments, the oscillation was forced with the loudspeaker at the first resonant frequency of the side-branches (113 Hz). The pressure difference across the shear layer was experimentally measured. It covered the St numbers from 0.25 to 1 and amplitudes of the acoustic particle velocity from 0.3% to approximately 50% of the flow velocity in the main pipe. The acoustic pressure was measured at the branch ends.

Tonon et al. (2011) studied oscillations driven by the instability of the air flow in a pipe system arranged with six equally spaced closed branches. They tried to reconstruct the scale of the Ommen compressor station system, in which high amplitude pulsations were reported. A countermeasure of detuning the length of the branches proved to be successful in their complex system.

Okuyama et al. (2012) studied the effect of the geometrical and flow parameters on the general acoustic resonance through air flow experiments at room temperatures and atmospheric pressure. They tried to use the Mach number close to actual boiling water reactors (0.01–0.24). Their experiments showed that for the coaxial branch experiments, the pressure amplitude showed a counter tendency to the case of a single branch. Also, they presented that the dimensionless acoustic pressure amplitude decreased as the cross-sectional ratio of the main pipe and the branch pipes decreased. They believed this was because the two branches were strongly coupled and formed a standing wave with negligible losses ratio. For the tandem branches, a large amplitude of more than ten times the single branch occurred as the distances between the

tandem branches were almost even multiples of the quarter-wavelength.

From the literature reviewed, it appears that a comprehensive study of acoustic resonance at frequencies above 100 Hz for laminar and turbulence flows and different geometries will help to understand better unsteady flow damping term.

2.3 Damping Models

In the current review, the developed unsteady friction models for laminar and turbulent flows are discussed. The available acoustic models are assessed based on their acoustic resonance predictions. Indeed, applying damping methodologies in acoustic resonance simulations influence their amplification predictions.

Studies by Foster and Parker (1964), Gerlach and Parker (1967), Ohmi and Iguchi (1982), Purdy et al. (1964), and Wylie and Streeter (1993) showed that damping with oscillatory or pulsatile flows was higher than with steady flows at the same mean velocity. Also, Kirmse (1979) and Purdy et al. (1964) showed that the instantaneous velocity profile of the laminar oscillatory and turbulence pulsating flows were not the same as the parabolic or flat shape of the steady laminar and turbulence flows. Other studies by Linney (1981), Margolis and Brown (1976), and Ohmi et al. (1981), discussed the transition frequency band for viscosity attenuation.

Although the boundary layer profile in steady flow is not time-dependent, it is so in pulsating/oscillating flows. Applying the steady friction formula for flows with acoustic waves cannot be accurate as the wall shear stress is time-dependent. Several friction models have been developed in the time domain for unsteady flows.

The friction term in unsteady flows has been studied based on 1D and 2D models. The studied 1D friction models can be categorized into four groups: first, the friction models based on the

instantaneous mean flow velocity (Hino et al., 1977); second, the friction models based on the instantaneous mean flow velocity and mean acceleration (Bughazen & Anderson, 1996); third, the friction models that, in addition to the instantaneous mean flow velocity and mean acceleration, are based on instantaneous convective acceleration (Brunone et al., 1991); and fourth, the friction models based on instantaneous mean flow velocity and radial diffusion (Svingen, 1997; Vennatro, 1996).

The 2D friction models can be categorized into two groups: first, the friction models based on the instantaneous flow velocity and the past velocity weight (Kagawa et al., 1983; Schohl, 1993; Shuy, 1995; Suzuki et al., 1991; Trikha, 1975; Vardy, 1992; Vardy et al., 1993; Vardy & Brown, 1995/1996/2003; Vitkovsky et al., 2004; Urbanowicz & Zarzycki, 2012; Ziekle, 1967), and second, the friction models based on lateral flow velocities in the cross-section area (Chen & Veshagh, 1993; Eichinger & Lein, 1992; Pezzinga, 1999; Vardy & Hwang, 1991).

2.3.1 Laminar Flow Damping Models

The Darcy-Weisbach and Hazen-Williams formulae for wall shear stress, which were developed for steady flows, have historically been used for unsteady flows. They formulae can apply as long as the wall shear stress expressions are assumed to be unchanged with time (Wylie & Steeter, 1993). Daily et al. (1956) first found out that the difference between the steady-state friction model prediction and the unsteady experimental result was an additional unsteady friction term. D'Souza and Oldenburger (1964) formulated frequency response equations for a laminar flow using the linearized Navier–Stokes equations and transformed them to the Laplacian domain. Their expression included the effects of fluid viscosity on pressure wave damping. They compared their predictions against experiments and found that fluid viscosity and

frequency increased the damping effects, and concluded that the viscous shear-stress terms were important to predict proper amplification.

Zielke (1967) modeled the damping of water hammer waves with a frequency-dependent friction model. His model is believed to be one of the most rigorous methodologies in water hammer wave prediction for laminar and low turbulence flows (Re < 11000) (Budny et al., 1989). Zielke's model assumes that the flow is fully developed, the convective terms are negligible, and the velocity profile remains axisymmetric. His model also addressed the reason for the faster attenuation of higher frequencies than the lower ones. The reason was addressed to the level of the changing mean flow velocity, which affected the instantaneous friction term. Zielke's model, in both frequency and time domains, were developed in later studies. Since his model needed a huge amount of memory storage and CPU time, several researchers tried to reduce its computational time. First, Zielke's model developed the weighting function, which was simplified by Trikha (1975) using a series of three exponential expressions. The approximated weighting function resulted in a low demanding computational method. Kagawa et al. (1983) and Schohl (1993) also simplified Zielke's method by using a higher number of exponential terms. They tried to simplify his method with higher accuracy than the previous simplified methods. Moreover, Shuy (1995) approximated the weighting function of Zielke's model in terms of the instantaneous mean cross-section velocity and acceleration. The advantage of his proposed equation was that it did not involve complex expressions as compared to Zielke's method. Later, Vardy and Brown (2004) approximated Zielke's weighting function to reduce the computational time. They increased the accuracy of Trikha's methodology. They also stated that the model could be used for both laminar and turbulent flows. For laminar unsteady flows, Vitkovsky et al. (2004) extended Zielke's approximated weighting function by Kagawa et al.

(1983) by optimizing the coefficients to minimize the error between their predictions and Zielke's predictions. Recently, Urbanowicz and Zarzycki (2012) used the LSQNONLIN MATLAB function to fit the new weighting function with the original Zielke weighting function. They showed that the numerical results based on the new weighting function were closer to the original results of Zielke than the previous simplified weighting functions in the time domain.

The 2D unsteady friction approaches based on specific illustrations of the wall layer in the laminar flow was studied by different researchers. Ohmi et al. (1980) studied the pulsatile flow in the pipes and introduced three flow pattern types, i.e., quasi-steady, intermediate, and inertia dominant. For wall shear stress and friction loss, Ohmi et al. (1981) also introduced a multilayer model with dissimilar analytical representations. Furthermore, Ohmi et al. (1985) calculated the wall shear stress from quasi-2D momentum equation based on the calculated pressure gradient from average 1D equations. Bratland (1986) simulated the transient compressible pipe flow through a multilayer friction model to represent the frequency dependence of the friction and the radial variation of the kinetic energy. A friction model for laminar flows was also developed by Eichinger and Lein (1992) to measure the cross-sectional distribution of instantaneous flow velocity based on empirical K-epsilon (k-ε models).

Although analyses with different developed damping terms generally showed a good prediction of the water hammer wave propagation in laminar flows, they have not been verified against the acoustic wave resonance experimental data. Indeed, water hammer waves happen at low frequencies (<60 Hz) and diminish after some reflections, and they are different from the acoustic resonance reflected waves.

2.3.2 Turbulent Flow Damping Models

The transient response of the turbulent pipe flow with a frequency-dependent friction has been investigated since the early 1930s. Wood (1937) and Rich (1945) developed models in that the friction term was proportional to the velocity transients in order to simulate frictional effects in the turbulent flow. Wood (1937) found out that the approximated viscous effect by the linear term did not accurately predict the exact viscous effect.

Daily et al. (1956) developed an unsteady friction model for turbulent flow by using experimental coefficients. The applied coefficients in their model were dependent on the instantaneous mean flow velocity and the instantaneous local acceleration. Brown et al. (1969) and Margolis and Brown (1976) studied viscous effects in turbulent flow for small-amplitude sinusoidal instabilities. They used semi-empirical analytical models and compared their predictions with the experiments and found out that in the boundary layers at high Re and high oscillating frequency, the velocity distribution was more sophisticated than the laminar flow.

Wood and Funk (1970) proposed a model called the two-region model. They recommended it for general transient turbulent flow conditions in a tube. A simple laminar boundary-layer model was used to describe the viscous effects. They found that the model was deficient in high Re turbulent flows and turbulent boundary layers could not be simplified as laminar boundary layers.

Ohmi et al. (1976) suggested multi-regional time-independent eddy viscosity models of two, three, four, and thirteen regions, and predicted the acoustic velocity and pressure profiles in oscillating turbulent flows. They believed that the characteristics of the flow were well defined with analytical solutions of the four-region model proposed by von Kármán (1939).

By using the instantaneous velocity profile, an eddy viscosity model for the low frequency pulsating turbulent pipe flow was developed by Ohmi et al. (1978). They modeled the velocity profile by a four-region approximation and used the finite difference method to calculate the steady and oscillating eddy viscosities. Moreover, based on the flow patterns in the turbulent pipe flow, some frequency-dependent friction models were developed by Ohmi et al. (1980/1981/1985).

Analogous to Ohmi's model (1978), Kita et al. (1980) introduced time-dependent eddy viscosity approximations. They divided the pipe into five continuous radial areas and used the approximate eddy viscosity as the empirical connection among them.

By assuming the instantaneous acceleration and the instantaneous convective acceleration, Brunone (1991) developed a viscous loss model. To represent the unsteady turbulence structure, Eichinger and Lein (1992) applied k-ε in their model. They took the benefit of the time dependency of the eddy viscosity. They also reported that their velocity profile predictions for different unsteady flows agreed well with the experiments.

A development in the computer's computational speed and storages helped researchers to study on 2D models. In order to define the average cross-sectional velocity profile in 1D models, empirical coefficients or weighting functions were needed, but for 2D models, dividing the pipe flow into several layers and using analytic and experimental approximations, the actual cross-sectional velocity profile can be obtained.

For a low Re turbulence flow, Vardy and Hwang (1991) recommended a quasi-2D friction model. Their model distributed the flow in the pipe to 5 regions in which the lateral velocity terms were calculated among the nearby areas. Chen and Veshagh (1993) also developed a two-region friction model. For the adjacent wall and core areas, they used the law of the wall and the

instantaneous velocity profile respectively. Afterwards, a quasi-2D model based on Newton's law in the viscous sublayer and the mixing length hypothesis in the turbulent zone was developed by Pezzinga (1999).

In the literature on water hammer, the extensively used turbulence models were algebraic models (Ohmi et al., 1985; Pezzinga, 1999; Silva-Araya and Chaudhry, 1997/2001; Vardy and Hwang, 1991), in which the eddy viscosity was expressed as some algebraic function of the mean flow field. Other sophisticated models (such as the k-ε model, which require additional differential equations for eddy viscosity) have also been tried by Eichinger and Lein (1992). These models were comparatively studied by Ghidaoui (2001).

Trikha (1975) believed that Zielke's formula results could be reasonable for low Re turbulent flows, but Vardy and Brown (1993) advised not to use Zielke's formula outside the laminar flow regime. Vardy and Brown (1993) also mentioned that applying Zielke's formula to turbulent flows showed less error for short period pulses. Vardy and Brown (1995/2003) modeled the frequency-dependent friction model for the unsteady turbulent flow throughout water hammer and derived a convolution integral. They used the frozen turbulence hypothesis with the assumption that eddy viscosity was time invariant. To assess the accuracy of their prediction models, Zhao and Ghidaoui (2004) studied water hammer waves using the k-ε turbulence model. They showed that the frozen turbulence model could not capture the dissipation of the water hammer waves in turbulent flow correctly when the flow rate was increased or decreased. Their predictions using k-ε turbulence model showed better agreement with the experimental results.

Raise et al. (2009) also used CFD to study water hammer waves in unsteady turbulent flow in a straight pipe. They used Wilcox k-ω turbulence model. Their predictions were in good agreement with the experimental results of Bergant et al. (2001). Bergant et al. (2001)

experimentally investigated water hammer waves in turbulent flows for Re=5600. For turbulent flows, although the CFD has been successfully used to study water hammer waves by using k-ε and *k*-ω turbulence models, it has not been used to study acoustic wave resonance.

Indeed, the application of most friction models described above was focused on water hammer analysis. The experimental validations of these models were also performed under the conditions of very low frequency (i.e., less than 50Hz), which were suitable for the water hammer phenomena. The friction model capabilities for the frequency response analysis under a high oscillating frequency and a high Re turbulent flow was unfolding.

2.4 Numerical Methods

By using computers after the fifties, the researchers had commenced to apply numerical methods to solve the differential equation systems. Some of the methods that have been recommended to solve the water hammer equations include the Method of Characteristics (MOC), Finite Differences (FD), Wave Characteristic Method (WCM), Finite Elements (FE), and Finite Volume (FV). The MOC method has been one of the most popular among the other approaches, because it provides the required accuracy, numerical efficiency and programming simplicity (Ghidaoui et al., 2005; Wylie & Streeter, 1993; Zhao & Ghidaoui, 2004). Indeed, in a review of commercially available water hammer software packages, it was found that eleven out of fourteen software packages used MOC schemes (Ghidaoui et al., 2005). Details about these methods can be found in Chaudhry and Hussaini (1985), Ghidaoui and Karney (1994), Szymkiewicz and Mitosek (2004), Wood et al. (2005), and Zhao and Ghidaoui (2004).

The 1D numerical methods were also used to approximate the velocity and pressure perturbations in a piping system. Wood et al. (1966) presented the Lagrangian method. Wood

(2005) showed that for large pipe system problems, the Lagrangian method needed less CPU time than the MOC. Although the second order FD method proposed by Chaudhry and Hussaini (1985) showed better results than the first order MOC, the method required more execution time and storage requirement. Guinot (2003) used the first-order FV Gudonov-type method for water hammer problems. Zhao and Ghidaoui (2004) compared his developed second-order explicit FV Gudonov-type method with MOC and found that the second-order explicit FV Gudonov-type method needed much less CPU time than the MOC with space-line interpolation. Ghidaoui et al. (2005) provided a review of each technique.

2.5 Aeroacoustics Simulations

For aero-acoustic problems in branched piping systems, a two-dimensional model was recommended by Nelson et al. (1983) and Bruggeman et al. (1991) to predict the acoustic resonance and hydrodynamic conditions required for the self-sustained excitation.

Bruggeman et al. (1989/1991) found that the moving vortices excite the acoustic oscillation by simulating the flow at the opening of the resonated side-branches. In their developed model, the acoustic pressure triggered by the oscillated shear layer was independent of the acoustic amplitude. Their method accurately predicted the frequency of oscillations produced by moving flows in a pipe system with closed side branches, but over-predicted the measured amplitude by about 6 times for pipes with a circular cross-section. Graf (1989) developed Bruggeman's vortex bulb model by involving the imaginary component of the excitation source. This assumption led him to consider the phase shift between shear layer excitation and acoustic oscillation. Dequand et al. (2003) and Kriesels et al. (1995) suggested models added prediction of the flow velocity resonance range and the amplitude of acoustic pulsations to the Bruggeman et al. (1991) model.

Kriesels et al. (1995) used a 2D model based on the vortex blob method to simulate the flow in T-junctions and analyzed the acoustic power produced by the separated shear layers. Their studies tried to realize the excitation mechanism and find the flow velocity range that caused acoustic excitation, but their models were not proposed to predict the amplitude of pulsation. Afterward, several models and numerical methods were used to predict the pulsation amplitude as a function of the flow velocity. Radavich et al. (2001) solved compressible, unsteady, and turbulent Navier–Stokes equations with an implicit and non-iterative method to model a 2D T-Junction. Their simulation demonstrated the results of the flow visualization study reported by Ziada (1994), but was unable to correctly predict the amplitude of pulsation. It was under-predicted by 50%. Dequand et al. (2003) tried to model a coaxial branch case using Euler equations for 2D compressible flow. For a 2D coaxial simulation, their method enhanced the prediction accuracy of the maximum pulsation amplitude to less than 40% of the experimental results. Also, their amplitude predictions were sensitive to the flow condition. Arthurs and Ziada (2009) performed a numerical analysis of the acoustic mode shapes and frequencies to investigate the aero-acoustic response of an annular duct. They used the ABAQUS FE software. The finite element model found all the possible eigenvalues by solving the Helmholtz equation in three dimensions. Since the simulations were performed to predict resonant frequencies, the effects of the flow were not considered in the solver. The results of the numerical simulations were validated against experimental results. The frequency of the oscillations and the phase shift between the oscillations at the branch ends were predicted well. For the branches at which the length of the branch over its diameter was less than 2, the frequency of the first mode was not well predicted.

Martınez-Lera et al. (2009) simulated acoustic source for 2D incompressible laminar flow in

T-junctions. They modeled their case with a commercial software, Fluent 6.3. Based on the width of the branches, they modeled their cases for a Re less than 3000 and exempted the effect of turbulence. They claimed that their results were in good agreement with numerical approaches that were more sophisticated. Graf and Ziada (2010) proposed a model for predicting the pulsation behavior of double side branched systems for various depths of the side branches and different static pressures by assuming empirical source terms. Each sound source was measured experimentally in double side branch systems. Due to the fact that the pressure of the source was measured experimentally for highly turbulent flowing air in pipes, they believed the proposed model was suitable for predicting the self-sustained oscillations in industrial applications. Also, the model was capable of predicting resonant frequencies and flow velocities at which the resonances started. Moreover, they employed the energy balance method to predict the self-sustained oscillations. In this method, the frequency of oscillations was approximated by the Eigen-Frequency of each mode. The amplitude of the oscillation was estimated using a balance between the time-averaged acoustic source power and the time-averaged acoustic power losses. Another method for the acoustic source estimation was presented by Tonon et al. (2011). Tonon et al. (2011) developed a model by linking the Bruggeman et al. (1987/1991) model and the empirical approach of Graf and Ziada (2010) to predict the amplitude of oscillation of any mode. They found that the first predicted mode using their model showed the oscillation amplitude within a 20 percent accuracy for a row of side branches of equal length and within a 50 percent accuracy when the system was detuned by varying the side branch length. Nakiboglu et al. (2012) investigated the vortex and branch resonance interaction for single and multiple branches. They applied the Martınez-Lera et al. (2009) methodology in their investigations. They successfully investigated the flow velocity and the sound intensity effects on the aero-acoustic

sources. Their studies have not been validated for the turbulent pipe flow.

Although the models and the numerical methods discussed above have shown promise in predicting moderate amplitude pulsations for 2D applications, they do not seem suitable for problematic industrial situations, which involve nonlinear and large amplitude pulsations excited by three-dimensional (3D) turbulent flows.

2.6 Conclusions of the Review

The previous researches discussed in this chapter support the following broad conclusions:

a) The reviews of the experimental studies showed that most of them were conducted for water hammer, aero-acoustic, or frequencies less than 100 Hz.
b) The effects of the tubes' wall materials, thicknesses, and different branch configurations on the acoustic resonance have not been investigated experimentally. There was no comprehensive experimental investigation in the frequency range that had occurred in the nuclear industry.
c) An unsteady and frequency-dependent frictional effect in fluid flow in pipes is a function of flow conditions and liquid properties. The effect of frictional contribution in turbulent flow damping needs to be further investigated, because it has not been fully understood. Also, some experiments to explore the damping effect in the turbulent flow in a broad frequency range need to be conducted.
d) As most of the available numerical studies are based on laminar, 2D, and restricted turbulence flow simulations, they are still required to be validated quantitatively against the experimental data for a high Re turbulent pipe flow.

e) The numerical simulation of acoustic waves in water hammer applications was done in many studies. To predict the damping of the water hammer waves, several researchers developed formulations for laminar and turbulent flows. They approximated the Navier–Stokes equations to determine the frequency-dependent damping terms. Although the analyses with differently developed damping terms generally showed a good prediction of the water hammer wave propagation in laminar flows, they were not verified against the acoustic wave resonance experimental data.

f) The focus of the self-sustained oscillation experiments was on the systems with single, tandem, and coaxial side branches of different sizes and distances with air flow. Since those studies were based on air flow rather than liquid flow, it is unknown how it can be applied directly to liquid flow.

g) The aero-acoustic resonances for branched configurations were studied, and it was concluded that each geometrical variation influenced both the pulsation frequencies and the pulsation amplitudes of the branches. Further investigations with water instead of air, and an additional explicit excitation source to study their influences on the main line and the branches' frequency resonances and amplifications in the frequency range of 20–500 Hz are necessary.

h) Although there are some studies for water hammer prediction using the CFD solution, the subject has not been studied for acoustic resonance problems.

i) Therefore, a better understanding of the acoustic resonance phenomenon is required for computer codes to accurately analyze this phenomenon for the complex systems found in nuclear reactors.

Chapter 3 Experimental Strategy

3.1 Introduction

Simple and trustworthy experiments of acoustic resonance in small fluid-filled piping systems can provide an abundance of useful data. Indeed, assessing the acoustic resonance behavior of a straight pipe and a simple branch system is crucial to understand the resonant frequency and the resonant amplitude of complex piping networks, such as is found in a nuclear reactor. In a complex piping system, different parts may have different parameters, such as sizes, sonic velocities, materials and so on. A simple system with a low level of uncertainty helps to examine the effects of these parameters on the acoustic resonance.

This study aims to create a benchmark data for a few simple tubing systems and experimentally quantify the effects of wall thickness, material, and geometry on acoustic resonance at different boundary conditions. To do so, four straight tubes with different wall thicknesses and materials and five different branch configurations with open- and close-ended outlets are examined. Some of these experiments are performed for laminar and turbulent mean flows. The acoustic pressure, temperature, and flow velocity are measured for all the experiments. Finally, the results are obtained for the frequency range of 20–500 Hz.

This chapter starts with descriptions of the experimental system as well as the measuring instruments used in this study. The measurement procedures employed to perform acoustic resonance experiments and data presentation are then explained.

3.2 Overview of the Experimental System

An experimental system is designed and built at the University of Manitoba to study acoustic resonance in fluid-filled tubes with zero and non-zero mean velocities for different wall thicknesses and materials. This experimental system consists of five principal subsystems: pipelines, water supply, shaker and cylinder, data acquisition system and instruments. These five subsystems are positioned at constraint locations with a constant room temperature in order to isolate them from mechanical vibrations and temperature variations. Schematic diagrams of the test loops are shown in Figures 3.1, 3.2, and 3.3 respectively.

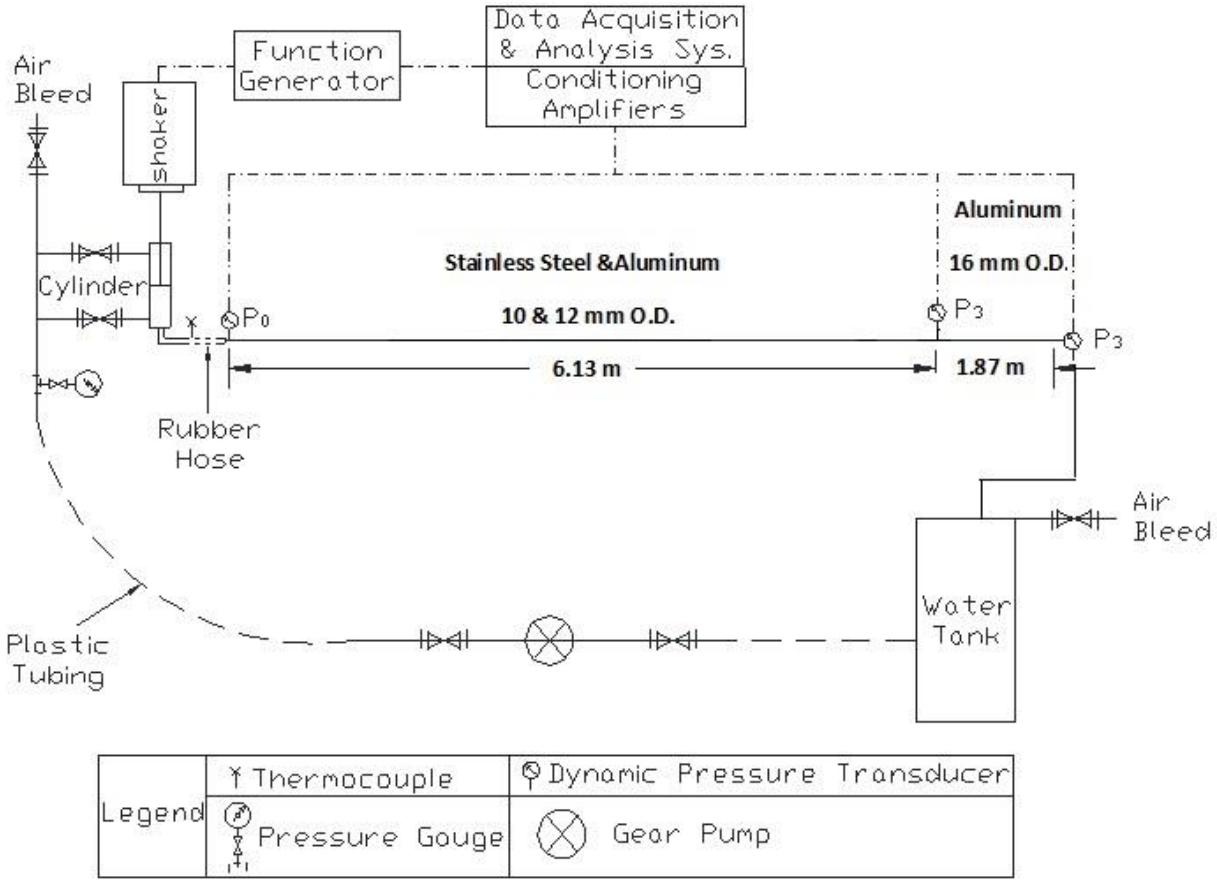

Figure 3.1: Schematic Diagram of the Straight Tube Experiments

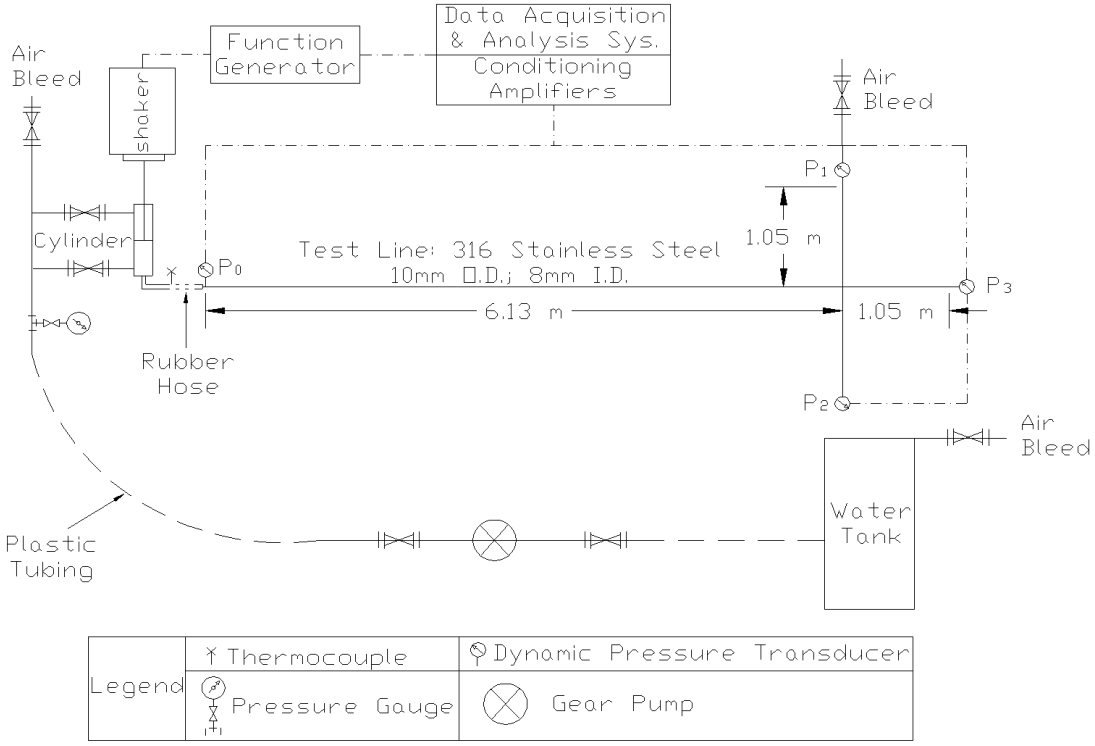

Figure 3.2: Schematic Diagram of Elbow and Equal Branches Experiments

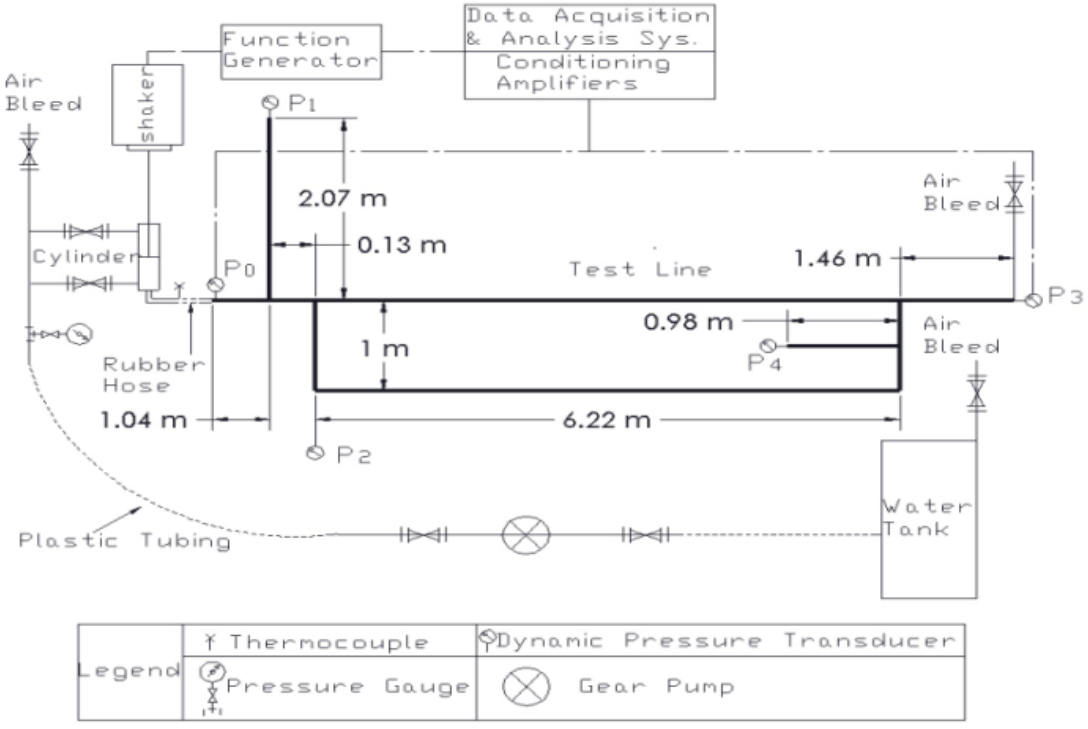

Figure 3.3: Schematic Diagram of the Unequal Branch and Complex Experiment

3.2.1 The Pipeline System

In the present study, twelve sets of experiments (with and without flow) are designed. The test lines are made of type 316 stainless steel (SS) and type 6061 Aluminum (Al) tubes with an inner diameter (I.D.) of 8 mm and outside diameter (O.D.) of 10, 12, and 16 mm. The 1st and 2nd experiments consist of two tubes with the same length (6.13 m) and I.D. (8 mm) and two different wall thicknesses of 1 mm and 2 mm respectively, made from SS tubing. In the 3rd experiment, the Al tube with the same dimension of the SS tube in the 2nd experiment is tested. The 4th experiment is designed for the 8 m length tube formed from two Al tubes of unequal length (6.13 & 1.87 mm) with two different wall thicknesses (2 & 4 mm respectively).

In the 5th experiment with elbow configuration and the 6th and 7th experiments with equal size branched configurations, SS tubes with 8 mm I.D., 10 mm O.D., 6.13 m length for the main line, and 1.05 m elongation for the elbow and branches are investigated. The 6th experiment with a T-branch and the 7th experiment with one upward branch and one straight line are shown in Figure 3.2. In the 8th experiment conducted, two unequal size branch SS tubes (1.05 & 2.07 m) with the same I.D. and O.D. of the equal branches experiments are studied. The side branches are formed by two T-junctions placed along a mainline tube.

For the 9th experiment, a combination of different wall thicknesses (1 & 2 mm), materials (SS and Al), and unequal branches (2.07 and 0.98 m) is examined.

The 1st, 8th and 9th experiments are also studied for different inflow conditions, and they are assumed as the 10th, 11th and 12th experiments. For the last six experiments, the acoustic field can show the resonant peaks, which are related to the closed side branches and the mainline tube segment. These peaks occur at the resonance frequencies estimated from $f_n = (2n - 1) \times c_0/ (4L)$.

Since junction elements with I.D. $_{\text{side branch}}$/I.D. $_{\text{mainline}}$ = 1 are widely used in industrial

applications, our study uses only side branches with an I.D. equal to the mainline tube I.D. Each junction element presents rounded edges with a radius of curvature of about $r_{corner}=0.1I.D_{side\ branch}$.

The test lines are supported at 25 cm intervals by cushioned clamps to minimize line vibrations. A short rubber hose (~10 cm length) is also located between the cylinder and the test lines to minimize the structure-born vibrations from the cylinder and shaker.

3.2.2 Water-Supply System

The water supply system involves a Stenner M45 Model peristaltic pump to pressurize the system with distilled water. The system is pressurized since the water maintains a gauge pressure of 413.6–551.5 kPa (60–80 psig). Water is pumped from a distilled water tank into the system to avoid being mixed with air. The water is circulated by an Oberdorfer N2000 Model gear pump. To eliminate water hammer effects on the water-feed loop, two plastic tubes are located at the upstream and downstream ends of the gear pump section. A filter system used in the experiments extracts undesirable particles from the water. In order to vent the moving air bubbles and the trapped air from the experiments without changing the system pressure, a Honeywell PV100 (PV Series Super Vent) air separator is located after the gear pump. It is installed in the horizontal line. A 200 liter water tank also stores water for the open-ended experiments. In summary, the water-supply system pressurizes and circulates air-free water to the experimental tubes. The tank, the peristaltic pump and the gear pump used are depicted in Figure 3.4.

3.2.3 Shaker and Cylinder

An LDS V408 Model electromechanical shaker (fixed by a personally designed aluminum support to minimize its vibration, shown in Figure 3.5) is driven on a double-acting cylinder to create oscillating pressure waves. The cylinder is located at the upstream end of the test lines. Moreover, to stabilize the applied force on the shaker, the inlet and the outlet ports of the cylinder are connected to the water-feed loop. The exit of the cylinder is also attached to a plastic tube to minimize system noises. The sketch of an adaptor designed to align the shaker and cylinder is displayed in Appendix A.

a)

b)

c)

Figure 3.4: a) Tank b) Gear Pump c) Peristaltic Pump

3.2.4 Measurement System

3.2.4.1 Shaker Control

To vary the amplitude and frequency of the input sine waves to the shaker, an LDS PA100E-CE amplifier, an NI PCI-6731 high-speed analog output board, a function generating program 'Function Generator' (NI LabVIEW 7.1 is used as a system interface and is shown in Figure 3.6), and a PC station are employed.

Figure 3.5: Shaker and Cylinder

3.2.4.2 Data Conditioning and Acquisition System

A PCB model 482A16 signal conditioner, an NI PCI-4472 8-channel dynamic signal acquisition board, a data acquisition program 'DAQ-Test' and a PC station are utilized to receive signals from the pressure transducers (system interface is shown in Figure 3.7). The conditioned pressure signals are transmitted to the ports on a National Instruments board (Model NI PCI-4472-8) with 24-bit resolution. Since the board can be operated in 8 simultaneous acquisition modes, it is able to sample the data at the rate of 102.4 kS/s, in which $k = 10^3$ and S is the number of samples. A

total of four pressure transducers are employed, so the effective sampling rate is not reduced. In essence, two considerations are required to determine whether this sampling rate is adequate or not. First, for a characterization of the acoustic pressure in the frequency domain, the sampling rate should be at least twice the maximum frequency of interest (Nyquist theorem). Second, for the representation of the acoustic pressure in the time domain, at least five samples per cycle is required; however, a minimum of 10 samples per cycle is more appropriate (Bendat & Piersol, 2010). Considering these requirements together, the acquisition system should have a sampling rate of at least 10 times as high as the maximum test frequency, which is approximately corresponded to 5000 Hz. This value is approximately a factor of 20 lower than the acquisition rate of 102.4 kS/s per channel. In addition, it is important to realize that not only does this type of board consists of one A/D (analog / digital) converter, but also the acquisition of 8 pressure signals is accomplished using a multiplexing technique.

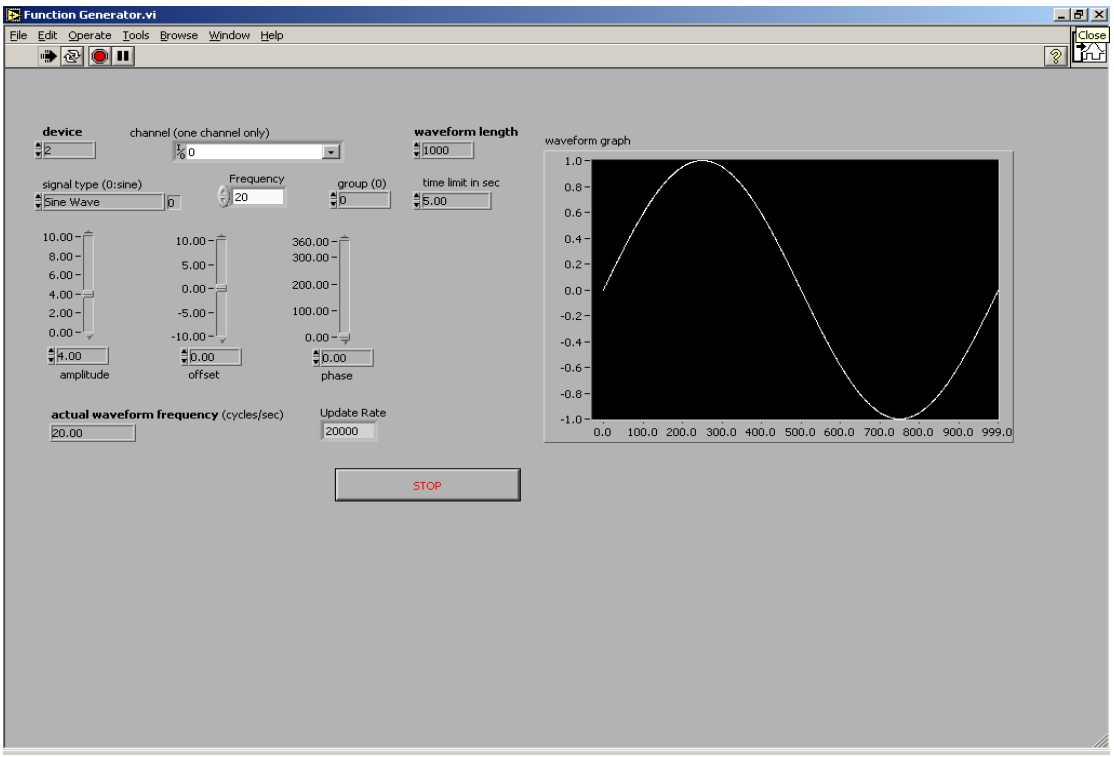

Figure 3.6: The Function Generating Interface 'Function Generator'

The scan interval is also defined as the time required for going from a recorded point corresponding to pressure transducer No. 1, through the sequence of the other three transducers, and return to the channel of transducer No. 1. This scan interval is basically the inverse of the maximum data acquisition rate per channel ($1/102.4\times10^3$), which approximately corresponds to 10 μs.

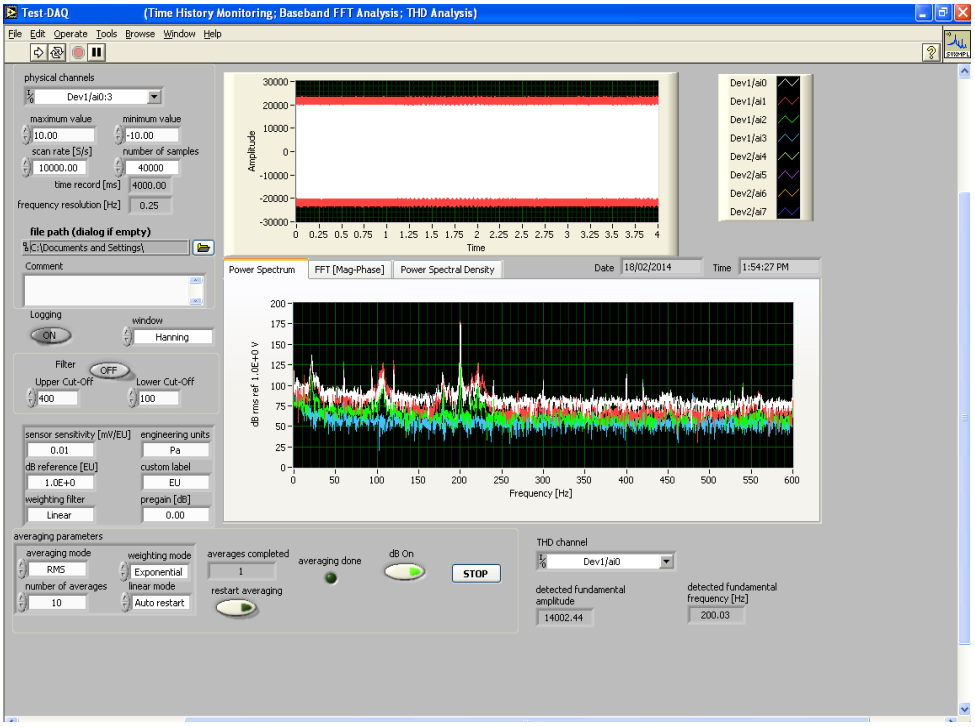

Figure 3.7: The 8-Channel Data Acquisition Interface 'DAQ-Test'

3.2.4.3 Dynamic Pressure Measurement

The acoustic pressure is measured with PCB 112A22 pressure transducers along the inlet (upstream), outlet (downstream), and some other specified locations of the tubes. They are labeled as P_0 for inlet and P_1, P_2, and P_3 for specified locations or outlets. The resolution of the transducers is 0.001 psi and the rise time is 2 μs. Since the dynamic pressure transducers used in

the experiments are new and factory calibrated, an on-field calibration is not performed. Each pressure transducer is also flush mounted to the interior surface of the tube. The sketch of the designed transducer holders are shown in Appendix A. The distance between the surface of the mounted pressure transducers and the centerline of the test lines is short enough (~8 mm) to not distort the signals. This mounting arrangement ensures that for the range of frequencies in this investigation, no signal distortion effects are generated at the tube interior in the region between the face of the transducer and the tube inner surface.

The signals from the dynamic pressure transducers are routed to the multi-channel signal conditioner PCB model 482A16. This multi-channel conditioner permits the self-determining adjustment of the pressure transducer signal gains. Thus, it is possible to employ the same value of gain for all the acoustic pressure measurements. This gain adjustment is important to meet the required voltage input levels of the A/D board. The outputs from the conditioner are connected to the NI PCI-4472 8-channel data acquisition board, which stores the data at a PC for detailed post-processing. The program 'DAQ-Test' controls the data acquisition, filters the noises, and performs a simple on-line analysis.

3.2.4.4 Static Pressure Measurement

To measure the system pressure, a new static pressure gauge is placed before the cylinder.

3.2.4.5 Temperature Measurement

The K-type thin thermocouples are mounted on T-junctions at the upstream and downstream

ends of the system to measure the water temperature. The thermocouples are connected to a PC to store the data every 30 minutes. K-Type provides measurements with an accuracy of ±1°C. The thermocouples are brand new and calibrated using two point method (at ice and boiling points). The following procedure is followed to calibrate the thermocouples.

1- Distilled water is used for making cubic ice and boiling water.

2- The thermocouples are stirred in the Pyrex glasses contained ice and water and boiling water.

3- Temperatures data are recorded three times in ice bath and boing water.

4- The following correlation is used to calibrate the thermocouples.

T= Z* Thermocouple reading + S1

Where T is calibrated temperature in ^{o}C, Z is difference between standard boiling and ice points (99.25-0) temperatures over the difference between uncalibrated readings of boiling and ice points temperatures and S1 is difference between standard ice temperature and multiplication of Z and ice bath temperature.

3.2.4.6 Flow Rate Measurement

To measure the mean velocity of the experiments with flowing fluid, the OMEGA FTB4607 turbine flow meter is employed. The FTB4607 series of flow meters are highly accurate and feature a high frequency pulse output, which is suitable for the flow rate indication. The mean velocity pulse outputs are read with the OMEGA DPF700 series rate meter and stored in the PC every 5 minutes. The flow meter is factory calibrated and located at the downstream of the gear pump to measure the flow rate. The flow rate is attained from the manufacturer provided data at which the pulse rate is multiplied with a flow rate constant (75.7 Pulses per U.S. Gallon/Minute).

3.3 Experimental Procedure

3.3.1 Air-Bubbles Venting

Even the presence of small amounts of air bubbles in the liquid is able to largely influence the frequency response of a fluid-filled tube. An obvious consequence is the sound speed reduction in a liquid test line. Before commencing each test, the test line is filled with water, pressurized, and carefully vented to remove trapped air to prevent the existence of air bubbles in the test line. Also, by employing the air separator, any remnant trapped air or entry air bubbles in the system are vented out into the atmosphere.

3.3.2 System Pressure Control

After the removal of the air bubbles, all the equipment are turned on. The system pressure is increased by employing the peristaltic pump, or decreased by opening the ball valves. The ball valves are located at the upstream and downstream ends of the experimental system.

3.3.3 Mean Velocity Measurement

For the wide range of measurements during the course of this investigation, it is necessary to have an accurate and repeatable means to determine the mean flow velocity. The flow meter is brand new and factory calibrated. For the experiments that include the mean flow, velocities are adjusted by the gear pump.

3.3.4 Sound Speed Measurement

To check the accuracy of the test due to existence of air bubbles, the sonic velocity of water is measured before each experiment. Because the sonic velocity of water is very sensitive to small amount of air bubbles in system, the sonic velocity of water is measured for all the tests at different system pressures and frequencies. These sonic velocities are compared with each other at each test and with the theoretical sound speed. The theoretical sonic velocity calculation is given by Chaudhry (1987) as

$$C=C_0[1+\Psi\left(\frac{K}{E}\right)]^{-\frac{1}{2}} \quad (3.1)$$

where C_0 is the liquid sonic velocity, K and E are the bulk modulus of elasticity of fluid and Young's modulus of elasticity of the line. For a thin wall, ψ (non-dimensional parameter) which describes the elastic properties of the pipe takes the form of

$$\Psi=2(1+v)[\frac{(R^2+r^2)-2vr^2}{R^2-r^2}] \quad (3.2)$$

If the calculated sonic velocity has a large deviation from the measured one, it is assumed that air bubbles are trapped in the fluid line. Releasing the air is repeated several times until a constant sonic velocity is obtained. To avoid air bubbles from entering the tested system, distilled water is pumped into the system.

The sonic velocity is measured by shutting off the system and inducing pulses at different frequencies, in the frequency range of interest (every 50 Hz for straight-lines and every 25 Hz for branches and elbow experiments) and data are stored every 0.0001 s. By dividing the distance

between the pressure transducers by their measured time delay, the sonic velocity is obtained. Before starting the test, the line is filled with water and pressurized for more than 100 psi, which is more than the experimental system pressure, and carefully vented to remove trapped air through the ball valves. To ensure that the measured sonic velocity is accurate, the air releasing is repeated several times to get the constant results close to the calculated speed of sound. By using the air separator after the gear pump, a complete release of the air bubbles is insured. The moving and trapped air bubbles in a fluid-filled system influence the propagation velocity of a pressure wave in the pipeline and shift resonant frequencies. Kobori, Yokoyama, and Miyashiro (1955) showed that small air content decreases the speed of sound from that in pure water. The method of measuring sonic velocity in a fluid-filled line was established by Chaudhry (1987).

3.3.5 Pressure Control

The acoustic wave frequency for every test is increased manually and then holds until the steady acoustic pressure is obtained. To measure the acoustic pressure accurately, the tested frequencies are increased at 2 Hz for the off-resonance regions and 0.25 Hz for the resonance peaks. The static fluid pressure is also hand-logged every hour.

3.3.6 Data Processing

A fast Fourier transform (FFT) analysis is applied to the time series acoustic pressure data using a NI LabVIEW 7.1 FFT analysis program. The FFT analysis interface is shown in Figure 3.8. Thus, to get the amplitude of the acoustic pressure at a chosen point on the test lines, the

measured acoustic pressure at that point is normalized by the upstream value P_0. By normalizing measured acoustic pressure with the upstream acoustic pressure the effects of vibrations and any disturbances before upstream pressure are omitted.

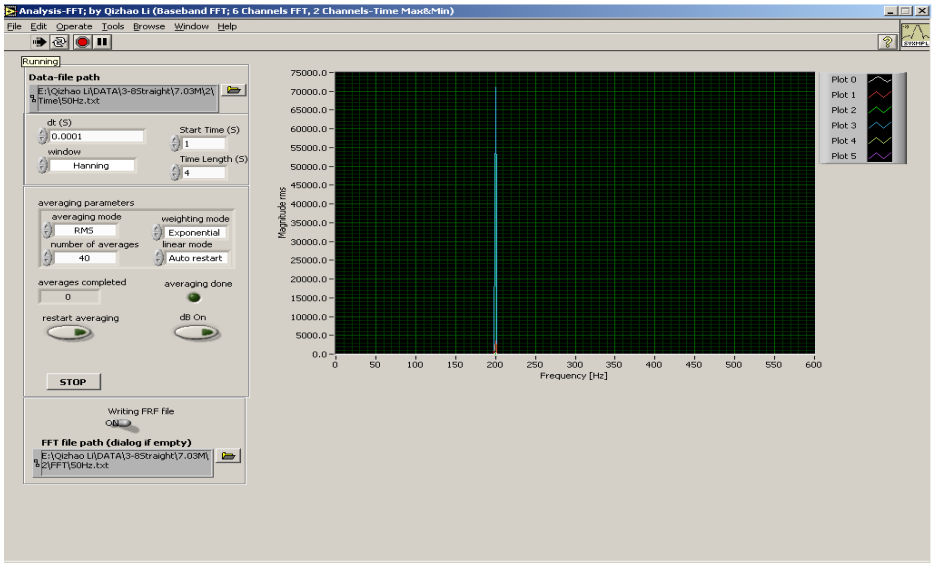

Figure 3.8: FFT Analysis Interface 'Analysis-FFT'

The main parameters for spectral analysis using the FFT must be properly defined to get adequate resolution in the frequency domain and at the same time minimize the amount of collected data. To define correct values for each parameter, averaging of the test series is performed using broadband noise input. The parameters are the number of samples acquired per data set, the sampling rate and the number of data sets that are employed to obtain an average. The sampling rate (f_s) is defined to meet the Nyquist theorem. This value equals to the frequency resolution (Δf) multiplied by the number of samples per data set (n_s). Once the sampling rate is determined for each experiment, the number of samples should be at least according to $n_s = f_s/\Delta f$. To determine the value of Δf, another set of experiments is performed. In this work, the interested frequency range is from 20–500 Hz. Therefore, the sampling rate of the acoustic

pressures is set at 10,000 samples/second in each experiment. Also, to meet the requirement of frequency resolution of 0.25 Hz in the post processing of the data, the recorded time is 8 seconds for all the experiments. This is deemed to be adequate. The experimental results show that Δf = 0.25 Hz adequately characterizes the system response while providing acceptable frequency resolution at both the low and high ends of the resonant frequency range. The presented results are obtained by averaging a total of 10 data sets at the resonant points. The uncertainty values indicate that averages of 10 data sets are adequate for estimating standard deviation. For example, the uncertainty value at the 3rd resonant peak of the 1st experiment, which is measured 10 times, is indistinguishable from the value determined from a larger number of measurements, up to a total of 30 times, within an uncertainty of ±0.43%. According to Newland (1993), an accuracy of σ /m can be estimated using the relationship σ /m $\approx$ 1/ $\sqrt{B_e * T}$, in which σ and m are the standard deviation and the mean value of the measurement respectively. B_e is the effective bandwidth of the spectral window and T is the record length. Using the effective value of record length T, the results of σ/m is estimated at about 0.316. In the assessment of Newland (1993), it is indicated that the value of $\sigma/m=\frac{1}{3}$ is generally acceptable. This assessment is employed for resonant peaks of all the experiments. The measurements for all the resonant peaks are tabulated in Appendix C.

3.4 Data Presentation

Since the focus of this study is on the resonant frequency and amplitude, most of the changes in color levels are concentrated at different trends of experiments and predictions. Complete families of spectra are provided in separate figures to allow a perspective on acoustic pressure

versus frequency and identification of high values of pressure amplitude. The Y direction in the plots that show the normalized acoustic pressure over frequency is presented on a logarithmic scale. This is an effective approach to identify resonance and non-resonance frequencies.

Chapter 4 Linear Wave Solution Model Description

4.1 Introduction

While designing and maintaining a nuclear reactor, it is vital to make sure that under any operation circumstances, acoustic resonance does not occur. As the experimental data are not always available for designers or operators, trustworthy theoretical or numerical methods are required to study reactors acoustic responses.

In this study, the acoustic pressure variation due to the explicit excitation imposed on the fluid-filled tubing system is studied using LWS. LWS is employed to identify the resonant frequency and amplitude of the tubes with different wall thicknesses, materials, and geometries. The effects of the tube material and wall thickness are taken into account on the sonic velocity and frequency-dependent friction terms.

In this study, the ABAQUS commercial software 6.12 is utilized to analyze the acoustic pressure responses of the rigid tubes with different geometries and outlet boundary conditions subjected to an inlet sinusoidal pressure excitation.

To begin with, the constant damping parameter is described and, thereafter, the details concerning the implementation of the six developed unsteady friction methods (Kagawa et al., 1983; Schohl, 1993; Trikha, 1975; Urbanowicz & Zarzycki (2012); Vardy & Brown, 2004; Vitkovsky et al., 2004) on ABAQUS are discussed and presented. The assessed frequency-dependent friction methodologies are based on a convolution of the past flow conditions with a weighting function. The weighting functions are formed by theoretical analyses using different assumptions on the flow conditions. Subsequently, other details like the boundary conditions as

well as the initial values employed in ABAQUS are given. This study seeks to determine LWS capabilities in predicting frequency resonances and amplifications of the tested pipeline systems. The ABAQUS general formulation can be found in Appendix B.

4.2 Constant Damping Parameter

The earliest water hammer analyses by Allievi (1902), Frizell (1989), and Joukowski (1989) neglected viscous dissipation. In those pulsating and oscillating flow simulations with neglected viscous dissipation, the ratios of the outlet to inlet pressure amplitude were much larger than measured. Studies by Brown et al. (1969), D'Souza and Oldenburger (1964), Gellach and Parker (1967), and Purdy et al. (1964) showed that the pressure amplitude ratio changes in unsteady flows were because of the presence of viscous dissipation.

The overall unsteady flow behavior explanation needs the continuity, momentum and energy equations together with constitutive relations describing the fluid properties and, in the case of turbulence flow, some turbulence models. The energy equation does not need to be solved for the flows without heat addition. The viscous dissipation can be found by dissecting the momentum equation.

The general equation of the motion of a viscous and compressible fluid in vector notation when the Newtonian stress tensor is inserted into the equation of motion is:

$$\rho \frac{D\bar{v}}{Dt} = -\nabla p + \left(\frac{1}{3}\mu + \lambda\right)\nabla(\nabla.\bar{v}) + \mu\nabla^2\bar{v} + \rho\bar{g} \tag{4.1}$$

where μ (shear viscosity) and λ (volume viscosity) are considered constant. The operators in equation (4.1) are gradient, divergence and Laplacian. The volume viscosity is noticeable in

liquid pulsating flows, since it shows a viscous dissipation during fluid condensation and expansion. Hirai and Eyring (1958) stated that volume viscosity is large at high frequencies.

Disregarding the body force and substituting the substantial derivative with its equivalent of

$$\frac{D\bar{v}}{Dt} = \bar{v}\,(\nabla.\,\bar{v}) + \frac{\partial \bar{v}}{\partial t}$$

Equation (4.1) becomes:

$$\rho\frac{\partial \bar{v}}{\partial t} - \rho\bar{v}\,(\nabla.\,\bar{v}) = -\nabla p + \left(\frac{1}{3}\mu + \lambda\right)\nabla(\nabla.\,\bar{v}) + \mu\nabla^2\bar{v} \tag{4.2}$$

An assumption can be made that the $\rho\bar{v}\,(\nabla.\,\bar{v})$ term on the left hand side can be ignored because it is negligible compared to the other terms. If so, equation (4.2) becomes:

$$\nabla p + \left(\frac{1}{3}\mu + \lambda\right)\nabla(\nabla.\,\bar{v}) - \mu\nabla^2\bar{v} + \rho\frac{\partial \bar{v}}{\partial t} = 0 \tag{4.3}$$

Expressing the equation in cylindrical coordinates and assuming there is no radial flow, equation (4.2) becomes dependent only on the axial velocity. In the oscillating and the pulsating flows in a pipe, there are some existing radial flow perturbations and the axial flows in a pipe cross-section are not the same, especially when they are close to the wall. In the simplified 1D calculations, the radial velocity is ignored everywhere, and the axial velocity is constant at a specific point. These assumptions become less valid as the pipe diameter becomes large.

Considering a 1D flow with only x direction velocity, equation (4.3) becomes

$$\frac{\partial p}{\partial x} + \left[\left(\frac{1}{3}\mu + \lambda\right)\frac{\partial^2 v}{\partial x^2} - \mu\frac{1}{r}\frac{\partial}{\partial r}\left(r\frac{\partial v}{\partial r}\right)\right] + \rho\frac{\partial v}{\partial t} = 0 \tag{4.4}$$

In equation (4.4), the second term in the bracket represents the frictional effects. This term can be calculated numerically if the velocity in axial and radial directions is known in every cross-section. Due to the unknown distribution of the axial velocity in the radial direction of 1D simulation, the dissipation term in the bracket needs to be simplified by some approximations. The easiest simplification could assume the viscosity in the dissipation term equal to zero. This assumption is valid for lossless fluid flow. A better approximation could assume that dissipation is proportional to the mean velocity or to the square of the mean velocity. Wood (1937) assumed that dissipation was proportional to velocity. The term in the bracket in equation (4.4) is assumed to be a damping factor times the cross-section average velocity.

$$\frac{\partial p}{\partial x} + \mu \mathrm{F} v_{average} + \rho \frac{\partial v_{average}}{\partial t} = 0 \qquad (4.5)$$

Substituting μ F with r gives the same equation that is solved with ABAQUS. The r refers to the volumetric drag.

A better approximation of the viscous dissipation in equation (4.4) can be obtained by the numerical evaluation of the viscous damping term. The assessment of the viscous terms based on numerical approximations can improve the understanding about oscillating and pulsating flows.

4.3 Damping Factors from Unsteady Flow Friction Factors

For a transient laminar flow, Zielke (1967) developed a frequency-dependent viscous dissipation prediction method. He used the method of characteristics solution for water hammer problems. In his simulations, velocities of the earlier times were used to predict the time variation of the

$\mu F v_{average}$ term in an approximate Navier–Stokes equation (4.5). Zielke (1967) and Zielke et al. (1969) and showed that the energy dissipation for higher frequencies was larger in the unsteady laminar flow compared to the steady flow. Also, they mentioned there were no quantitative results for turbulent flow.

4.4 Frequency-Dependent Friction Expressions for Laminar Flow

The 1D momentum and the continuity equation of fluid lines are:

$$\frac{\partial p}{\partial X} + \rho \frac{\partial V}{\partial t} + R(t) = 0 \tag{4.6}$$

$$\frac{1}{K}\frac{\partial p}{\partial t} + \frac{\partial V}{\partial X} = 0 \tag{4.7}$$

when the frictional effect of the laminar flow is frequency-dependent, borrowing from Zielke (1967), R(s) and V(s) are Laplace transforms of R (t) and V (t) respectively and can be shown to be:

$$R(s) = \frac{2\rho s}{(j\lambda)\frac{J_0(j\lambda)}{J_1(j\lambda)} - 2} V(s) \tag{4.8}$$

where J_0 and J_1 are the zero and first order first kind Bessel functions respectively; $\lambda = r\sqrt{\frac{s}{\upsilon}}$; Setting $R_a(s)$ as a non-dimensionalized parameter of R(s) over V(s);

$$R_a(s) = \frac{R(S)}{V(S)\rho s} \tag{4.9}$$

From Goodson and Leonard (1972), for a 4-terminal fluid transmission line:

$$Z(s)=\frac{\rho c}{\pi r^2}\left[1-\left(\frac{2J_1(j\lambda)}{(j\lambda)J_0(j\lambda)}\right)\right]^{-1/2} \quad (4.10)$$

$$\Gamma(s)=\frac{sL}{c}\left[1-\left(\frac{2J_1(j\lambda)}{(j\lambda)J_0(j\lambda)}\right)\right]^{-1/2} \quad (4.11)$$

In equation (4.9), both steady and frequency-dependent friction terms are considered. Assuming M*(s)* = $\left[1-\left(\frac{2J_1(j\lambda)}{(j\lambda)J_0(j\lambda)}\right)\right]^{-1/2}$ from equation (4.7) and (4.8)

$$R_a(s)=M(s)-1 \quad (4.12)$$

Zielke (1967) gave the inverse Laplace transformation of R(s) as:

$$R(t)=\frac{8\rho v}{r^2}v(t)+\frac{4\rho v}{r^2}\int_0^t w'(t-t_1)\frac{\partial v}{\partial t}(t_1)dt_1 \quad (4.13)$$

where $\tau\equiv\frac{v}{r^2}t$; $w'\equiv w(\tau)$

and introduced $w(\tau)$ for $\tau \geq 0.01$ and $\tau < 0.01$

Some researchers (Kagawa et al., 1983; Schohl, 1993; Trikha, 1975; Vardy & Brown, 2004; Vitkovsky et al., 2004; Urbanowicz & Zarzycki, 2012) approximate W (τ) and their approximate expressions are displayed as:

$$W(\tau)\approx W_{apr}(\tau)=\sum_{i=1}^{N} m_i e^{-n_i\tau} \quad (4.14)$$

where m_i, n_i and N are determined based on approximated weighting functions by those researchers. From equations (4.12), (4.13), and (4.14) an approximate expression in the frequency domain can be applied in ABAQUS and found as follows:

$$R_{aU}(s)=\frac{4v}{r^2}\sum_{i=1}^{N} m_i e^{-n_i\tau}\frac{m_i}{s+n_i\frac{v}{r^2}} \quad (4.15)$$

4.5 Model Description

The models in this study are a circular tube with a constant cross-section area. At the inlet, a sinusoidal pressure excitation is applied. The outlet is closed or open to a big tank (400 Liter) and the outlet boundary conditions for close- or open-ended cases are assumed zero velocity perturbation or zero pressure perturbation, respectively. The cases are simulated according to the dimensions of Figures 3.1, 3.2, and 3.3.

4.6 Material and Boundary Conditions

For the acoustic medium, the bulk modulus ($K = \rho c^2$), the volumetric drag, and the frequency-dependent damping terms are defined. To include the structural effect on sonic velocity, the bulk modulus is defined according to the calculated sonic velocities from the Chaudhary equation (1987). The thermal effects are not considered since the temperature is assumed to remain constant. An acoustic pressure impulse is applied at the left-most node of the main lines.

Table 4.1: ABAQUS Material Properties

	1 mm Wall Thickness Stainless Steel Tube	2 mm Wall Thickness Stainless Steel Tube	2 mm Wall Thickness Aluminum Tube	2 & 4 mm Wall Thicknesses Aluminum Tubes
Bulk Modulus, K (N/m^2)	2000480660.72	2124947859.8552	1886020489.82	1873693143.92
H_2O Density ,ρ (Kg/m^3)	998	998	998	998

4.7 Modeling Assumptions

The analyses are done with the following assumptions:

a) The problems are 1D.

b) A harmonic pressure excitation of a single frequency is applied at the inlet and the amplitude of the inlet pressure force is unity.

c) The other end of the models is defined as P'=0 for non-reflective boundaries or rigid walls for reflective ones.

d) The fluid temperatures are set according to the experiments (23^oC). The systems static pressure is about 450 kPa. The material properties are set according to Table 4.1

e) A volumetric drag is used (13200). This value is an empirical value obtained in the Canadian nuclear industry by matching the computational results with the experimental data.

Chapter 5 ANSYS-CFX Model Description

5.1 Introduction

The focus of this chapter is on the CFD modeling of the acoustic resonance, with and without flow in a straight fluid-filled tube. The FE-based FV model ANSYS-CFX 14.5 is used to predict the resonance frequency and amplification. The theories implementing in ANSYS-CFX 14.5 for the turbulence modeling will be presented. Then boundary condition definitions and the mesh studies for the simulations are discussed.

5.2 Motivation and Importance of Present Simulation

The analyses of structures have been broadly done with finite element methods. Several industries (e.g. Nuclear and Automotive industries) have benefited from the FE analysis in design and maintenance phases. Finite element commercial software such as ABAQUS has been used in the nuclear industry to simulate acoustic wave propagation in fluid-filled pipes for several years. On the other hand, CFD codes like ANSYS-CFX have been applied for simulating flowing fluids in mechanical engineering analysis. The investigation of CFD method capabilities for the acoustic wave propagation analysis in fluid-filled tubes might develop this field of analysis. This part of the thesis has two approaches. One, it tries to identify how accurately the CFD code (with or without flow) predicts the resonant frequency. Second, it tries to identify how

trustworthy codes can predict the amplitudes at resonance and non-resonance points in the frequency range of interest.

5.3 ANSYS-CFX Code Description

ANSYS-CFX is a cell-vertex finite volume code and implements coupled implicit and pressure-based solution technique. As the pressure and velocity are co-located, p-v decoupling is handled using a Rhie-Chow approach. The flow variables are stored at the mesh element vertices. ANSYS-CFX uses unstructured FE-based FV method. In this method, variable changes across each element arise from the use of shape functions, which is common in FE techniques. It is also a node-based code. ANSYS-CFX collects control volumes around the element vertices and produces polyhedral control volumes. Its coupled solver estimates all the hydrodynamic equations as a single system. When one iteration is finished, the velocity field and the pressure almost satisfy both momentum and mass conservation—but not completely. This is because of the nonlinear equations. Iteration is still desired, but as momentum and mass continuity are always satisfied, far less iterations are required than with the SIMPLE algorithm. Typically, ANSYS-CFX requires only a few dozen iterations to converge, although a segregated solver would need hundreds or thousands. For the large meshes, this approach causes significant reductions in runtimes. Automated algorithms improve solver convergence behavior in cases with poor quality meshes.

5.3.1 The Governing Equations of ANSYS-CFX 14.5

In ANSYS-CFX, continuity and conservation of momentum equations for laminar flow are expressed in the following form:

$$\frac{\partial \rho}{\partial t}+\frac{\partial}{\partial x_j}(\rho u_j)=0 \tag{5.1}$$

$$\frac{\partial}{\partial t}(\rho u_i)+\frac{\partial}{\partial x_j}\left(\rho u_i u_j\right)=\frac{\partial}{\partial x_j}\left[-p\delta_{ij}+\mu\left\{\frac{\partial u_i}{\partial x_j}+\frac{\partial u_j}{\partial x_i}\right\}\right]+B_i \tag{5.2}$$

where ρ is density, t is time, x is Cartesian coordinate directions, u_i is the fluid's velocity in the direction of axis ith, jth component acting on the faces of the fluid element perpendicular to axis i, δ_{ij} is 1 if i=j, otherwise is zero, p is pressure, μ is dynamic viscosity of the fluid, and B_i is body force.

For an incompressible and isotropic Newtonian fluid, ANSYS-CFX employs this equation for shear stress σ_{ij} in terms of an arbitrary coordinate system as:

$$\sigma_{ij}=-p\delta_{ij}+\mu\left\{\frac{\partial u_i}{\partial x_j}+\frac{\partial u_j}{\partial x_i}\right\} \tag{5.3}$$

5.3.2 ANSYS-CFX Turbulence Modeling

Turbulence is a complex process, primarily due to the fact that it is three dimensional, unsteady, and involves several scales. Most of the flowing fluids in industrial cases are turbulent. The

Navier–Stokes equations, without any additional information, are able to define both laminar and turbulent flows.

The most developed turbulence models are based on statistics. The two exceptions to this in ANSYS-CFX are the Large Eddy Simulation model and the Detached Eddy Simulation model. Also, the Direct Numerical Simulation (DNS) as one of the most accurate methods to model the flows would need very high calculating power. In the current study, a Reynolds-averaged Navier–Stokes **(**RANS) based on turbulence model and the SST model is employed.

5.3.2.1 Two-Equation Turbulence Models

Although two-equation turbulence models are more complicated than the zero equation models, they are employed in ANSYS-CFX for better computational accuracy.

In two-equation models, the turbulent kinetic energy and the dissipation rate of the turbulent kinetic energy are found after solving their transport equations. The computed turbulent kinetic energy is used to calculate the turbulence velocity scale. The turbulent kinetic energy and its dissipation rate are typically used to approximate the turbulent length scale.

The conservation of momentum is:

$$\frac{\partial}{\partial t}(\rho u_i)+\frac{\partial}{\partial x_j}\left(\rho u_i u_j\right) = -\frac{\partial P}{\partial x_i}+\frac{\partial}{\partial x_j}\left[\mu\left\{\frac{\partial u_i}{\partial x_j}+\frac{\partial u_j}{\partial x_i}\right\}\right]-\frac{\partial}{\partial x_j}(\rho\overline{u_i u_j})+B_i \tag{5.4}$$

where $\rho\overline{u_i u_j}$ is the Reynolds stress. In this model, the Reynolds stress is linked to the mean flow, i.e.

$$-\rho\overline{u'_i u'_j} = \mu_t\left(\frac{\partial\bar{u}_i}{\partial x_j}+\frac{\partial\bar{u}_j}{\partial x_i}\right)-\frac{2}{3}\delta_{ij}(\rho k+\mu_t\frac{\partial u_k}{\partial x_k}) \tag{5.5}$$

where k is the turbulent kinetic energy, μ_t is the turbulence viscosity and δ_{ij} is 1 if i=j, otherwise it is zero. The turbulence kinetic energy is defined with respect to transport equation (SST). In the current study, the $\frac{\partial u_k}{\partial x_k}$ term is negligible.

The conservation of momentum equations that are used in two-equation models, considering the Reynolds stress assumption becomes:

$$\frac{\partial}{\partial t}(\rho u_i)+\frac{\partial}{\partial x_j}(\rho u_i u_j) = -\frac{\partial P'}{\partial x_i}+\frac{\partial}{\partial x_j}\left[(\mu+\mu_t)\left\{\frac{\partial u_i}{\partial x_j}+\frac{\partial u_j}{\partial x_i}\right\}\right]+B_i \quad (5.6)$$

where P' is the modified pressure. It is found from the summation of static pressure and the multiplication of density and turbulence kinetic energy ($P' = P + \frac{2}{3}\rho k$).

5.3.2.2 The k-omega Model in ANSYS ANSYS-CFX 14.5

The $k-\omega$ model is developed by Wilcox (1986). It solves one transport equation for the turbulent kinetic energy k, and one for the turbulent frequency ω. The stress tensor is calculated from the eddy-viscosity concept.

The near-wall treatment is assumed to be an advantage of the $k-\omega$ turbulence model for a low Re. This model expects to be more rigorous than the $k-\varepsilon$ model at a low Re, because it does not include the complex nonlinear damping functions. A near-wall resolution for the $k-\omega$ model at a low Re is much lesser than $k-\varepsilon$ ($y^+ < 0.2$ for $k-\omega$ model and at least $y^+ < 2$ for $k-\varepsilon$ model).

5.3.2.2.1 Shear Stress Transport (SST)

The SST $k-\omega$ model used in ANSYS-CFX was developed by Menter (1993) as a two-equation eddy-viscosity model. The turbulence viscosity for the $k-\omega$ model is defined as:

$$\mu_t = \rho \frac{k}{\omega} \tag{5.7}$$

The SST model has the robustness of the k-ω turbulence model near walls with capabilities of the k-ε model away from the walls. It employs a blending function to combine the k-ω and the k-ε turbulence models between the near-wall region and the free stream. The definition of the turbulent viscosity is modified to account for the transport of the turbulent shear stress. The following equation shows the eddy viscosity calculation for the SST model:

$$\mu_t = \frac{a_1 k \rho}{\max(a_1 \omega, SF_{2)}} \tag{5.8}$$

where k and ω are the turbulence kinetic energy and the specific turbulence dissipation respectively, F_2 is a blending function, a_1 is 0.31, and S is the magnitude of the strain rate.

SST uses a blending function (F_2) to restrict the limiter to the wall boundary layer, as the underlying assumptions are not correct for free shear flows. S is an invariant measure of the strain rate. F_2 is defined in the turbulence viscosity term. This function equals to 1 near the surfaces and reduces to zero outside the boundary layer.

$$F_2 = \tanh(arg_2^2) \tag{5.9}$$

where,

$$arg_2 = \max\left(\frac{2\sqrt{k}}{\beta' \omega y}, \frac{500\,\nu}{y^2 \omega}\right) \tag{5.10}$$

where y is the wall distance. By solving the following transport equations, the turbulence kinetic energy and the turbulence dissipation are given as:

$$\frac{\partial(\rho k)}{\partial t}+\frac{\partial}{\partial x_j}\left(\rho u_j k\right)=\frac{\partial}{\partial x_j}\left[\left(\mu+\frac{\mu_t}{\sigma_{k3}}\right)\frac{\partial k}{\partial x_j}\right]+P_k-\beta'\rho k\omega+P_{kb} \tag{5.11}$$

$$\frac{\partial(\rho\omega)}{\partial t}+\frac{\partial}{\partial x_j}\left(\rho u_j \omega\right)=\frac{\partial}{\partial x_j}\left[\left(\mu+\frac{\mu_t}{\sigma_{\omega 3}}\right)\frac{\partial \omega}{\partial x_j}\right]+(1-F_1)2\rho\frac{1}{\sigma_{\omega 2}\omega}\frac{\partial k}{\partial x_j}\frac{\partial \omega}{\partial x_j}+\alpha_3\frac{\omega}{k}P_k-\beta_3\rho\omega^2+P_{\omega b} \tag{5.12}$$

where F_1 is the blending function. The buoyancy production and the dissipation terms (P_{kb} and $P_{\omega b}$) that describe the influence of the buoyancy forces are assumed to be zero in the current study. The turbulence production term, P_k, is calculated using equation (5.11).

The F_1 function is:

$$F_1=\tanh(arg_1^4) \tag{5.13}$$

where,

$$arg_1=\min[\max(\frac{2\sqrt{k}}{\beta'\omega y},\frac{500\,\nu}{y^2\omega}),\frac{4\rho k}{CD_{K\omega}\sigma_{\omega 2}y^2}] \tag{5.14}$$

$$CD_{K\omega}=\max(2\rho\frac{1}{\sigma_{\omega 2}\omega}\frac{\partial k}{\partial x_j}\frac{\partial \omega}{\partial x_j},10^{-10}) \tag{5.15}$$

The following function calculates, α_3, β_3, σ_{k3}, and $\sigma_{\omega 3}$constants where ϕ is α, β, σ_k or σ_ω.

$$\phi_3=F_1\phi_1+(1-F_1)\phi_2 \tag{5.16}$$

The other constants in the k-ω model used in the simulations are

$\alpha_1=0.553167,\ \alpha_2=0.440355,\quad \beta_1=0.075,\quad \beta_2=0.0828,\ \sigma_{\omega 1}=2.0,\ \sigma_{\omega 2}=1.16822,$ $\sigma_{k1}=1.176647$, $\sigma_{k2}=1.0$ and $\beta'=0.09$.

5.4 Boundary Conditions

An opening boundary condition allows the fluid to cross the boundary surface in either positive or negative flow directions. In the simulated cases, acoustic pressure fluctuates at the inlet side and the opening boundary condition is specified with a relative pressure value:

$$P_{opening}=P_{spec} \tag{5.17}$$

The ANSYS-CFX transient calculation is performed using P_{spec} as the sinusoidal pressure wave multiplied by 2% of the relative pressure added to the difference pressure (ΔP) of the outlet and the inlet. The component direction is chosen to be normal to the boundary condition. The magnitude of the velocity at the opening boundary is part of the solution. The outlet boundary condition is defined as zero static pressure for open-ended cases and zero velocity for the close-ended ones. No slip is chosen for the wall boundary condition. The medium turbulence intensity is set to 5% at the inlet and the flow direction is normal to the boundary.

Since the simulations are presumed as axisymmetric, symmetry boundary conditions are applied on the faces of zero and one degrees of the model.

5.5 Wall Treatment

In the SST model, ANSYS-CFX uses the automatic wall treatment to find a solution in the areas close to the wall. In this method, y^+ is recommended to be less than one.

The viscous sublayer ($u_{\tau v}$) and the log layers ($u_{\tau l}$) friction velocities are defined as:

$$u_{\tau v} = \left(\frac{\mu}{\rho}\left|\frac{\Delta u}{\Delta y}\right|\right)^{1/2} \tag{5.18}$$

$$u_{\tau l} = \frac{u}{\frac{1}{\kappa} log y^{+} + B} \quad (5.19)$$

where κ and B are 0.41 and 5.2 respectively. The friction velocity calculated from the viscous sublayer friction velocity and log layers friction velocities are as follows:

$$u_{\tau} = (u_{\tau v}{}^{4} + u_{\tau l}{}^{4})^{1/4} \quad (5.20)$$

And y^{+} is:

$$y^{+} = \frac{\rho \Delta y u_{\tau}}{\mu} \quad (5.21)$$

where Δy is the wall-normal space between the 1st and the 2nd mesh points from the wall.

5.6 Range of Fluid Properties

Numerical modelling of the flow field is carried out for a straight horizontal line with a 6.13 m length and an 8 mm I.D. (same as the experiments). Computations are performed for water having a temperature of 23°C (density ρ = 997 kg/m^3, viscosity μ= 0.8899×10^{-3} Kg/m.s, and static pressure P=413700 Pa), within the turbulence range of the liquid flow (Re ≈ 16000). The SST is used as a turbulence model.

The steady-state condition runs for the laminar and turbulence models as an initial condition for transient analysis and determines the inlet and the outlet difference pressure for each case.

The steady-state simulations ensure that the solution satisfies the following two conditions:

- The maximum residual root mean square error (RMSE) values have reduced to less than 1×10^{-5}.

- The domain has imbalances of less than 0.05%.

For the transient simulations, the analysis must be set as transient under the "Analysis type" option. The duration of simulation and the time step must then be determined and applied to the model. The duration of simulation depends on the type of analysis dictated by the excitation frequency and the flow condition (laminar or turbulence). The convergence criteria for the simulation time is set as the max $\{P_{(t1-t100)}*100/ P_t\} <1\%$. For an acoustic wave propagation problem, it is required to determine the time step as a function of the acoustic Courant number C_n. The closer the Courant number is to unity, the more accurate the results are. Indeed, for the simulated cases a minimum 0.004 s is required to meet the unity requirement. The adequate time steps find out in the mesh dependency, from 8×10^{-5} to 1.7×10^{-5}, based on the excitation frequency.

The properties of the medium (water) are chosen based on its thermodynamic properties. They are defined in the Constant Property Liquids option of ANSYS-CFX. There is no addition of heat in the predictions, and the thermal condition is assumed to be isothermal. The fluid temperature is set to be at 23°C for all the cases. Although it is usual to consider water as incompressible and of a uniform density, this is clearly not true. Capturing acoustic waves traveling through water needs slight compressibility. The degree of compressibility of a fluid has strong implications for its dynamics. The compressibility of water is a function of pressure and temperature. Because the speed of sound is defined in classical mechanics as

$$c^2 = \left(\frac{\partial P}{\partial \rho}\right)_S \tag{5.26}$$

where ρ is the density of the material, it is therefore found, through methods of replacing partial derivatives, that the isentropic compressibility can be expressed as

$$\beta_T = \frac{1}{\rho\, c^2} \tag{5.27}$$

By defining the compressibility of water as (5.0038×10^{-10}), a sonic velocity equal to the thinner SS straight line tube is obtained. For the simulated cases, acoustic pressure is defined as the sinusoidal pressure at the inlet boundary condition. The magnitude of the velocity at the opening boundary is the part of the solution.

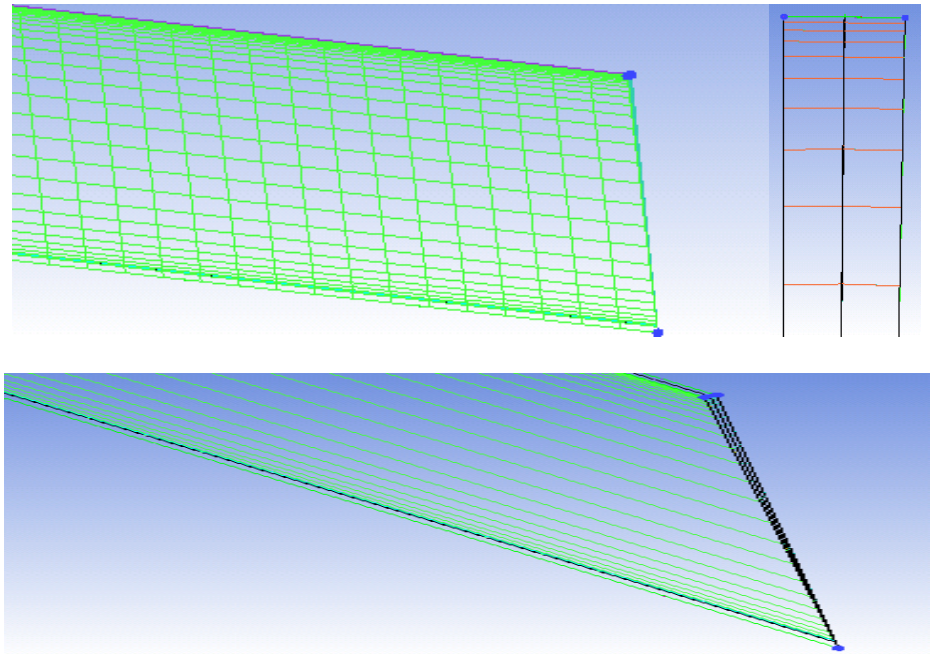

Figure 5.1: Different Views of Generated Mesh

5.7 Mesh Generation

The ANSYS ICEM CFD meshing software generates the meshes in the current study. Different views of the generated meshes are shown in Figure 5.1.

Since the flow in the model is axisymmetric, only one degree (1/360) of the tube volume is modeled. As the running time steps are very small in the simulations, this assumption highly reduces the time of convergence. To capture the turbulence effect and viscosity near the wall, non-uniform distributed meshes are used in the radial direction.

5.8 Mesh Dependency Study

The density of cells in a computational grid desires to be fine enough to capture the required flow details, but not to be so fine that the overall number of cells in the domain becomes excessively large. The problems described by large numbers of cells require more time to solve. The computations carried out on excessively coarse grids or grids of improper geometrical mesh quality may have considerable influence on the propagation of numerical errors and result in an imprecise solution.

Table 5.1: Grids Data Used for Mesh Study of the Simulations

Mesh Parameters	***Grid 8404***	***Grid 21004***	***Grid 25204***	***Grid 56004***	***Grid 62404***	***Grid 68804***	***Grid 93604***	***Grid 94881***
Axial Nodes	100	250	300	400	400	400	600	400
Radial nodes	22	22	22	36	40	44	40	40
Angular nodes	3	3	3	3	3	3	3	6

The mesh study is carried out for nine mesh sizes (6100, 6700, 9100, 10400, 16750, 18300, 46000, 69000, and 97604 elements) at different time steps. For each numerical grid, the

following geometrical measurements of mesh quality are compared: axial, radial, and angular nodes, and for the 1st fixed node wall distance (8×10^{-6} mm). Table 5.1 shows the data grid used for the mesh study of the simulations.

To choose a proper time step for the transient simulations, the mesh study is performed at 5 different time steps for the minimum required frequency. Figures 5.2–5.4 show how axial, radial, and angular grid changes affect the accuracy of pressure perturbation ratio. The value of the outlet over the inlet perturbed pressure (normalized pressure) is used to evaluate mesh dependency and time-step selection.

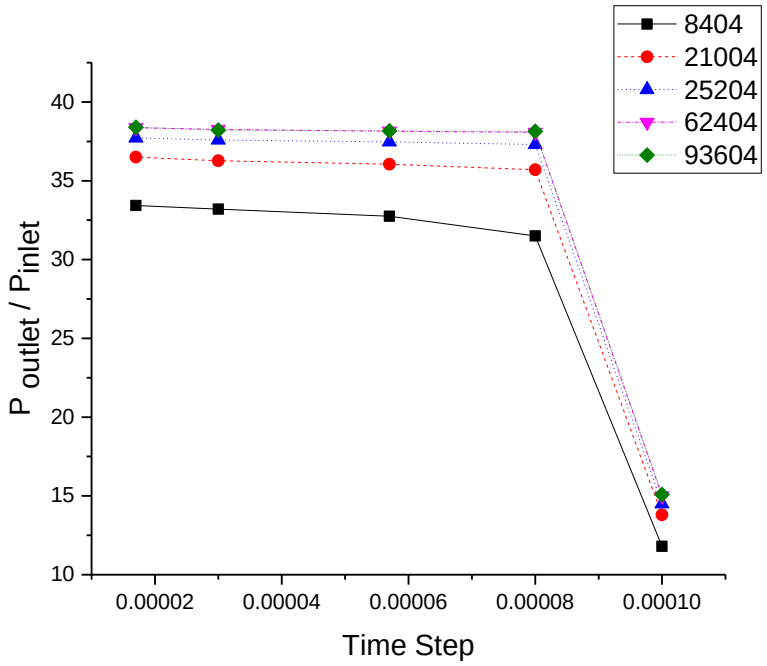

Figure 5.2: Effect of Axial Grid Changes to the Accuracy of Pressure Perturbation Ratio

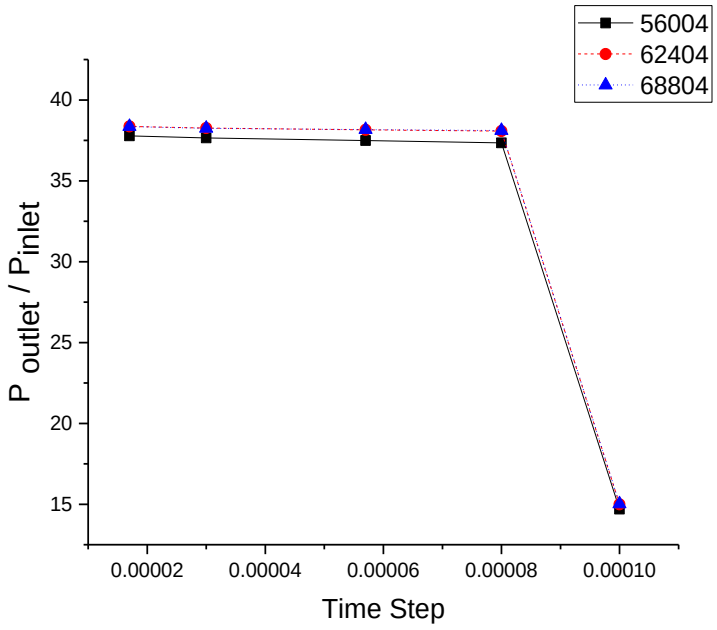

Figure 5.3: Effect of Radial Grid Changes to the Accuracy of Pressure Perturbation Ratio

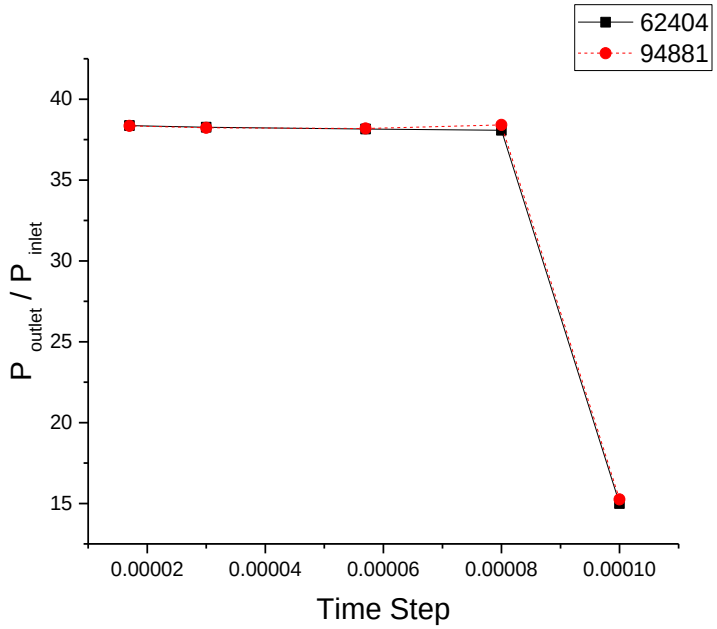

Figure 5.4: Effect of Angular Grid Changes to the Accuracy of Pressure Perturbation Ratio

5.2: Percentage Difference of Normalized Acoustic Pressure With the Axial Grid Changes

Compared Grids	***Time Step(s)***				
	$1*10^{-4}$	$8*10^{-5}$	$5.7*10^{-5}$	$3*10^{-5}$	$1.7*10^{-5}$
	Normalized pressure Difference (%)				
8404 & 21004	14.49	11.76	9.15	8.46	8.41
21004 & 25204	4.82	4.28	3.78	3.51	3.23
25204 & 62404	3.33	2.04	1.78	1.75	1.69
62404 & 93604	2.19	0.15	0.10	0.07	0.05

Table 5.2 displays the percentage difference of the normalized pressure for three mesh densities with the axial grid changes .The results are compared for 5 different time steps (1×10^{-4}, 8×10^{-5}, 5.7×10^{-5}, $3\times10^{-5,}$ 1.7×10^{-5}) at 50 Hz.

As it can be concluded from the data on the axial quality parameters shown in Table 5.2, the best grid seems to be one of the density 62404 elements. The results from grid 62404 show less than 1% difference from grid 93604 predictions for time steps smaller than 8×10^{-5}. In Table 5.1, the dimensionless values y+ (dimensionless wall distance to the first node of the computational grid) have also been calculated to be less than one. As to the results of grid 25204 elements, there are more deviations (more than 1.5%) from grid 62404 for all the time steps.

For the next step, grid 62404 is evaluated by changing +/- 10% in the radial scale. Table 5.3 shows the percentage difference of normalized pressure for the three mesh densities with the radial grid changes.

Table.5.3 shows the maximum percentage difference of the pressure ratios between different mesh densities. From the results, grid 62404 with 400 axial nodes and 40 nodes in the radial direction are assumed to be adequate. The maximum percentage difference between the results of

grids 62404 and 68804 is 0.17 % for the lowest time step. As the first near-wall distance is selected to be small enough, the y^+ value obtained is less than 1 for all the cases.

5.3: Percentage Difference of Normalized Acoustic Pressure with the Radial Grid Changes

Compared Grids	***Time Step (s)***				
	$1*10^{-4}$	$8*10^{-5}$	$5.7*10^{-5}$	$3*10^{-5}$	$1.7*10^{-5}$
	Normalized pressure Difference (%)				
56004 & 62404	2.01	1.91	1.73	1.59	1.53
62404 & 68804	1.73	0.17	0.07	0.04	0.02

To investigate the effect of the number of angular nodes, the same investigation on the pressure ratio with the same time steps and frequency is done for 2 different angular nodes on grids 62404 and 94881. Table 5.4 indicates that grid 62404, with 3 nodes in the angular direction, produces pressure ratios very close to 6 angular nodes at time steps lower than 8×10^{-5}. As our problem is 2D the selected numbers of angular nodes are adequate.

Table 5.4: Percentage Difference of Normalized Acoustic Pressure with the Angular Grid Changes

Compared Grids	***Time Step (s)***				
	$1*10^{-4}$	8*10-5	$5.7*10^{-5}$	$3*10^{-5}$	$1.7*10^{-5}$
	Normalized pressure Difference (%)				
62404 & 94881	1.7	0.8	0.1	0.08	0.06

The mesh study results indicate that grid 62404 is adequate to predict pressure perturbation with 8×10^{-5} time step at 50 Hz. The maximum exciting frequency in the simulations is supposed to be 500 Hz. Finding out proper time steps for the whole frequency range requires pressure perturbation investigation at grid 62404 (as an adequate mesh size) for the 5 different time steps at 500 Hz.

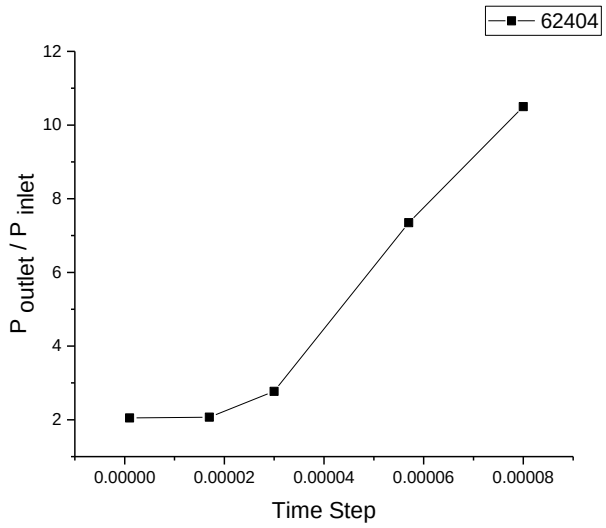

Figure 5.5: Time step Investigation for the Highest Frequency

As it can be concluded from Figure 5.5, a time step of 1.7×10^{-5} is appropriate for the highest frequency. For better accuracy, this time step is chosen for the entire frequency range.

Chapter 6 Results and Discussions

6.1 Introduction

Acoustic resonance is studied experimentally and numerically through seven different geometries for different wall thicknesses and materials in the frequency range of 20–500 Hz.

First, the acoustic resonances of a closed-end straight line for different materials and wall thicknesses are investigated; second, a straight test line same as the experiment with thinner SS material is studied for open-ended no flow and a turbulent flow; third, the effect of different branched configurations and flowing fluid on frequency and amplitude responses for close- and open-ended mainlines are investigated. ABAQUS FEA 6.12 and ANSYS-CFX 14.5 are used to simulate frequency resonance and amplitude of the experiments.

6.2 Results and Discussions

6.2.1 Sonic Velocity Measurement

According to the "organ-pipe" equation for straight pipes, $f_n = (2n-1) \times c/4L$, where n=1, 2, 3…, the frequency resonance can be predicted if the sound speed (c) is known. In the straight line experiments, sonic velocities are measured three times in every 50 Hz. In 10 mm O.D. SS tube, the measured sound speed is about 1409.195 m/s, which is 0.46% smaller than the calculated value of c=1415.8 m/s determined from Chaudhry's equation (3.1). For the thicker tube, the

measured sound speed is about 1429.58 m/s. The calculated sound speed from equation (3.1) shows 0.62% difference from the measured value. For the Al tube, the measured sound speed is about 1366.22 m/s, which is 0.61% less than the value of c=1374.7 m/s given by equation (3.1). For the test with two different wall thicknesses (2 mm and 4 mm), the measured sound speed is about 1370.2 m/s, which is a 0.58% difference from the calculated value from equation (3.1). As Figure 6.1 displays, acoustic waves travel in the test line at 3946 (millisecond) ms and 3987 ms for P_0 and P_1, respectively. It shows a time delay in the signals. To obtain the sonic velocity, the measured distance between the transducers is divided by the time delay.

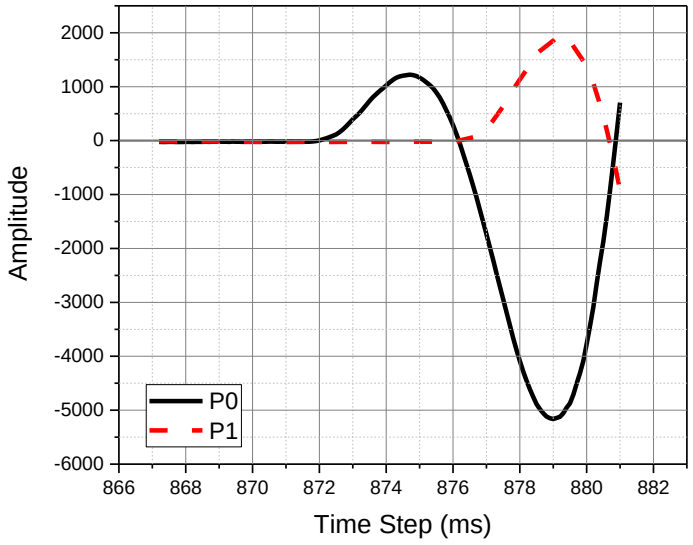

Figure 6.1: Velocity Measurement at 150Hz 10 mm O.D. SS Tube (c=1409.195 m/s)

The sonic velocity is also measured for every 25 Hz in the frequency range of interest (20–500 Hz) for elbow, equal branch geometry experiments. In the 7.18 m elbow test line, the speed of sound is measured to be 1409.846 m/s, which is 0.71% smaller than the calculated value of c=1419 m/s determined from equation (3.1). Almost the same sound speeds are recorded for T-

Branch (1408.843 m/s) and with one upward branch and one straight line (1408.961 m/s). These measurements show 0.67% difference from the calculated sound speed values

For the unequal branch and complex experiment configurations, the sound speed is measured at about 1419.122 m/s and 1424.342 m/s respectively, which shows that the measured sound speed of unequal branch and complex experiments are 0.41% and 0.46% smaller than the calculated value of c = 1425 m/s and c = 1431 m/s determined from equation (3.1).

6.2.2 Experimental Results

6.2.2.1 Close-Ended Straight Lines

The schematic diagram of the first four experiments with straight lines is shown in Figure 3.1. P_1 is assumed to be the inlet pressure transducer for all the cases. Also, P_3 is considered as the outlet pressure transducer. Table 6.1 summarizes the lengths, I.D., O.D., materials, and working conditions of the six straight line experiments. All the tests are carried out with pure de-aired water at a temperature of 23^{o}C and a system pressure of 0.41 MPa.

Table 6.1: Straight Lines Experiment Conditions

Experiment	***6.13 m Closed- End***	***6.13 m Closed- End***	***6.13 m Closed- End***	***8 m Closed- End***
Test Line Length (m)	6.13	6.13	6.13	8
Test Line O.D. (mm)	10	12	12	12 & 16
Test Line I.D. (mm)	8	8	8	8
Tube Material	Stainless steel 316	Stainless steel 316	Aluminum 6061	Aluminum 6061
Flow Rate (m/s)	0 & 2.1	0 & 2.1	0 & 2.1	0 & 2.1

The experimental results are shown in Figures 6.2, 6.3, 6.4, and 6.5 for 10 mm and 12 mm O.D. SS tubes, 12 mm O.D. Al tube, and Al tubes with two different wall thicknesses (2 mm and 4 mm respectively). Four resonant peaks are obtained for the first three experiments. For the Al tube with 12 mm O.D., the resonant peaks occur at lower frequencies than the SS tube for the same wall thickness due to the lower sonic velocities. In the experiment with two different wall thicknesses, six resonant peaks are recorded. Table 6.2 tabulates the measured resonant amplitudes and frequencies for the four close-ended straight lines.

Table 6.2: Resonant Frequency and Amplitude Measurements for Straight Lines

		1	***2***	***3***	***4***	***5***	***6***
Stainless steel 6.13 m length Closed End (10 mm O.D)	**Amp**	62.5	35.3	23.5	14.6	-	-
	Freq. (Hz)	56.25	173.25	289	400.75	-	-
Stainless steel 6.13 m length Closed End (12mm O.D)	**Amp**	66.4	37.6	26.6	15.6	-	-
	Freq. (Hz)	56.75	175	289.75	404	-	-
Aluminum 6.13 m length Closed End (12mm O.D)	**Amp**	59.2	29.8	17.8	10.8	-	-
	Freq. (Hz)	54.5	164.75	277.25	389.75	-	-
Aluminum 8 m length Closed End (12mm & 16 mm O.D)	**Amp**	40.5	25	15.38	10.86	7.99	5.98
	Freq. (Hz)	40.75	132	218	306.25	384	468.5

From the experimental data, the following are observed:

a) The simple linear regression model is applied to fit the straight lines to the resonant amplitude peaks using the least square error method. Since the Pearson correlation coefficients for all the fitted lines are more than 0.9, the lines are fitted well to the resonant amplitude peaks. The results show that the highest and the lowest slopes of the fitted lines are obtained for the thicker wall thickness SS and Al tubes with two different wall thicknesses respectively.

b) It can be seen that the minimum non-resonance amplitudes decrease with an increase in frequency. The slopes of the fitted lines for the non-resonance troughs are almost the

same for both the SS tubes. The Al tube with 12 mm O.D. has a lower slope for the non-resonance troughs compared to the SS tubes.

c) For the same length and wall thickness, the Al tube resonant amplitude is 10% less than the SS amplitude for the 1^{st} peak. For the 4^{th} peak, the Al amplitude is 56% less than the SS, which demonstrates that the Al tube with the lower Young's modulus absorbs more acoustic wave energy than the SS tube.

d) In the experiment with the two different wall thicknesses, the non-resonance troughs trend is not the same as the other experiments with a single O.D. Also, due to the different sonic velocities that interact with each other as well as high energy absorption in the sections with different O.D.s, the resonant peaks are more damped compared to the single O.D. Al tube.

6.2.2.2 Open-Ended Stainless Steel Straight Line

Herein, the acoustic resonance for an open-ended tube is investigated. A straight test line (length of 6.13 m & I.D. 8 mm) at zero mean flow and turbulent mean flow with Re = 16766.4 is studied. The test line outlet is connected to a water tank. The acoustic pressure is measured at four locations (P_0 at 0, P_1 at 1.45, P_2 at 2.54, and P_3 at 4.54 m). The maximum acoustic pressure at each point is normalized by the maximum acoustic pressure of the inlet pressure transducer (P_0).

Four resonant peaks can be clearly seen in Figures 6.2, 6.3, and 6.4, which show normalized acoustic pressure spectra versus frequency taken from the three different locations (P_1, P_2, and P_3) for the zero and turbulent mean flows. The following observations are made:

a) At the zero flow case, the amplitudes of the first three peaks do not increase or decrease with the same trend. It shows that the resonant amplitudes do not decrease by increasing the frequency, same as the close-ended case.

b) The turbulent flow increases amplifications over the zero flow case at the 1st, 2nd, 3rd, and 4th resonant peaks, but these increments are not the same for all the peaks. For the first three peaks from zero to turbulent flow, the amplification increases are within 20%.

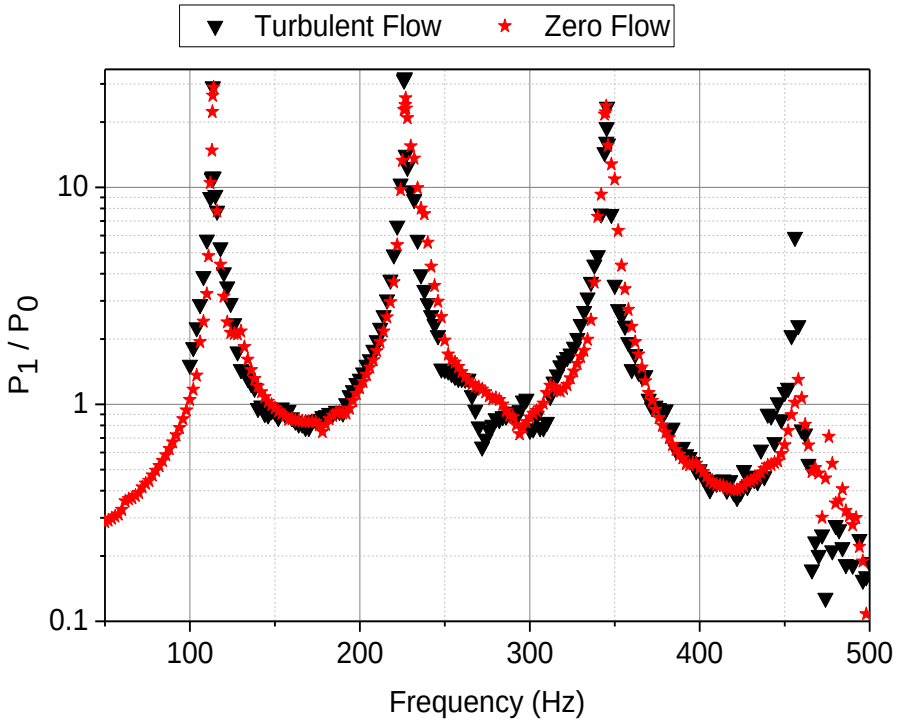

Figure 6.2: Comparison between Zero and Turbulent Mean Flow Results of the "6.13 m long 10 mm O.D SS Open-Ended Experiments" at 1.45 m

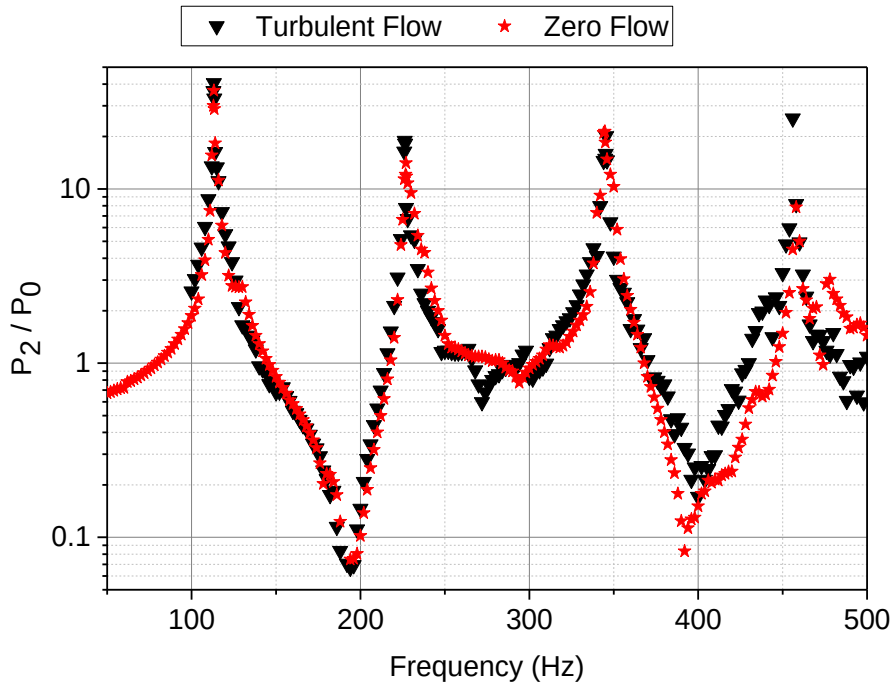

Figure 6.3: Comparison between Zero and Turbulent Mean Flow Results of the "6.13m long 10 mm O.D SS Open-Ended Experiments" at 2.54 m

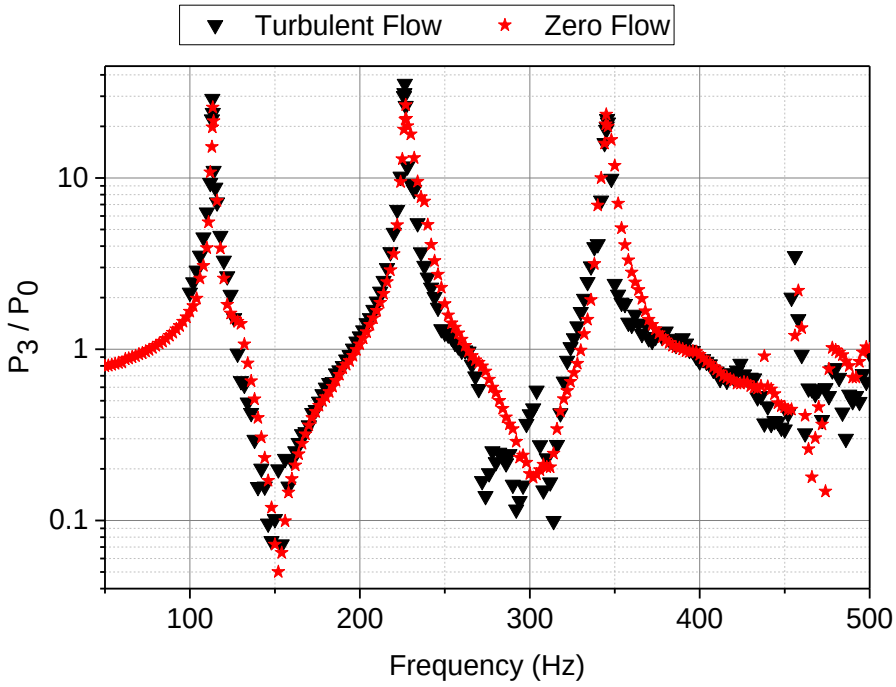

Figure 6.4: Comparison between Zero and Turbulent Mean Flow Results of the "6.13m long 10 mm O.D SS Open-Ended Experiments" at 4.65 m

c) For the turbulent mean flow case, the amplitudes of the 4th resonant peaks at P_2 and P_3 are increased significantly over the zero flow case at about 2 and 6 times respectively. It shows that the turbulent flow has a significant effect on the amplitudes at frequencies higher than 350 Hz. These increases are important, since the prediction tool currently being used by the nuclear industry assumes a zero mean flow. The reason for the increase in the amplitude at higher frequencies might be caused by the interaction of the higher frequencies and turbulent fluctuations. Further investigations for very high Re (~ 60000) are needed.

6.2.2.3 Equal Branches and Elbow

The main object of the elbow and equal branches experiments is to study the effect of the elbow and the different equal branch configurations on the resonant frequency and amplification. The T-Branch, shown in Figure 6.5, is referred to Branch 1, and the case with one upward branch and one straight line is referred to Branch 2 (Figure 6.6.). P_0 is assumed to be the inlet pressure transducer for all the cases. The outlet pressure transducers for Branch 1 and Branch 2 experiments are P_1 and P_2 and P_1 and P_3, respectively. All the tests are carried out with pure water, 6.13 m length of main line, 1.05 m length of branch, 8 mm I.D., 10 mm O.D., in a temperature of 23^{o}C, and a system pressure of 0.41 MPa.

The data on resonant frequencies and amplitudes are collected similar to the tests described in the "Straight line experiments" section and tabulated in Table 6.3. Five resonant peaks are measured in the frequency range of interest. For the experiments with branches, the data are recorded at the outlets of the branches.

Table 6.3: Elbow & Equal Branches Resonant Amplitude and Frequency Measurements

Experiment line mode	*7.18 m elbow*		*6.13 m main line with tee of two 1.05 m braches*		*6.13 m main line with two 1.05 m braches(one up one straight)*	
	Freq. (Hz)	**Amplification**	**Freq. (Hz)**	**Amplification**	**Freq. (Hz)**	**Amplification**
1	48.75	64.3	42.75	55.1	43	48.5
2	143.50	40.4	136.75	35.1	136.25	29.2
3	244.75	26.5	241.5	22.9	241	18.8
4	340.5	18.8	345.75	9.1	345.5	7.85
5	440.25	10.3	456	15.7	455.5	11.8

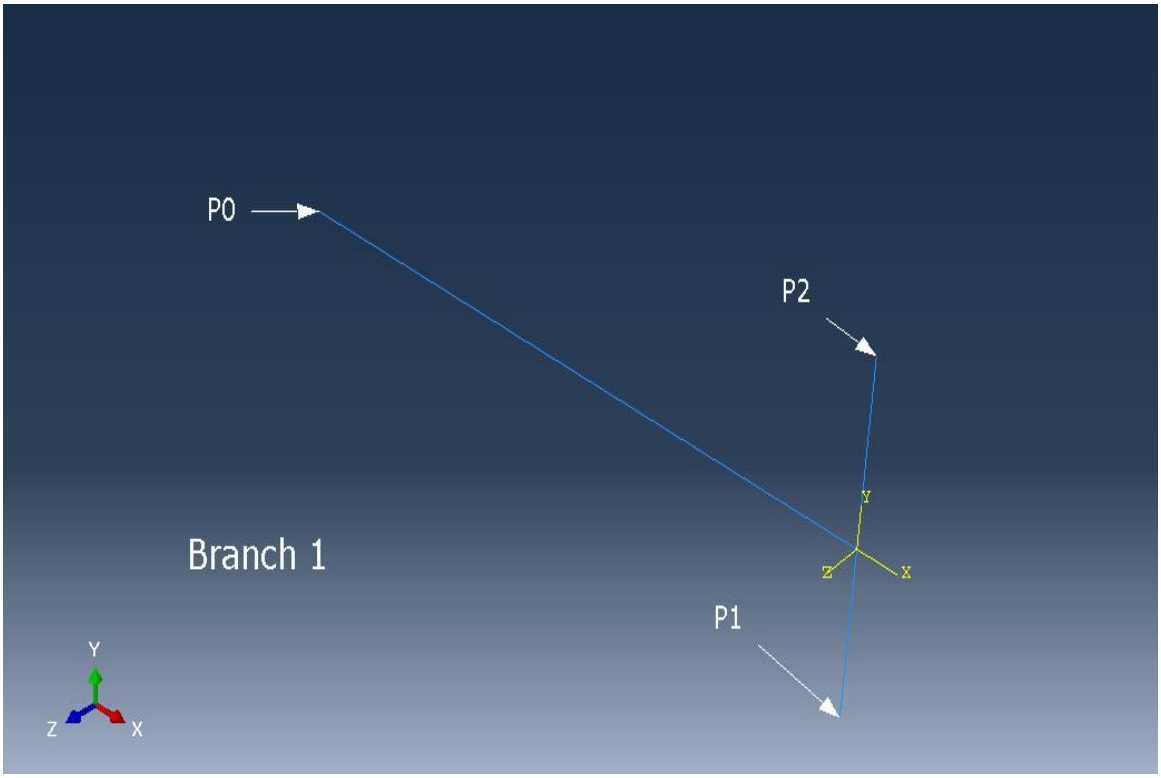

Figure 6.5: Schematic diagram for Branch 1

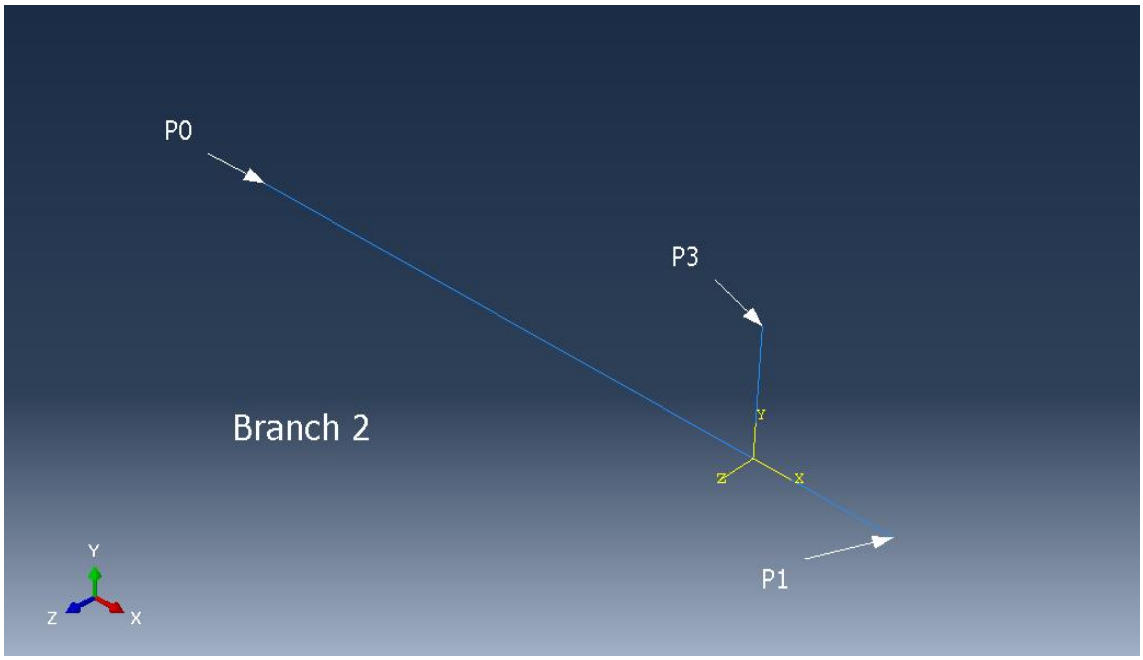

Figure 6.6: Schematic diagram for Branch 2

.

From the experimental data, the following are observed:

a) The simple linear regression model is applied to fit a straight line to the resonant amplitude peaks using the least square error method. For the Branch 1 and Branch 2 experiments, the amplitude of the last resonant peaks increase compared to the 4^{th} resonant peaks, and the regression model is applied to the first four resonant peaks. The results show that the highest and the lowest slopes of the fitted lines are obtained for Branch 1 and Branch 2, respectively.

b) In comparison to the straight line experiment where the fluid-filled tubes have the same wall thickness and material, the elbow experimental results show a higher slope of fitted line for the resonant peaks, which indicates that the elbow configuration increase the energy absorption and damp more energy than the straight line.

c) The resonant frequency measurements for the equal branch configurations show a

maximum of 0.5 Hz difference in their values, which means that different equal branch configurations have no significant effect on resonant frequencies.

d) The magnitudes of the slopes indicate that changing the equal branch configuration influences the resonant peaks amplitudes. The Branch 1 configuration shows a higher slope and a higher value for the last peak than Branch 2. The resonant amplitude in Branch 2 at the 1^{st} peak is 12% less than the Branch 1 amplitude. For the 4^{th} peak, it is 34% less than the Branch 1 resonant amplitude. It can be due to the fact that the traveling acoustic pressures hit the close-ended branches and amplify each other at the T-junction, which means that the acoustic waves reflected from the branches meet the reflected waves from the T-junction and these interactions create higher amplification at the Branch 1 configuration than the Branch 2 configuration.

e) It can be seen that the minimum non-resonance amplitudes do not decrease constantly with an increase in frequency, which means that the trough amplitudes decrease with increasing frequency, but there are some troughs where their amplitudes increase with increasing frequency.

6.2.2.4 Close-Ended Unequal Branch & Combined Parameters

The unequal branch and the combination of unequal branches, different materials, and wall thicknesses configurations are shown in Figures 6.7 and 6.8, respectively. The mainline is designated with an 8.85 m length and maintained in a fixed position on the pipe supports. The upstream of the tube is connected to a rubber hose. Pressure transducers are deployed in order to obtain pressure measurements at the outlet of the branches, as well as on the inlet and outlet of

the mainline. In following the notations of the acoustic pressure measurements, the pressure transducer at the first branch close to the upstream of the mainline is designated as P_1 and that at the subsequent branch as P_2, and that on the Al branch close to the mainline outlet as P_4. The P_3 transducer measures data at the main line outlet. All the measurements are herein normalized with the mainline inlet pressure transducer P_0. The succeeding two experiments are designed to study the effects of an unequal branch configuration and a combination of all the investigated parameters, i.e., wall thickness, material, and unequal branches, on the frequency resonance and amplification. Table 6.4 summarizes the experimental conditions on the unequal branches and the combination of all the investigated parameters. The unequal branch experiment includes 2.07 m upward and 1.0 m downward branches, referred to as Branch 3. The experiment with all the considered parameters is denoted as the "Combined Experiment". In the Combined Experiment, the pressure transducer notations are the same as that of the Branch 3 experiment, except for P_4 that is used as the Al branch pressure transducer. All the tests are carried out with pure water, 8 mm I.D., zero main flow, and at a temperature of 23°C and a system pressure of 0.41 MPa.

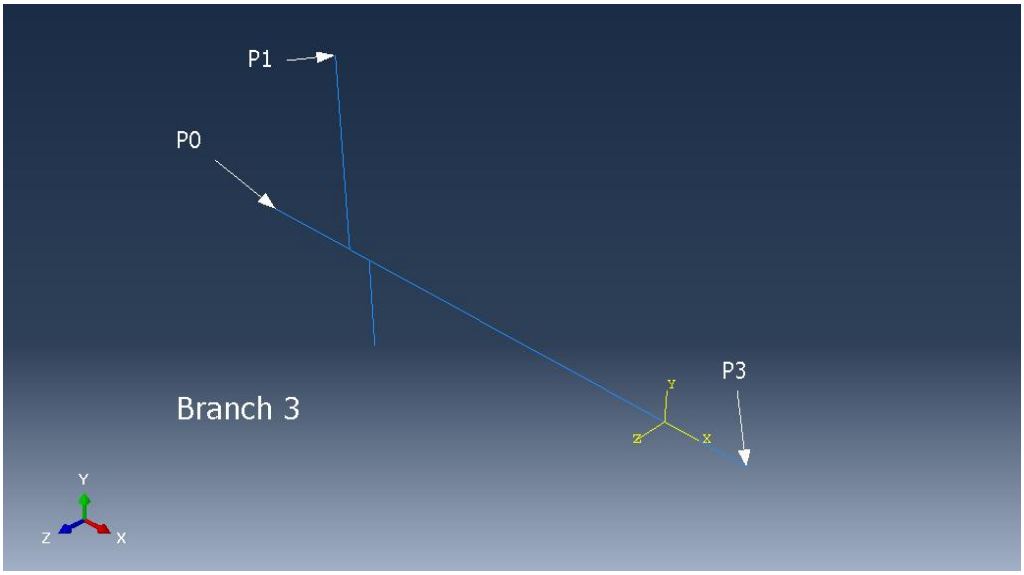

Figure 6.7: Schematic diagram for Branch 3

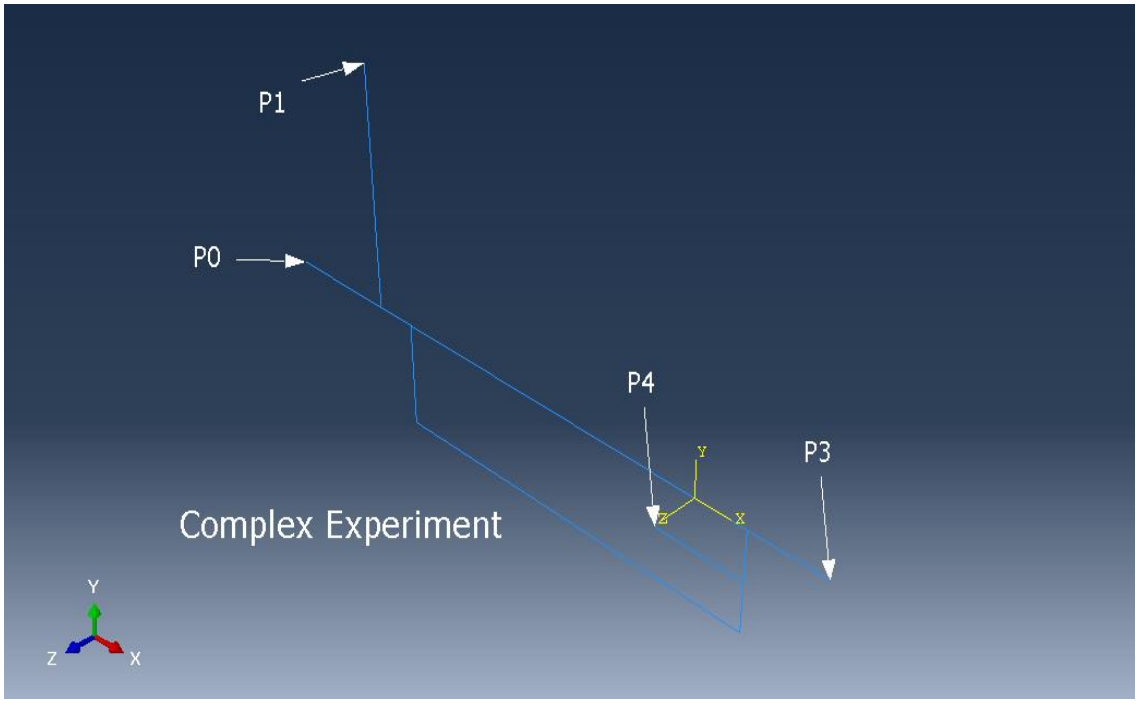

Figure 6.8: Schematic diagram for Complex Experiment

Table 6.4: Unequal Branches Experiment Conditions

Experiment	***Branch3***	***Combined Experiment***
Main Test Line Length (m)	8.85	8.85
Branch Length (m)	2.07	2.07
Branch Length (m)	1.0	8.20
Branch Length (m)	-	0.98
Test Line O.D. (mm)	10	10&12
Tube Material	Stainless steel 316	Stainless steel 316 & Aluminum 6061

The data on resonant amplitudes and frequencies are collected similar to the tests described in the straight line experiments and equal branches sections and tabulated in Table 6.5 and 6.6 for Branch 3 and Combined Experiment, respectively.

Table 6.5: Branch 3 Resonant Amplitudes and Frequencies

Mode	*Main line*	*2.07 m St Branch*
Frequency (Hz)	46	46
Amplitude	54	15.7
Frequency (Hz)	106.25	106.25
Amplitude	16.9	39.2
Frequency (Hz)	173	173.5
Amplitude	3.36	5.75
Frequency (Hz)	235.75	235.25
Amplitude	11.9	16.8
Frequency (Hz)	301	301.5
Amplitude	18.94	8.87
Frequency (Hz)	379	378.75
Amplitude	7.44	4.36
Frequency (Hz)	400.5	400.25
Amplitude	34.7	9.09
Frequency (Hz)	455.5	455.75
Amplitude	4.95	14.86

Table 6.6: Combined Experiment Resonant Amplitudes and Frequencies

Mode	*Main line*	*2.07 m St Branch*	*1 m Aluminum Branch*
Frequency (Hz)	32.25	32.25	32.25
Amplitude	51.5	16.2	55.7
Frequency (Hz)	89.75	89.5	89.5
Amplitude	14.88	17.65	13.42
Frequency (Hz)	103	103	102.75
Amplitude	4.47	9.86	4.65
Frequency (Hz)	148.25	148	147.75
Amplitude	4.1	10.5	3.58
Frequency (Hz)	185.5	185.75	212.25
Amplitude	5.25	4.45	3.95
Frequency (Hz)	231.25	212.5	231.25
Amplitude	2.95	5.32	1.88
Frequency (Hz)	247.75	247.5	280
Amplitude	2.12	1.32	6.86
Frequency (Hz)	280.25	280	310
Amplitude	1.54	3.54	3.46
Frequency (Hz)	310.5	310.25	351
Amplitude	9.22	4.83	31.2
Frequency (Hz)	351	350.75	391.25
Amplitude	15.1	15.91	3.14
Frequency (Hz)	391.5	391.25	428.25
Amplitude	3.45	5.65	3.42
Frequency (Hz)	428.25	428.5	469
Amplitude	3.89	2.47	3.65
Frequency (Hz)	-	468.75	-
Amplitude	-	4.81	-

From the experimental data, the following are observed:

a) The trend of decreasing resonant amplitude with increasing frequency that is obtained for the straight lines or the first four peaks of the equal branches is not obtained for the Branch 3 configuration.

b) The resonant frequency measurement represents a difference of a maximum of 0.75 Hz between the branch and the mainline. This difference of less than 1 Hz and with respect to the measurement at two different location of the system is acceptable.

c) The measured resonant amplitudes are not the same for the branch and the mainline. At the 1^{st} and the 6^{th} resonant peaks of the mainline, the resonant amplitudes are almost 4 times bigger than the branch values. The amplitude measurement at the 7^{th} resonant peak shows that the resonant amplitude at the branch is almost 4 times bigger than that of the mainline. These results imply that although the branch distance to the inlet is less than the distance to the mainline outlet, the traveling acoustic waves in the unequal branch system causes significant damping and reduction in the amplitude of the branch at the 1^{st} and 6^{th} peaks (less than 400 Hz). Despite those reductions for the branch resonant amplitudes, the damping of the mainline is higher than that of the branch at the 7^{th} resonant peak (higher than 400 Hz). It should be noted that for frequencies lower than 400 Hz, less than a 100% increase in resonant amplitudes are not considered large increments.

d) The number of resonant peaks for Complex Experiment compared to the Branch 3 experiment increases. The higher number of peaks is due to the more number of junctions and the mainline length.

e) The resonant frequency measurement same as the Branch 3 represented a difference of maximum 0.75 Hz. This difference of less than 1 Hz with respect to the measurement at

different locations of the system is also acceptable.

f) The results for the measured resonant amplitudes are not the same for the first side branch, the Al branch, and the mainline outlet. The maximum value of the resonant amplitudes in the Complex Experiment is almost 70% less than the highest magnitude of the resonant peak in the Branch 3 experiment, which means that with a combination of different wall thicknesses, materials, and an addition of more junctions at the same frequency range of the Branch 3, the maximum value of the resonant amplitude decreases. This phenomenon is attributed to the higher energy absorption at the Al section and sophisticated interactions between the reflecting waves at the junctions.

g) The resonant amplitude magnitudes at the 1^{st} peak of the mainline outlet and the Al branch are reported to be almost 3.5 times bigger than the 2.07 m branch. The resonant amplitude of the last peak at the mainline is less than one (0.45) and that is 10 times smaller than the first branch (2.07 m) resonant amplitude value. It implies that for the last three resonant peaks (frequencies more than 350 Hz), the first branch resonant amplitudes are higher than the main line, especially at the last resonant peak.

6.2.2.5 Open-Ended Branch 3

A main purpose of the present investigation is to determine whether acoustic resonance is influenced by the mean flow velocity generated eddies at the corner of the junctions when they coincides with natural resonant frequencies in unequal branches. First, it is desirable to measure acoustic resonance with separate velocity and acoustic pressure sources for laminar, turbulent, or

fully turbulent flows. Second, the flow parameters regularly used to characterize the frequency of oscillation, such as the St, are connected with acoustic resonances.

The acoustic resonances of the Branch 3 configuration that correspond to variations of inflow velocities are investigated for the four inflow conditions (Re = 0, 2100, 8450, 20754). These different inflow conditions are generated via adjustable speed gear pump installed in a test loop. The measurements are reported for the 2.07 m branch (P_1), 1 m branch (P_2), and mainline outlet (P_3). All the tests are carried out with pure water, 8 mm I.D., in a temperature of 23^{o}C and system pressure of 0.41 MPa.

Resonant amplitudes and frequencies data are collected similar to the tests described in Branch 3 close-ended section. From the experimental data the following are observed:

a) Figure 6.9 shows for the case of the shorter branch (1 m), noticeable resonant peaks are visible for the zero, laminar, and turbulent mean flows. Strengths of these peaks are high for the all cases at the frequencies less than 130 Hz. For the zero flow case at P_2, the maximum value of the resonant peaks is almost 25% less than the Branch 3 close-ended experiment. Figure 6.9 also indicates clearly the increase in amplitudes of the higher resonant peaks with increasing mean velocity. The increments in the resonant amplitudes of the first three peaks from zero to turbulent mean flows are less than 30%. For the last two peaks from zero to the turbulent flow with Re=20754, the resonant amplitudes rise at about 2.5 times. The considerable effect of the turbulent mean flow on the resonant amplitudes for the frequencies higher than 350 Hz is also presented for the straight line experiment. For the Branch 3 case, the flow effect on the resonant amplitude is significant for the frequencies higher than 250 Hz, which is lower than the straight line value.

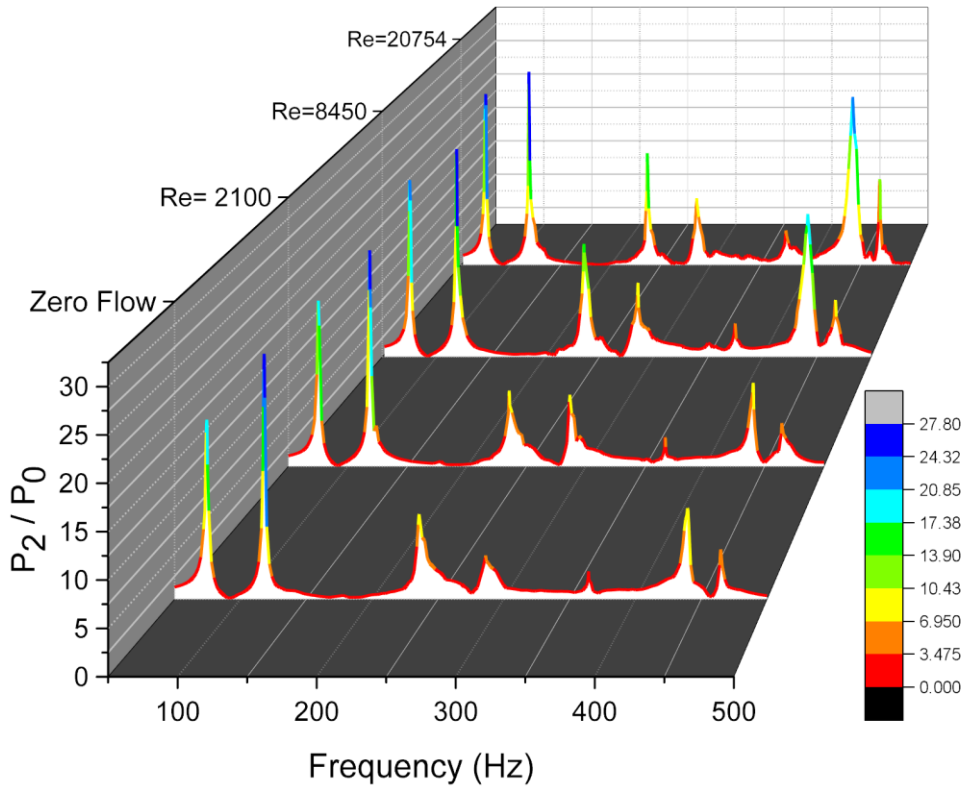

Figure 6.9: Comparison between Experimental Results at Different Mean Velocities "Branch 3, 1 m Branch"

The results also indicate that for the system with unequal branches, the turbulent mean flows considerably shift the resonant frequencies. Increasing flow velocity significantly changes the frequency of resonances; the variations are within 10.75 Hz. For the frequencies less than 350 Hz, the difference between zero flow and turbulent flow measurements are less than 1 Hz. The maximum difference of 10.75 Hz is obtained at the 6^{th} resonant peak. The resonant frequency shifts with increasing mean flow velocity were found to be small in the straight line experiments. The larger shifts obtained in the branched experiments imply that branches can significantly shift the resonant frequency. This is important as a reactor contains long pipes and complex branches. Hence, shifting of the resonant peaks is expected to occur in reactors and needs to be well understood.

b) Figure 6.10 shows for the case of the longer branch (2.07 m), same as the shorter one the considerable resonant peaks are visible for the zero, laminar, and turbulent mean flows at the frequencies less than 130 Hz. The highest amplitude is obtained for the 2nd resonant peak that is almost twice as the resonant amplitude of the shorter branch. The resonant amplitudes of the first three peaks (less than 200 Hz) show a maximum increment of 15% from zero to a fully turbulent flow. For the frequencies higher than 200 Hz, the resonant amplitudes are increased considerably from zero flow to turbulent flow. Especially for the frequencies higher than 400 Hz, the resonant peaks are amplified by about 3 to 4 times. These increments are even higher than the shorter branch. It indicates that the longer length of the branch and the first junction fluctuations influence on the second junction amplitudes. Also, Figures 6.9 and 6.10 show for the higher frequencies (after 400 Hz), the resonant amplitudes in the longer branch increase further from zero to turbulent mean flows than the shorter one.

c) Two notable similarities exist between the plots of Figures 6.9 and 6.10. First, the onset of a clearly definable increment in resonant amplitude with increasing flow velocity for frequencies higher than 200 Hz is of the order of Re > 8500. Note that for Re > 8500, for the shorter branch, as many as five well-defined peaks are amplified considerably from zero to turbulent flows. The second noteworthy aspect of Figures 6.9 and 6.10 plots is that in both plots from 40–250 Hz and 450–500 Hz, considerable resonant peaks are visible, although in Figure 6.10, another excitation range from approximately 270–410 Hz is also illustrated. The common range of frequencies is therefore associated with the generation of large-amplitude pressure peaks.

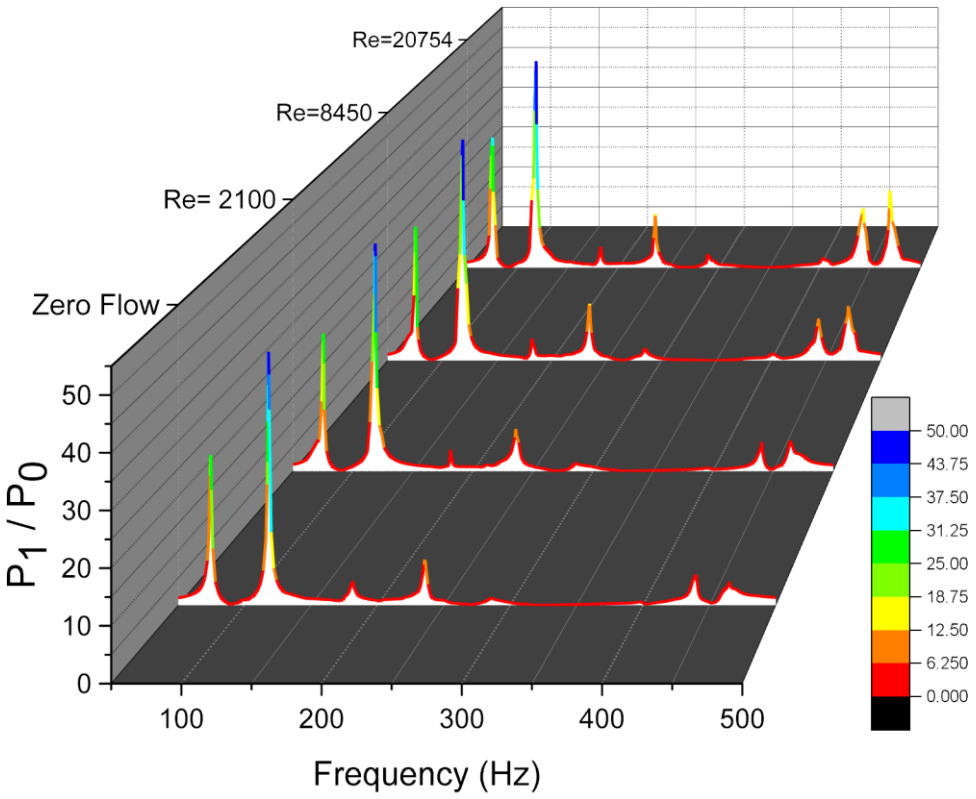

Figure 6.10: Comparison between Experimental Results at Different Mean Velocities "Branch 3, 2.07 m Branch"

d) Figure 6.11 depicts the mainline resonant amplitudes measurement magnitudes are less than the branches. It is due to the fact that the results are obtained at the outlet very close to the tank that most of the acoustic energies of the acoustic waves are damped out. Also, at the mainline outlet, with the open-ended boundary condition, lower numbers of resonant peaks with lesser amplifications than the close-ended mainline case are obtained. Clearly, three considerable resonant peaks are shown for the cases with turbulent flow from 150 Hz to 400 Hz. These resonant peaks for the zero flow and laminar flow cases give values less than 1. For the last two peaks, the resonant amplitudes from zero to fully turbulent flow are increased by about a factor of 2. The resonant amplitudes results show that the maximum values are obtained for the

frequencies higher than 400 Hz. These values are higher for the cases with the turbulent mean flows. The influence of the turbulent flows on the higher frequency resonant peaks is also seen for the branches. These observations support the idea that unsteady friction losses may vary meaningfully from zero to turbulent flows.

In terms of resonant frequencies the turbulent mean flow velocities also shift the resonant frequencies of the mainline. The maximum shifting is obtained at about 8.5 Hz. This shifting for the frequencies less than 250 Hz are less than 2 Hz. It confirms that mean flow velocity influences on the resonant frequencies are not significant for the lower frequencies.

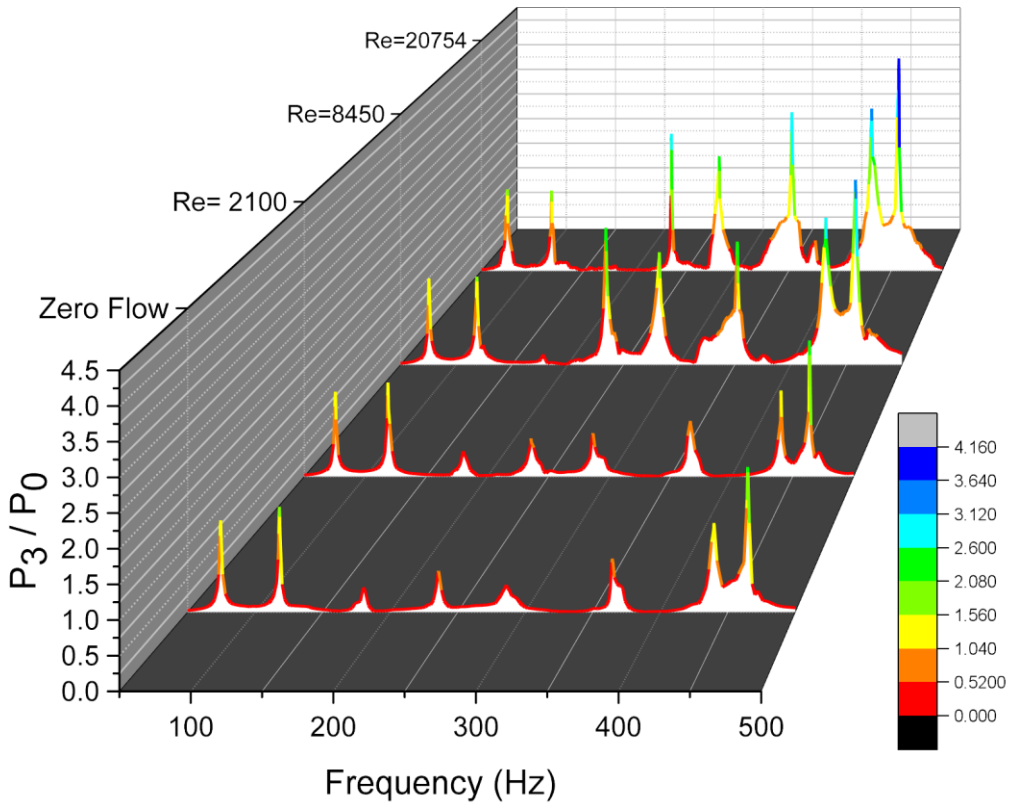

Figure 6.11: Comparison between Experimental Results at Different Mean Velocities “Branch 3, Mainline”

Table 6.7: Resonant Amplitudes and Frequencies for 1 m Branch, Branch 3

	Re=0	*Re=2100*	*Re=8450*	*Re=20754*
Frequency (Hz)	74.5	75.25	75.25	74.75
Amplitude	19.6	20.01	23.4	24.6
Frequency (Hz)	118	118.25	118.5	118
Amplitude	26.8	26.1	27.5	27.8
Frequency (Hz)	235.75	235.5	235.75	236.5
Amplitude	9.28	9.15	14.95	16.1
Frequency (Hz)	286.25	286.5	285.5	286
Amplitude	4.78	8.66	9.81	9.6
Frequency (Hz)	364.5	366.5	375	375.25
Amplitude	3.04	3.51	4.41	4.96
Frequency (Hz)	439.5	440.5	441.75	442.25
Amplitude	9.94	10.1	18.92	24.2
Frequency (Hz)	464.75	464.5	467.25	469.25
Amplitude	5.44	5.23	7.52	12.33

The measured resonant amplitudes and frequencies are collected in Table 6.7 for 1 m branch at different Re. The seven excited peaks against St numbers for 1 m branch are also plotted at Figure 6.12. They are shown at three different mean flow velocities.

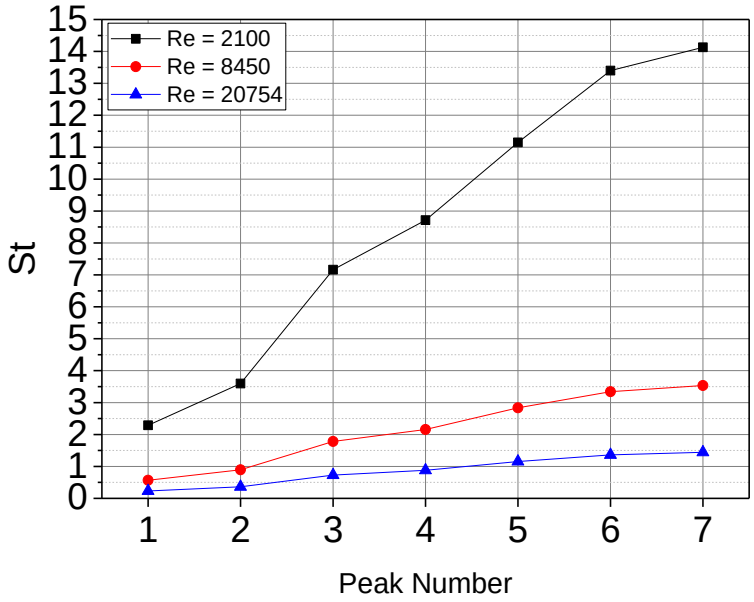

Figure 6.12: Comparison between St numbers at Seven Resonant Peaks for Three Re "Branch 3, 1 m Branch"

The St numbers are calculated based on the I.D. of the branch. For the zero mean flow, the St number is assumed to be zero. All the seven resonant peaks for the highest Re are excited within St range of 0.23–1.44, and from Table 6.7, the dimensionless amplitude of the 2nd peak of the flow with Re = 20754 is the strongest of all the resonant peaks. By decreasing the Re, the St numbers are increased. Therefore, the St values for the Re = 8450 and 2100 are in the ranges of 0.56–3.53 and 2.28–14.12, respectively.

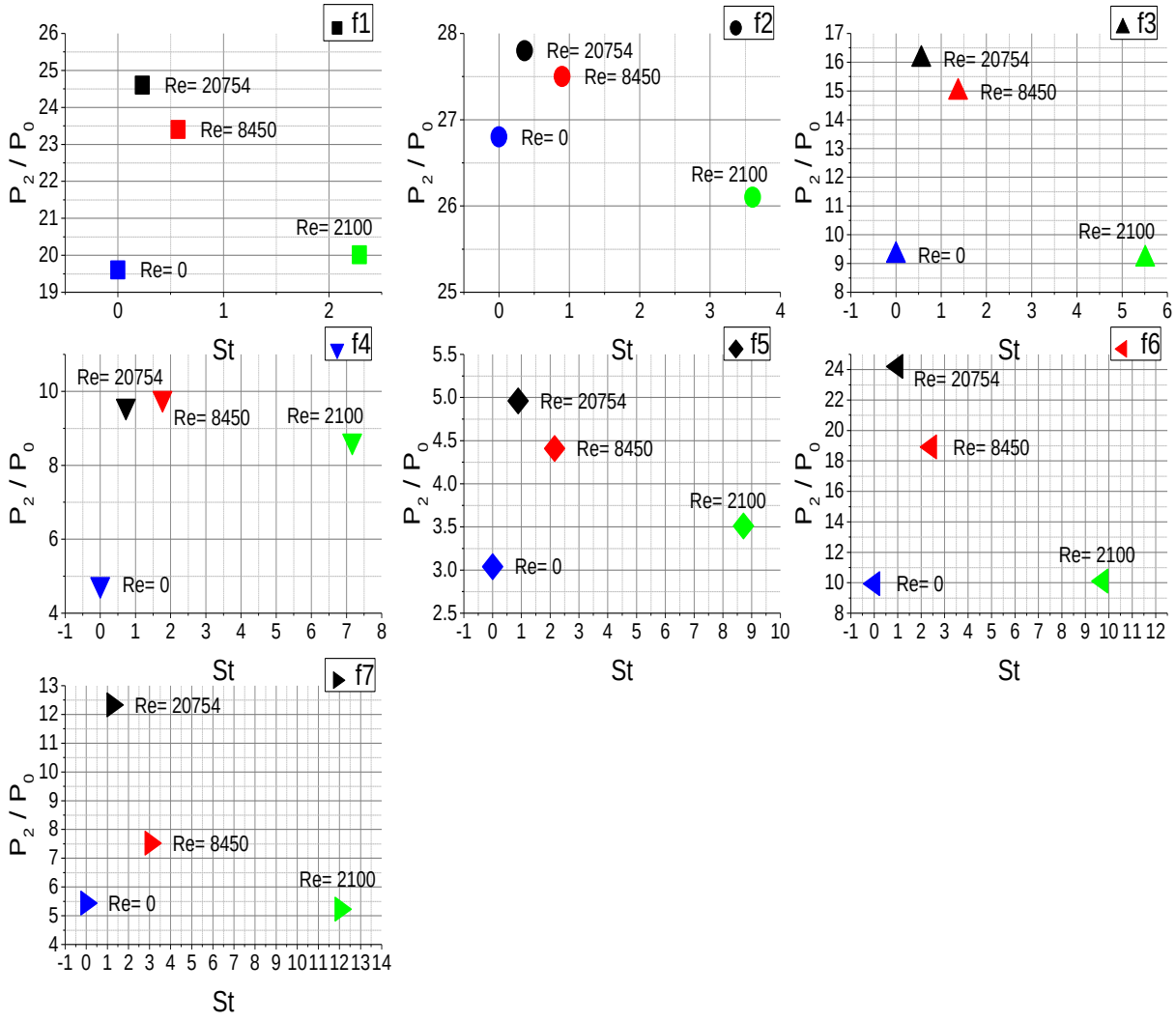

Figure 6.13: Comparison between Dimensionless Amplitude against the St numbers at Four Re "Branch 3, 1 m Branch"

An appropriate way to present acoustic resonance data against flow velocity is to plot the excited peaks against the St numbers for all tested Re, as already shown in Figure 6.12, or dimensionless resonant amplitude against the St number, as is shown in Figure 6.13. The St number is the inverse of the flow velocity and, therefore, decreasing the flow velocity is equivalent to moving from left to right along the St axis. Figure 6.13 illustrates that for the 1 m branch there is an optimal St number for each Re at which a significant increment in resonant amplitude occurs; approximately 8.71 for the case with Re = 2100, 2.15 for the case with Re = 8450, and 1.36 for the case with Re = 20754. These optimal St numbers and the associated resonant amplitudes depend on the local and global system parameters, such as geometry, acoustic attenuation and boundary conditions at the system terminations (Ziada, 2010).

Figure 6.14 presents the St numbers against the all seven resonant peaks of the 2.07 m branch for three tested Re.

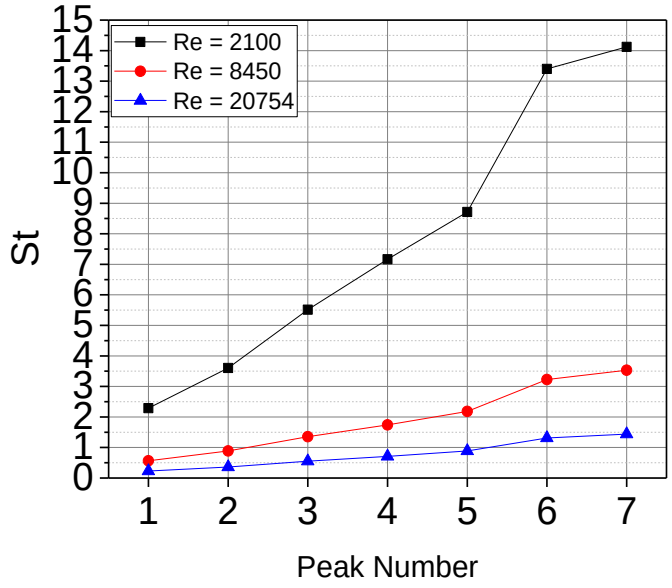

Figure 6.14: Comparison between St numbers at seven Resonant Peaks for four Re "Branch 3, 2.07 m Branch"

In Figure 6.15, the normalized acoustic pressure peaks at the closed end of the longer side branch for the three tested Re are plotted against the St numbers. It illustrates that there is an optimal St value for each case at which the maximum resonance amplitude increments from zero to laminar and turbulent flows occur; approximately 14.12 for the case with Re = 2100, 3.55 for the case with Re = 8450, and 1.44 for the case with Re = 20754. As can be seen, there are some differences between these values and the values obtained for the shorter branch. These differences are attributed to the different length of the branches that make different acoustic damping. Also, the interaction between the acoustic waves and the flowing fluid generated eddies at the first and the second T-junctions are different.

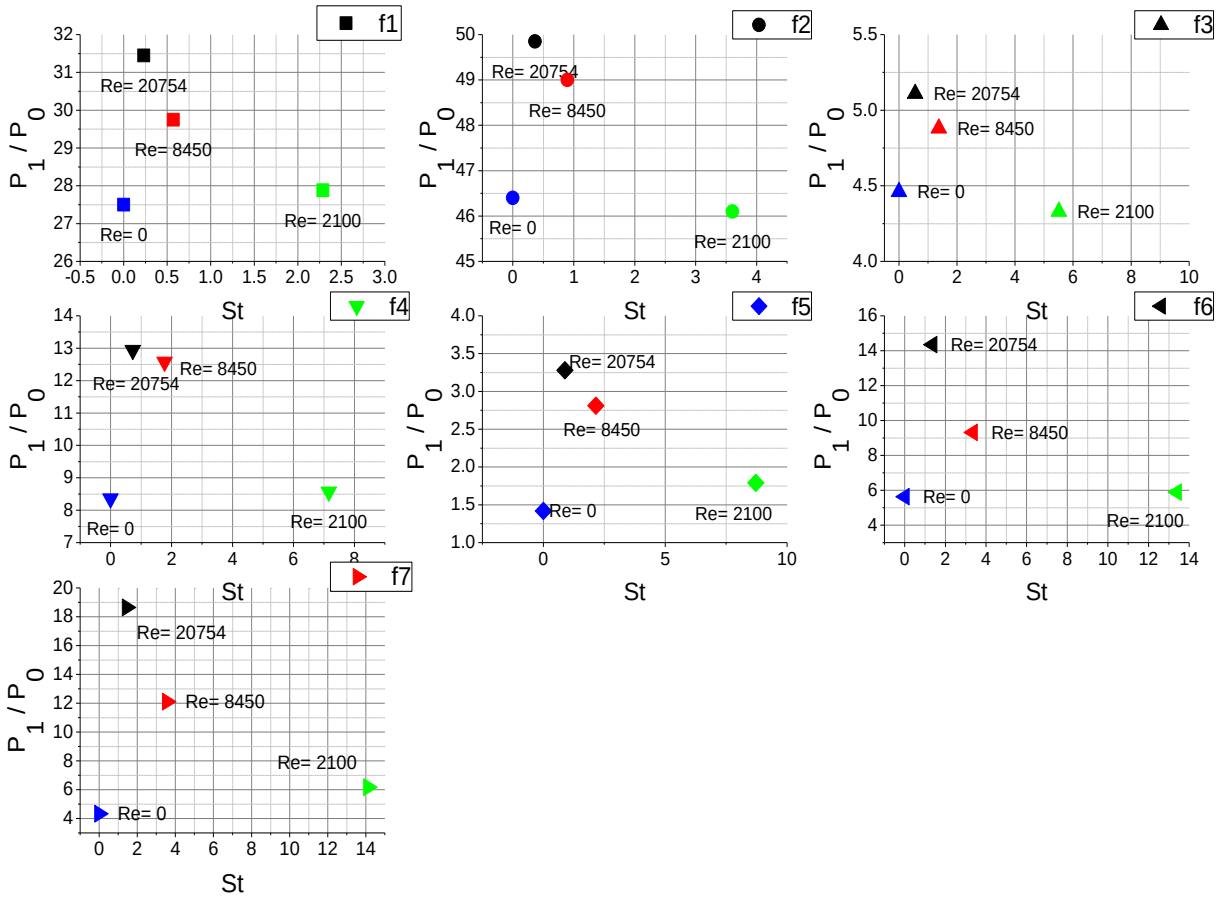

Figure 6.15: Comparison between Dimensionless Amplitude against the St numbers at four Re "Branch 3, 2.07 m Branch"

Resonant amplitudes and frequencies data at four different Re are collected in Table 6.8 and 6.10 for 2.07 m branch and mainline, respectively.

Table 6.8: Resonant Amplitudes and Frequencies for 2.07 m Branch, Branch 3

	Re=0	***Re=2100***	***Re=8450***	***Re=20754***
Frequency (Hz)	74.25	75.25	75.5	74
Amplitude	27.5	27.88	29.75	31.45
Frequency (Hz)	118	118.5	118.5	118.5
Amplitude	46.4	46.1	49	49.85
Frequency (Hz)	181.5	181.25	181.75	182.5
Amplitude	4.46	4.33	4.88	5.11
Frequency (Hz)	235.75	235.5	234.25	236.75
Amplitude	8.36	8.57	12.58	12.94
Frequency (Hz)	286.25	286.5	284.75	288.75
Amplitude	1.42	1.79	2.81	3.28
Frequency (Hz)	439.5	440.5	443.25	443
Amplitude	5.63	5.89	9.32	14.35
Frequency (Hz)	464.75	464.25	470.25	469.75
Amplitude	4.33	6.17	12.1	18.65

Table 6.9: Resonant Amplitudes and Frequencies for Mainline of Open ended Branch 3

	Re=0	***Re=2100***	***Re=8500***	***Re=20754***
Frequency (Hz)	74.5	75.5	75.5	75.5
Amplitude	1.36	1.39	1.55	1.59
Frequency (Hz)	118	118.5	118.5	118.5
Amplitude	1.56	1.54	1.58	1.57
Frequency (Hz)	235.75	235.75	234.25	235.5
Amplitude	0.608	0.624	2.46	2.68
Frequency (Hz)	286.25	286.5	282.25	282.5
Amplitude	0.405	0.710	2.02	1.95
Frequency (Hz)	364.5	366.25	352.25	353
Amplitude	0.792	0.911	2.21	3.10
Frequency (Hz)	439.75	440.5	431.75	431
Amplitude	1.32	1.41	2.64	3.17
Frequency (Hz)	464.75	463.75	458.25	457.5
Amplitude	2.15	2.23	3.32	4.15

.

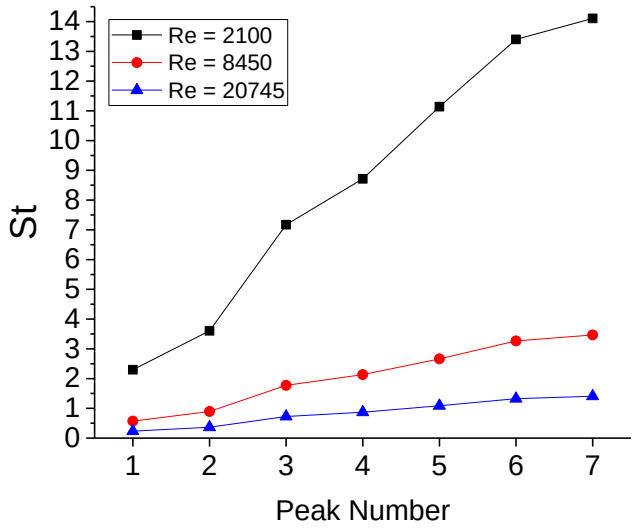

Figure 6.16: Comparison between St numbers at Seven Resonant Peak for four Re "Branch 3, Mainline Outlet"

Figure 6.16 presents the St numbers against all the seven resonant peaks of the mainline outlet. All the excited resonant peaks are within the St range of 0.23–1.41 for the highest Re number, and from Table 6.9, the dimensionless amplitude of the last resonant peak of the flow with Re = 20754 is the strongest of all the resonant peaks. The peak with the highest amplitude is not the same as the branches. Also, the upper value for St range of the highest Re is 0.03, smaller than the branches. For the laminar flow and the turbulent flow with Re = 8450, the St ranges are 2.29–14.12 and 0.57–3.46.

Figure 6.17 shows the variation of acoustic resonance peak amplitudes for the mainline outlet (P_3) at four different flow velocities. The plot directly compares normalized acoustic pressure versus velocity, at the test frequency range. Note that the values of resonant amplitude peaks for the mainline are amplified to a maximum by a factor of 4 from zero to turbulent flow. The important aspect of the plots of Figure 6.17 is that although the dominant resonant peaks in zero and laminar flows are almost negligible in the frequency range of 150–420 Hz, four resonant

peaks are visible in turbulent flow results. The maximum amplitudes are also obtained at the last resonant peaks for all the cases. An optimal St number for each case at which the maximum resonance amplitude increases from zero flow occur; approximately 14.1 for the case with Re = 2100, 3.46 for the case with Re = 8450, and 1.41 for the case with Re = 20754.

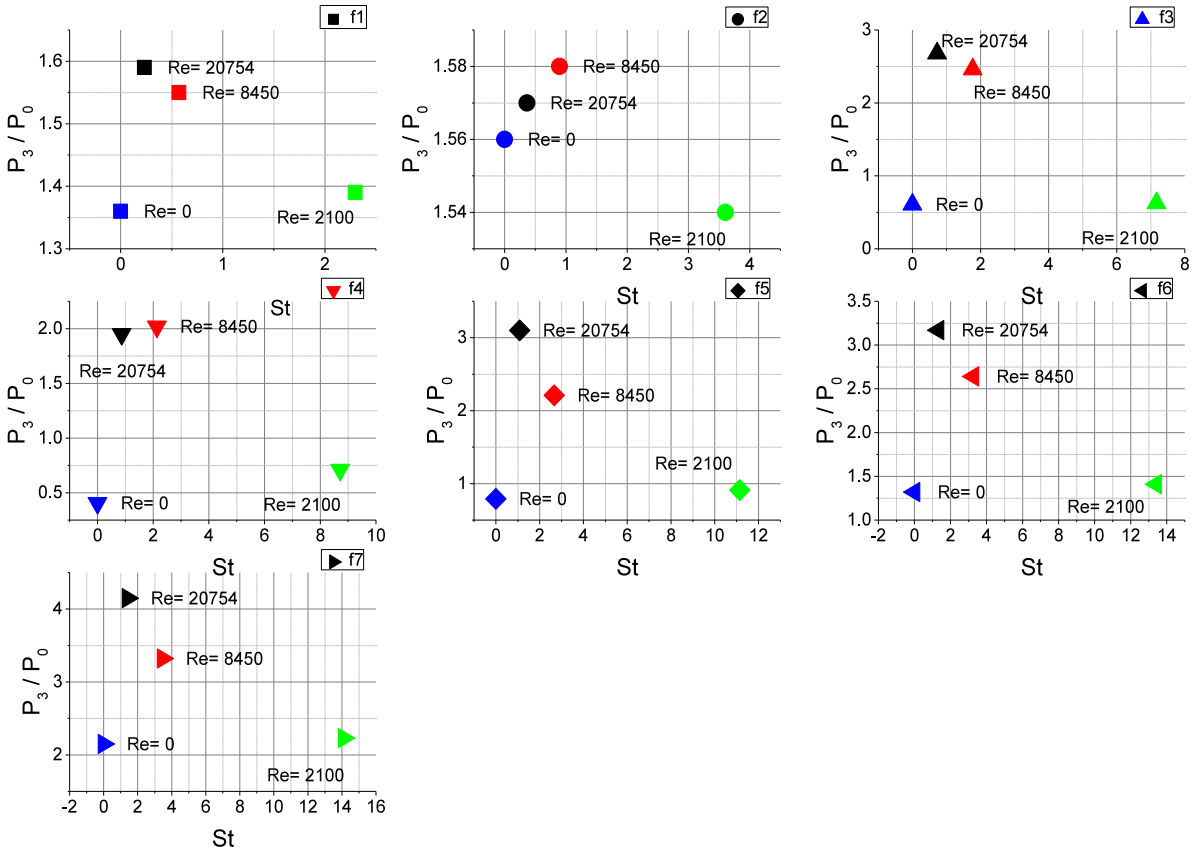

Figure 6.17: Comparison between Dimensionless Amplitude against the St numbers at four Re "Branch 3, Mainline"

6.2.2.6 Open-Ended Complex Experiment 2

The effect of the unequal branch geometry and flowing fluid generated eddies on the acoustic resonance are discussed in the previous section. Then, it is decided to check the complex geometry and flowing fluid generated eddies influence on the resonant frequency and resonant

amplitude. This is done by making some changes to the Complex Experiment close-ended geometry. The current geometry, shown in Figure 6.18, is referred to as "Complex Experiment 2". The measurements and predictions are done for two locations (P_1 and P_3). The P_1 in the Complex Experiment close-ended case is located at the outlet of the 2.07 m branch, and the branch is placed before the first junction of the loop. For the Complex Experiment 2 case, P_1 is located at the outlet of the 1.18 m branch, and the branch is placed after the first junction of the loop. The P_3 for the open-ended case is located 8 cm before the second junction of the loop instead of the mainline outlet. The acoustic resonances of the Complex Experiment 2 configuration, that correspond to variations of inflow velocities, are investigated for the three inflow conditions (Re = 0, 16200, 28500). All the tests are carried out with pure water, 8 mm I.D., in a temperature of 23^{o}C and system pressure of 0.41 MPa.

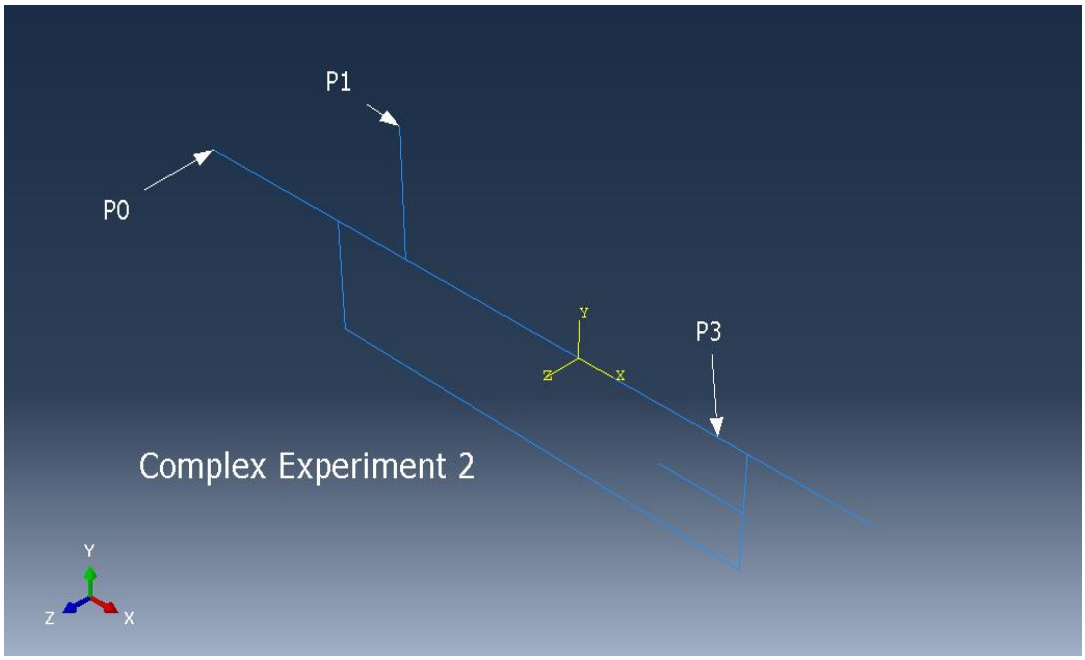

Figure 6.18: Schematic Diagram of Complex Experiment 2

Resonant amplitudes and frequencies data collected are similar to the tests described in close-ended section and are tabulated in Tables 6.10 & 6.11. Figures 6.19 and 6.20 show the normalized acoustic pressure amplitude measurements that correspond to variations of inflow velocity and frequency at P_1 and P_3, respectively.

Table 6.10: Resonant Amplitudes and Frequencies for 1.18 m Branch, Complex Experiment 2

	Re=0	***Re=16200***	***Re=28500***
Frequency (Hz)	61.25	61.5	61.5
Amplitude	27.5	21.65	21.7
Frequency (Hz)	95.75	96	96.25
Amplitude	8.8	8.86	9.07
Frequency (Hz)	129	130.25	131
Amplitude	3.46	3.84	3.97
Frequency (Hz)	182.75	182.75	183
Amplitude	2.87	3.28	3.78
Frequency (Hz)	196	196.5	196.25
Amplitude	2.42	3.3	3.58
Frequency (Hz)	254.75	255.25	255.75
Amplitude	8.34	10.18	11.43
Frequency (Hz)	289.75	291.75	292
Amplitude	4.43	7.33	8.42
Frequency (Hz)	314.25	315	315
Amplitude	6.15	10.49	13.2
Frequency (Hz)	372.75	373	372.75
Amplitude	1.82	2.95	3.25
Frequency (Hz)	398.5	400.25	400.25
Amplitude	7.28	12.06	13.15
Frequency (Hz)	445.5	448.25	448.75
Amplitude	2.01	3.58	4.39
Frequency (Hz)	472.5	474.25	474.25
Amplitude	9.84	12.91	13.92

From the experimental data the following are observed:

a) Figure 6.19 shows that for the case of 1.18 m branch, large amplitude resonant peaks are visible for the zero and turbulent mean flows. The strength of these peaks is high for all the cases at the frequency range of 60–500 Hz. Figure 6.19 also shows that with increasing frequency, the influence of the mean flow velocity on the acoustic resonance is

more dominant. The increments in the resonant amplitudes from zero to turbulent mean flows at the first six peaks (less than 240 Hz) are less than 35%. For the 7th to the 11th peaks from zero to the turbulent flow with Re = 28500, the resonant amplitudes rise about 2 times. The turbulent mean flow influence on the resonant amplitudes is more significant for the frequencies higher than 240 Hz. This value is very close to the frequency obtained for the open-ended outlet Branch 3 case at about 250 Hz. Hence, it is confirmed that more complicated geometries, such as that of a nuclear reactor, may influence the resonant frequencies at frequencies lower than the laboratory tested cases.

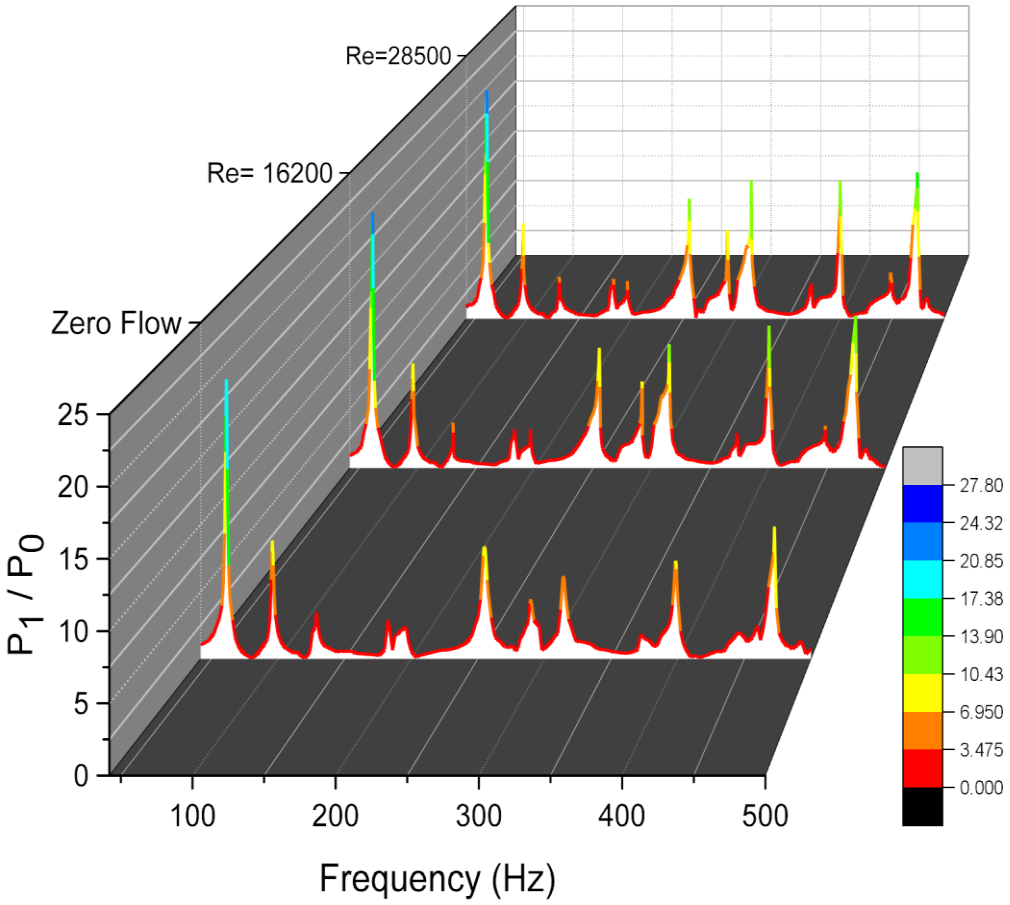

Figure 6.19: Comparison between Experimental Results at Different Mean Velocities "Complex Experiment 2, 1.18 m Branch"

The results also indicate that for the system with the complex geometry in the frequency range of 20–500 Hz, the mean flow velocity shifts the resonant frequencies. Increasing flow velocity changes the frequency of resonances, but the variations are less than 3.5 Hz. These shifts are different from the Branch 3 geometry, and it implies that different configurations might have different resonant frequency changes. This is important due to the fact that in a reactor or any complicated high pressure systems with pipe lengths of several miles and lots of subsystems, resonant frequencies might be shifted significantly with highly turbulent mean flows.

b) Figure 6.20 depicts that the highest resonant amplitude is obtained for the 1^{st} peak, which is almost one-third of the maximum resonant amplitude value at the 1.18 m branch. The resonant amplitudes for all peaks are given at the lower values than the branch. This is due to the fact that P_3 is closer to the open-ended outlet, and the acoustic energies are more damped than P_1. For the first three resonant peaks observed at the frequencies less than 200 Hz, a maximum increase of 35% in resonant amplitudes from zero to fully turbulent flow is reported. At the frequencies higher than 200 Hz and less than 400 Hz, the resonant amplitude increases from zero flow to turbulent flow are increased to maximum 45% at the 5^{th} resonant peak. At the 7^{th} resonant peak, the resonant amplitude value for the turbulent mean flow with Re = 28500 is more than twice that of the zero mean flow magnitude. The increases in resonant amplitudes from zero to turbulent mean flows at frequencies higher than 240 Hz are more significant for the branch. These observations show that the branch is more influenced with turbulent mean flow at the higher frequencies. It is attributed to the fact that the branch gives higher values of the resonant amplitudes, and is closer to the inlet than the P_3 at mainline.

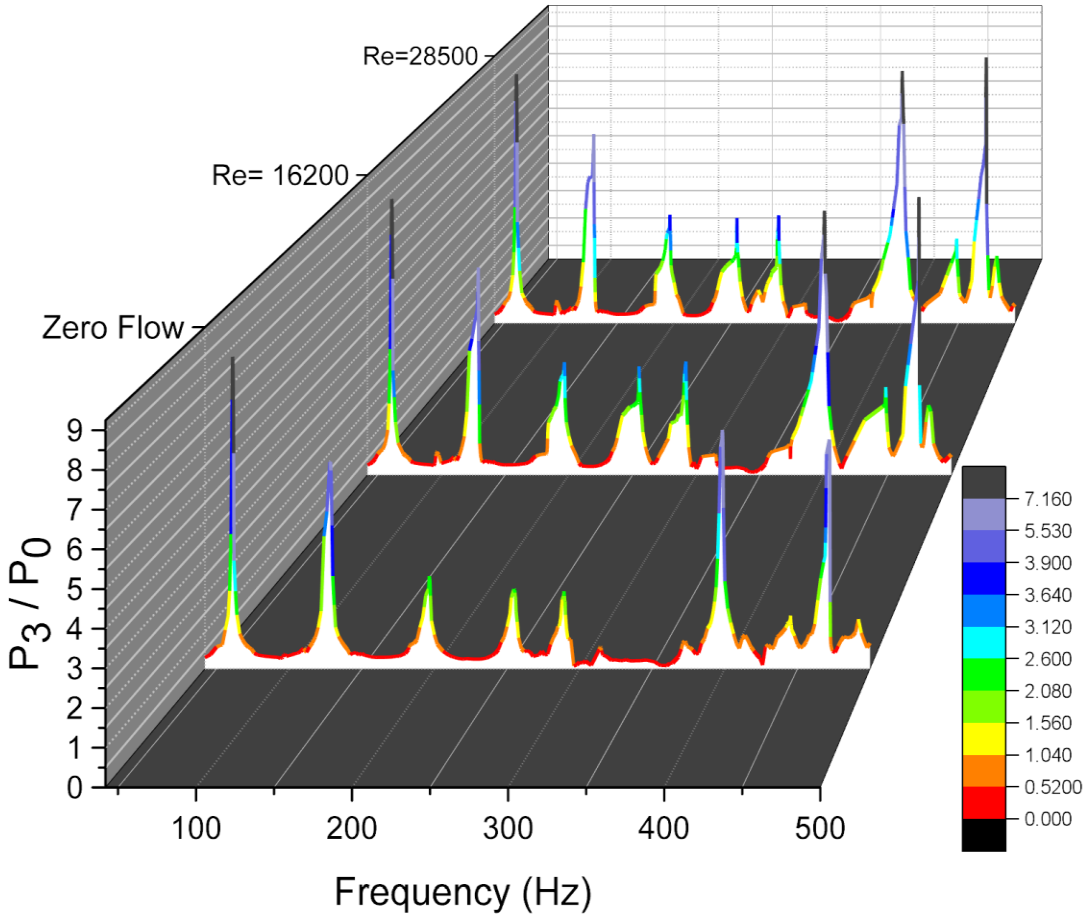

Figure 6.20: Comparison between Experimental Results at Different Mean Velocities "Complex Experiment 2, Mainline"

c) In terms of resonant frequencies, the mean flow velocities shift the resonant frequencies to a maximum of 3.25 Hz. This shifting, for the frequencies less than 250 Hz, are less than 2 Hz. It confirms that mean flow velocity influences the resonant frequency for the Complex Experiment 2 configuration, but its influence is different from the Branch 3 open-ended configuration.

Figure 6.21 plots the twelve excited peaks against St numbers for the 1.18 m branch at the two tested turbulent mean flow velocities.

6.11: Resonant Amplitudes and Frequencies at Mainline, Complex Experiment 2

	Re=0	***Re=16200***	***Re=28500***
Frequency (Hz)	61	61	61.25
Amplitude	8.45	8.51	8.62
Frequency (Hz)	128.5	128.75	129.25
Amplitude	5.61	6.4	6.55
Frequency (Hz)	196.5	196.5	196.25
Amplitude	2.51	3.48	3.76
Frequency (Hz)	254.75	255	255.25
Amplitude	2.16	3.35	3.64
Frequency (Hz)	289.25	291.75	292
Amplitude	2.1	3.5	3.74
Frequency (Hz)	398.25	400.5	400.75
Amplitude	6.47	8.15	8.74
Frequency (Hz)	445.25	448.5	448.75
Amplitude	1.44	2.71	2.93
Frequency (Hz)	469.75	474.5	474.5
Amplitude	6.21	8.58	9.2

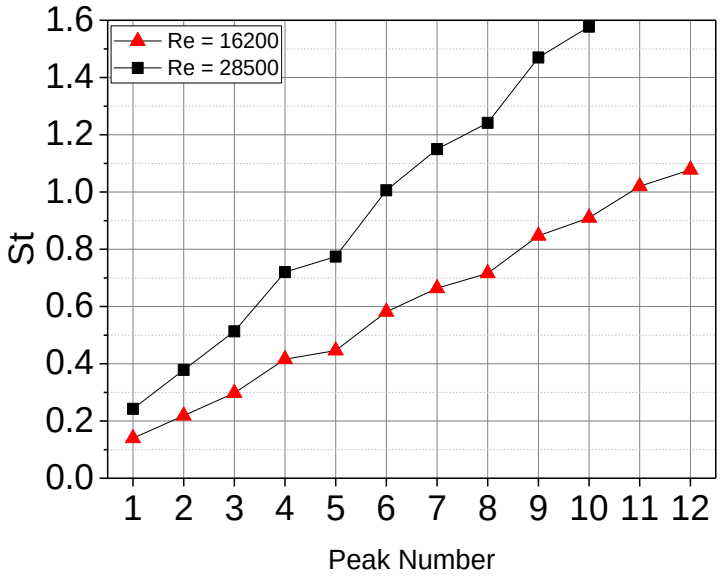

Figure 6.21: Comparison between St numbers at Twelve Resonant Peaks for Two Re "Complex Experiment 2, 2.07 m Branch"

The St numbers are obtained from the resonant frequencies, tube I.D., and the mean flow velocities of the branch. For the case with Re = 16200, the resonant peaks are excited within St

range of 0.24–1.86. The St numbers for the Re = 28500 are in the ranges of 0.13–10.7, and from Table 6.10, the dimensionless amplitude of the 1st resonant peak is the strongest of all the resonant peaks.

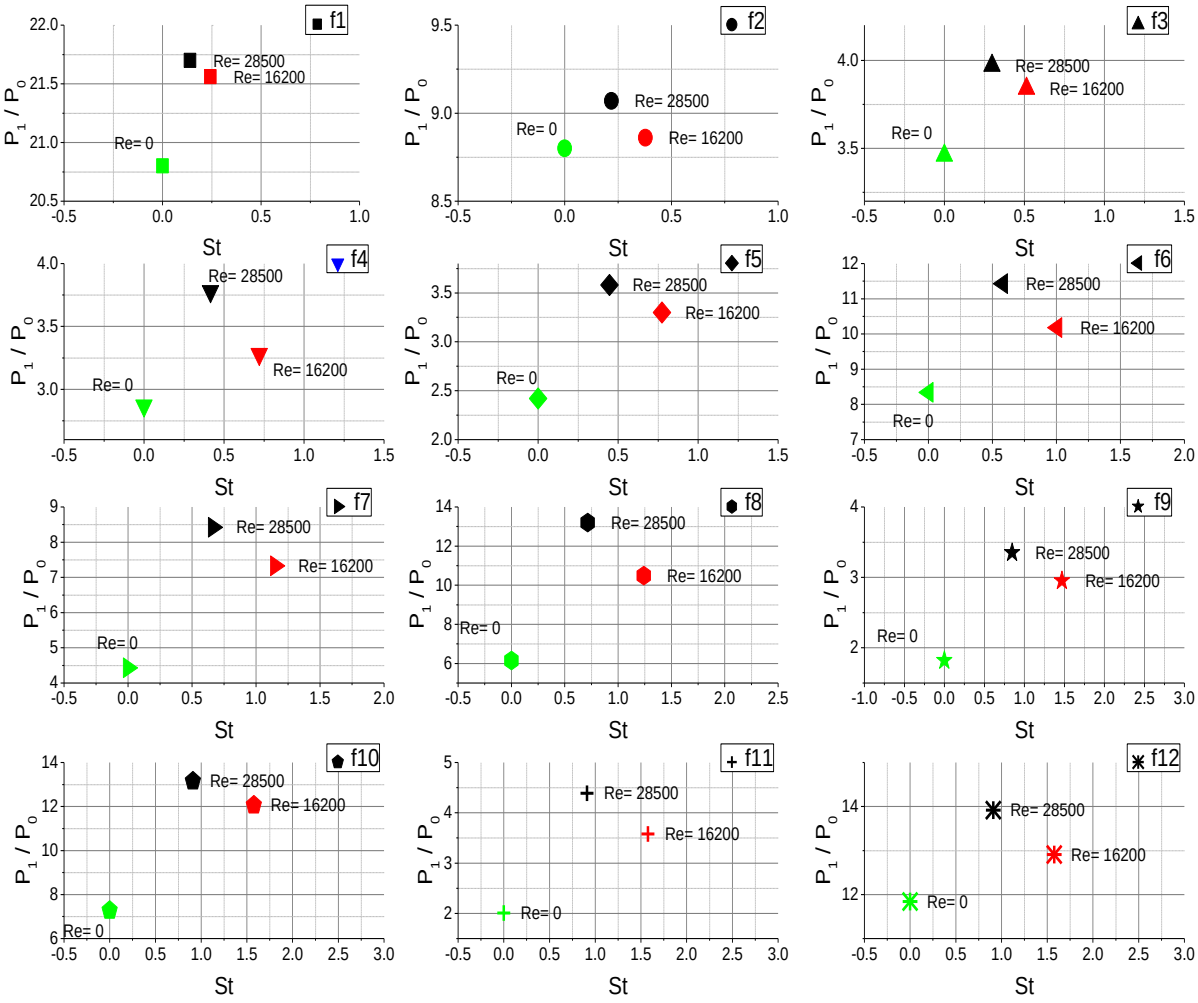

Figure 6.22: Comparison between Dimensionless Amplitude against the St numbers at Three Re "Complex Experiment 2, 1.18 m Branch"

The resonant amplitude peaks at P_1 are plotted against St numbers for all the tested Re, and they are shown in Figure 6.22. Figure 6.22 shows that there is an optimal St number for each

range, at which, the significant increment in resonant amplitudes occurs, which is approximately 1.14 for the case with Re = 16200, and 0.66 for the case with Re = 28500. These optimal St numbers and the associated resonant amplitudes are different from that of the Branch 3 open-ended experiment. The dissimilar values are because of the different geometries and acoustic attenuations of the two tested geometries. Figure 6.23 presents the St numbers against all the 8 resonant peaks of P_3 for the two tested Re values. All resonant peaks are excited within the same St ranges of P_1 for both the turbulent flows, and from Table 6.11, the dimensionless amplitude of the last peak of the flow with Re = 28500 is the strongest of all the resonant peaks.

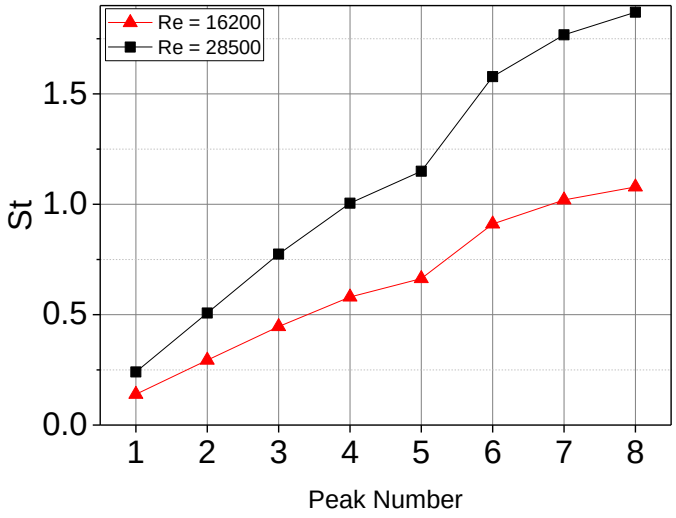

Figure 6.23: Comparison between St numbers at 8 Resonant Peaks for Three Re "Complex Experiment 2, Mainline"

In Figure 6.24, the resonant amplitudes at the mainline (P_3) are plotted against the St values for the three tested Re. Figure 6.24 shows that there is an optimal St number for each range at which the significant increase in resonance amplitude from zero to turbulent flows occurs, approximately at 1.005 and 0.58 for Re = 16200 and 28500, respectively. It can be seen that

there are some differences between these values and the values obtained for the branch. Four more resonant peaks are observed for the branch than the P_3 at the frequency range of the tests. These differences at St are attributed to the dissimilar measured locations that make different acoustic damping and higher numbers of resonant peaks for the branch. Also, P_1 is located close to the first junction, and P_3 is placed close to the third junction, therefore, the interactions between the acoustic waves and the flowing fluid created eddies at the first and the third junctions are different.

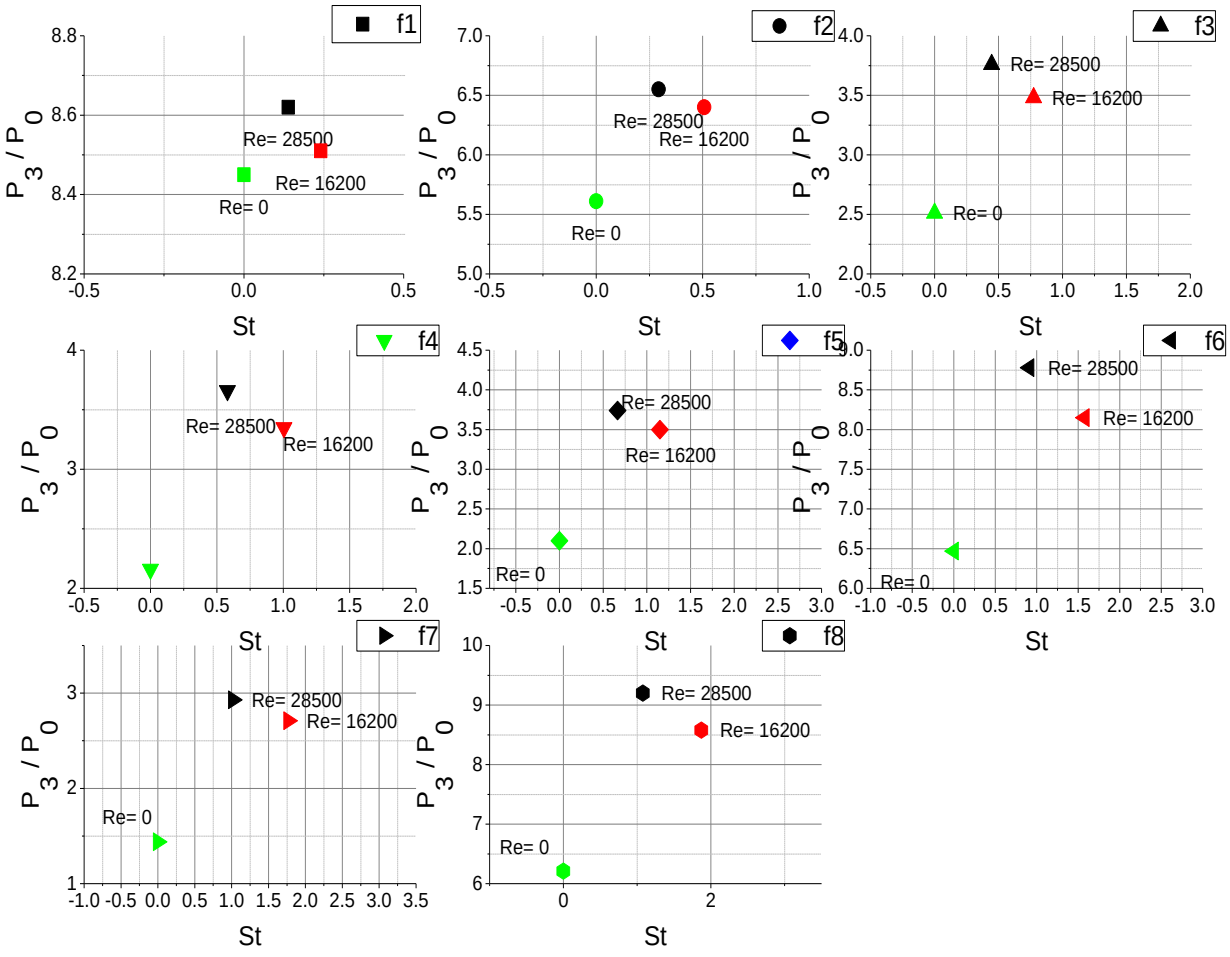

Figure 6.24: Comparison between Dimensionless Amplitude against the St numbers at Three Re "Complex Experiment 2, Mainline"

6.2.3 Resonant Frequency Predictions

6.2.3.1 LWS Using Constant VD and Frequency-Dependent Damping Methods

In this section, the damping methods of Kagawa et al. (1983), Schohl (1993), Trikha (1975), Urbanowicz and Zarzycki (2012), Vardy and Brown (2004), and Vitkovsky et al. (2004) and constant VD are assessed using LWS.

6.2.3.1.1 Straight line close-ended

The comparisons between the LWS using constant VD and the frequency-dependent damping methodologies and the measurements for SS tubes with 1 mm and 2 mm wall thicknesses, Al tube of 2 mm wall thickness, and Al tubes with two different wall thicknesses (2mm and 4 mm) are shown in Figures 6.25, 6.26, 6.27, and 6.28, respectively. They show the ratio of the outlet acoustic pressure amplitude to the inlet pressure amplitude with respect to frequency. All the resonant peaks are displayed separately to show the measured and the predicted acoustic resonances clearly. They are labelled as “a”, “b”, “c”, “d”, and “e” from the first to the last resonant peak respectively. The RMSE for the resonant frequency predictions compared to the experimental data are shown in Figure 6.29, for both the SS (10 mm and 12 mm O.D.) and the Al tubes.

In Figures 6.25 and 6.26, the resonant frequency predictions using a constant VD show a difference of less than 5.25 Hz from the experimental data for both the SS tubes. The maximum differences are obtained at the 4^{th} peak, which means that increasing the frequency increases the difference between the predictions and the measurements. It can be seen in Figure 6.27 that for

the Al tube with a 12 mm O.D., good agreement between the predictions and the measurements is obtained. For the Al tube experiment with two different wall thicknesses, constant VD predictions for all the 6 picks are less than 4.25 Hz. It indicates that the resonant frequency predictions using a constant VD are fairly good.

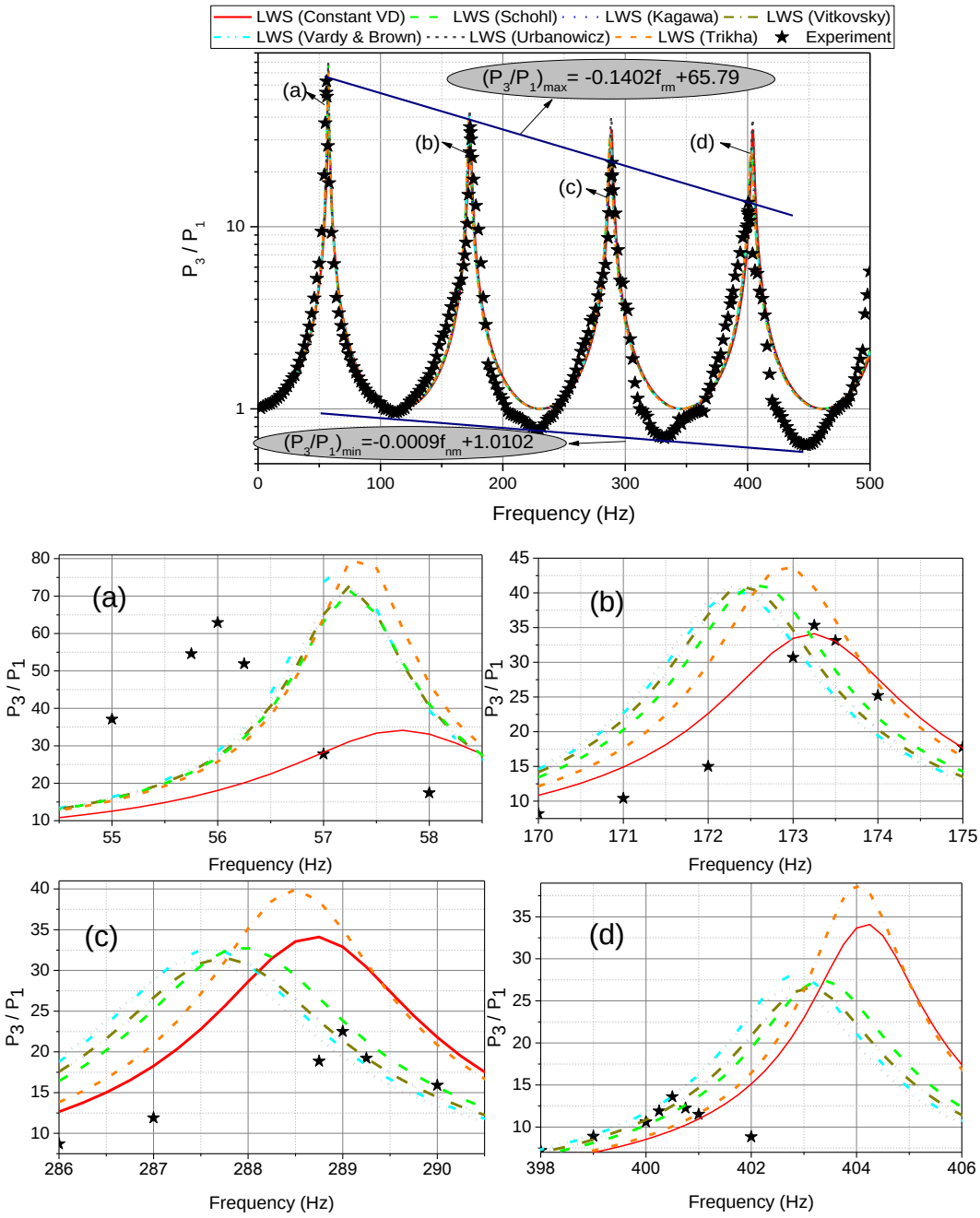

Figure 6.25: Comparison between Results of the "6.13m long 10 mm O.D. SS Close-Ended Experiment" and LWS Predictions

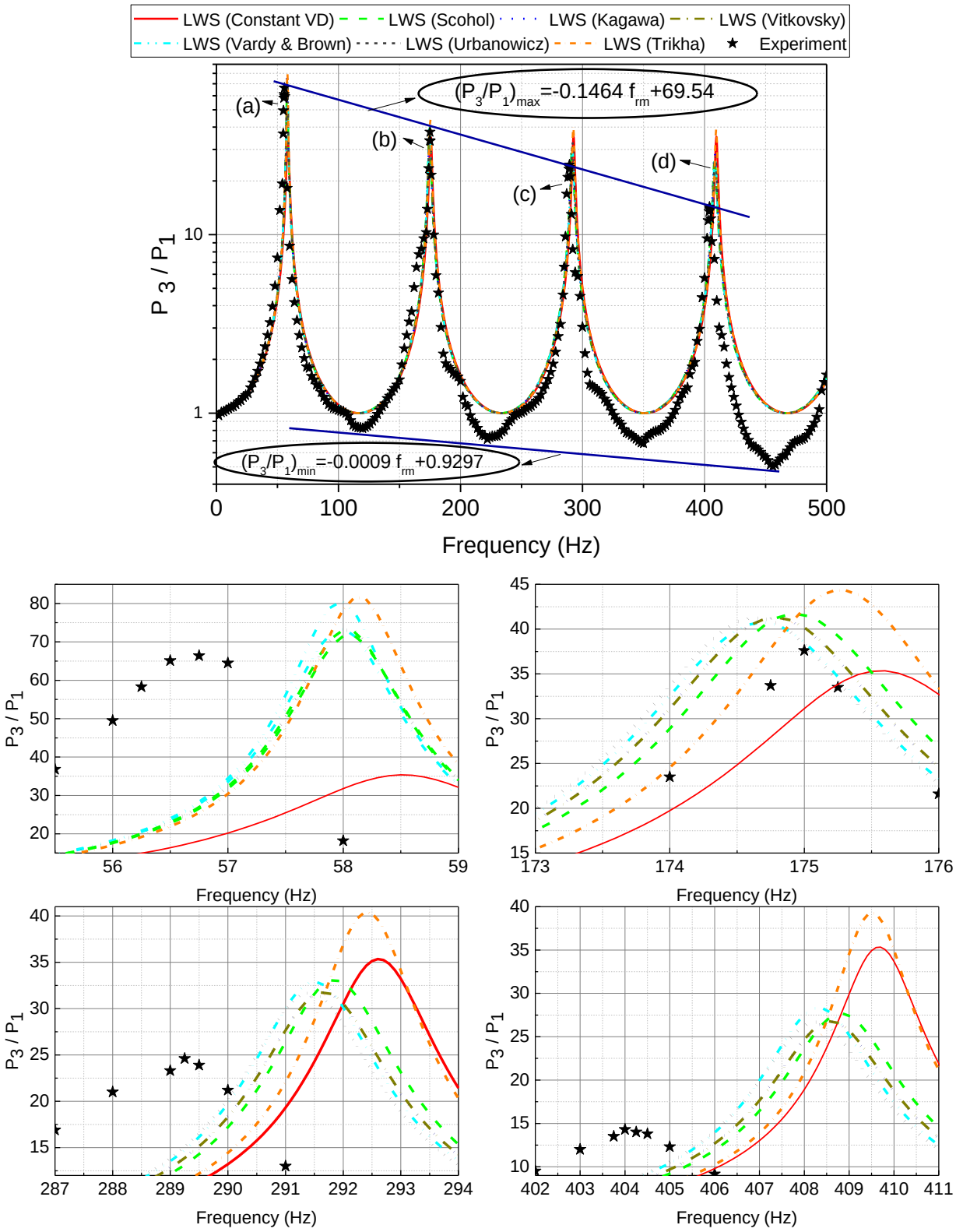

Figure 6.26: Comparison between Results of the "6.13m long 12 mm O.D. SS Close- Ended Experiment" and LWS Predictions

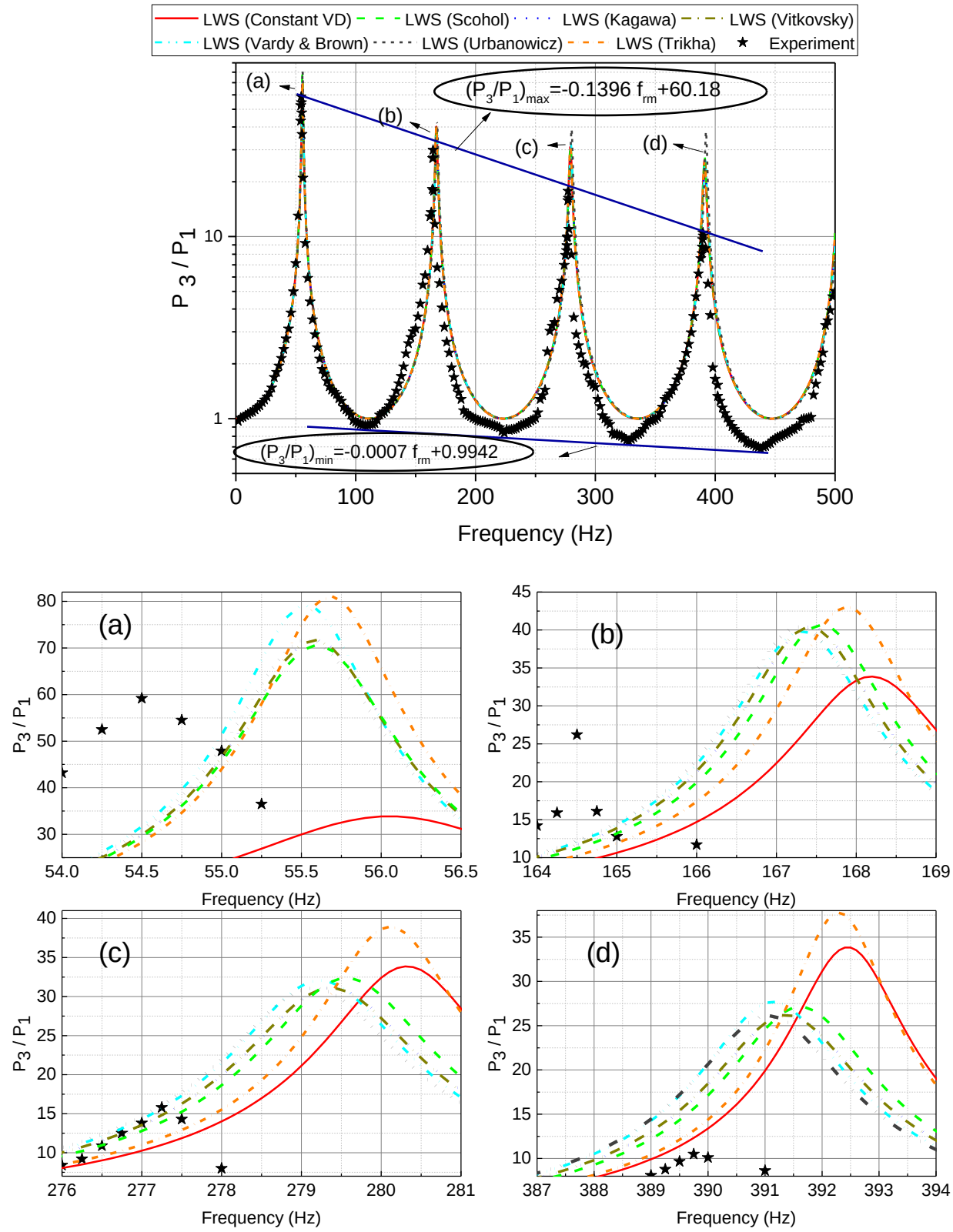

Figure 6.27: Comparison between Results of the "6.13m long 12 mm O.D. Al Close- Ended Experiment" and LWS Predictions

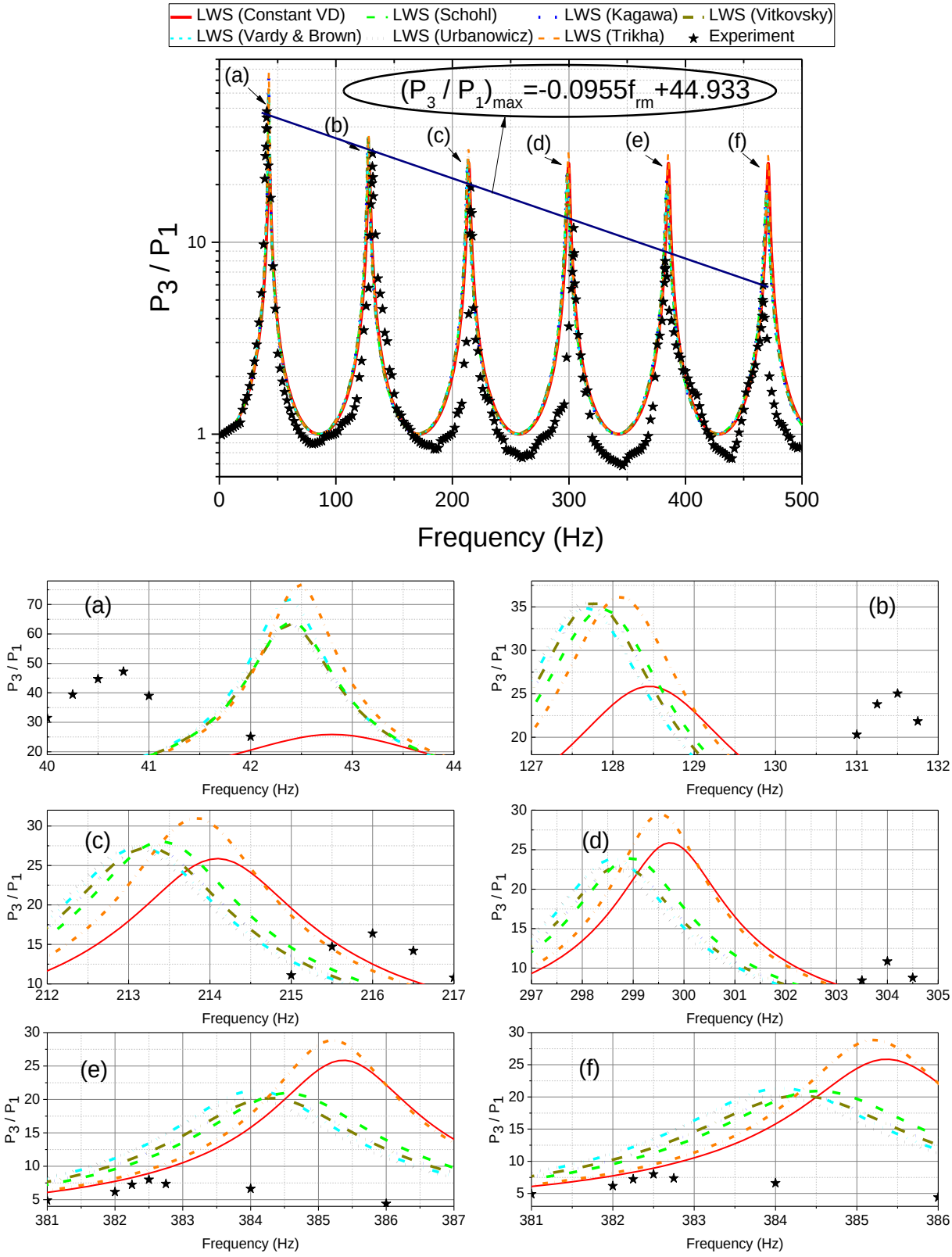

Figure 6.28: Comparison between Results of the "6.13 m long with 12 mm O.D & 1.87 m long with 16 mm O.D. Al Close-Ended Experiment" and LWS Predictions

Using the damping methods of Kagawa et al. (1983), Schohl (1993), Vardy and Brown (2004), Vitkovsky et al. (2004) and Urbanowicz and Zarzycki (2012), the resonant frequencies of the SS and Al tubes, shown in Figures 6.25, 6.26, and 6.27, are predicted with less than 4 Hz difference from the measurements. The two Al tubes with different wall thicknesses at the 4th resonant peak show the difference of a maximum of 5.25 Hz from the measurement. The differences from the measurements obtained by Trikha (1975) method are almost the same as that of the constant VD. Although there is an improvement in terms of the resonant frequency predictions with the assessed frequency-dependent methods over the constant VD method at the first three straight line cases, this improvement is not significant. Indeed, the 4 Hz or 5 Hz difference between the predicted and measured resonant frequency is deemed acceptable.

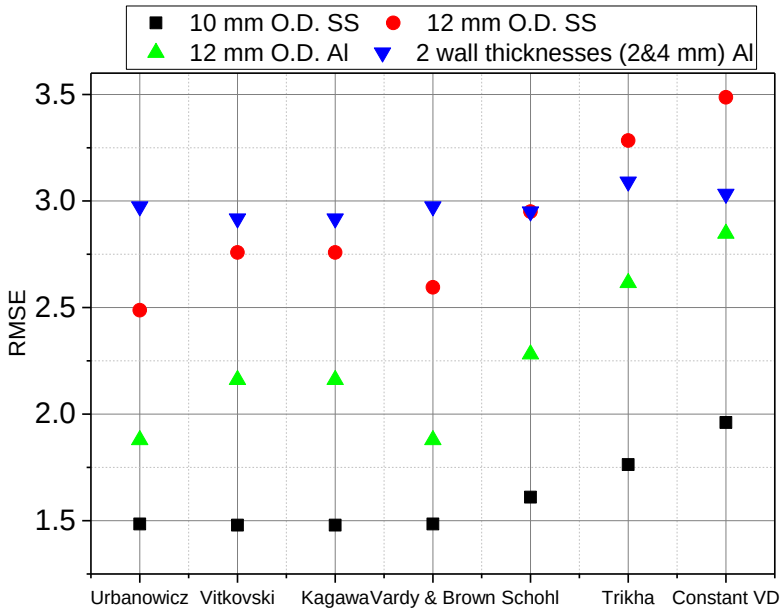

Figure 6.29: RMSE Values for Resonant Frequency Predictions

Figure 6.29 shows that using the damping terms of Vardy and Brown (2004) and Urbanowicz and Zarzycki (2012) give the lowest RMSE values in resonant frequency predictions for the

thinner SS tube and 12 mm O.D. Al tube respectively. All the prediction methods show the minimum RMSE values for 10 mm O.D. SS and maximum RMSE values for Al tubes with two different wall thicknesses. It implies that the resonant frequencies of the straight line with the single sound speed, lower wall thickness, and higher Young's modulus are better predicted with LWS using the assessed damping methods.

6.2.3.1.2 Straight Line Open-Ended

The predictions for the open-ended zero mean flow with the LWS using constant VD and the same frequency-dependent damping terms employed for the close-ended cases are compared against the experimental data in Figures 6.30- 6.32.

Figures 6.30, 6.31, and 6.32 show that for all the three locations (P_1, P_2 and P_3) a maximum difference of 4 Hz is obtained by the LWS using constant VD from the experimental data. This difference is considered acceptable and shows that the constant VD method accurately predicts the resonant frequencies for the tube with an open outlet end.

The damping method proposed by Trikha (1975) predicts the resonant frequencies almost similar to those predicted by the constant VD method. The resonant frequency predictions using the damping methodologies of Schohl (1993), Urbanowicz and Zarzycki (2012), and Vardy and Brown (2004) show less than 3 Hz difference from the experimental data. Although they show better agreement with the measurements than the constant VD method, the 1 Hz difference with respect to the percentage of the difference is not considerable.

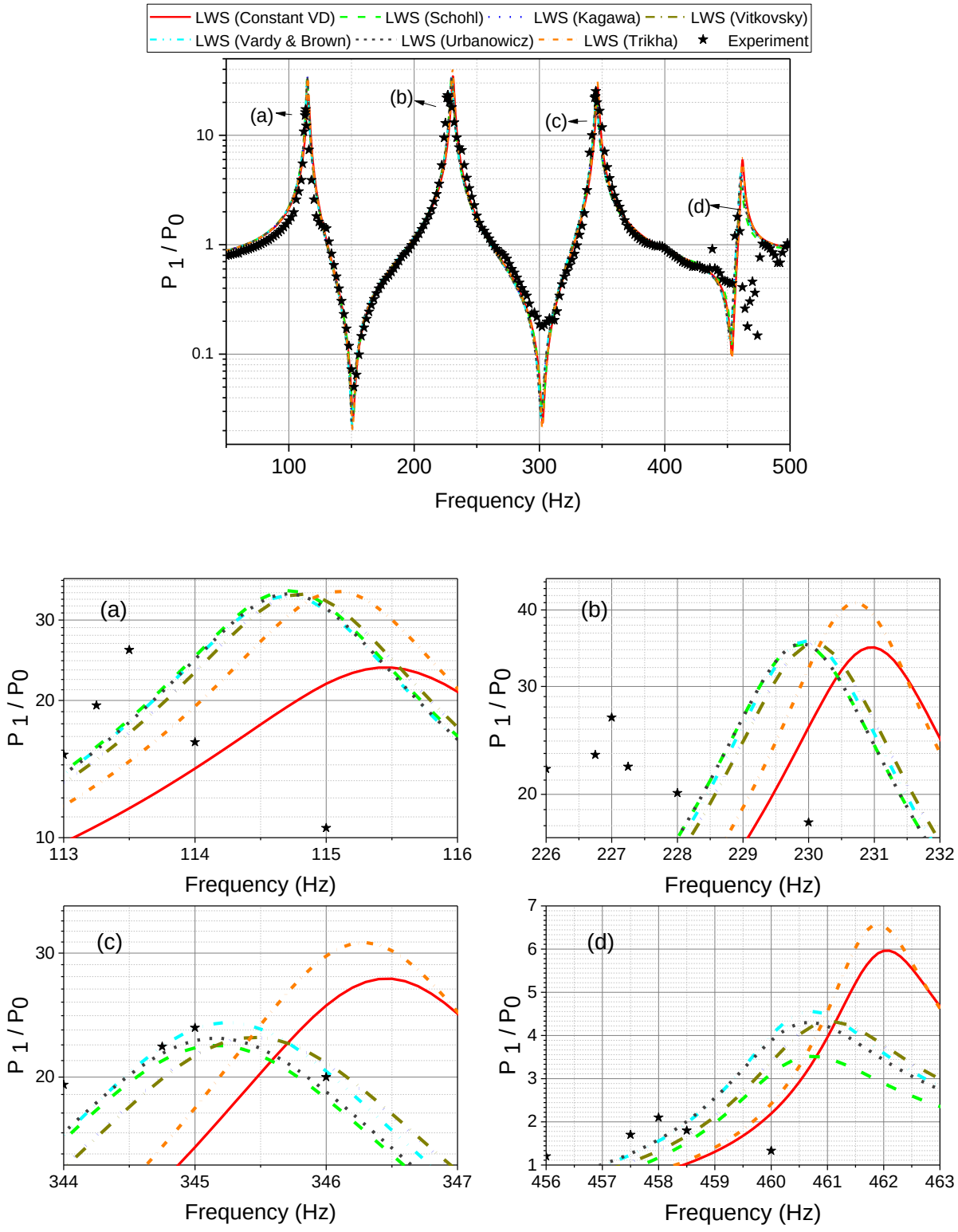

Figure 6.30: Comparison between Zero Flow Results of the "6.13m long 10 mm O.D. SS Open-Ended Experiments" at 1.45 m and LWS Predictions (a) 1st Peak (b) 2nd Peak (c) 3rd Peak (d) 4th Peak

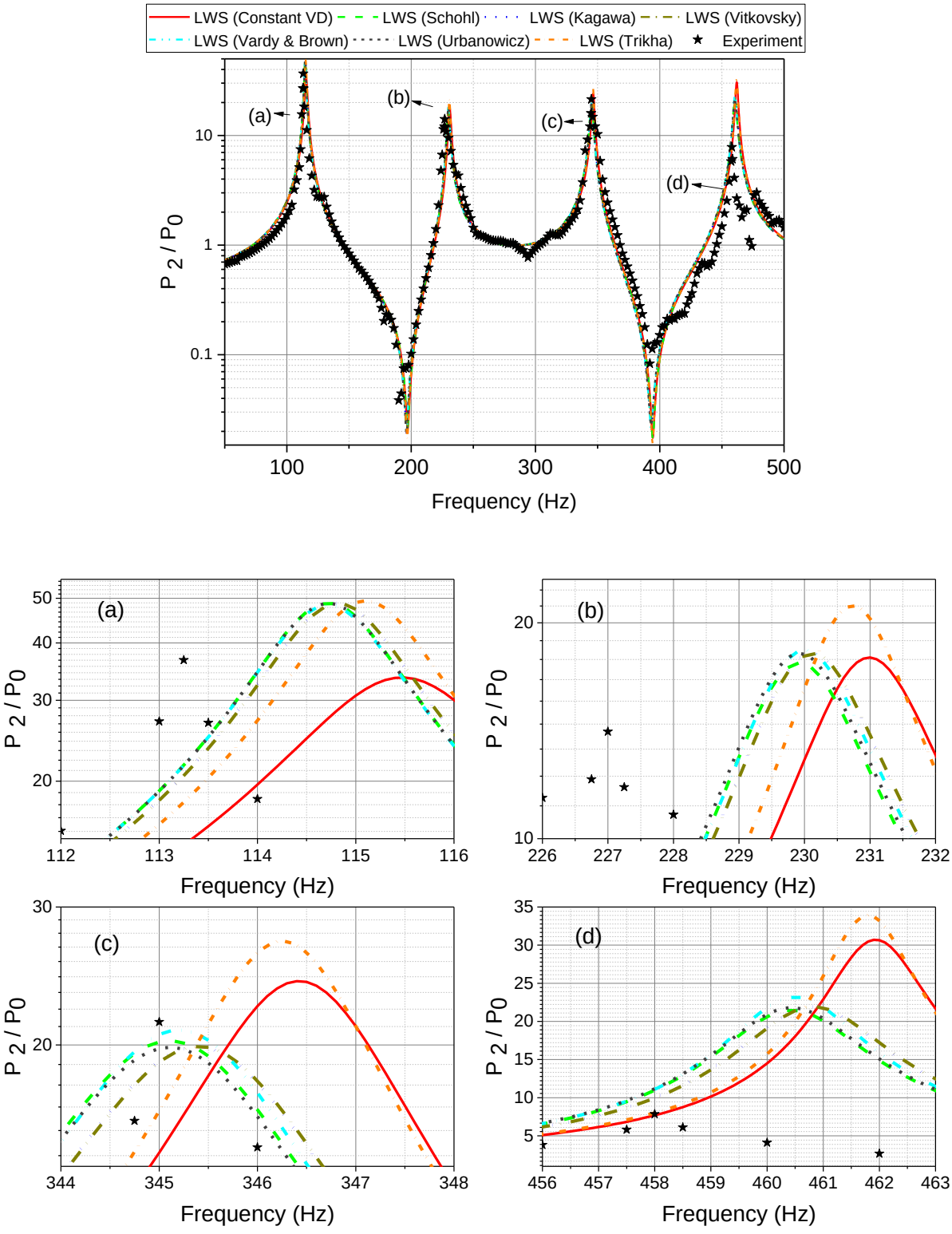

Figure 6.31: Comparison between Zero Flow Results of the "6.13m long 10 mm O.D. SS Open-Ended Experiments" at 2.54 m and LWS Predictions (a) 1st Peak (b) 2nd Peak (c) 3rd Peak (d) 4th Peak

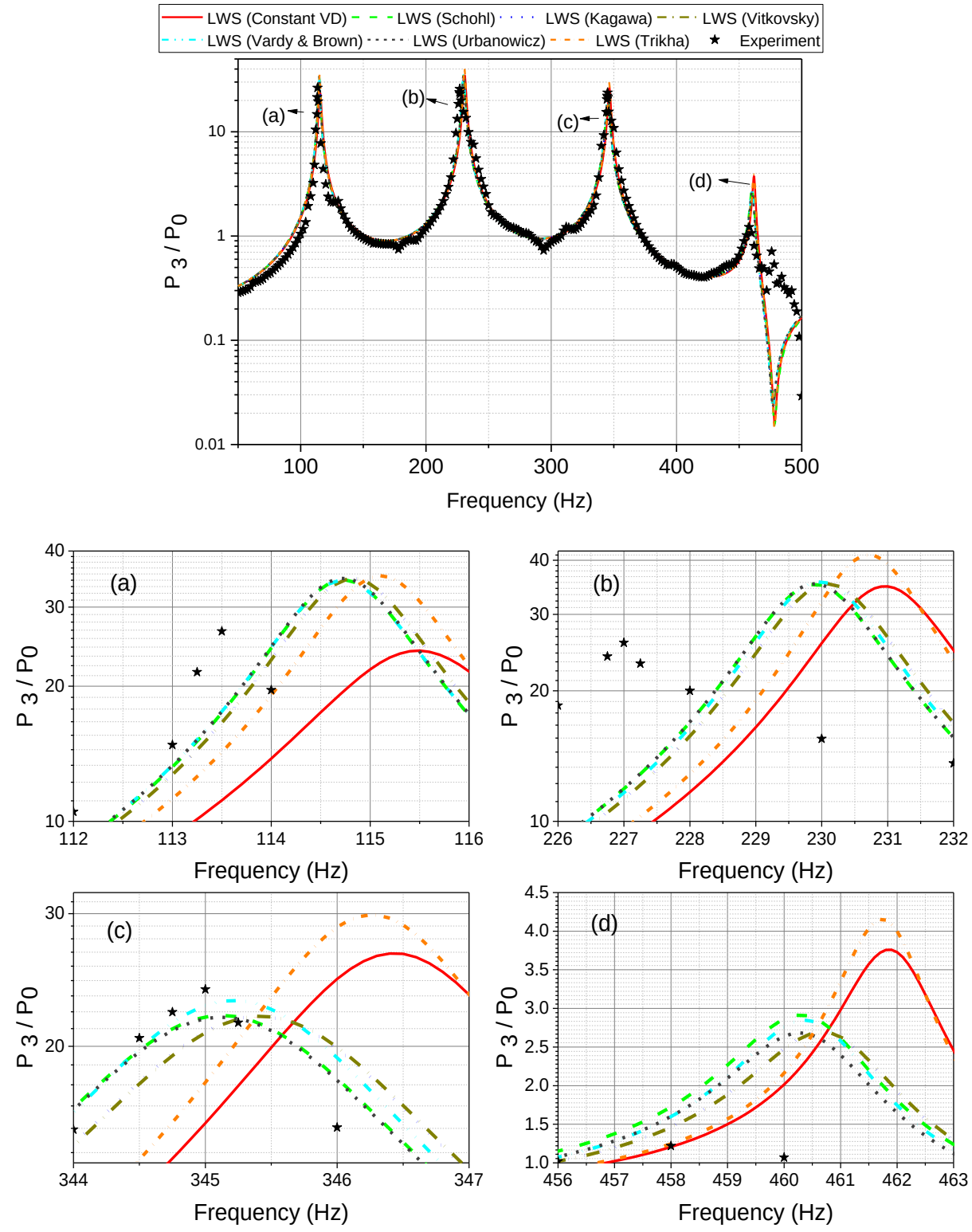

Figure 6.32: Comparison between Zero Flow Results of the "6.13m long 10 mm O.D. SS Open-Ended Experiments" at 4.65 m and LWS Predictions (a) 1st Peak (b) 2nd Peak (c) 3rd Peak (d) 4th Peak

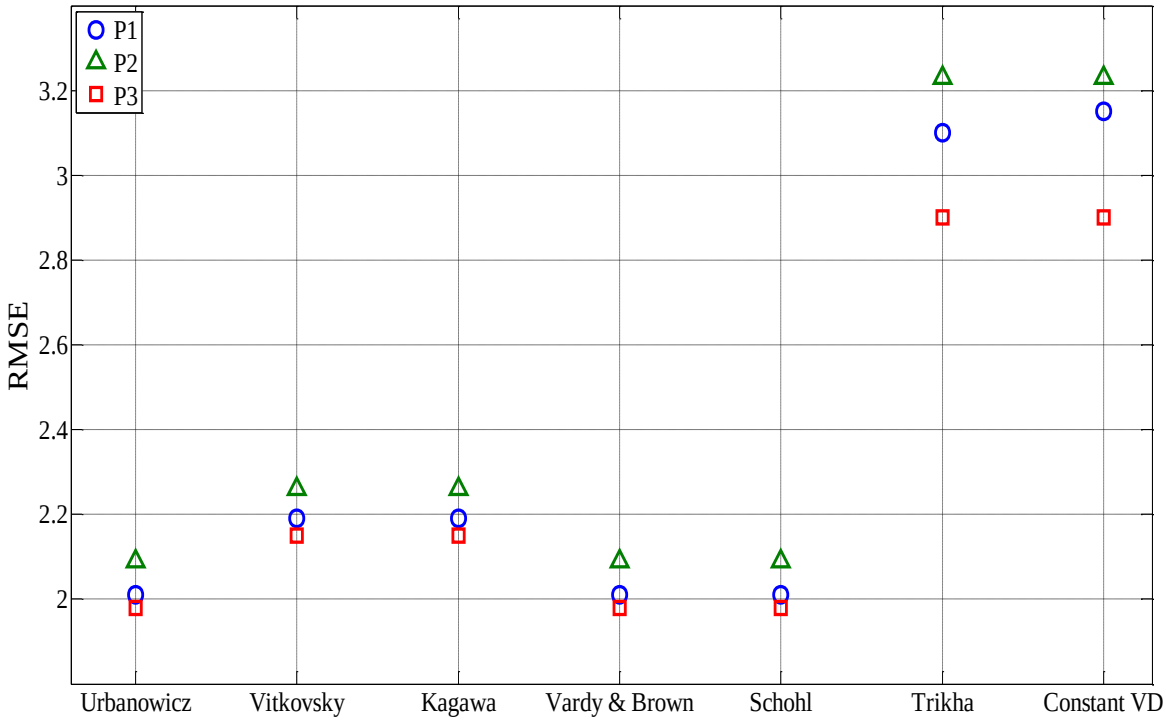

Figure 6.33: RMSE Values of Zero Mean Flow Resonant Frequency Predictions

Figure 6.33 shows that the RMSE values of the damping methodologies of Schohl (1993), Urbanowicz and Zarzycki (2012), and Vardy and Brown (2004) confirm the improvement in the prediction of resonant frequency with the frequency-dependent damping methods over the constant VD.

6.2.3.1.3 Equal Branches and Elbow

The comparisons between the LWS using constant VD, the LWS using frequency damping methodologies, and the measurements for elbow, Branch 1, and Branch 2 are shown in Figures 6.34, 6.35, and 6.36, respectively.

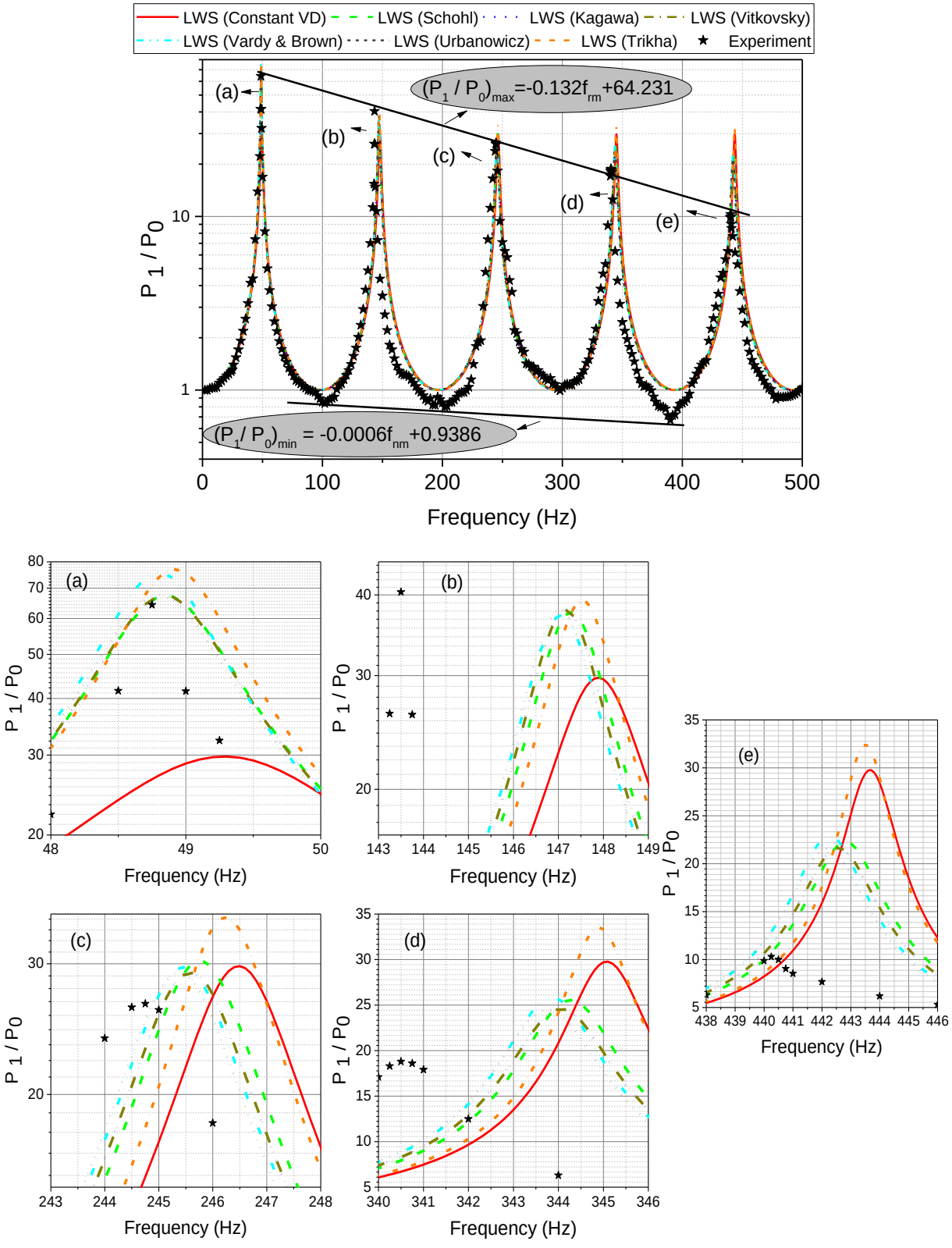

Figure 6.34: Comparison between Results of the "Length of 7.18 m, 10 mm O.D for Elbow SS Close-Ended Experiment" and LWS predictions

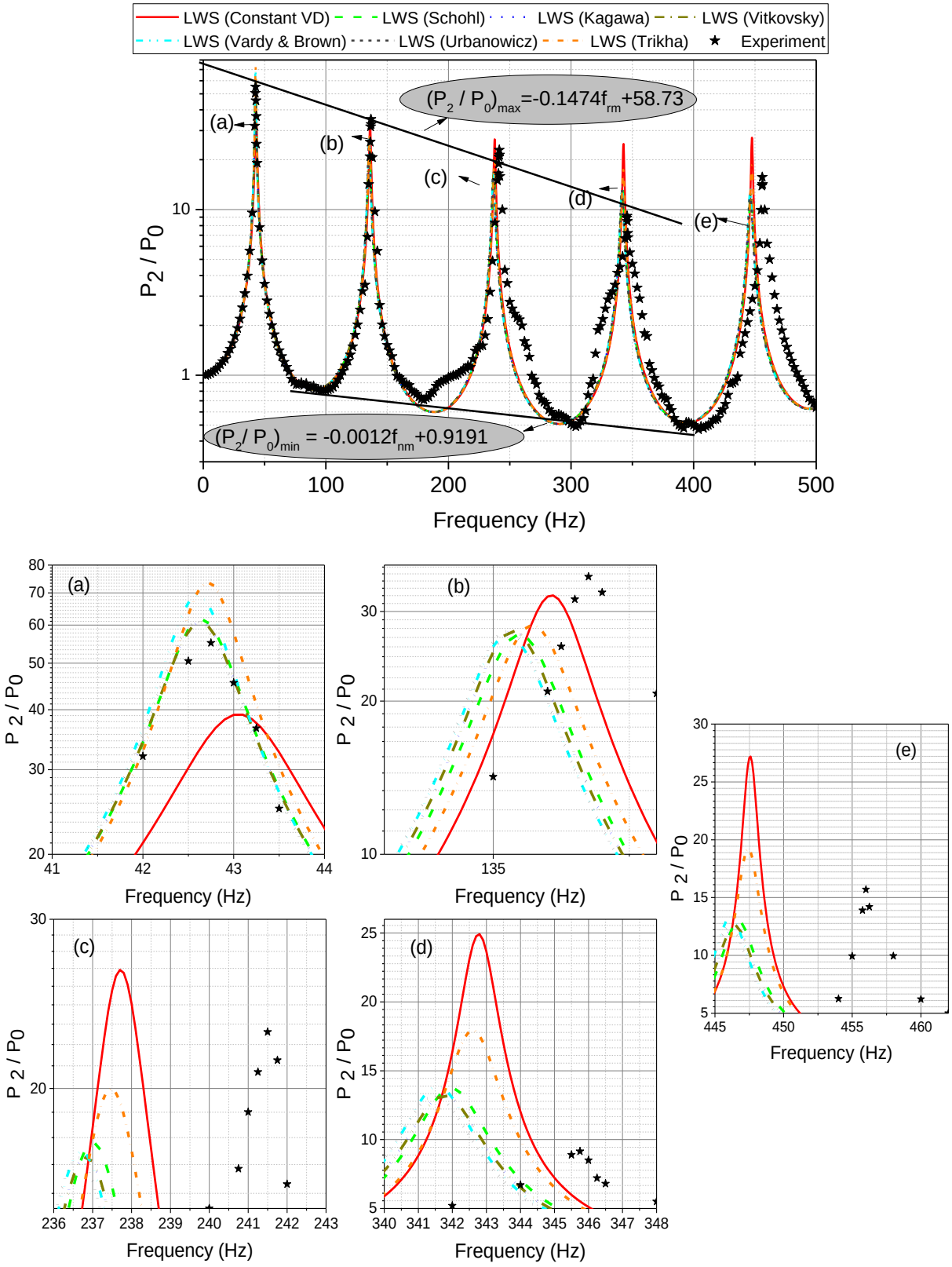

Figure 6.35: Comparison between Results of "Branch1 SS Close-Ended Experiment" and LWS predictions

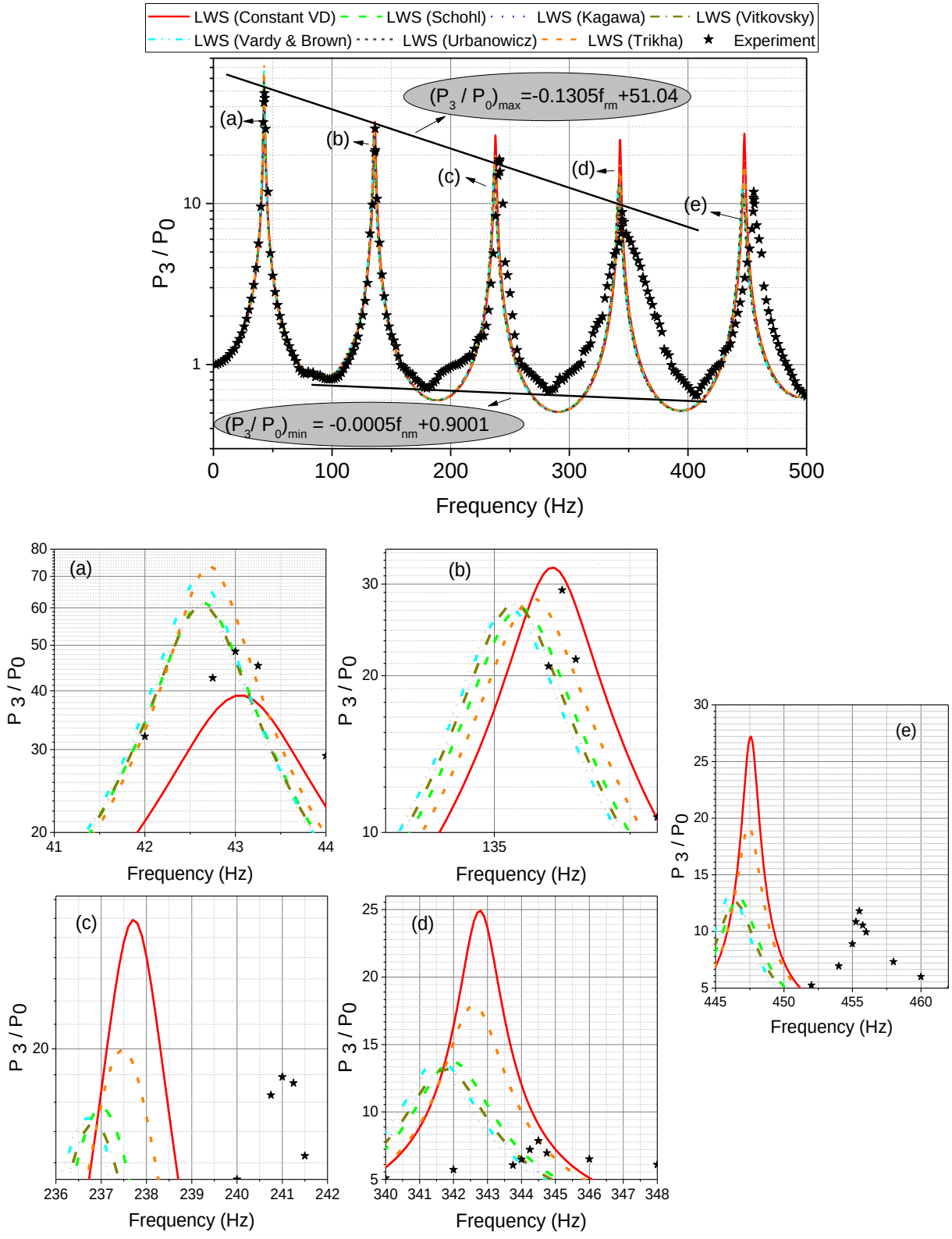

Figure 6.36: Comparison between Results of the "Branch 2 SS Close-Ended Experiment" and LWS predictions

In Figure 6.34, the resonant frequency predictions using a constant VD shows a maximum difference of 4.5 Hz from the experimental data for the elbow. This difference is considered acceptable. Figures 6.35 and 6.36 show that for the equal branch configurations, the first four peaks are predicted with less than 4.5 Hz difference from the experimental data. The differences between the constant VD predictions and the experiments increase to about 8.5 Hz and 8 Hz at the 5^{th} peak of Branch 1 and Branch 2, respectively. This indicates that the resonant frequencies for the elbow and the first four peaks of the equal branches are well predicted using a constant VD. Indeed, by increasing the frequency to more than 400 Hz, the constant VD is not able to adequately predict the resonant frequencies for the equal branch configurations.

Using the frequency-dependent damping methods of Kagawa et al. (1983), Schohl (1993), Urbanowicz and Zarzycki (2012), Vardy and Brown (2004), and Vitkovsky et al. (2004) decreases the difference between the resonant frequency predictions and the measurements of the elbow to less than 3.5 Hz.

Figure 6.37 shows that using the damping method of Urbanowicz and Zarzycki (2012) gives the lowest RMSE value in the resonant frequency prediction for the elbow. Compared to the straight line with the same material and wall thickness, the RMSE values for all the frequency-dependent and constant VD damping methods show the same trend. Although the Urbanowicz and Zarzycki (2012) damping method shows the lowest RMSE values for both the 10 mm O.D. straight line SS and the elbow configurations, these values are increased to about 35% from 10 mm O.D. straight line SS to the elbow tube. The constant VD RMSE value for the elbow, which is the same as that of the straight line tubes, represents the highest value compared to the other frequency-dependent methods. The RMSE values indicate that the resonant frequencies of the

straight line SS tube with the same wall thickness and material are better predicted than the elbow configuration.

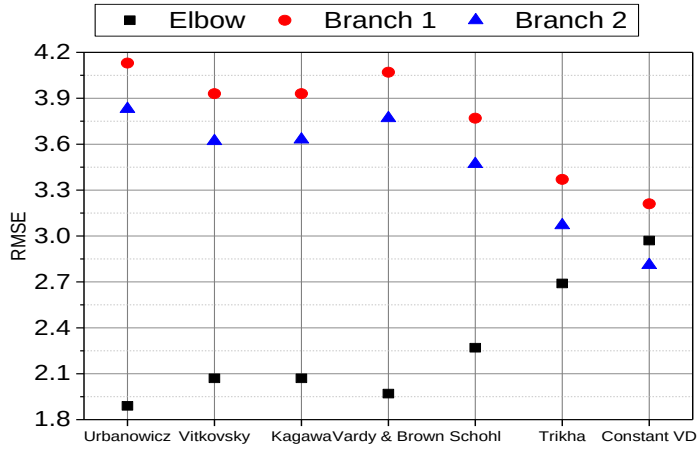

Figure 6.37: Resonant Frequency Predictions RMSE

For Branch 1 and Branch 2 configurations, the resonant frequencies of the first four peaks using the assessed frequency-dependent damping terms are predicted with less than 5.5 Hz difference from the experiments. The last resonant peaks similar to the constant VD method are not accurately predicted, and a maximum difference of 9 Hz is obtained from the experiments. In contrast to the straight line, the elbow tubes using the Trikha (1975) damping method to predict resonant frequencies depicts the lowest differences from the experiments. Although those differences are not less than 4.5 Hz from the experiments for the first four resonant frequency peaks and about 8 Hz difference for the last peaks, they show the lowest values among all the other assessed frequency-dependent damping methods. Figure 6.37 shows the RMSE values of the frequency-dependent damping methods of Kagawa et al. (1983), Schohl (1993), Urbanowicz and Zarzycki (2012), Vardy and Brown (2004), and Vitkovsky et al. (2004) for Branch 2 configuration are less than those of Branch 1, but they are about two times more than the elbow configuration. Although the Trikha (1975) damping method represents the lowest RMSE values

for both the equal branch configurations among the other assessed frequency-dependent damping methods, their values are higher than the constant VD RMSE values. The constant VD RMSE value for Branch 2 is still about 70% higher than the RMSE value of the Urbanowicz and Zarzycki (2012) damping method for the straight line SS tube. This means that the resonant frequencies are also better predicted for SS straight lines than the equal branch configurations.

Despite the straight line and elbow tubes, the resonant frequencies are not satisfactorily predicted for equal branch configurations at frequencies higher than 400 Hz, which means that the equal branch configuration shifts the resonant frequencies of the higher frequencies.

6.2.3.1.4 Close-Ended Unequal Branch & Combined Parameters

The comparisons between the LWS using constant VD, the LWS using the frequency-dependent damping methodologies, and the measurements for the first branch (2.07 m) and the mainline outlet of Branch 3 and the first branch (2.07 m), the Al branch and the mainline outlet of the Complex Experiment are shown in Figures 6.38, 6.39, 6.40 (a and b), 6.41 (a and b), and 6.42 (a and b), respectively. They show the ratio of the outlet end of the branch and the mainline to the inlet acoustic pressure amplitude with respect to frequency.

In Figures 6.38 and 6.39, the resonant frequency predictions using constant VD for Branch 3 show a maximum 5 Hz difference from the experimental data for the first three resonant peaks (less than 220 Hz). From the 4^{th} to the last resonant peaks, the differences from the measurements increase from 6 Hz to about 20 Hz. These differences for the last four peaks are not considered acceptable, which shows that the resonant frequencies of the tested unequal branch configuration are not predicted very well for frequencies higher than 220 Hz.

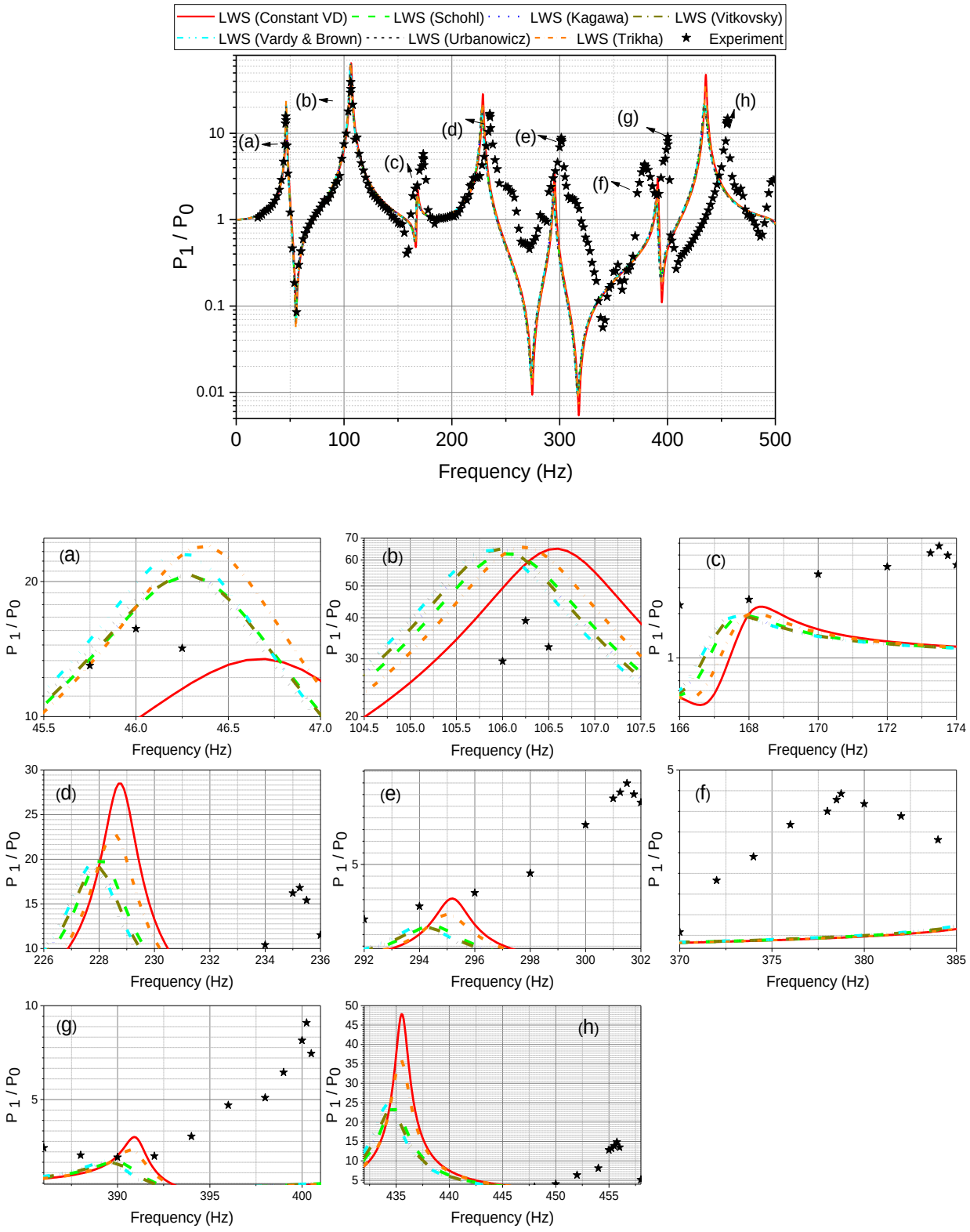

Figure 6.38: Comparison between Results of the "Branch 3 Experiment 2.07 m Branch", and LWS Predictions

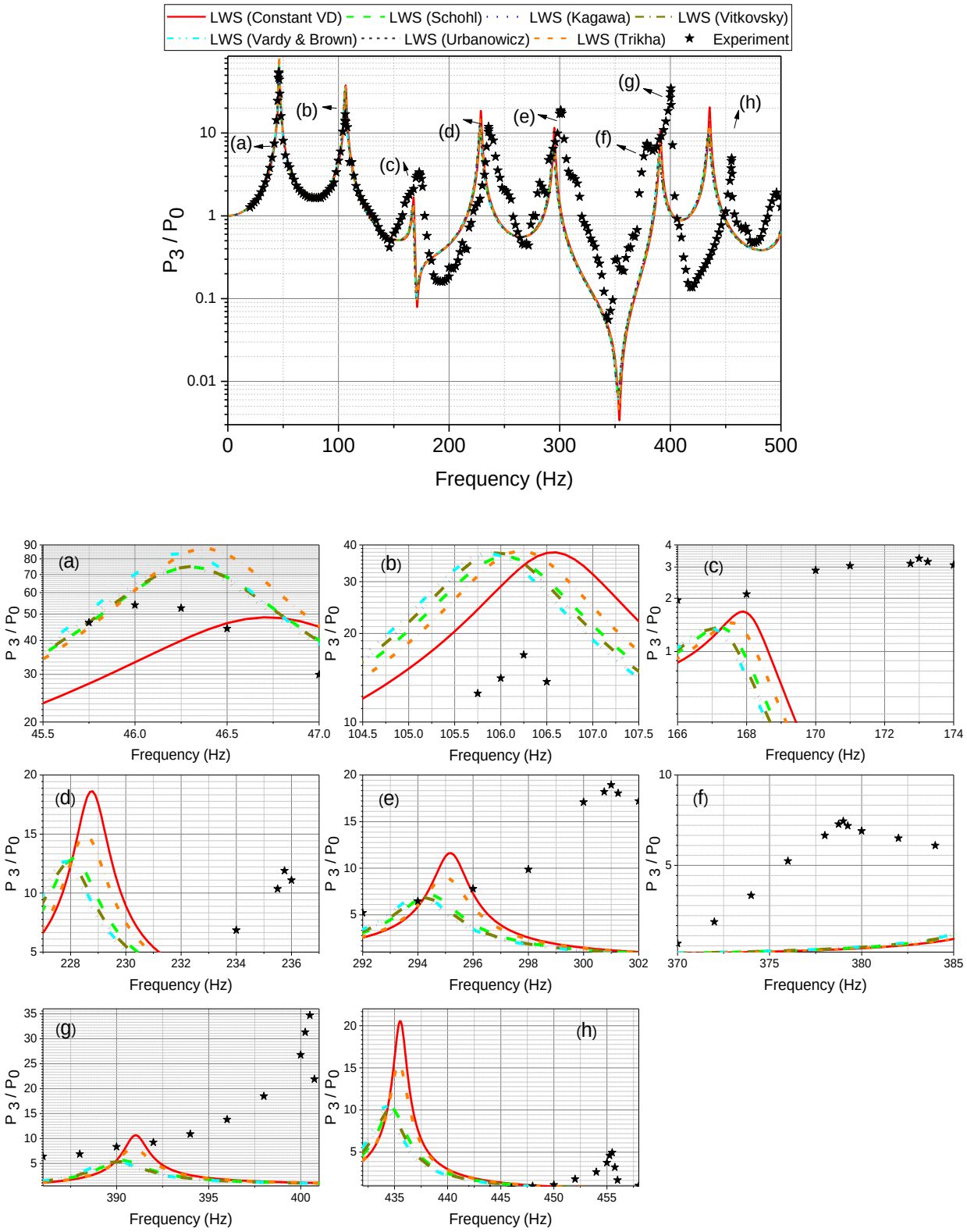

Figure 6.39: Comparison between Results of the "Branch3 SS Main line Experiment", and LWS Predictions

For the Branch 3 configuration, using the frequency-dependent damping methodology of Trikha (1975) gives the resonant frequency predictions that are very close to the constant VD predictions. Other investigated frequency-dependent damping methods predict resonant frequencies with the acceptable differences from the measurements for the first three resonant peaks. They do not decrease the differences between the predictions and the measurements for the last five peaks when compared with the Trikha (1975) method.

It can be seen in Figures 6.40, 6.41, and 6.42 (a and b) that for the Complex Experiment configuration, the first six peaks of P_4 are predicted with less than 4.5 Hz difference from the experimental data with constant VD method. The same difference between the constant VD predictions and the measurements are presented for the P_1 and P_3, except for the 5^{th} peaks where the differences increase to about 8 Hz. This indicates that the resonant frequencies are properly predicted with constant VD for the Complex Experiment configuration till 220 Hz except for the 5^{th} peak. Indeed, by increasing the frequency to more than 220 Hz, the difference between the constant VD predictions and the experimental data rises to about 17 Hz for the last resonant peaks. Same as Branch 3, constant VD does not satisfactorily predict the resonant frequencies higher than 220 Hz. It should be noted that the 5^{th} peaks of 2.07 m branch and the mainline outlet are not predicted with acceptable accuracies for the Complex Experiment configuration.

Figures 6.40, 6.41 and 6.42 (a and b) also show that using the frequency-dependent damping methods of Kagawa et al. (1983), Schohl (1993), Urbanowicz and Zarzycki (2012), Vardy and Brown (2004), and Vitkovsky et al. (2004) decrease the differences between resonant frequency predictions and measurements of the Complex Experiment when compared to the constant VD method. They reduce the differences to less than 7.5 Hz at the 5^{th} peaks of P_1 and P_3 and less than 16 Hz for the last peaks of all three locations. These improvements in resonant frequency

predictions are not good enough and the differences from the measurements are still considered unacceptable.

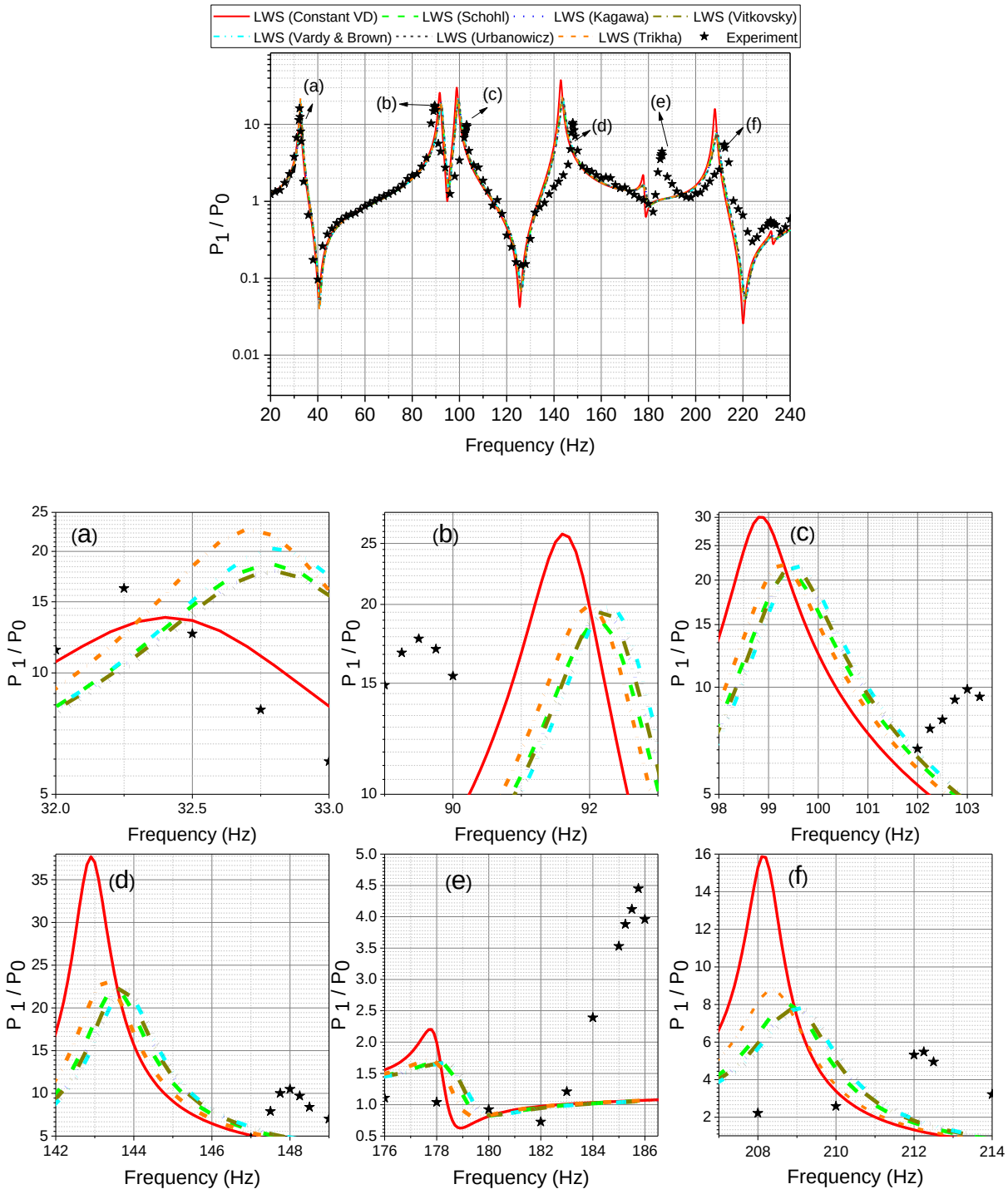

Figure 6.40a: Comparison between Results of the "Combined Experiment, 2.07 m Branch", and LWS Predictions

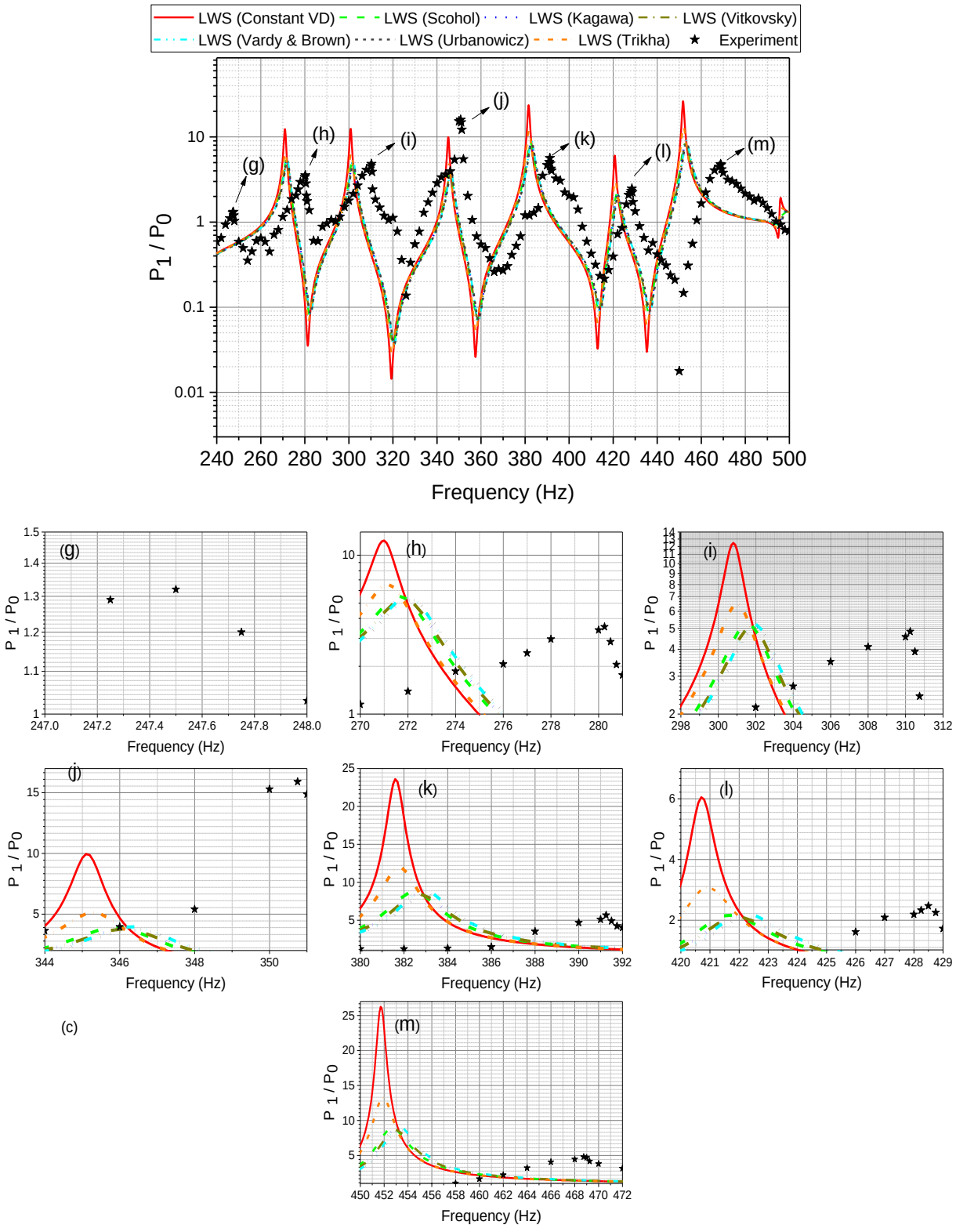

Figure 6.40b: Comparison between Results of the "Combined Experiment, 2.07 m Branch", and LWS Predictions

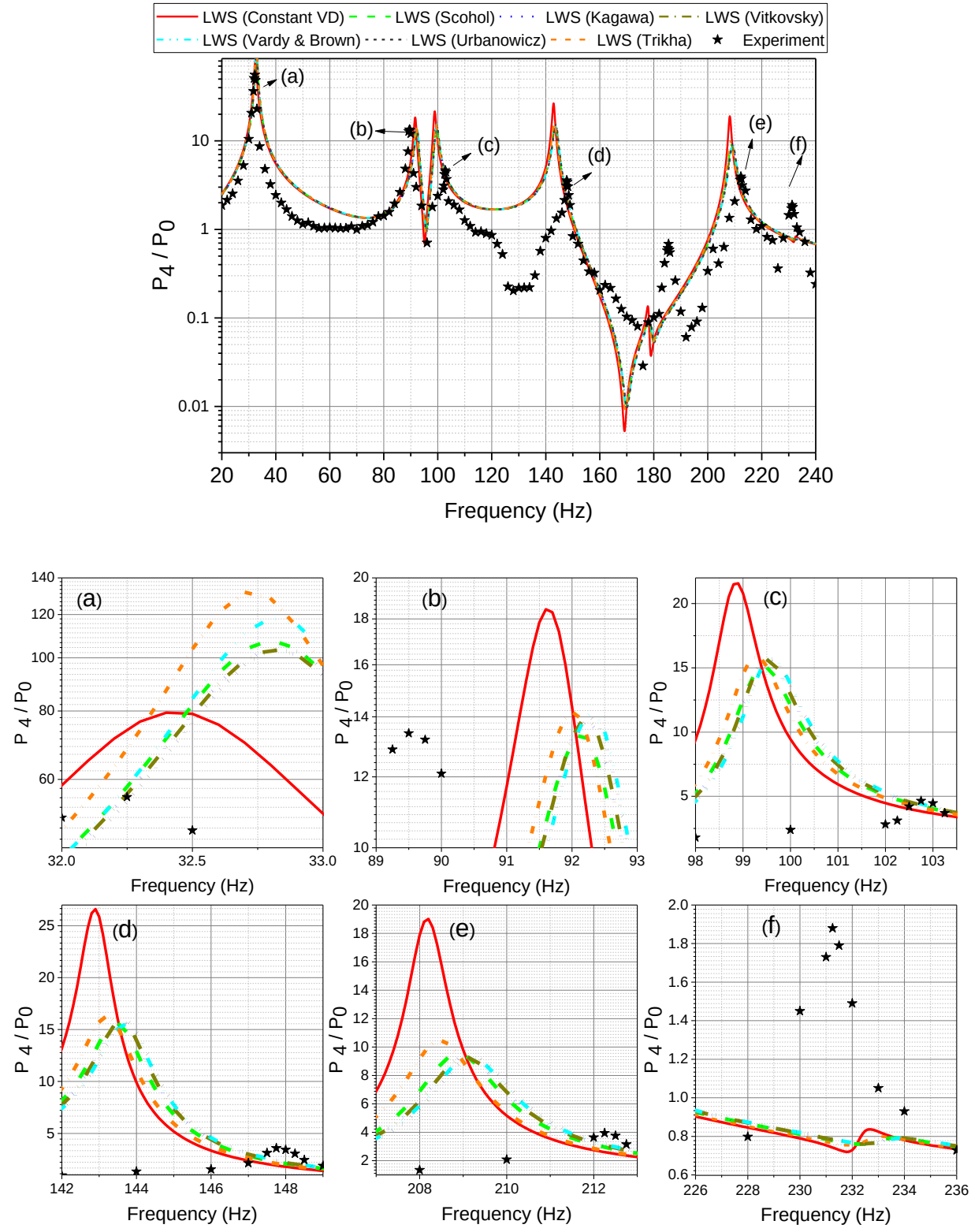

Figure 6.41a: Comparison between Results of the "Combined Experiment, Al, l m Branch", and LWS Predictions

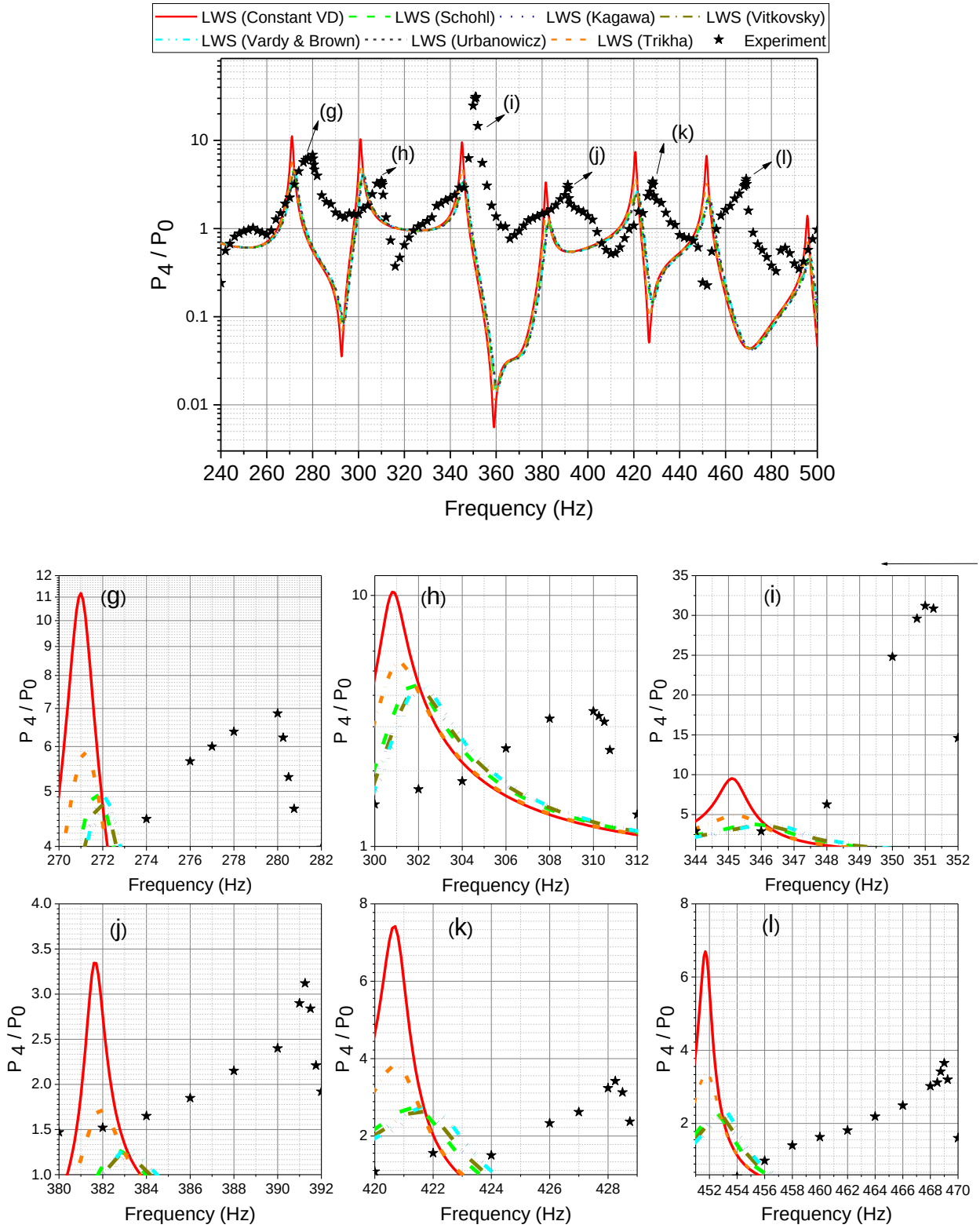

Figure 6.41b: Comparison between Results of the "Combined Experiment, Al, l m Branch", and LWS Predictions

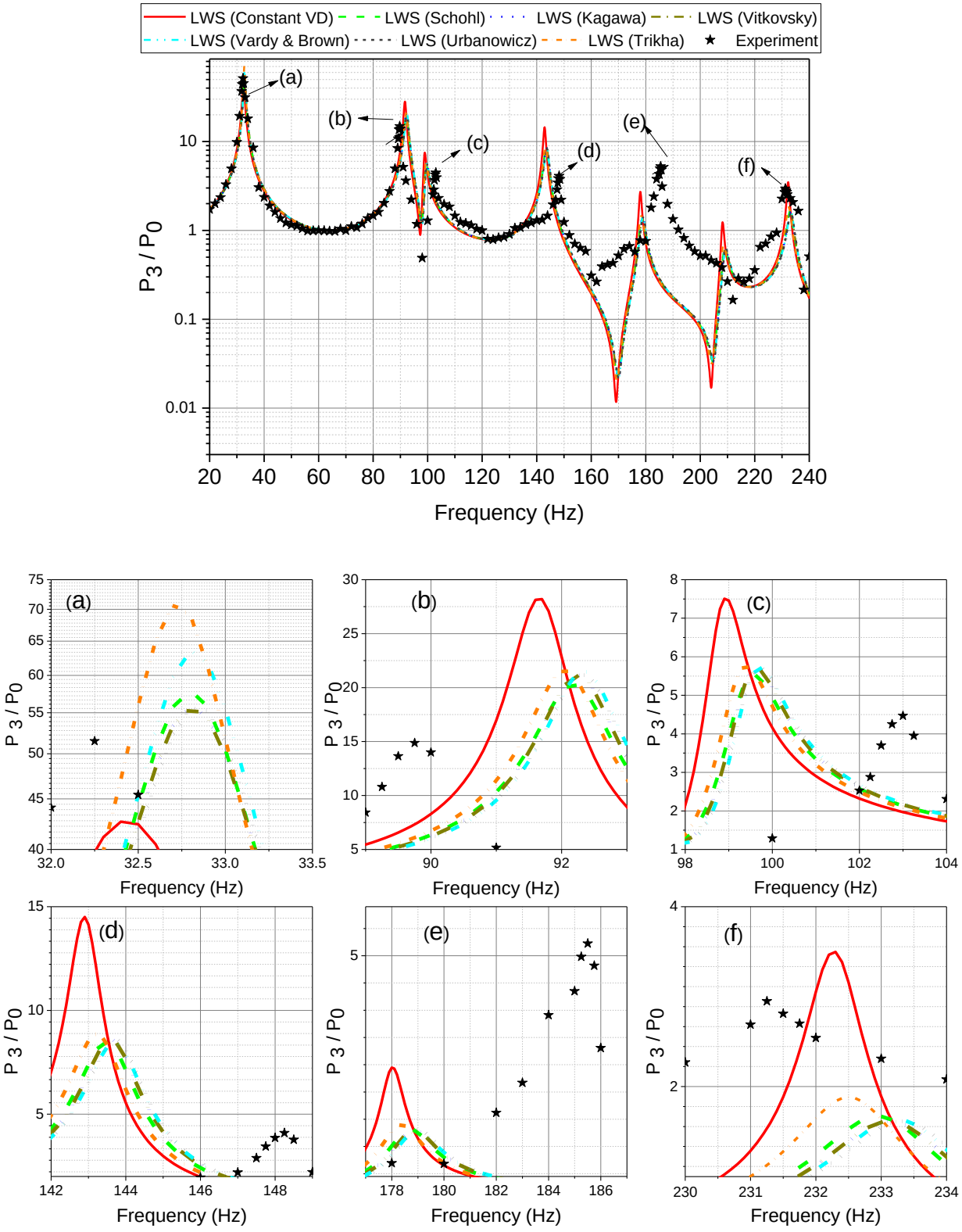

Figure 6.42a: Comparison between Results of the "Combined Experiment Main line", and LWS Predictions

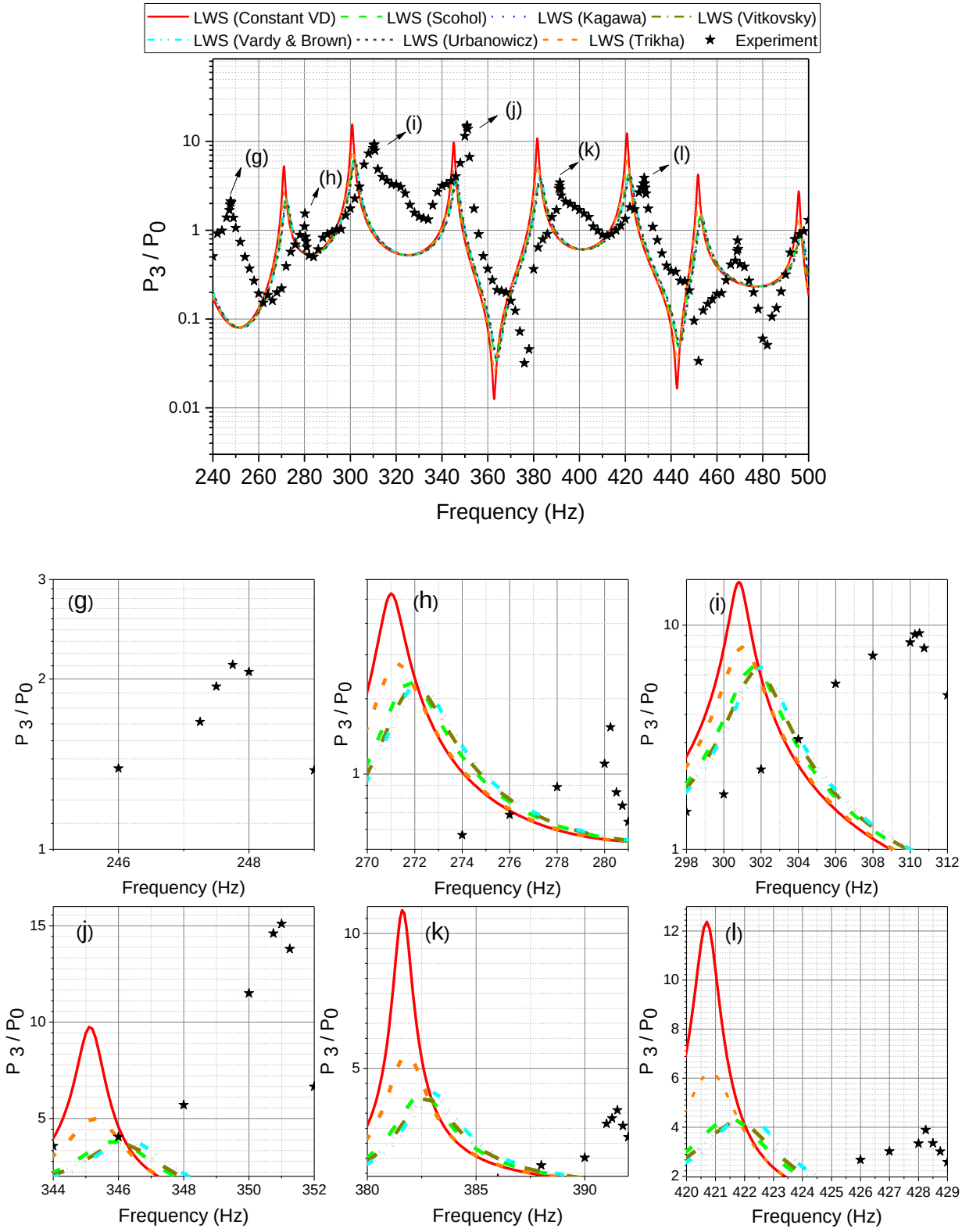

Figure 6.42b: Comparison between Results of the "Combined Experiment Main line", and LWS Predictions

Figure 6.43 shows that for Branch 3, using a constant VD gives the lowest RMSE value for the resonant frequency prediction. The Trikha (1975) method's RMSE value is very close to the constant VD value. These values are very close to the equal branch constant VD RMSE values. The damping methodologies of Urbanowicz and Zarzycki (2012), Vitkovsky et al. (2004) and Kagawa et al. (1983) are referred to as "UVK" for simplification. For the frequency-dependent methods of UVK, the Branch 3 RMSE values are almost twice the equal branches values.

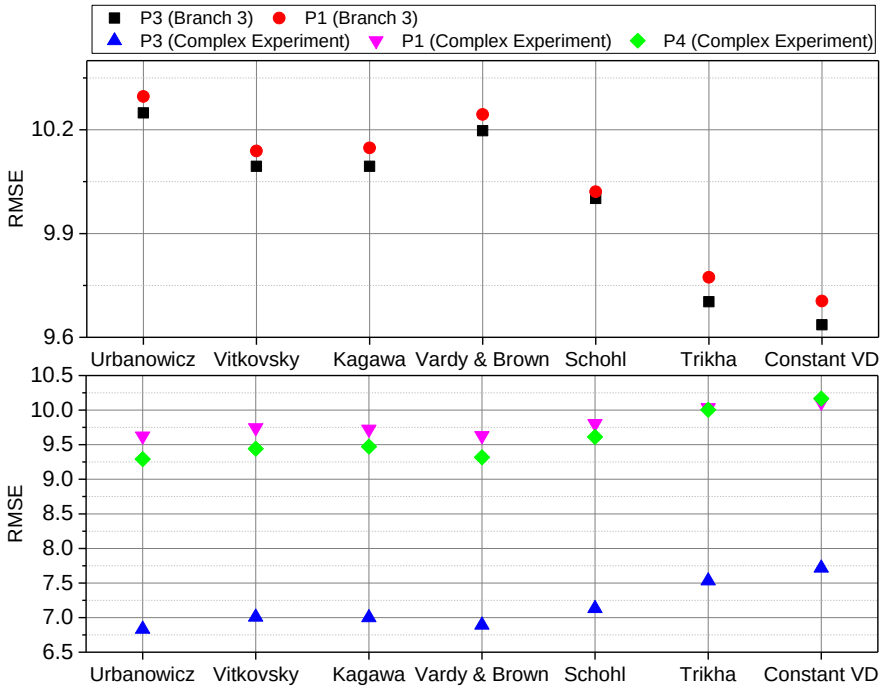

Figure 6.43: RMSE Values of Resonant Frequency Predictions

The Complex Experiment constant VD RMSE values for both the branches are close to the Branch 3 constant VD RMSE values. For the 2.07 m branch and the Al branch, using the damping methodologies of Urbanowicz and Zarzycki (2012) and Vardy and Brown (2003) gives the lowest RMSE values. The RMSE values of the mainline outlet show the lowest values compared to the 2.07 m and the Al branches values. Although the Urbanowicz and Zarzycki

(2012) damping methodology shows the lowest RMSE value for the Al branch, its value is almost 50% higher than the lowest RMSE value of the Branch 2 (equal branch) configuration. The RMSE values indicate that the resonant frequencies of the unequal branches and the Complex Experiment are not properly predicted by any of the examined methods.

The resonant frequency predictions for unequal branch and complex geometries are not accurately predicted for frequencies higher than 220 Hz, using the LWS. It becomes more evident that the predictions with LWS using the assessed damping methods might miss some physical effects, which may be more important for the higher frequencies than the lower ones in unequal branch configurations. The interactions of the different sonic velocities probably shift the resonant frequencies for the complex experiment configuration, and this effect may not be properly captured with the current models. Also, for the frequencies higher than 220 Hz, the resonant amplitudes are not well approximated even with UVK damping methodologies. These discrepancies between the acoustic resonance predictions and the experimental results again can be explained on the simplifications applied to model the unsteady friction terms.

6.2.3.1.5 Open-Ended Branch 3 (Zero and Laminar Mean Flows)

The comparisons between the acoustic resonance predictions and the measurements for the first branch (2.07 m), second branch (1 m), and mainline outlet of the Branch 3 are shown in Figures 6.44, 6.45, and 6.46, receptively. They show the ratio of the outlet to the inlet acoustic pressure amplitude with respect to frequency.

From Figure 6.44, for the first three resonant peaks (less than 220 Hz), the resonant frequency predictions using constant VD at P_1 show a maximum difference of 1 Hz from the experimental

data. For the same location of the Branch 3 close-ended case, at the first three resonant peaks the maximum difference from experiments is about 5 Hz. It means that the close-ended boundary condition of the mainline creates more reflections of the acoustics waves. Thus, the difference between resonant frequency predictions and the measurements increases. From the 4^{th} to the last resonant peak, the differences from the measurements increases from 3.5 Hz to about 25 Hz. The differences for the 4^{th}, 6^{th} and 7^{th} peaks at about 5, 25 and 12 Hz are not deemed acceptable. For the 6^{th} resonant peak with the highest difference between the prediction and the measurements, the maximum measured amplitudes are reported less than 1 and this difference can be ignored. The predictions show that resonant frequencies are not always well predicted for the frequencies higher than 220 Hz. For the close-ended Branch 3, the difference between the predictions and measurements are also deemed unacceptable for frequencies higher than 220 Hz.

It can be seen in Figure 6.45 that for the shorter branch (1 m) the same trend of differences from the experimental data is obtained. The maximum difference between constant VD predictions and experiments are presented for the 7^{th} resonant peak at about 12 Hz.

For the mainline outlet, shown in Figure 6.46, only the 1^{st}, 2^{nd} and the last two measured resonant peaks have amplitudes more than 1. Thus, the predicted resonant frequency peaks are only compared against those measured peaks. Again, at the 7^{th} resonant peaks the difference between constant VD prediction and measurement is about 12 Hz; this is not deemed acceptable. It indicates that the resonant frequencies are always properly predicted with constant VD till 220 Hz. Also, the resonant frequency predictions for all three locations (P_1, P_2 and P_3) present less differences from the measurements compared to the same locations of the Branch 3 close-ended mainline predictions.

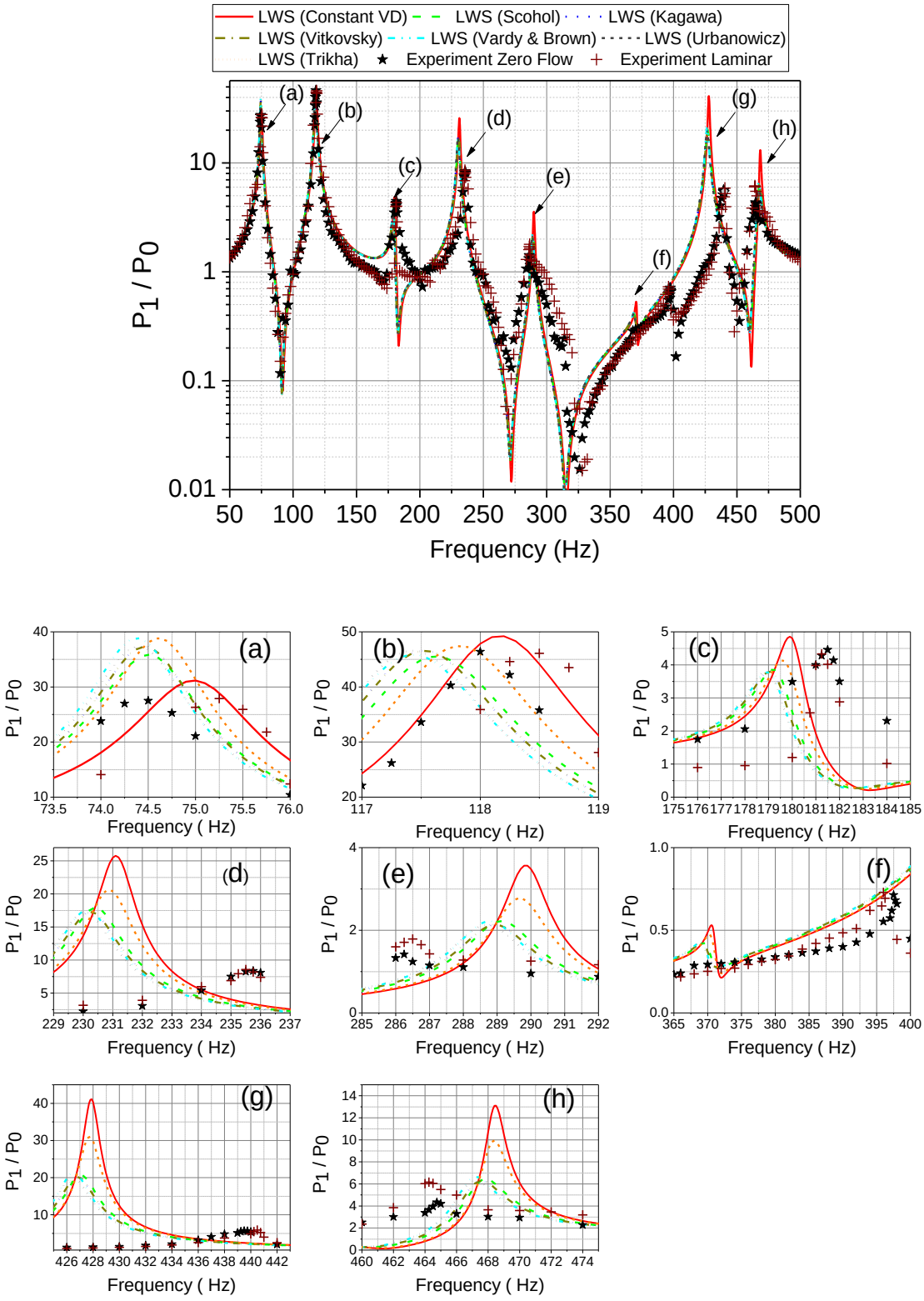

Figure 6.44: Comparison between Zero Flow & Laminar Flow Results of the Open-Ended "Branch 3, 2.07 m Branch" and LWS Predictions

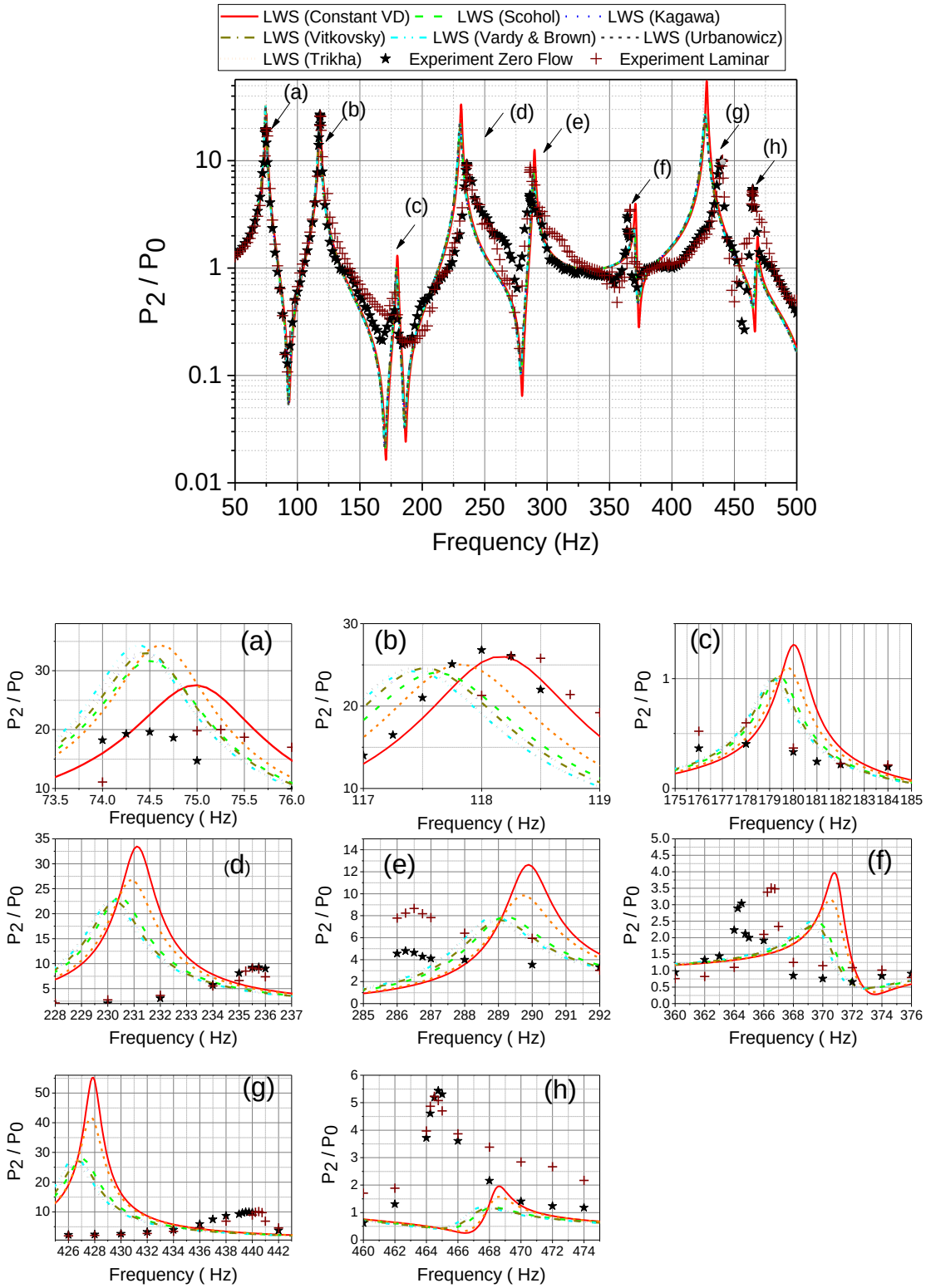

Figure 6.45: Comparison between Zero Flow & Laminar Flow Results of the Open-Ended "Branch 3, 1 m Branch" and LWS Predictions

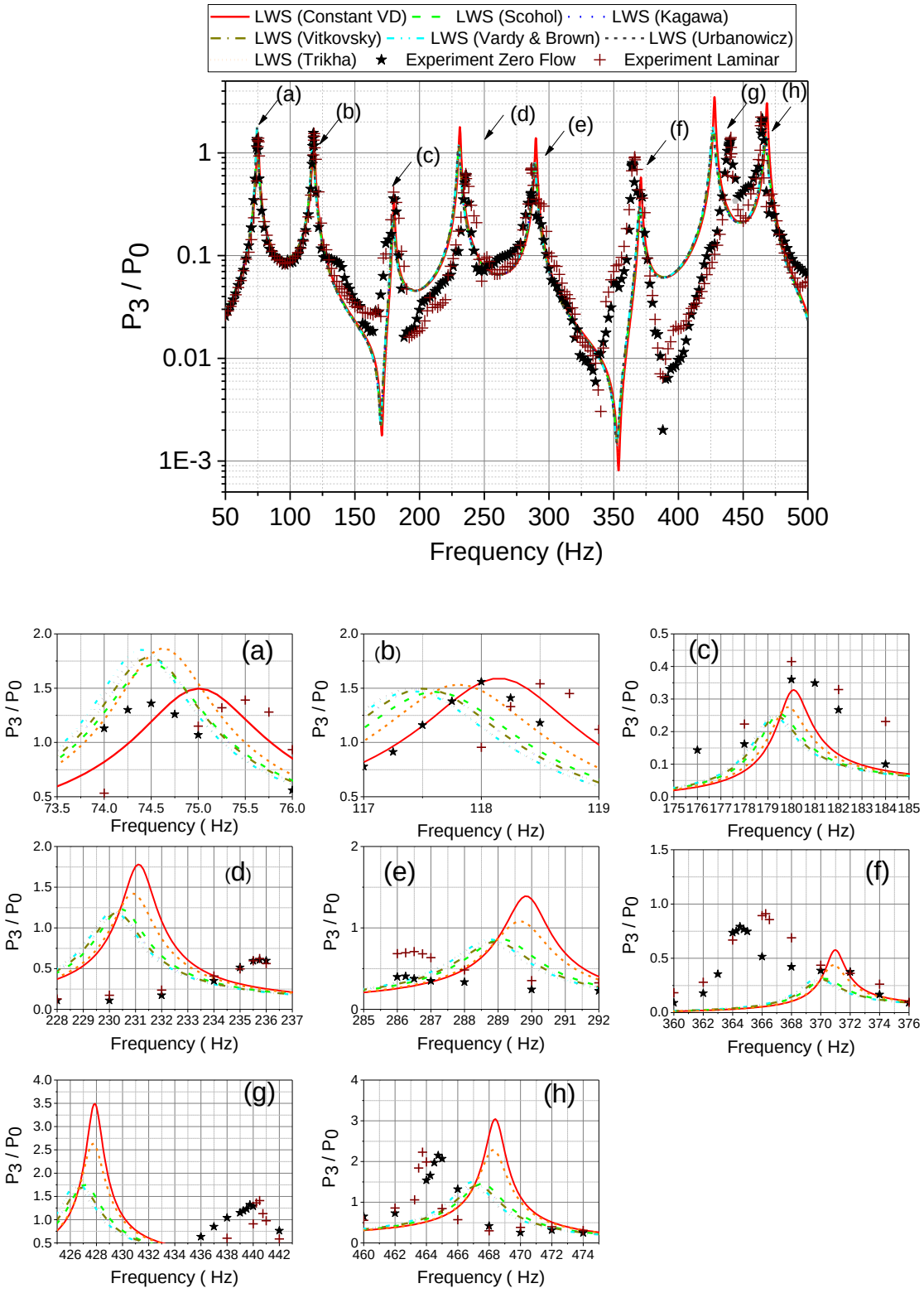

Figure 6.46: Comparison between Zero Flow & Laminar Flow Results of the Open-Ended "Branch 3, Mainline Outlet" and LWS Predictions

Using the frequency-dependent damping methodology of Trikha (1975) brings the resonant frequency predictions very close to the constant VD predictions. Other investigated frequency-dependent damping methods also predict resonant frequencies with acceptable differences from the measurements for the first three resonant peaks. They do not decrease the unacceptable differences between the predictions and the measurements compared to the Trikha (1975) method.

Figure 6.47 shows that for P_1 and P_3, using constant VD gives the lowest RMSE values for the resonant frequency prediction. Although using the other frequency-dependent damping methodologies gives higher RMSE values than the constant VD, the maximum difference between the frequency-dependent and constant VD methods is less than 10%. The Trikha (1975) method RMSE value is very close to the constant VD value. Comparing the open-ended RMSE values with Branch 3 close-ended values shows almost 50% decrement for P_1 and P_3 and 70% decrease for P_2. It is again confirmed that the resonant frequencies for the open-ended case are better predicted than the close-ended case.

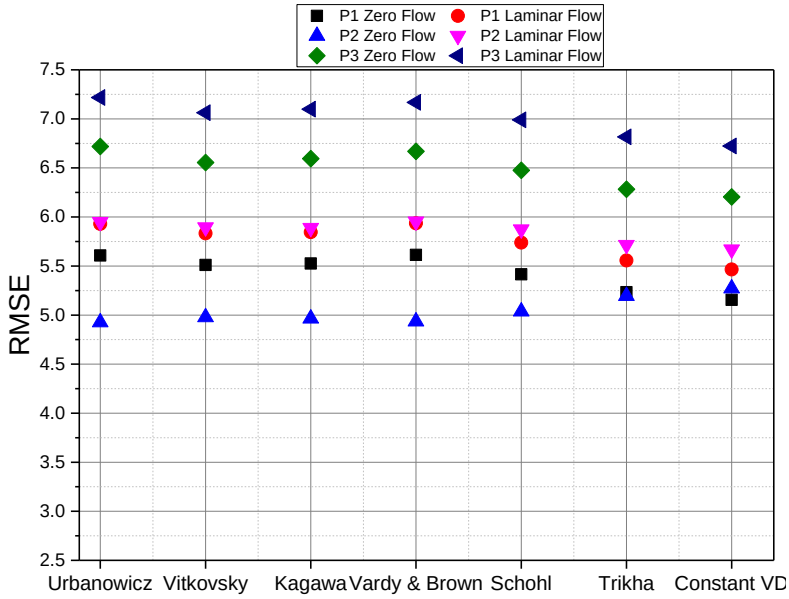

Figure 6.47: RMSE Values of Resonant Frequency Predictions (Zero & Laminar Mean Flows)

Figure 6.47 also shows that for the laminar flow case, the RMSE values are increased compared to the zero mean flow case. The increments for the branches and the mainline outlet are less than 15%. It indicates that the laminar mean flow does not considerably influences the resonant frequency predictions. Among all the assessed frequency-dependent damping methodologies, using the methods of Trikha (1975) gives the lowest RMSE value.

6.2.3.1.6 Open-Ended Branch 3 (Turbulent Mean Flow)

The comparisons between the LWS using constant VD, the LWS using frequency damping methodologies and the measurements for P_1, P_2, and P_3 are shown in Figures 6.48, 6.49, and 6.50, respectively. They show the ratio of the outlet to the inlet acoustic pressure amplitude with respect to frequency.

From Figure 6.48 at the 2.07 m branch, the resonant frequency predictions using constant VD show a maximum 2.5 Hz difference from the experimental data for the first three resonant peaks (less than 220 Hz). For the same location of the zero mean flow case, at the first three resonant peaks, the maximum difference from the experiments is obtained at about 1 Hz. Those values of differences for zero and laminar flows are considered acceptable. From the 4^{th} to the 7^{th} resonant peaks, the maximum differences from the measurements are increased from 5 Hz to about 27 Hz. The maximum differences for the 4^{th}, 6^{th} and 7^{th} peaks at about 5.5, 27 and 15 Hz are not considered acceptable. The differences for the 6^{th} and 7^{th} peaks are increased from zero to turbulent mean flow cases. It shows that resonant frequencies are not always well predicted for the frequencies higher than 220 Hz.

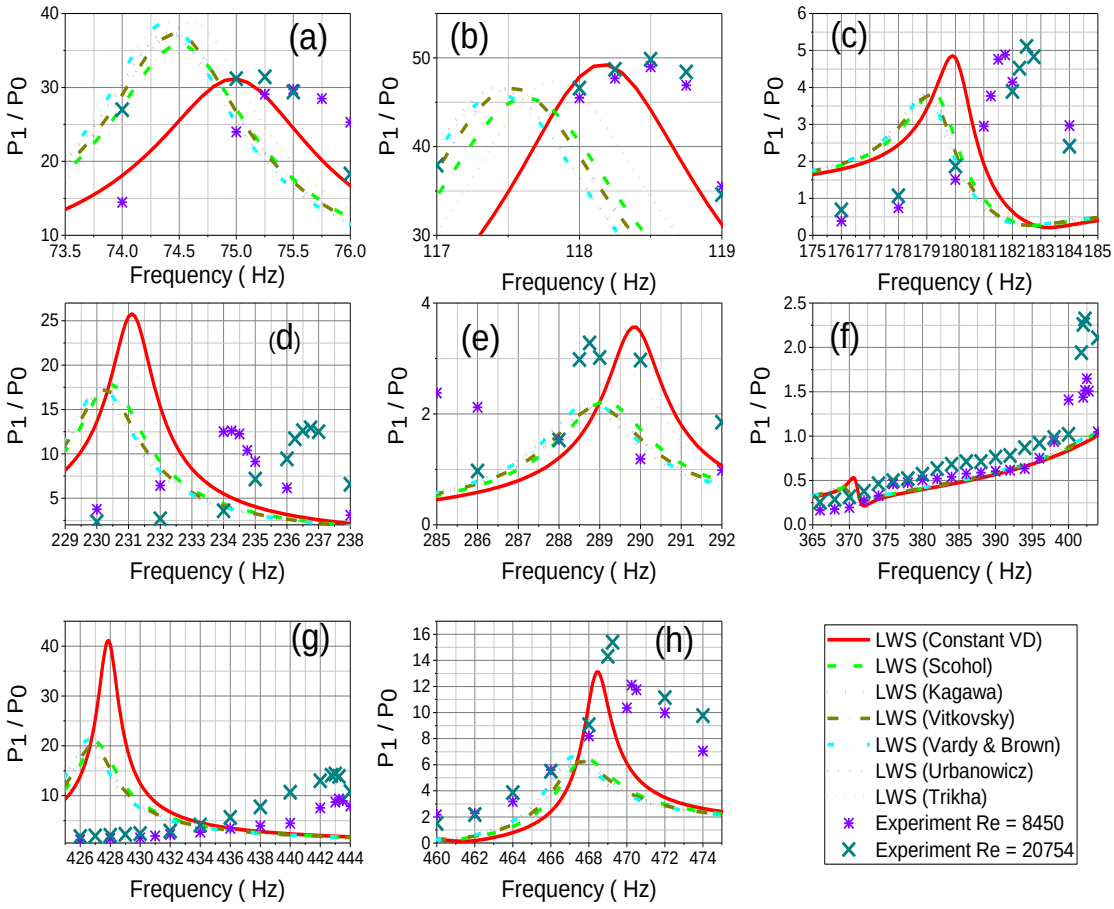

Figure 6.48: Comparison between Turbulent Results of the Open-Ended "Branch 3" side branch 2.07 m and linear wave solution predictions

It can be seen in Figure 6.49 that for the shorter branch (1 m), the maximum differences between constant VD predictions and experiments, presented for the 5th and 7th resonant peaks, are about 5 and 12.5 Hz respectively. At P_2, the maximum differences between resonant frequency predictions and measurements are not considerably increased from zero to turbulent mean flows.

At the mainline outlets of the zero and laminar mean flows, only the acoustic resonance predictions of the 1st, 2nd and the last two peaks are compared against measurements. For the turbulent mean flows, shown in Figure 6.50, all the seven peaks have magnitudes of more than 1,

and they are compared against the experimental data. After the 3rd resonant peak, the differences between predictions and the measurements increase to up to 19 Hz. For the zero and laminar flows, only the 7th resonant peak is not properly predicted using constant VD. The predictions indicate that, same as the zero and laminar mean flows, the resonant frequencies are always accurately predicted with constant VD till 220 Hz. For higher frequencies, the resonant frequency prediction differences from the measurements are increased from zero to turbulent flows.

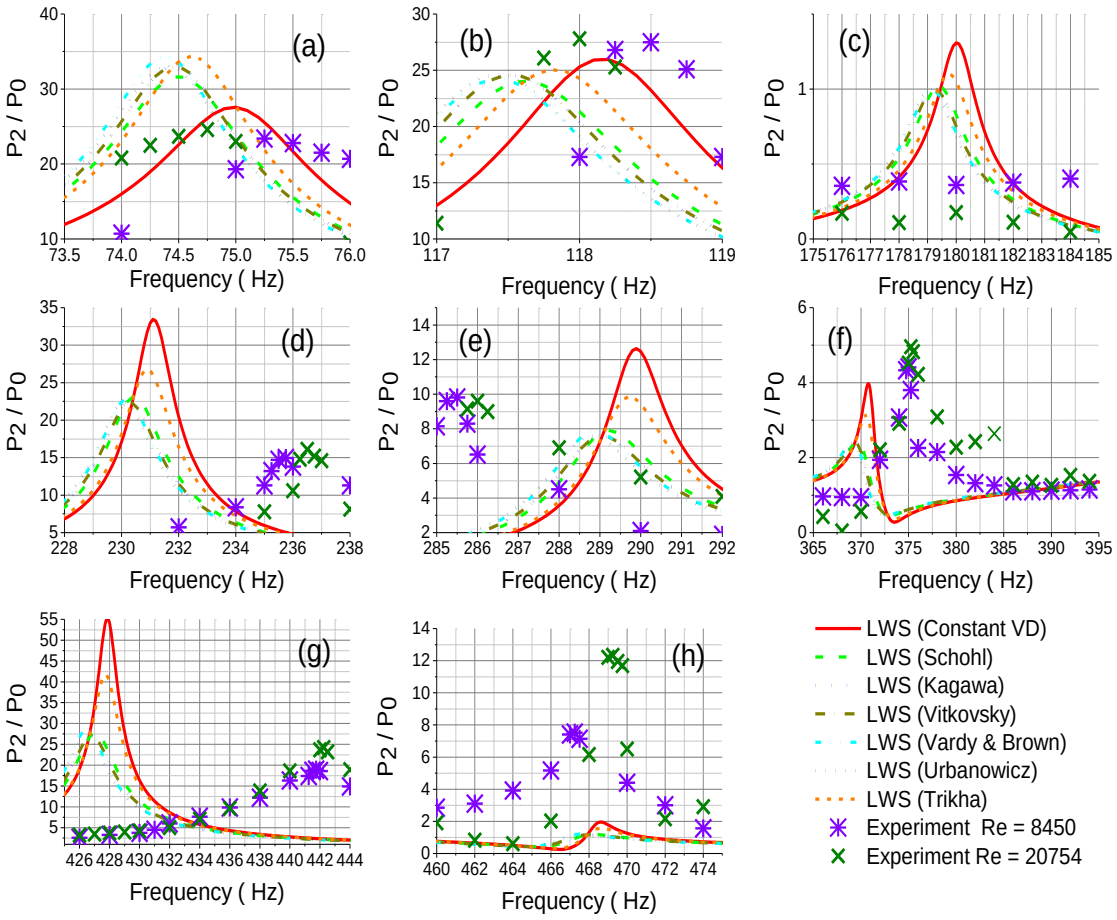

Figure 6.49: Comparison between Turbulent Results of the Open-Ended "Branch 3" Side Branch 1 m and LWS Predictions

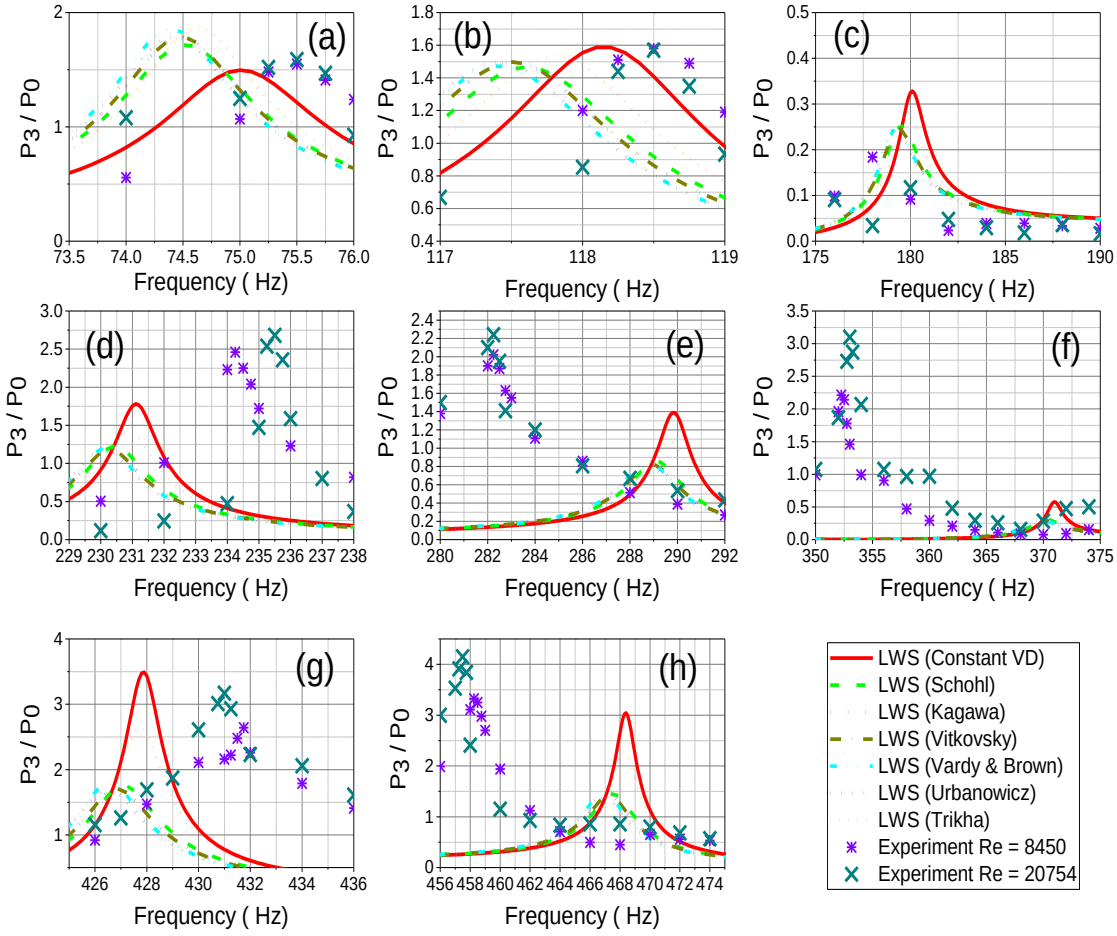

Figure 6.50: Comparison between Turbulent Results of the Open Ended "Branch 3" Mainline Outlet and LWS Predictions

The investigated frequency-dependent damping methodologies predict resonant frequencies with the acceptable differences from the measurements for the first three resonant peaks. Same as the zero and laminar mean flow, they do not decrease the unacceptable difference between the predictions and the measurements compared to the constant VD method.

Figure 6.51 shows that at P_1 and P_2, using constant VD method gives the lowest RMSE values in terms of the resonant frequency prediction. The differences between the RMSE values of the constant VD method and the highest RMSE values of the assessed frequency-dependent damping

methodologies are less than 15%. The lowest RMSE values at P_3 are obtained using Urbanowicz & Zarzycki (2012) and Vardy & Brown (2004) damping methodologies. Comparing the zero and laminar mean flows RMSE values with the turbulent mean flows RMSE values depicts 10–20% increments at P_1 and P_2 and 15–35% increases at P_3. The RMSE magnitudes confirm that the resonant frequencies for the zero and laminar flow cases are better predicted than the turbulent flow cases. The assessed damping methodologies do not consider the turbulent effect, and cannot capture the shifts on the resonant frequencies that are caused by turbulent flows.

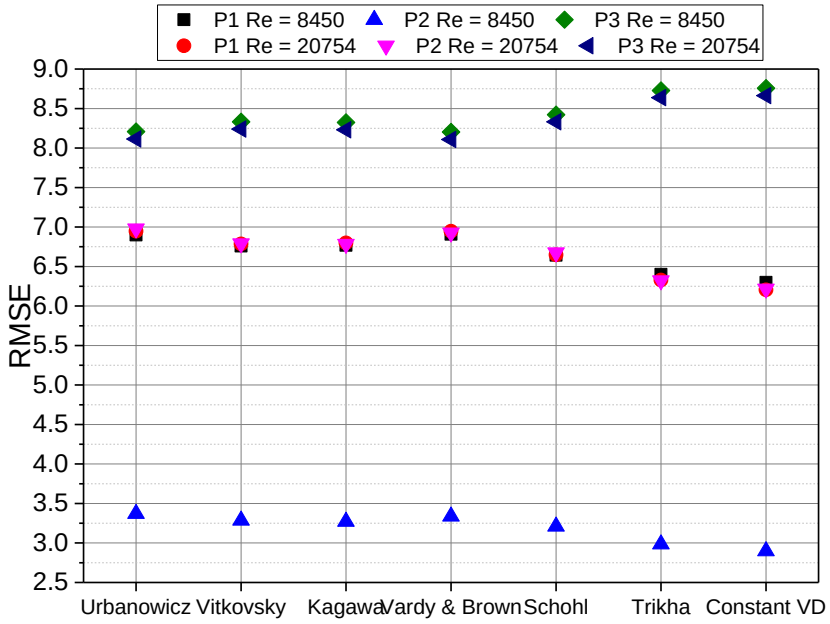

Figure 6.51: RMSE Values for Resonant Frequency Predictions (Turbulent Mean Flows)

6.2.3.1.7 Open-Ended Complex Experiment 2 (Zero and Laminar Mean Flows)

The comparisons between the LWS using constant VD, the LWS using the frequency damping methodologies acoustic resonance predictions and the measurements for the 1.18 m branch and the mainline of the Complex Experiment 2 are shown in Figures 6.52 and 6.53, respectively.

They show the ratio of the outlet to the inlet acoustic pressure amplitude with respect to frequency.

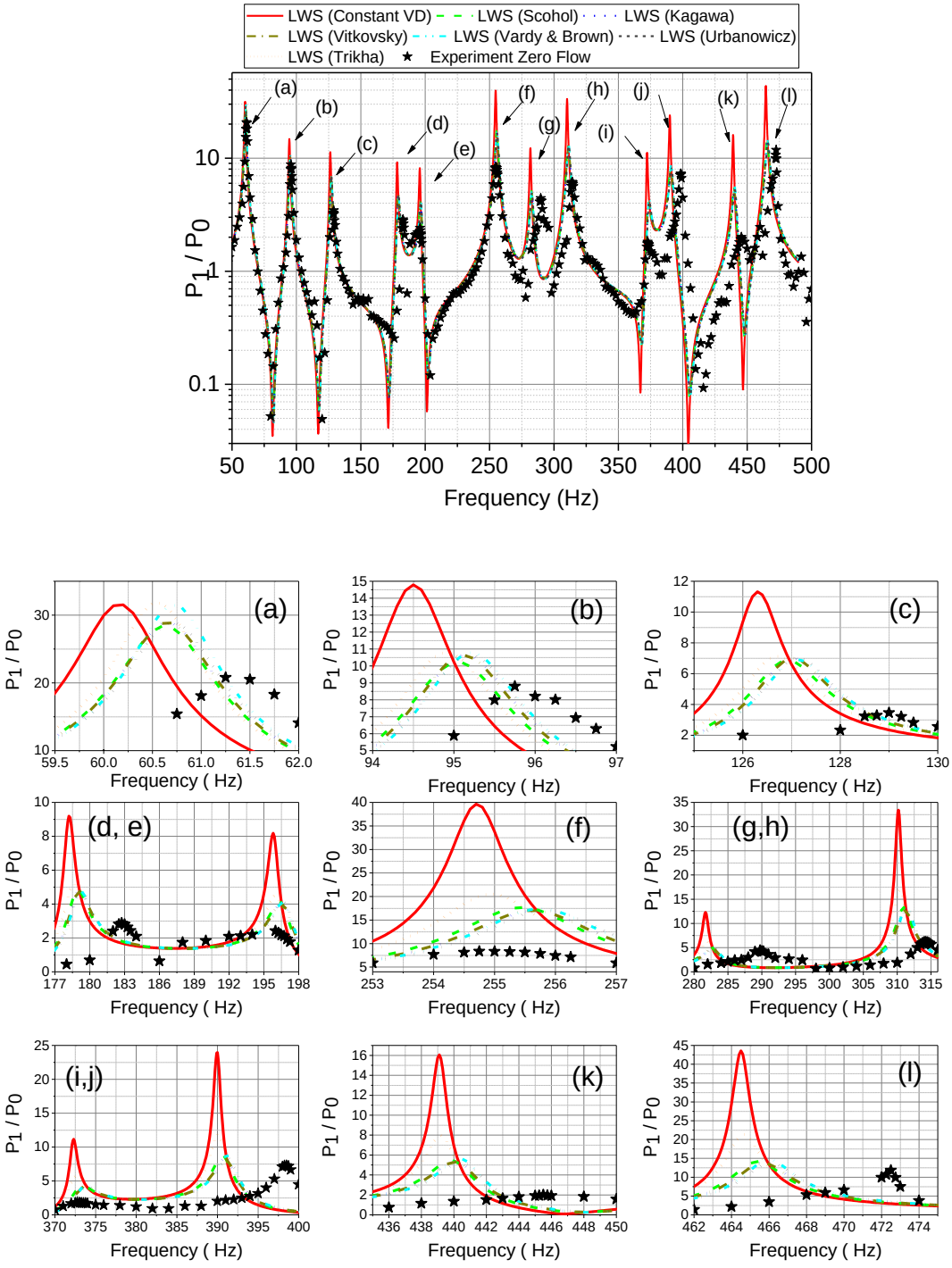

Figure 6.52: Comparison between Zero Flow & Laminar Flow Results of the Open-Ended "Complex Experiment 2, 1.18 m Branch" and LWS Predictions

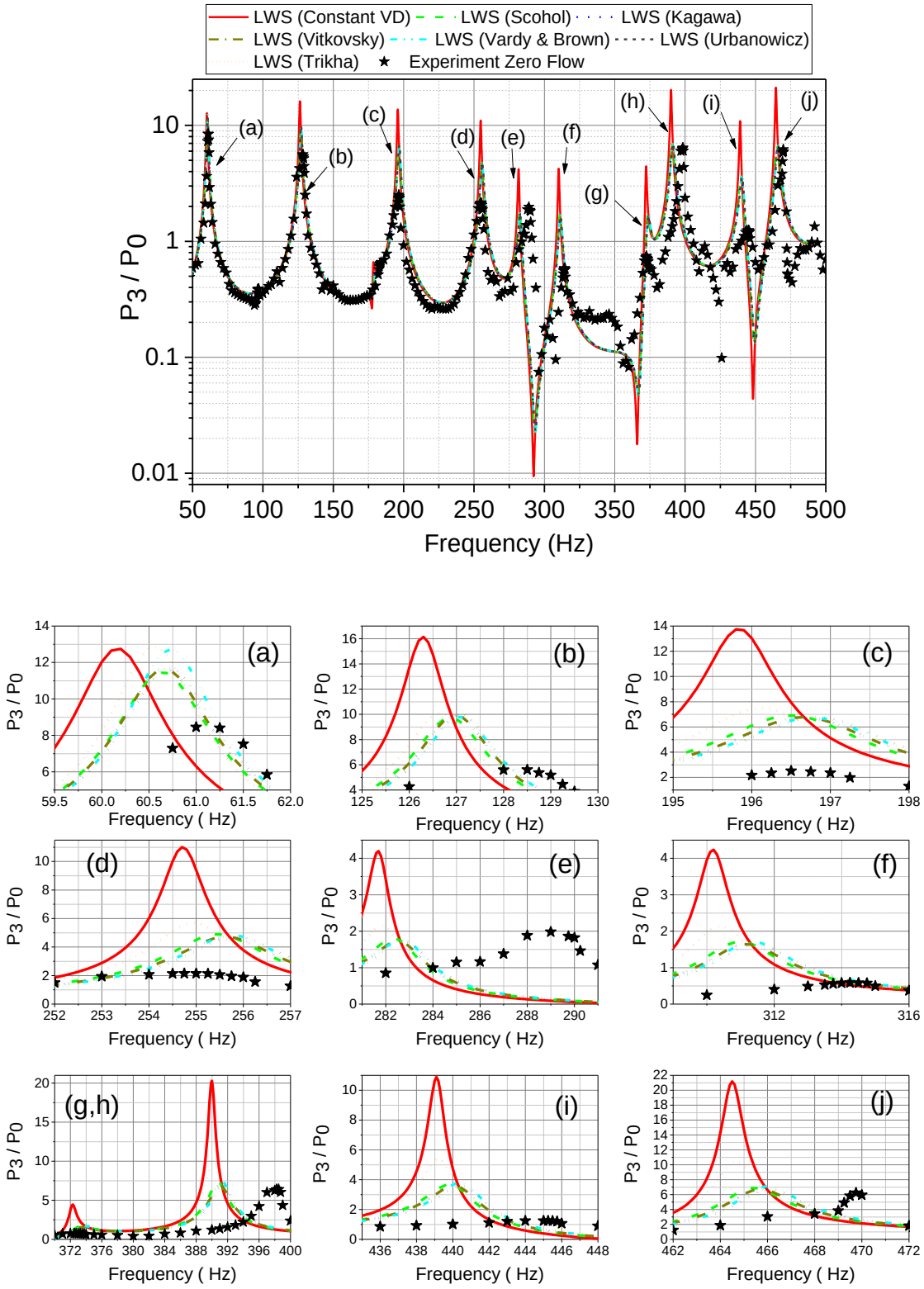

Figure 6.53: Comparison between Results of the Open-Ended "Complex Experiment 2, Main line", and LWS Predictions

It can be seen in Figure 6.52, that for the Complex Experiment 2 configuration, the first six peaks (less than 240 Hz) of P_1 predicted with constant VD give a maximum difference of 4.5 Hz from the experimental data. Figure 6.53 shows that at the same frequency range, the maximum difference between constant VD predictions and the experiments for P_3 are less than 1.25 Hz. It shows that till 240 Hz, the resonant frequencies are well predicted with constant VD for the Complex Experiment 2 configuration. Indeed, with the increase in frequency to more than 240 Hz, the differences between the constant VD resonant frequency predictions and the experimental data rise to a maximum of 8.5 Hz.

The resonant frequency predictions using the frequency-dependent damping methodology of Trikha (1975) are very close to the constant VD predictions. Using the frequency-dependent damping methods of Urbanowicz and Zarzycki (2012) and Vardy and Brown (2004) decreases the maximum difference between the resonant frequency predictions and the experiments to less than 7.25 Hz. The predictions with the assessed resonant frequency-dependent methods are improved compared to the constant VD method, but there are still some resonant peaks at frequencies higher than 240 Hz that are not well predicted.

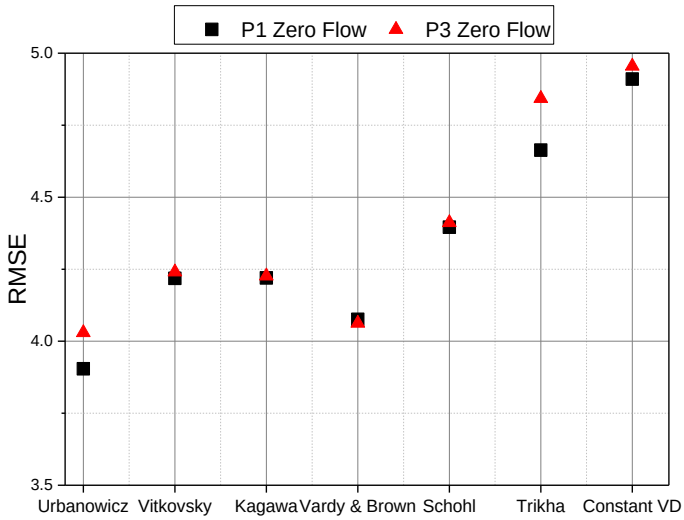

Figure 6.54: RMSE for Resonant Frequency Predictions (Zero & Laminar Mean Flows)

Figure 6.54 shows at P_1 and P_3, using constant VD gives the highest RMSE values for the resonant frequency prediction. For the Complex Experiment with the close-ended mainline outlet, the highest RMSE values are also obtained with the constant VD method. It indicates that with some changes in the configuration of the Complex Experiment 2 compared to Complex Experiment, and using the open-ended outlet mainline for the Complex Experiment 2, the RMSE values trends for the both configurations stay the same. However, using the frequency-dependent damping methodology of Urbanowicz and Zarzycki (2012) decreases the RMSE values to about 20% compared to the constant VD method. Comparing the RMSE values of the open-ended Complex Experiment 2 with Complex Experiment close-ended values shows almost 35–40% decrements for P_1, and 240–250% decrements for P_3. It is indicated that the resonant frequencies for the open-ended case are better predicted than for the close-ended case. The lower RMSE values for the P_3 in open-ended configuration can be reasoned to be due to the open-ended mainline outlet and the higher distance from the outlet. Also, both the P_1 and P_3 are located inside the loop and are closer to each other compared to the Complex Experiment closed-ended configuration in which both branch and mainline measured locations are placed outside of the loop.

6.2.3.1.8 Open-Ended Complex Experiment 2 (Turbulent Mean Flows)

The comparisons between the LWS using constant VD, the LWS using frequency-dependent damping methodologies, and the measurements at P_1 and P_3 are shown in Figures 6.55 and 6.56, respectively. They show the ratio of the outlet to the inlet acoustic pressure amplitude with respect to frequency.

From Figure 6.55 at $P_{1,}$ the first six resonant frequency peaks (less than 240 Hz) are predicted with maximum 5 Hz difference from the experimental data using constant VD method. For the same location of the zero mean flow case, at the first six resonant peaks, the maximum difference from experiments is obtained at about 4.5 Hz. The values of differences which are visible for the 3rd resonant peak of the turbulent flow with Re = 28500 are considered unacceptable. This difference is obtained for the lower frequencies than the zero mean flow case and in terms of percentage is higher than zero and laminar flow cases.

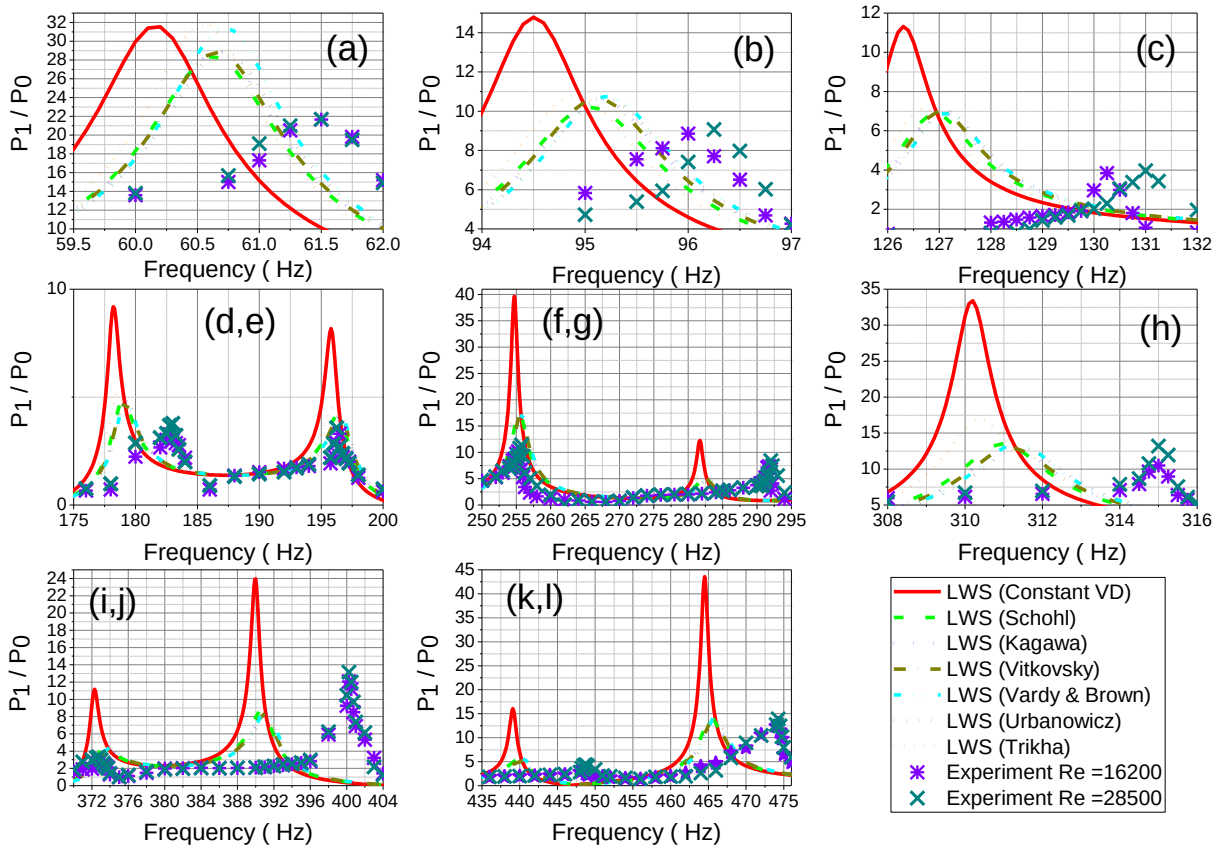

Figure 6.55: Comparison between Turbulent Results of the Open-Ended "Complex Experiment 2" Side Branch 1.18 m and LWS Predictions

At $P_{1,}$ from the 6th to the last resonant peaks, the maximum differences from the measurements are increased from 5 Hz to about 10.5 Hz. The maximum differences from the

measurements for the 7th, 10th, 11th and 12th resonant peaks at about 10.5, 10.25, 9.25, and 10 Hz respectively, are not deemed acceptable. The differences from measurements for the resonant peaks at frequencies higher than 240 Hz are increased from zero to turbulent mean flow cases.

Figure 6.56 shows that at the same frequency range, the maximum difference between constant VD predictions and the experiments at P_3 obtained for the 2nd resonant peak is at about 3 Hz. It indicates that the resonant frequency predictions for P_3 are considered acceptable till 240 Hz. At P_3, the differences from the measurements are increased to about 10.5 Hz for the last five peaks (more than 240 Hz). The predictions indicate that the resonant frequencies are not always well predicted with constant VD till 240 Hz. For higher frequencies, the prediction differences from the measurements increases significantly from zero to turbulent flows.

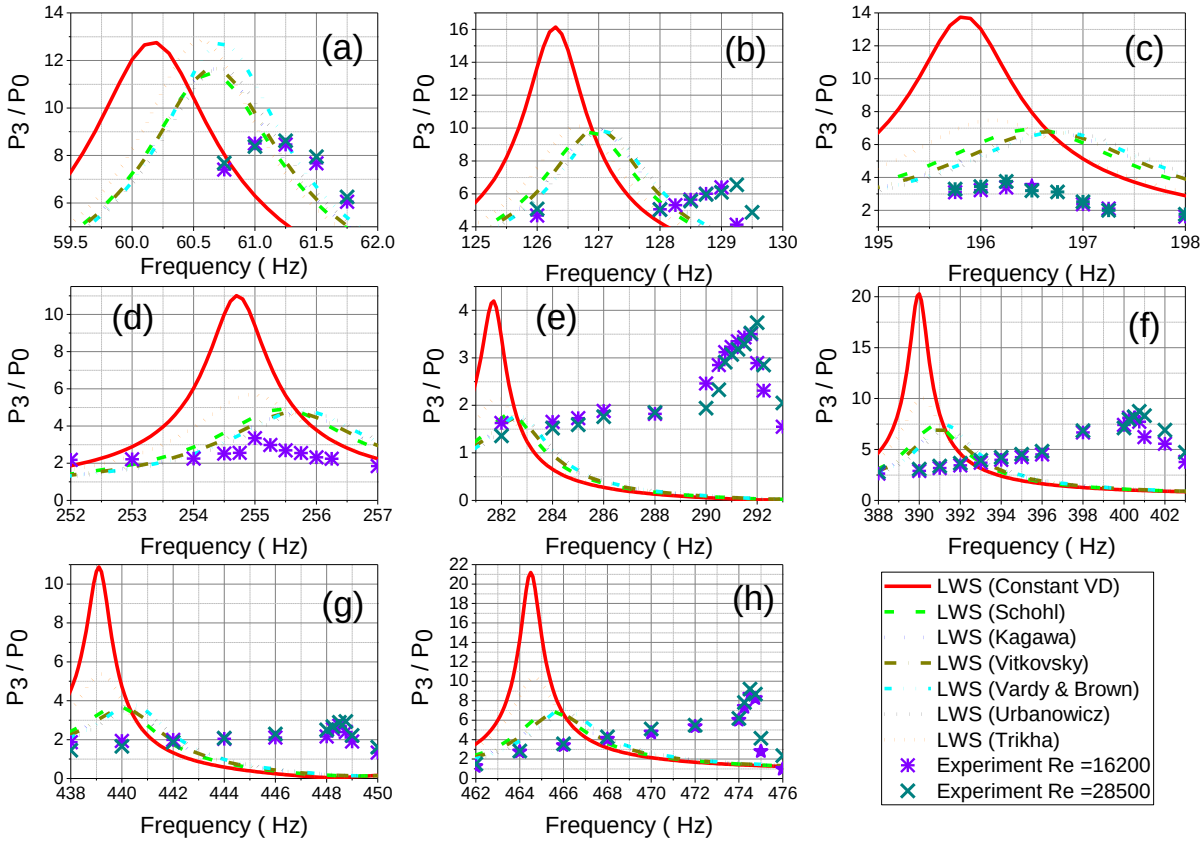

Figure 6.56: Comparison between Turbulent Results of the Open-Ended "Complex Experiment 2" Mainline and LWS Predictions

The frequency-dependent damping methods predictions at Figure 6.55 show that, for the first six resonant peaks, the differences between the resonant frequency predictions and the measurements decreases as compared to the constant VD method. The maximum difference is about 4 Hz. This 20% decrement compared to the constant VD method is an improvement in terms of resonant frequency prediction for the frequencies less than 240 Hz. Figure 6.56 shows that at P_3, for the frequencies less than 240 Hz, using the assessed frequency-dependent methodologies decreases the difference from the measurement to being less than 2.25 Hz. Same as the zero and laminar mean flow, the difference between the predictions and the measurements is considered acceptable. For the frequencies higher than 240 Hz, using the frequency-dependent damping methods of Urbanowicz and Zarzycki (2012) and Vardy and Brown (2004) decrease the maximum difference between the resonant frequency predictions and the experiments to less than 9.25 Hz. The predictions with the assessed resonant frequency-dependent methods, same as the zero and laminar mean flows, improve against the constant VD method, but there are still some resonant peaks at frequencies higher than 240 Hz that are not well predicted.

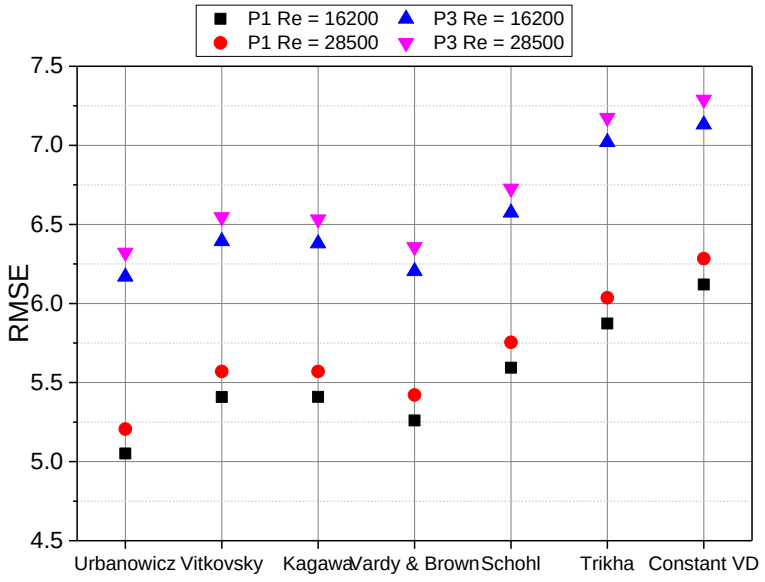

Figure 6.57: Resonant Frequency Predictions RMSE (Turbulent Mean Flows)

Figure 6.57 shows that at P_1 and P_3, using the constant VD method gives the highest RMSE values in terms of resonant frequency prediction. The bigger RMSE values are obtained for the higher Re. Indeed, using the frequency-dependent damping methodology of Urbanowicz and Zarzycki (2012) decreases the RMSE values by about 20% compared to the constant VD method. It means that for all the resonant peaks using the Urbanowicz and Zarzycki (2012), damping method improves the resonant frequency predictions compared to the constant VD and the other assessed damping methods. Comparing the turbulent mean flows RMSE values to the zero mean flow values depicts almost 30–35% increments for P_1 and 55–60% increments for P_3. It is again confirmed that the resonant frequencies for the zero mean flow case are better predicted than the turbulent mean flow cases.

6.2.3.2 The CFD Solution

6.2.3.2.1 Close-Ended Straight Line

In this section, the CFD solution is assessed for resonant frequency predictions. The comparisons between the CFD solutions and the measurements for the 1 mm and 2 mm wall thicknesses of SS fluid-filled tubes and 2 mm wall thickness of the Al fluid-filled tubes are shown in Figures 6.58, 6.59, and 6.60, receptively.

Figures 6.58 and 6.59 show that the resonant peaks of the thinner and thicker SS tubes are predicted within 1.25 Hz. This is obtained from comparing numerical predictions with experimental measurements. Figure 6.60 also shows that for the Al tube with 12 mm O.D., which is the same as the SS tubes, the CFD solution predicts the resonant frequency accurately.

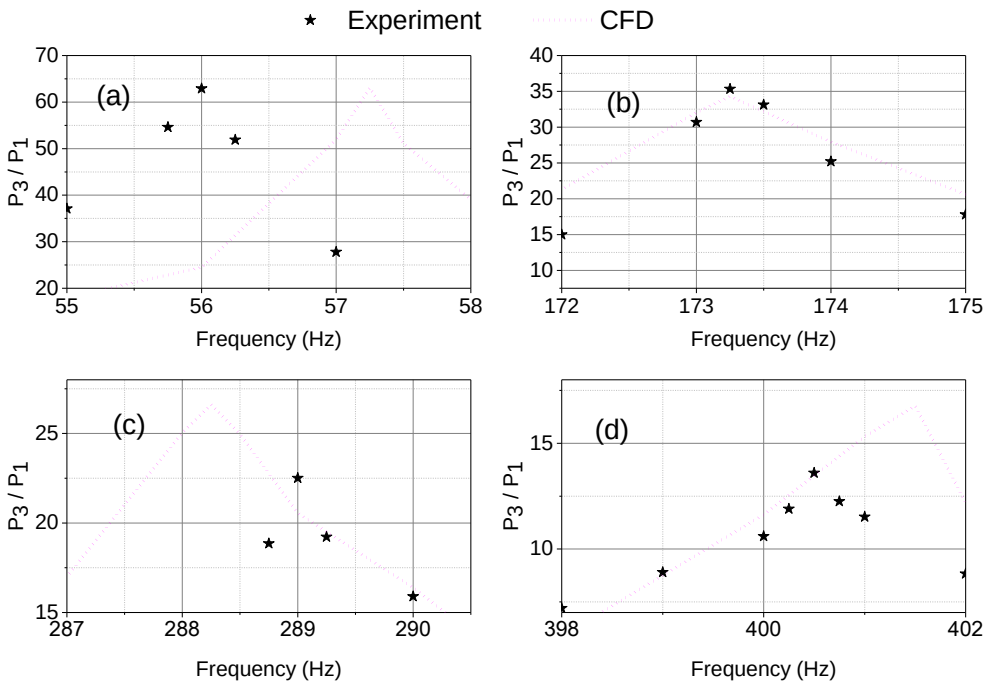

Figure 6.58: Comparison between Results of the "6.13 m long 10 mm O.D. SS Close- Ended Experiment" and CFD

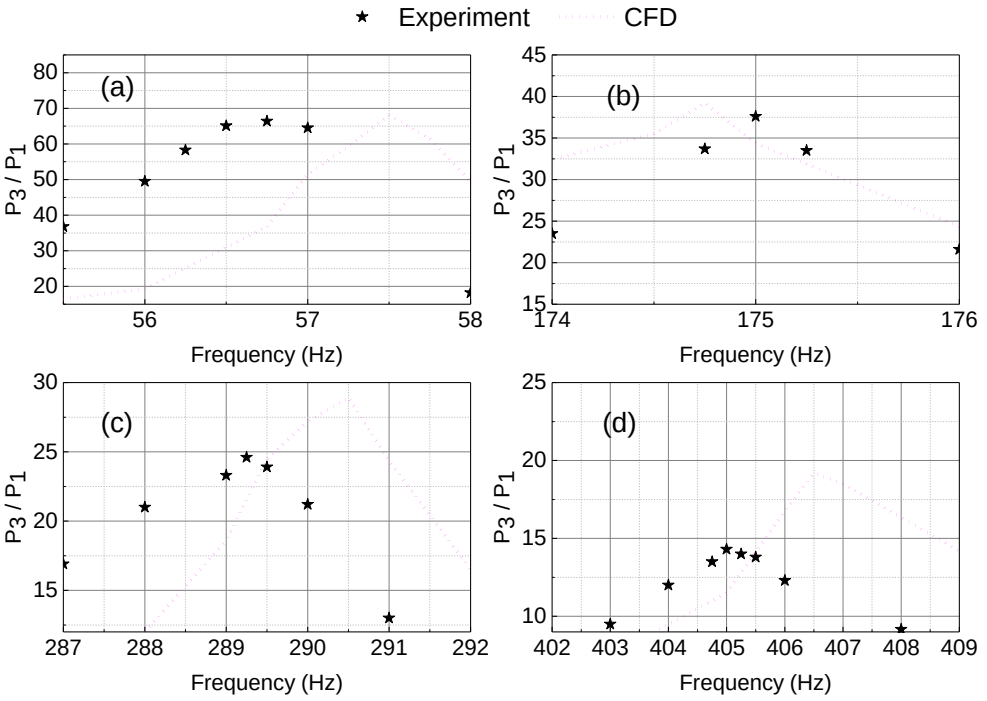

Figure 6.59: Comparison between Results of the "6.13m long 12 mm O.D. SS Close- Ended Experiment" and CFD

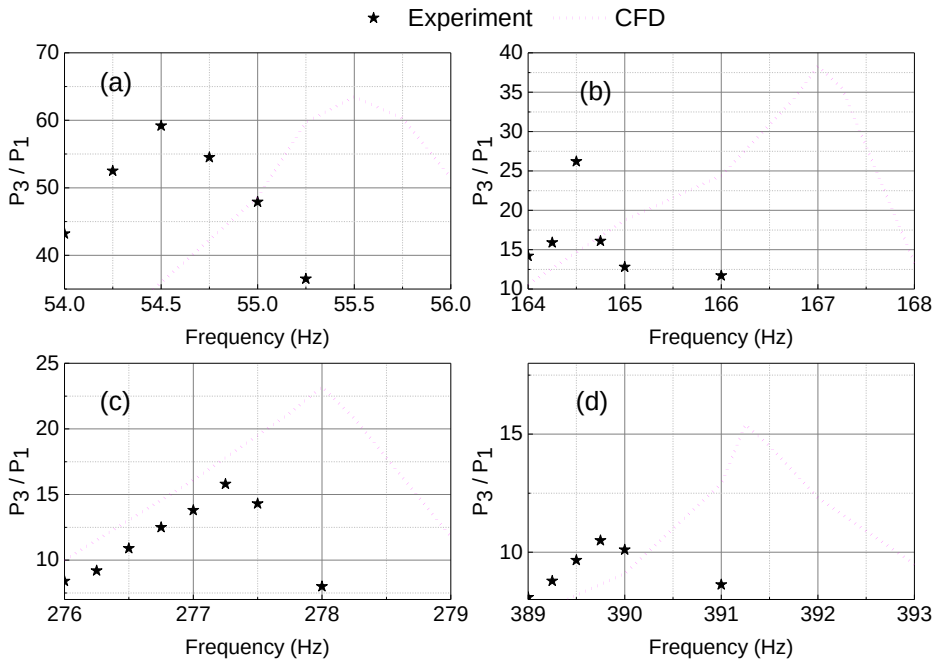

Figure 6.60: Comparison between Results of the "6.13m long 12 mm O.D. Al Close- Ended Experiment" and CFD

The CFD solution RMSE values are almost 1/2 and 2/3 of the best RMSE values that are obtained with the LWS using the UVK damping methodologies. It indicates that the predicted resonant frequencies with CFD solution are closer to the experimental results than the LWS using constant and the assessed frequency-dependent damping methods. Exactly the same geometric data and sonic velocities are used in both LWS and CFD codes. Therefore, any difference in the resonant frequency predictions between the two codes is the result of the more complete equations solved with CFD.

6.2.3.2.2 Open-Ended Straight Line for Zero Mean Flow

The predictions for the zero mean flow with the CFD solution are compared against the experimental data in Figures 6.61–6.63.

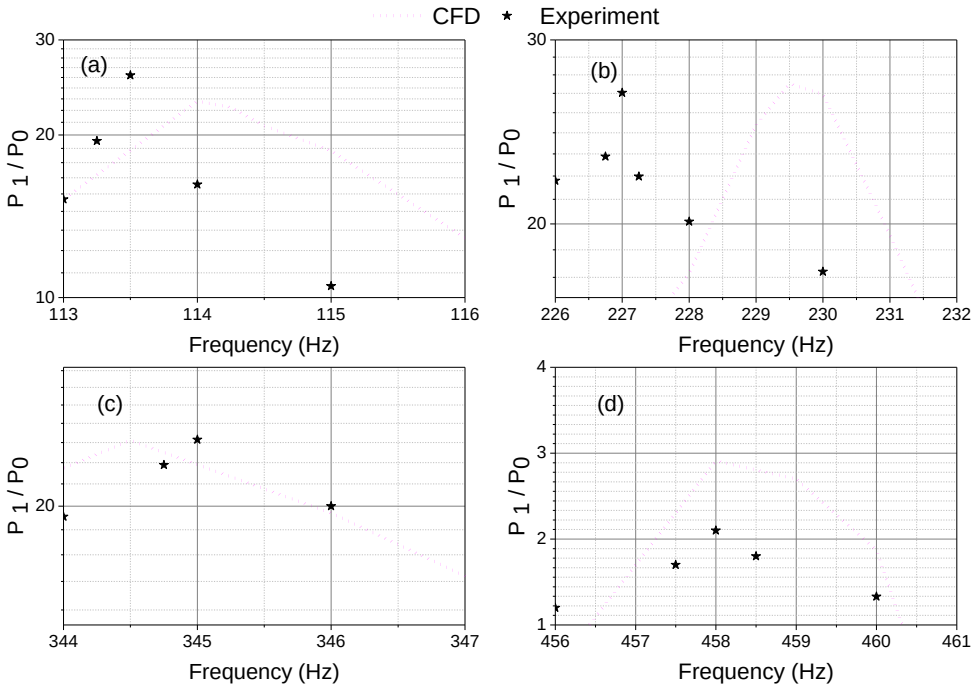

Figure 6.61: Comparison between Results of the "6.13m long 10 mm O.D SS Open- Ended Experiment" and CFD at P_1

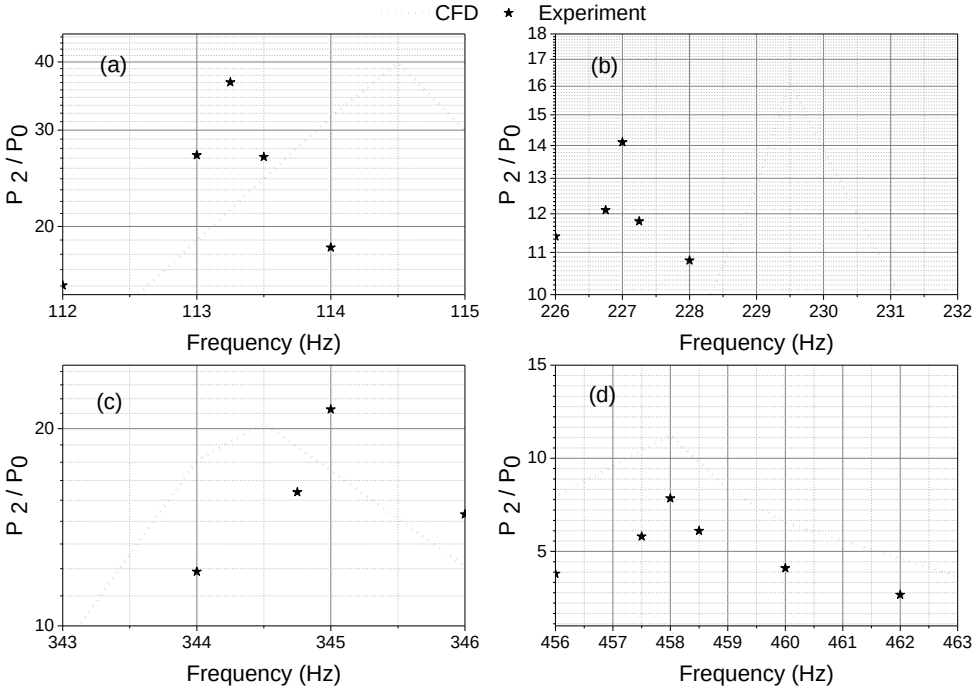

Figure 6.62: Comparison between Results of the "6.13m long 10 mm O.D SS Open- Ended Experiment" and CFD at P_2

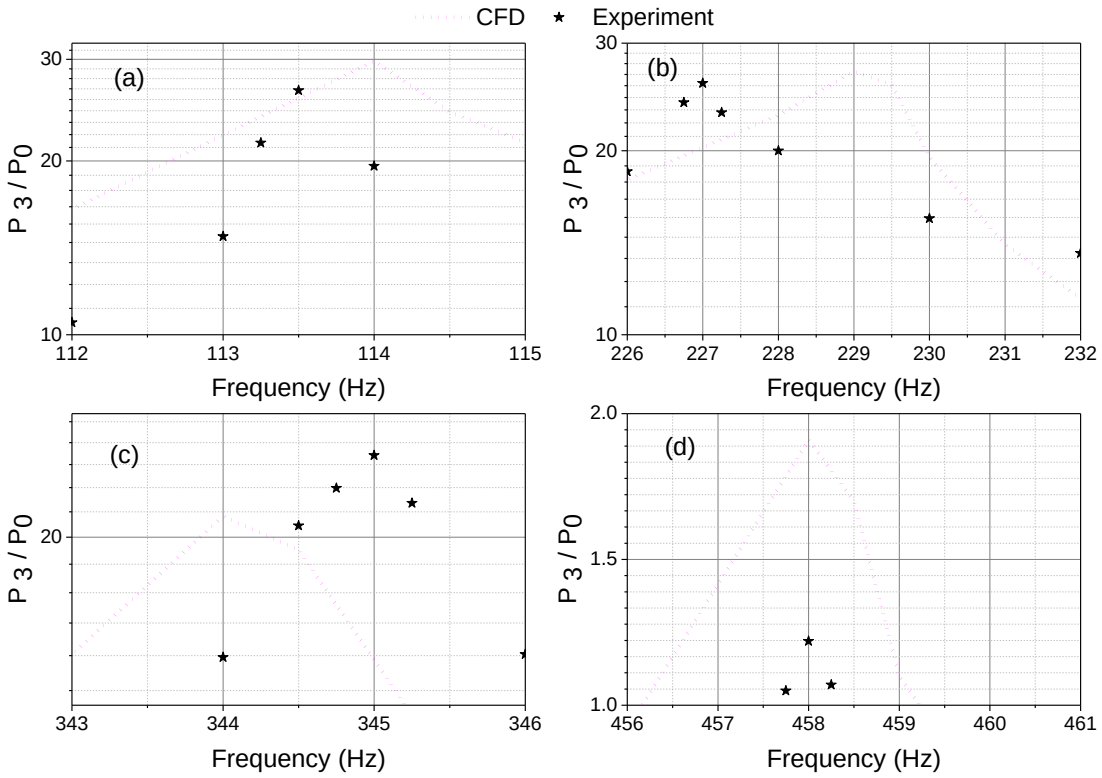

Figure 6.63: Comparison between Results of the "6.13m long 10 mm O.D SS Open- Ended Experiment" and CFD at P_3

From Figures 6.61–6.63, the resonant frequency predictions with the CFD solution show a maximum difference of 2.5 Hz from the measured values, which is less than the LWS using the damping methods values. The RMSE values of the CFD solution are also less than the RMSE values of the frequency-dependent damping methodologies of Schohl (1993), Urbanowicz and Zarzycki (2012), and Vardy and Brown (2004) and the constant VD method. It means the resonant frequencies for all the four resonant peaks are predicted better with the CFD solution than the LWS using the frequency-dependent damping methodologies and constant VD. Again, the reason may be likely the more complete equations solved with CFD.

6.2.4 Resonant Amplitude Predictions

6.2.4.1 LWS Using Constant VD and Frequency-Dependent Damping Methods

6.2.4.1.1 Straight line close-ended

First, the resonant amplitude prediction using the constant VD method is assessed. From the amplitude prediction relative errors given in Figure 6.64, for both the SS tubes (10 mm and 12 mm O.D.), the constant VD only predicts the 2nd resonant peaks with acceptable values of relative errors. Also, Figure 6.65 shows that the constant VD RMSE values for both SS tubes are high compared to other assessed damping methods.

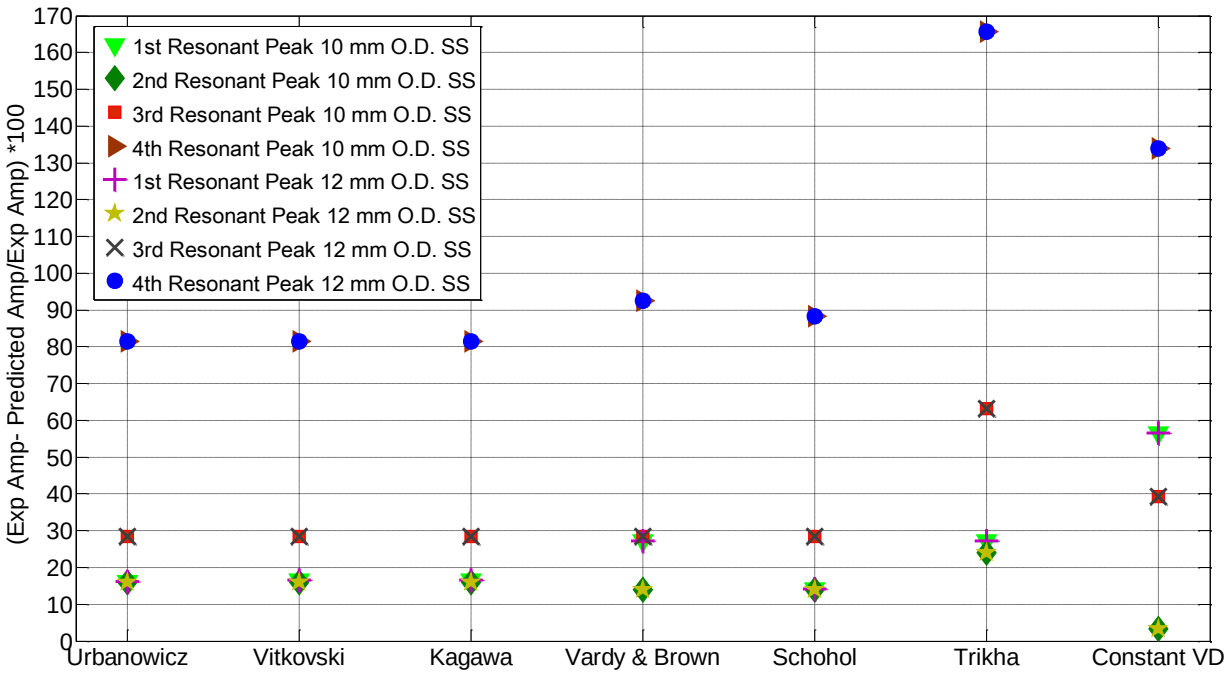

Figure 6.64: Resonant Amplitude Prediction Relative Errors for SS Tubes

For the Al tube with 12 mm O.D. and Al tubes with two different wall thicknesses as shown in Figure 6.66, is same as the SS tubes; only the 2nd peaks are well predicted. The RMSE values

for the Al tubes are higher than the RMSE values of the SS tubes. It indicates poor agreement between the resonant amplitude predictions and the measurements for the SS and the Al tubes. The resonant amplitude predictions using constant VD have the same magnitude for all the resonant peaks. Therefore, a constant VD cannot capture the feature of decreasing resonant amplitude with increasing frequency, and it is not recommended for accurate resonant amplitude prediction.

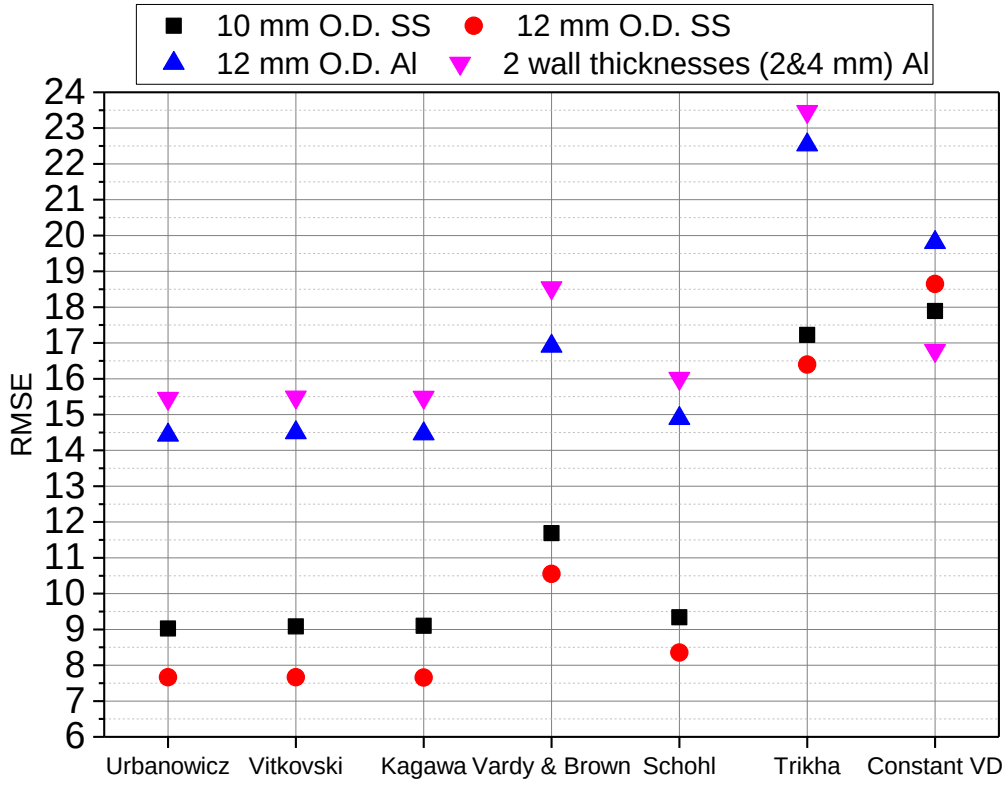

Figure 6.65: Resonant Amplitude Predictions RMSE

Figure 6.66 shows the resonant amplitude relative errors for the Al tube with 12 mm O.D and Al tubes with two different wall thicknesses. The relative errors of 19% by Schohl (1993) for the 1st resonant peak, 30.5% by Vardy and Brown (2004) for the 2nd resonant peak, and 85% and 148% by Kagawa et al. (1983), Urbanowicz and Zarzycki (2012), and Vitkovsky et al. (2004) for

the 3rd and 4th resonant peaks are obtained. It indicates that only the first two resonant peaks are predicted well. For the case with two different wall thicknesses, only the 2nd resonant peak is predicted with a minimum of 37% relative error using all the assessed damping methods. Figure 6.66 shows that for the Al tubes same as the SS tubes, the amplitude predictions using the Trikha (1975) damping methodology gives the lowest accuracy.

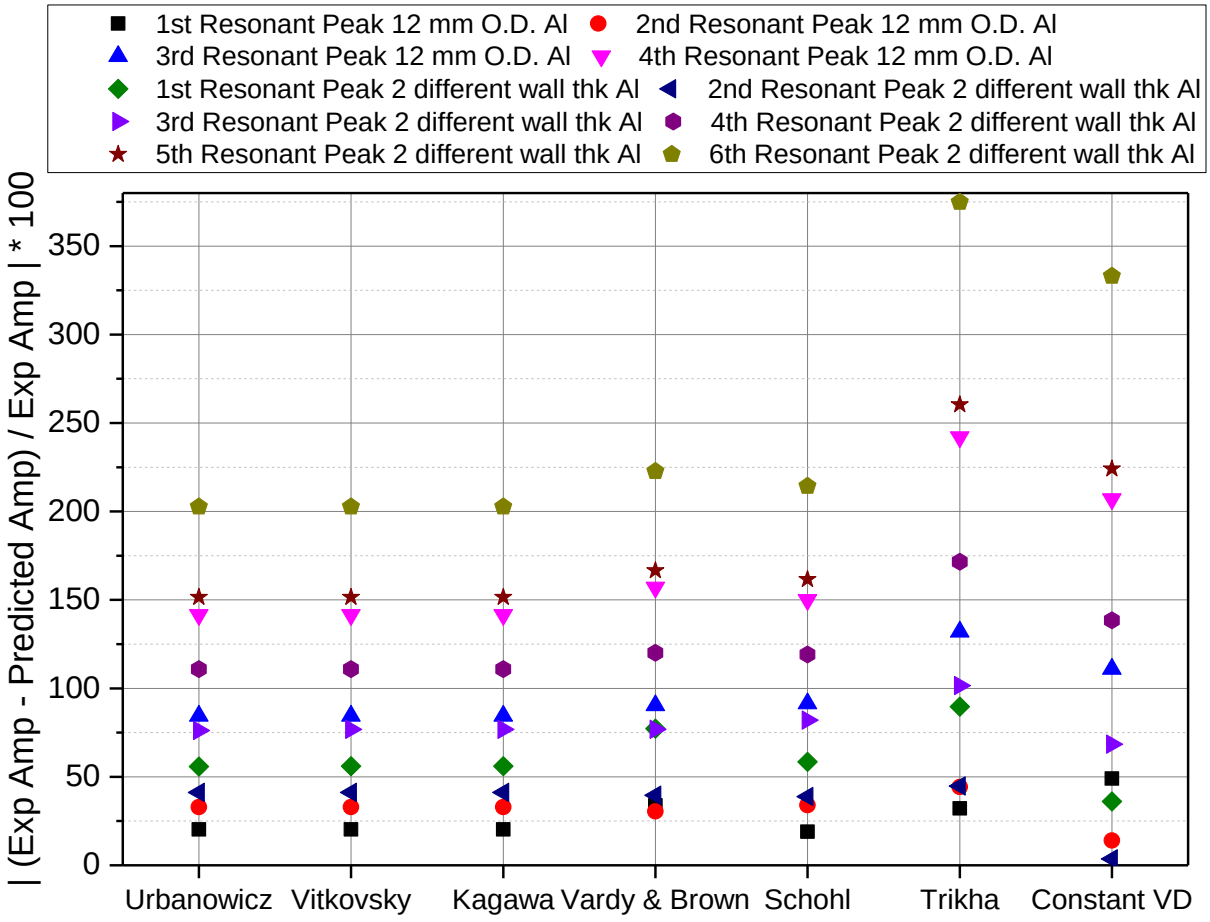

Figure 6.66: Resonant Amplitude Prediction Relative Errors for 12 mm O.D. and two Different Wall Thicknesses Al Tubes

Same as the SS tubes, using the UVK damping methodologies gives the lowest RMSE values. Also, it should be noted that the RSME values for the Al tube with 12 mm O.D. are almost twice the SS tube RMSE values with the same wall thickness and boundary conditions. It can be

because of higher fluid-structure interaction effect on the Al tube than the SS tube. Al being a lighter material than SS absorbs the energy of the acoustic waves more than SS. The effect of different materials is only applied on the sonic velocity. A higher movement of the Al tube in the radial direction is not considered in the assessed methods.

Since the resonant amplitudes for the frequencies less than 300 Hz in SS tubes and frequencies less than 250 Hz in Al tube with 12 mm O.D. are accurately approximated using the UVK damping methodologies, the discrepancy between the resonant amplitude predictions and the experimental results of the higher frequencies maybe due to the simplifications applied to the unsteady friction terms. Although for the assessed frequency-dependent damping methodologies the unsteady component of the friction terms are obtained from the simplified 2D axis-symmetric Navier–Stokes equations, they are applied in the 1D model that are limited by the assumption of 1D flow along the pipe. Also, the assessed damping methodologies are developed for water hammer applications, which occur in low frequencies (less than 60 Hz).

The current findings show that as long as the inverse frequency at the inlet boundary condition is higher than the ratio of the length of the tube over the speed of sound, the resonant amplitude predictions with the assessed damping methodologies are closer to the experimental data. It means that for ($\frac{L}{\lambda}$ <1), the prediction relative errors compared to the experiments increase with increasing frequency. Therefore, for the investigated tube sizes, using the UVK damping methodologies are recommended for the resonant amplitude predictions when the frequencies are less than 300 Hz and 250 Hz for the SS and Al tubes respectively. The Trikha (1975) and constant VD methods are not recommended for resonant amplitude predictions.

6.2.4.1.2 Straight Line Open-Ended

Figure 6.67 shows the first three resonant peaks at P_1, P_2, and P_3 are predicted with less than 34% relative errors using the constant VD method. For the 4th resonant peak, the relative errors are increased to 140%, 180%, and 195% at P_1, P_2, and P_3, respectively. It means that the constant VD accurately predicts the resonant amplitudes for frequencies less than 350 Hz. The maximum relative error for the first three resonant peaks of the open outlet end case is less than the same case with close-ended outlet. It can be due to the fact that for the close-ended case, the reflective boundary condition significantly distorts the incident waves and the constant VD is not able to capture the true resonant amplitude.

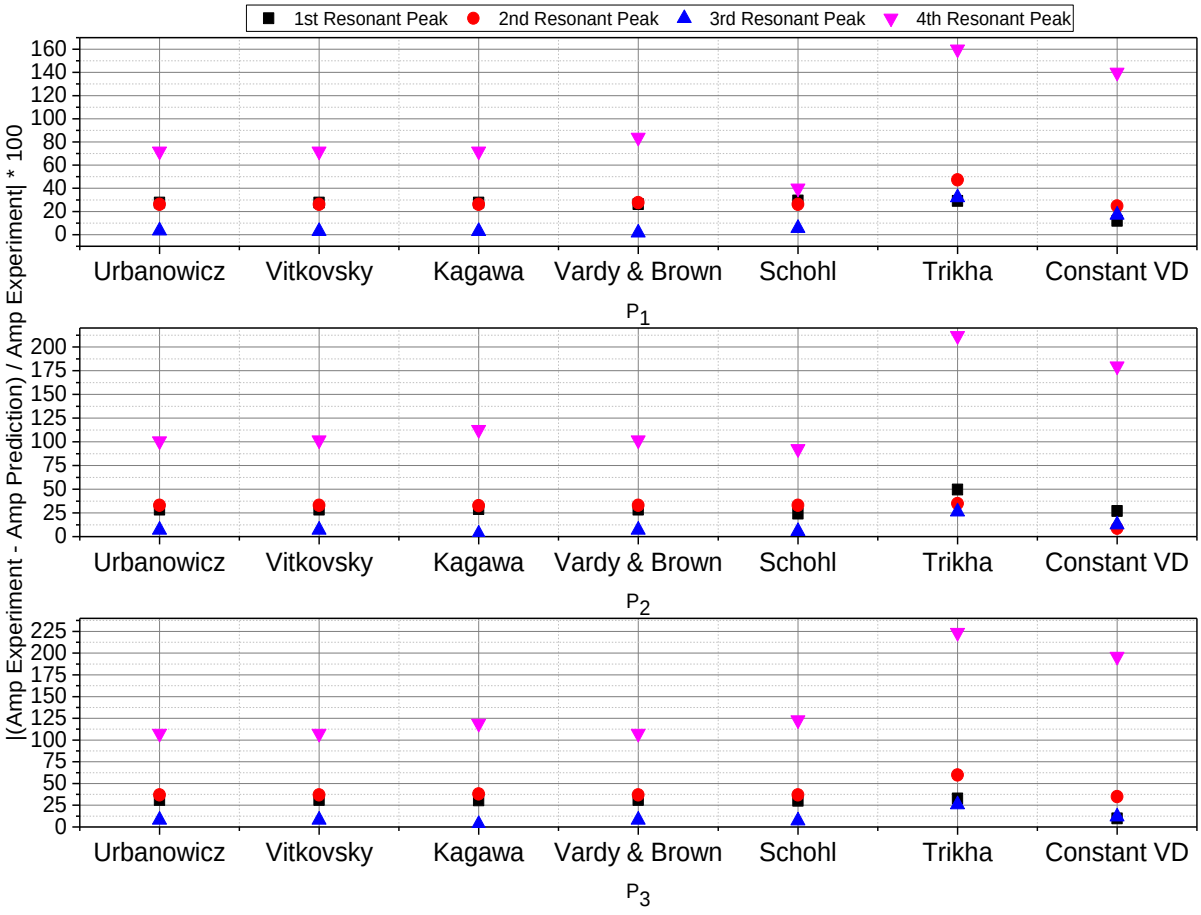

Figure 6.67: Resonant Amplitude Prediction Relative Errors for Zero Flow

Even though the resonant amplitudes decrease with increasing frequency for the close-ended cases, this trend is not captured for the open-ended case. The reason may be that the constant VD predicts the resonant amplitudes for the open outlet end case better than the close outlet end case.

As Figure 6.67 also displays, the resonant amplitudes at P_1, P_2, and P_3 are predicted with relative errors of less than 36% for the first three resonant peaks using the UVK damping methodologies.

The 4^{th} resonant peak is not accurately predicted with the assessed frequency-dependent damping methods. For the 4^{th} peak, the constant VD predictions are worse than the frequency-dependent damping methods.

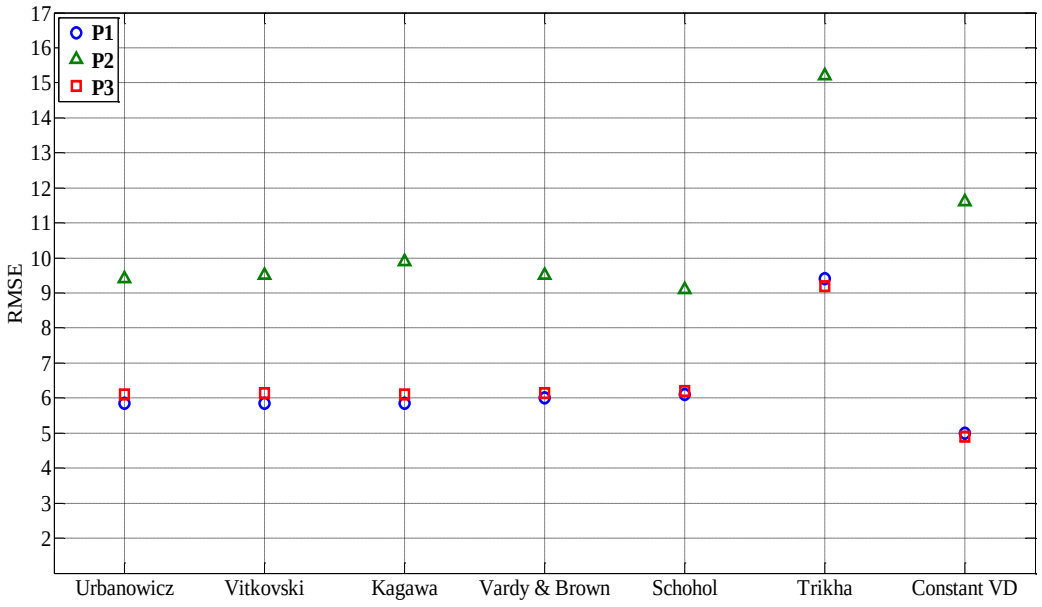

Figure 6.68: RMSE Values of Zero Mean Flow Resonant Amplitude Predictions

Figure 6.68 shows that the RMSE values of the frequency-dependent damping methodologies are close to the constant VD RMSE values. It can be a coincidence that the resonant amplitude predictions with the chosen VD value of 13200 give the relative errors close to the assessed damping methodologies.

6.2.4.1.3 Equal Branches and Elbow

Initially, the resonant amplitude prediction using the constant VD is assessed. For the elbow shown in Figure 6.69, only the 2nd and 3rd peaks are properly predicted. Similar to the straight line tubes, the resonant amplitude predictions using constant VD give the same magnitude for all the resonant peaks and cannot capture the feature of the decreasing resonant amplitude with increasing frequency.

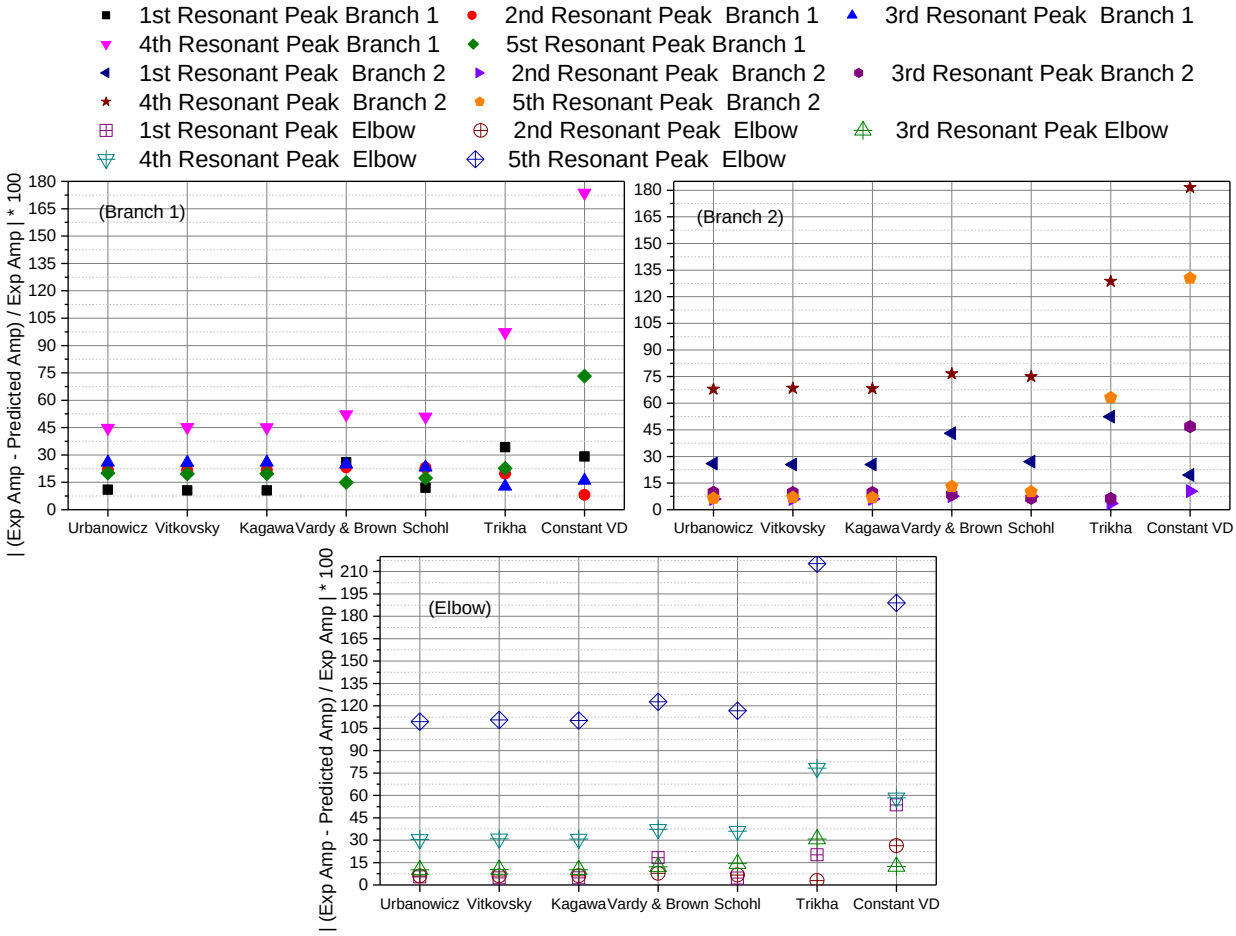

Figure 6.69: Resonant Amplitude Prediction Relative Errors for Elbow, Branch 1 and Branch 2

The relative errors in the amplitude predictions for the Branch 1 configurations given in Figure 6.69, the constant VD method predicts the first three resonant peaks with the acceptable

values of relative errors. For Branch 2, only the first two resonant peaks are predicted with less than 25% of relative errors, which mean that for Branch 1 with the T-junction, resonant amplitudes for higher frequencies are better predicted than they are in Branch 2. The relative errors indicate a poor agreement between the resonant amplitude predictions and the measurements for the equal branches at the 4^{th} and 5^{th} resonant peaks. Also, Figure 6.70 shows that the constant VD RMSE values for both the equal branches are high compared to the other assessed damping methods.

Figure 6.69 also displays the resonant amplitude relative errors for the assessed frequency-dependent damping methodologies. For Branch 1, the first three and the last resonant peaks are predicted with less than 30% relative errors using the damping methodologies of Kagawa et al. (1983), Schohl (1993), Urbanowicz and Zarzycki (2012), Vardy and Brown (2004), and Vitkovsky et al. (2004). The predictions obtained with the Trikha (1975) method also have less than 35% relative errors. The constant VD only predicts the first three peaks with less than 30% relative errors, and the 4^{th} and 5^{th} peaks are predicted with 170% and 72% relative errors respectively. The resonant amplitude predictions with the assessed frequency-dependent methodologies show considerable improvement over the constant VD method for Branch 1 configuration. The damping methodologies of UVK and Vardy and Brown (2004) also give the acceptable amount of relative errors for the first three and the last resonant peaks of Branch 2. For the 4^{th} peak of Branch 2, the relative errors of the assessed damping methodologies are more than Branch 1. For the elbow, the UVK damping methodologies only predict the first four resonant peaks with less than 30% relative errors.

Figure 6.70 shows an increase in the RMSE values from Branch 1 to Branch 2 and from Branch 2 to the elbow. The LWS using Trikha (1975) damping method gives the highest RMSE

values among the assessed frequency-dependent methodologies and the lowest accuracy. Same as the straight line tubes, using the damping methodologies of UVK give the lowest RMSE values in resonant amplitude predictions.

The relative errors and the RMSE values show that the first four resonant peaks for the elbow and the first three and the last peaks for the equal branches configurations are satisfactorily predicted using the UVK damping methodologies. This means that even the assessed frequency-dependent methodologies are unable to always predict the acoustic resonances accurately for the assessed geometries.

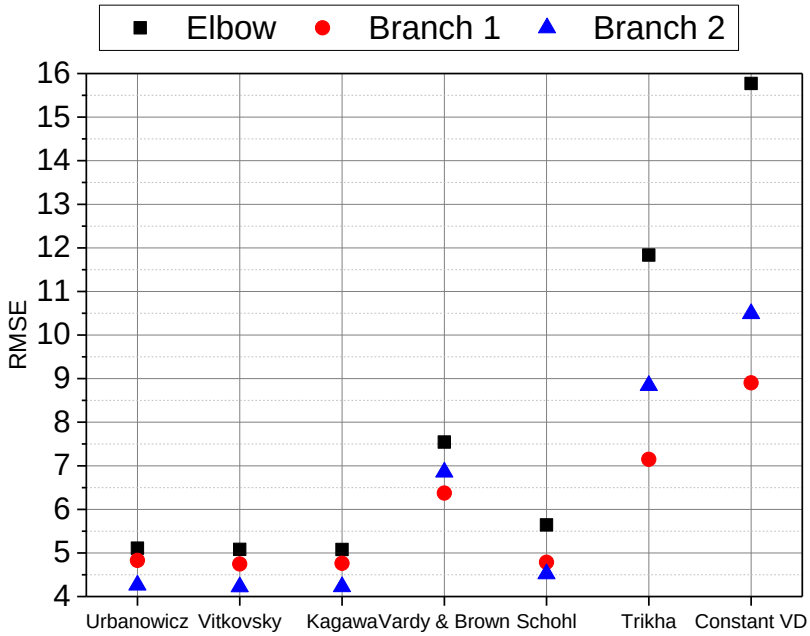

Figure 6.70: RMSE Values for Resonant Amplitude Predictions

For both the Branch 1 and 2 configurations, the width of the 4th resonant peaks predictions with the assessed frequency-dependent methodologies and constant VD method are quite narrow compared to the corresponding measurements (see Figures 6.35 and 6.36). This disagreement is an important finding, since it is at the 4th resonant peak of the equal branch configurations where

the trend of the decreasing amplitude with increasing frequency is changed. The difference between the predictions and the measurements can be reasoned to the fact that the minimum troughs of the non-resonance amplitudes before and after the 4th resonant peak are not accurately predicted. Also, due to the complex interactions between the reflected acoustic waves at the T-junction, the LWS using the assessed methods are not able to predict these complex interactions at the junction. The complex interactions between the acoustic waves at the junctions might not be captured with 1D model using the unsteady friction models.

Also, for the frequencies higher than 350 Hz in the elbow tube and for the frequencies between 250 Hz and 400 Hz in equal branch configurations, the resonant amplitudes are not approximated well using the UVK damping methodologies. These discrepancies between the acoustic resonance predictions and the experimental results may be due to the simplifications that are applied to model the unsteady friction terms. The current findings of the elbow show that with the value of $\frac{L}{\lambda} < 1.5$, the prediction relative errors compared to the experiments increase with an increase in the frequency. This value is higher than the values of the SS and the Al straight tubes. Therefore, for the tested tube sizes of the elbow, using the UVK damping methodologies are recommended for the resonant amplitude predictions, when the frequency is less than 350 Hz.

6.2.4.1.4 Close-Ended Unequal Branch & Combined Parameters

The amplitude prediction relative errors for Branch 3 using all the assessed methodologies are tabulated in Tables 6.12 and 6.13 for P_1 and P_3, respectively. From the amplitude prediction relative errors given in Figure 6.71 and Tables 6.12 and 6.13, the constant VD predicts only the

1st resonant peak with acceptable values of relative errors for the Branch 3 configuration. The predictions for the 2.07 m branch are better than those of the mainline outlet. For the last resonant peak of the P_3, the prediction relative error is increased to about 315%.

The important finding that should be noted here is the thickness of the 4th and 5th peaks predictions compared to the experiments (see Figures 6.38 and 6.39). The prediction peaks are narrower than the measurements. Also, for the frequency range of 250 Hz to 350 Hz, some points are predicted with amplitudes of less than 1 and at the same points the measurements of the amplitudes are reported up to 3. It should be pointed that although only one resonant peak is predicted between 350 Hz and 400 Hz for both P_1 and P_3, measurements show two resonant peaks at this frequency range.

Table 6.12: Branch 2.07 m (P_1) Relative Errors (%) for Branch 3, Close Ended

Peak Number	Urbanowicz	Kagawa	Vitkovsky	Vardy & Brown	Schohl	Trikha	Constant VD
1st	✓ 23.47305	✓ 23.65269	✓ 23.53293	! 38.14371	✓ 23.47305	! 43.77246	✓ 19.58084
2nd	✗ 65.61224	✗ 65.38265	✗ 65.30612	✗ 64.08163	✗ 60.07653	✗ 67.55102	✗ 65.71429
3rd	✗ 66.6087	✗ 66.6087	✗ 66.6087	✗ 66.78261	✗ 66.26087	✗ 65.04348	✗ 61.3913
4th	✓ 14.34524	✓ 14.52381	✓ 14.46429	✓ 16.30952	✓ 18.57143	✓ 36.07143	✗ 69.52381
5th	✗ 77.46336	✗ 77.42954	✗ 77.44081	✗ 76.47125	✗ 76.50507	✗ 70.46223	✗ 61.89402
6th	✗ 62.20183	✗ 62.06422	✗ 62.08716	✗ 60.3211	✗ 61.05505	! 46.55963	✓ 31.00917
7th	✗ 81.87019	✗ 81.80418	✗ 81.81518	✗ 80.9681	✗ 81.32013	✗ 74.36744	✗ 66.90869
8th	✗ 55.65276	✗ 57.33513	✗ 56.393	✗ 65.67968	✗ 60.76716	✗ 143.2705	✗ 221.6016

Figure 6.71 and Tables 6.12 and 6.13 also show resonant amplitude predictions relative errors at Branch 3 using the assessed frequency-dependent damping methodologies. The 1st, 4th, and 6th resonant peaks at P_3 are predicted with less than 30% relative errors using the damping methodologies of UVK and Schohl (1993). For the other resonant peaks, the relative errors are in the range of 60% to 100% at P_3. At P_1, only the 1st and 4th peaks are well predicted and other

peaks are predicted in the range of 55% to 82%. The predictions using the damping method of Trikha (1975) result in the highest relative errors among the other tested damping methods. The constant VD method only predicts the first peaks of both measured locations with less than 20% relative errors. It shows some improvements in the resonant amplitude predictions with the assessed frequency-dependent methodologies over the constant VD method, but these improvements only bring the 4th and 6th resonant peaks to an acceptable range of relative errors.

Table 6.13: Mainline outlet (P_3) Relative Errors (%) for Branch 3, Close Ended

Peak Number	Urbanowicz	Kagawa	Vitkovsky	Vardy & Brown	Schohl	Trikha	Constant VD
1st	✓ 16.92188	✓ 17.32813	✓ 17.26563	✓ 30.76563	✓ 17.03125	✓ 36.67188	✓ 23.9375
2nd	✗ 123.1361	✗ 122.7811	✗ 122.6627	✗ 121.0651	✗ 115.9172	✗ 125.9763	✗ 123.3136
3rd	✗ 59.46131	✗ 59.44048	✗ 59.49107	✗ 59.8631	✗ 59.27381	✗ 56.63393	! 49.96726
4th	✓ 5.29412	✓ 5.54622	✓ 5.46218	✓ 7.22689	✓ 9.32773	✓ 25.29412	✗ 56.38655
5th	✗ 63.72756	✗ 63.67476	✗ 63.67476	✗ 62.14361	✗ 62.19641	✗ 52.32313	! 38.59556
6th	✓ 26.74731	✓ 26.35753	✓ 26.47849	✓ 22.17742	✓ 24.05914	✓ 8.87097	! 43.14516
7th	✗ 84.29395	✗ 84.21037	✗ 84.23631	✗ 83.31412	✗ 83.71758	✗ 76.65706	✗ 69.30836
8th	✗ 100.8081	✗ 101.8182	✗ 101.4141	✗ 113.5354	✗ 107.2727	✗ 213.7374	✗ 314.9495

The amplitude relative errors for Complex Experiment using all the assessed methodologies are tabulated in Table 6.14 for P_1, Table 6.15 for P_4 and Table 6.16 for P_3. As Figure 6.72 and Tables 6.14-6.16 show for Complex Experiment configuration, the LWS using the constant VD gives the resonant amplitude prediction relative errors that are different from Branch 3 values. At P_3, the 1st and 6th resonant peaks are predicted with less than 20% of the relative error and the 5th and 10th resonant peaks are predicted within 50% relative errors. Also, at P_4, only the 10th resonant peak is predicted with less than 10% of relative error. The highest relative errors are obtained at the 4th and 8th resonant peaks of P_3 and P_4. At 2.07 m Branch (P_1), the 1st peak is only satisfactorily predicted at about 15% relative errors. Those predictions indicate that the relative

errors for the lower frequencies are not always less than that of the higher frequencies. For different locations (P_1, P_3, and P_4), the lowest and the highest relative error values are not obtained at the same resonant peaks. Indeed, for those two investigated configurations (Branch 3 and Complex Experiment), the constant VD is not recommended for the accurate resonant amplitude prediction.

Table 6.14: Branch 2.07 m (P_1) Relative Errors (%) for Complex Experiment, Close Ended

Peak Number	Urbanowicz	Kagawa	Vitkovsky	Vardy & Brown	Schohl	Trikha	Constant VD
1st	✓ 10.45062	✓ 10.45679	✓ 10.47531	✓ 25.8642	✓ 14.44444	! 40.24691	✓ 15.30864
2nd	✓ 10.87388	✓ 10.84074	✓ 10.84663	✓ 12.58402	✓ 6.40652	✓ 12.79881	! 46.58215
3rd	✗ 121.2177	✗ 121.1167	✗ 121.1744	✗ 122.4	✗ 112.7455	✗ 123.4618	✗ 204.7997
4th	✗ 113.0133	✗ 112.6207	✗ 112.5188	✗ 108.8128	✗ 110.5328	✗ 119.2639	✗ 259.0315
5th	✗ 62.38831	✗ 62.40382	✗ 62.4173	✗ 62.54135	✗ 62.25528	✗ 61.45955	✗ 50.52652
6th	! 46.85207	! 46.88158	! 46.71861	! 46.95789	✗ 50.49737	✗ 64.81241	✗ 198.2023
7th	✗ 301.6242	✗ 302.2008	✗ 301.897	✗ 313.4023	✗ 317.5288	✗ 393.4856	✗ 836.3773
8th	! 49.75819	! 49.97316	! 49.85989	✗ 54.15	✗ 55.6887	✗ 84.01158	✗ 249.1576
9th	✓ 4.29648	✓ 4.37578	✓ 4.35756	✓ 8.47453	✓ 8.57598	✓ 33.89772	✗ 157.9497
10th	✗ 76.31301	✗ 76.26015	✗ 76.27241	✗ 75.0836	✗ 75.36003	✗ 67.84651	! 37.4242
11th	! 49.23894	! 49.6731	! 49.56726	✗ 57.98336	✗ 54.82867	✗ 112.194	✗ 317.5784
12th	✓ 14.98502	✓ 14.68381	✓ 14.80364	✓ 9.90931	✓ 12.18097	✓ 24.7332	✗ 145.0085
13th	✗ 79.97297	✗ 80.77568	✗ 80.54137	✗ 91.20852	✗ 85.70665	✗ 175.5697	✗ 445.9921

Table 6.15: Aluminum Branch (P_4) Relative Errors (%) for Complex Experiment, Close Ended

Peak Number	Urbanowicz	Kagawa	Vitkovsky	Vardy & Brown	Schohl	Trikha	Constant VD
1st	✗ 85.82284	✗ 86.49431	✗ 86.5025	✗ 112.4356	✗ 93.58266	✗ 136.5263	! 42.55517
2nd	✓ 3.89173	✓ 3.76148	✓ 3.77295	✓ 5.44083	✓ 0.55298	✓ 5.6111	! 37.47124
3rd	✗ 237.6108	✗ 237.148	✗ 237.1518	✗ 239.1645	✗ 223.9099	✗ 241.1398	✗ 364.0069
4th	✗ 341.6006	✗ 340.8785	✗ 341.0201	✗ 333.0609	✗ 335.8008	✗ 354.5034	✗ 643.1215
5th	✗ 135.3418	✗ 135.0415	✗ 135.263	✗ 135.4013	✗ 141.418	✗ 164.4884	✗ 381.4476
6th	✗ 394.4681	✗ 393.8372	✗ 394.3027	✗ 394.5931	✗ 407.2346	✗ 455.7069	✗ 911.5521
7th	✓ 30.80875	✓ 30.73848	✓ 30.707	✓ 28.79738	✓ 27.98819	✓ 14.5812	✗ 62.84461
8th	✓ 22.68815	✓ 22.7763	✓ 22.76214	✓ 27.45549	✓ 27.53844	✗ 56.45925	✗ 198.1616
9th	✗ 88.36167	✗ 88.33888	✗ 88.33513	✗ 87.76487	✗ 87.89901	✗ 84.26256	✗ 69.42404
10th	✗ 61.00446	✗ 60.92739	✗ 60.89713	✗ 58.83217	✗ 59.58344	! 45.17293	✓ 6.51401
11th	✓ 22.90497	✓ 22.67719	✓ 22.59795	✓ 18.48684	✓ 20.46345	✓ 11.64474	✗ 116.9474
12th	! 39.37151	! 39.15507	! 39.09178	✓ 35.58959	! 37.44356	✗ 77.47753	✗ 83.44411

Table 6.16: Mainline Outlet (P_3) Relative Errors (%) for Complex Experiment, Close Ended

Peak Number	Urbanowicz	Kagawa	Vitkovsky	Vardy & Brown	Schohl	Trikha	Constant VD
1st	8.01942	8.38835	8.38835	23.45631	12.48544	37.5	17.15
2nd	42.54032	42.06989	42.00269	44.48925	36.55914	44.62	88.98
3rd	27.74049	27.51678	27.51678	28.18792	23.71365	28.86	67.79
4th	109.9432	109.772	109.6663	105.9878	107.3856	116.1	253.8
5th	72.41429	72.43543	72.45086	72.74343	72.10933	70.35	48.22
6th	45.2739	45.23559	45.28441	44.62203	43.49085	36.2	18.56
7th	23.84811	23.79481	23.86274	22.94104	21.36698	11.22	64.98
8th	45.58442	45.84416	45.77922	49.87013	51.55844	79.22	241.6
9th	31.86551	31.7462	31.77874	29.14317	29.06725	12.36	69.09
10th	75.66887	75.60934	75.6196	74.39073	74.67742	66.91	35.48
11th	12.66319	12.99681	12.89739	19.28406	16.96203	60.17	214.9
12th	10.61789	11.03711	10.86605	17.51947	14.44605	64.31	225.7

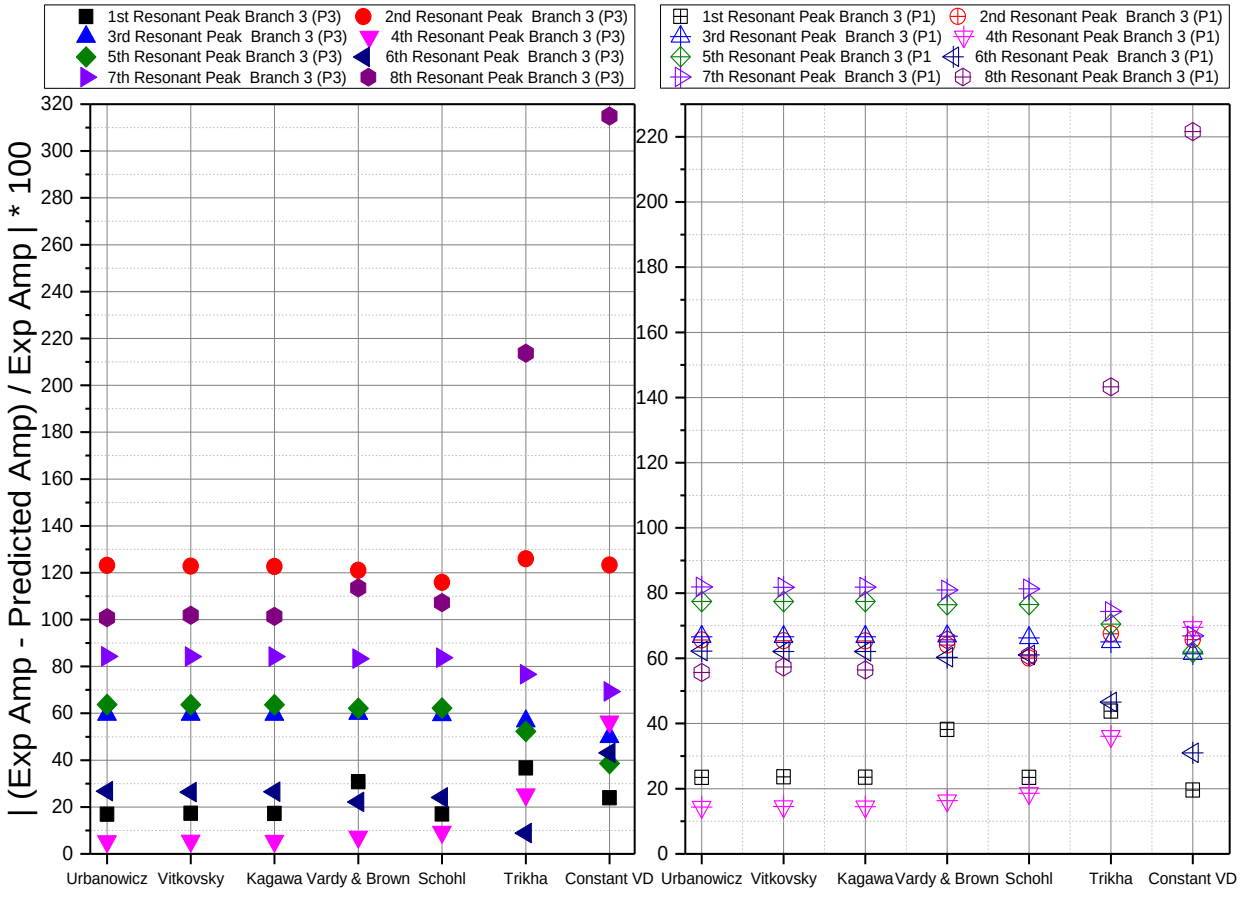

Figure 6.71: Resonant Amplitude Prediction Relative Errors for Branch 3

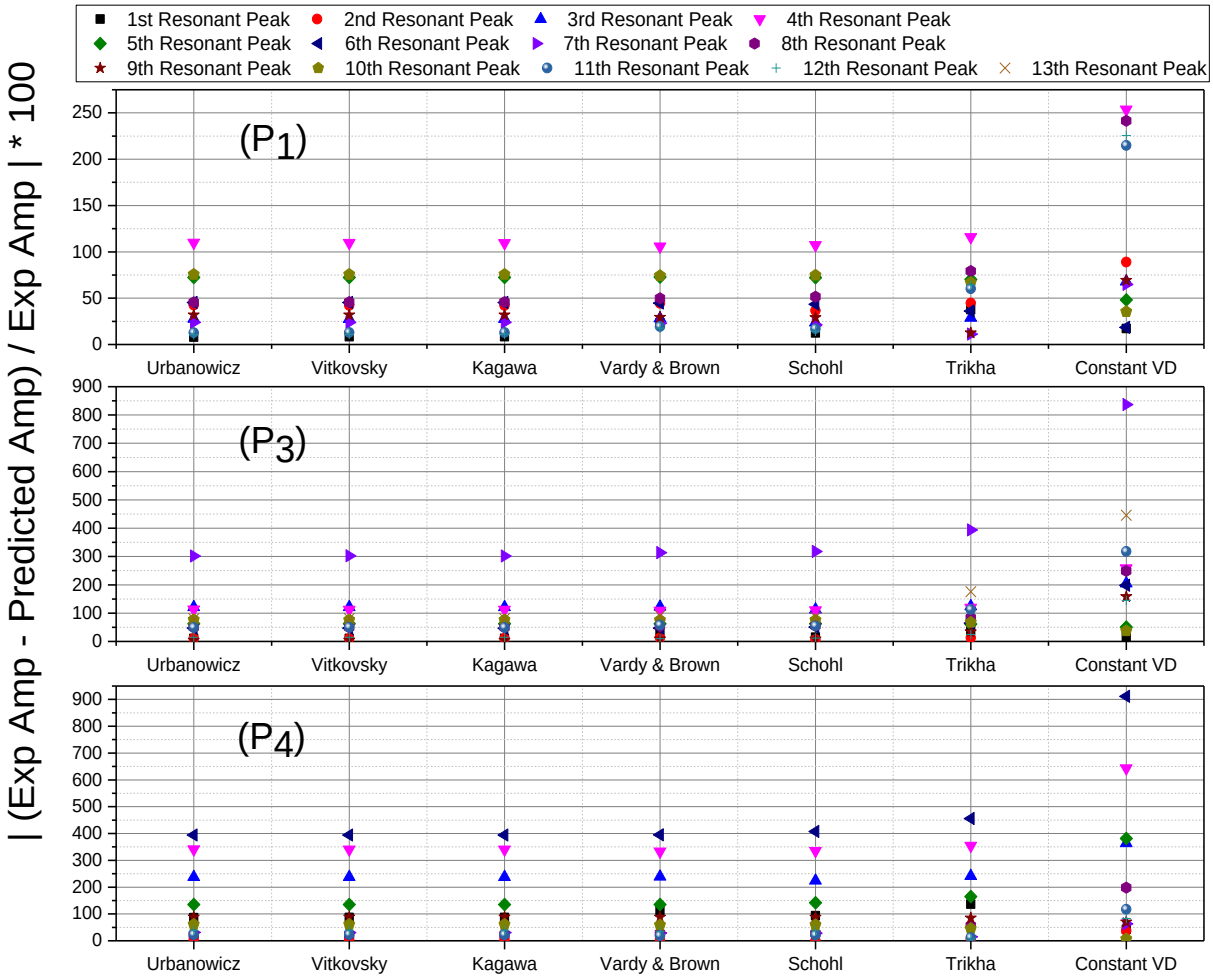

Figure 6.72: Resonant Amplitude Prediction Relative Errors for Complex Experiment

Figure 6.72 and Tables 6.14-6.16 also show that for the Complex Experiment at P_4, all the assessed frequency-dependent damping methodologies except the damping method of Trikha (1975) give the acceptable amount of relative errors for the 2nd, 7th, 8th, and 11th resonant peaks. For the same location, using the constant VD only predicts the 10th resonant peak with less than 10% relative error, which shows that there is no specific frequency range that proves that all the resonant peaks are well predicted. At P_1, the same damping methods predict the 1st, 2nd, 9th and 10th resonant peaks with less than 15% relative errors. For the mainline outlet (P_3), the 1st, 3rd, 7th, 9th, 11th, and 12th resonant peaks are predicted with less than 30% of the relative errors using

UVK, Schohl (1993) and Vardy and Brown (2004). The numbers of peaks predicted with less than 30% of the relative errors for the mainline are higher than the 2.07 m and the Al side branches. The predictions show that only some of the resonant peaks with the acceptable values of relative errors are common among all the three assessed locations of the Complex Experiment.

Figures 6.40-6.42 also represent the fact that for frequencies higher than 250 Hz, the thicknesses of the predicted resonant peaks are less than the measurements. It implies that the complex configuration same as the Branch 3 configuration influences the higher frequency resonant peak thicknesses, which are not captured by the assessed methodologies.

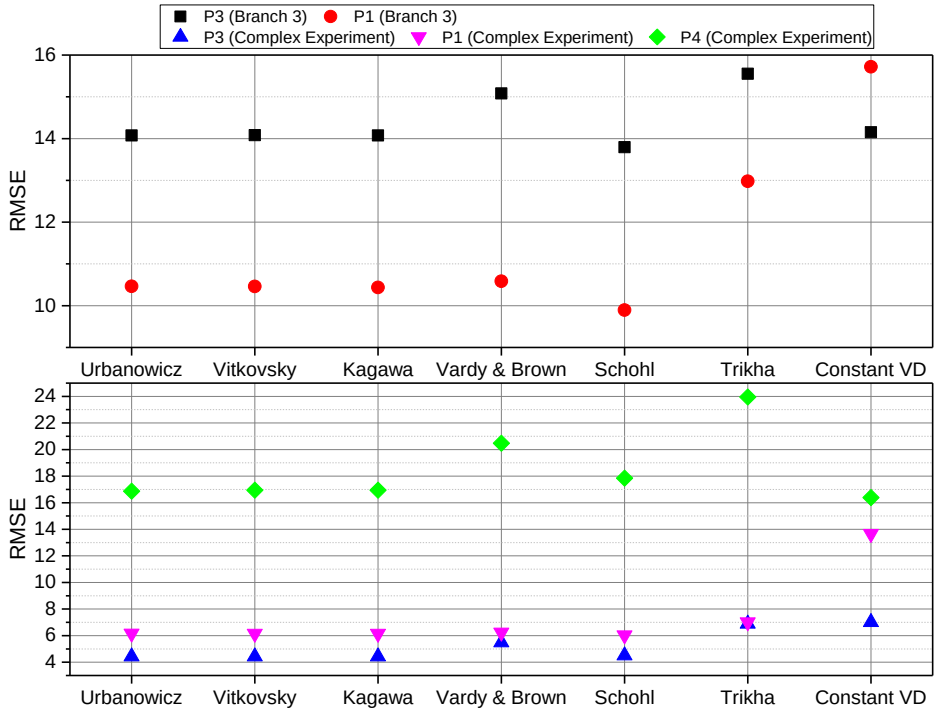

Figure 6.73: RMSE values of Resonant Amplitude Predictions

Figure 6.73 shows that for Branch 3 at the mainline outlet, the resonant amplitude RMSE values obtained by the assessed frequency-dependent methods are higher than the branch. The lowest RMSE value is obtained using the Schohl (1993) damping methodology. It indicates that

the resonant amplitudes of the branch are better predicted than the mainline outlet. The better predictions for the branch can be attributed to the fact that at the two consecutive junctions, the traveling acoustic waves interact with each other and then hit the closed end of the mainline outlet. The constant VD RMSE value for the branch is less than the mainline and its value is almost the same as the values of the UVK methodologies, which means that the constant VD method cannot predict the resonant amplitudes better than the other assessed frequency-dependent methods.

For the Complex Experiment, the RMSE values obtained for all the assessed damping methods are less than Branch 3 at the mainline and 2.07 m branch. The RMSE values of the Al branch are almost three times bigger than the other two locations. The reason for this can be explained by the fact that the lowest sonic velocity of the Al tube interacts with the highest sonic velocity of the thicker SS tube at the T-junction of the Al tube. Also, the traveling acoustic waves from the other two junctions meet each other at the Al T-junction, and these interactions are not well captured by the assessed methods. The damping methodologies of the UVK give the lowest RMSE values for all the three assessed locations. The RMSE value of the Al branch obtained with the constant VD method, same as the assessed frequency-dependent damping methodologies is higher than the 2.07 m branch and the mainline values. The constant VD resonant amplitude RMSE value of the branch closed to the inlet is almost three times bigger than the UVK damping methodologies. These values indicate better resonant amplitude predictions with UVK methods over the constant VD.

Figure 6.74 displays the ABAQUS acoustic resonance simulation for Combined Experiment. Standing waves and their interactions are visible.

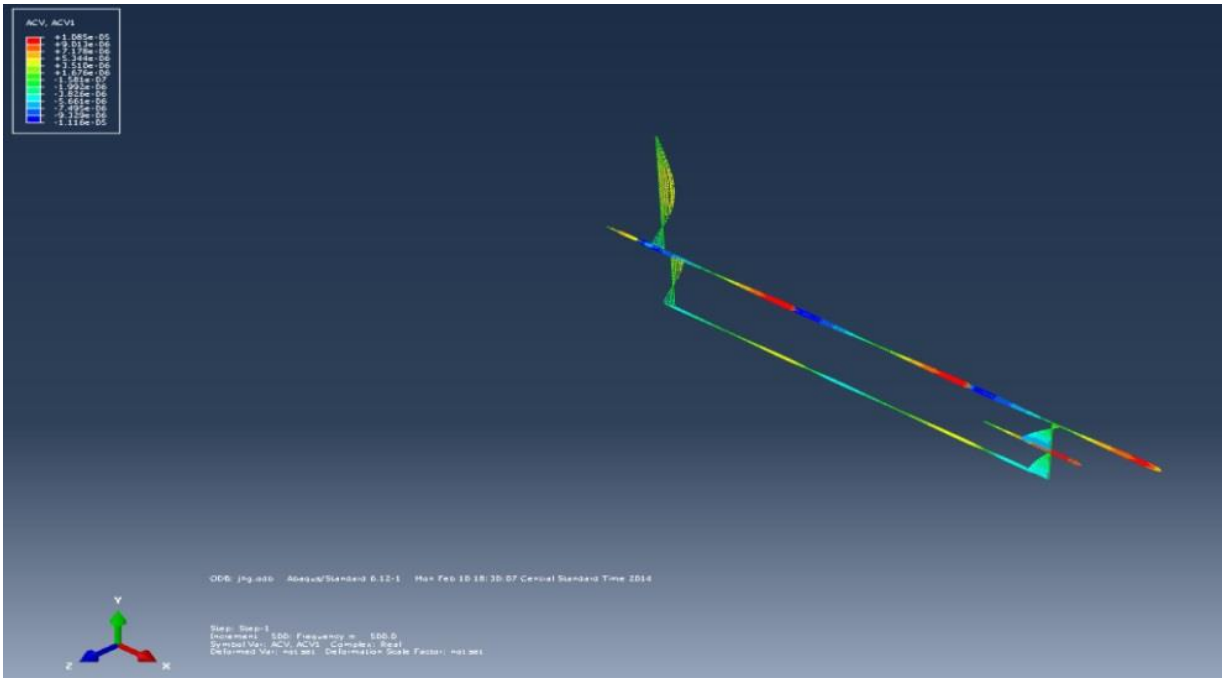

Figure 6.74: ABAQUS Wave Propagation Simulation

6.2.4.1.5 Open-Ended Branch 3 (Zero and Laminar Mean Flows)

The amplitude relative errors for all the assessed methodologies are tabulated in Tables 6.17 and 6.18 for P_1, Tables 6.19 and 6.20 for P_2 and Tables 6.21 and 6.22 for P_3. From the amplitude prediction relative errors for zero mean flow given in Figure 6.75 and Tables 6.17-6.22, at P_2, the constant VD predicts only the 2nd and 5th resonant peaks with acceptable values of relative errors. At P_3, the first two resonant peaks, and at P_1, the first three resonant peaks are predicted with less than 30% relative errors. The predictions for the longer branch show lower values of the relative errors in comparison to the shorter one. Also, lower values of relative errors are given for the open-ended mainline. The prediction relative errors indicate that the constant VD only predicts the 2nd resonant peaks of all three locations well. The maximum relative error for the higher

resonant peaks is obtained for the 6th peak at about 600%. For all locations (P_1, P_2, and P_3) the highest relative error values are given at the frequency range of 200–480 Hz.

Table 6.17 : Branch 2.07 m (P_1) Relative errors (%) for zero flow

Peak Number	Urbanowicz	Kagawa	Vitkovsky	Vardy & Brown	Schohl	Trikha	Constant VD
1st	✓ 36.10	✓ 35.74	✓ 35.63	! 41.35	✓ 30.54	! 41.40	✓ 13.27
2nd	✓ 0.47	✓ 0.02	✓ 0.14	✓ 1.15	✓ 1.84	✓ 2.24	✓ 6.04
3rd	✓ 14.66	✓ 14.68	✓ 14.72	✓ 15.22	✓ 13.20	✓ 7.14	✓ 8.86
4th	✗ 106.22	✗ 106.52	✗ 106.41	✗ 110.07	✗ 114.25	✗ 146.52	✗ 208.34
5th	✗ 50.10	✗ 50.37	✗ 50.37	✗ 56.48	✗ 56.58	✗ 95.55	✗ 150.95
6th	✗ 256.63	✗ 258.70	✗ 258.25	✗ 279.34	✗ 268.53	✗ 452.19	✗ 630.11
7th	! 45.23	! 46.16	! 45.87	✗ 53.70	! 49.37	✗ 129.68	✗ 202.57

Table 6.18: Branch 2.07 m (P_1) Relative errors (%) for Laminar flow

Peak Number	Urbanowicz	Kagawa	Vitkovsky	Vardy & Brown	Schohl	Trikha	Constant VD
1st	✓ 34.24	✓ 33.89	✓ 33.78	! 39.42	✓ 28.76	! 39.48	✓ 11.73
2nd	✓ 1.13	✓ 0.63	✓ 0.51	✓ 0.51	✓ 1.20	✓ 2.91	✓ 6.73
3rd	✓ 12.10	✓ 12.12	✓ 12.16	✓ 12.68	✓ 10.59	✓ 4.35	✓ 12.13
4th	✗ 101.16	✗ 101.46	✗ 101.36	✗ 104.93	✗ 109.00	✗ 140.48	✗ 200.78
5th	✓ 19.08	✓ 19.29	✓ 19.29	✓ 24.14	✓ 24.21	✗ 55.13	✗ 99.07
6th	✗ 240.89	✗ 242.87	✗ 242.43	✗ 262.59	✗ 252.26	✗ 427.81	✗ 597.88
7th	✓ 1.92	✓ 2.57	✓ 2.37	✓ 7.86	✓ 4.83	✗ 61.19	✗ 112.34

As Figure 6.75 shows, although for the laminar flow case the constant VD resonant amplitude relative errors trends for all the three locations are same as the zero mean flow, the magnitudes of the minimum and the maximum relative errors are different. At P_1 and P_2, the relative errors of the last three peaks decrease from zero to laminar flow, but the minimum value of the relative errors is still about 45%. It seems that from zero mean flow to laminar flow, the resonant amplitude predictions with the acceptable magnitude of the relative errors are the same. Therefore, for the unequal branches with the open-ended mainline outlet, the constant VD method is not recommended for an accurate resonant amplitude prediction.

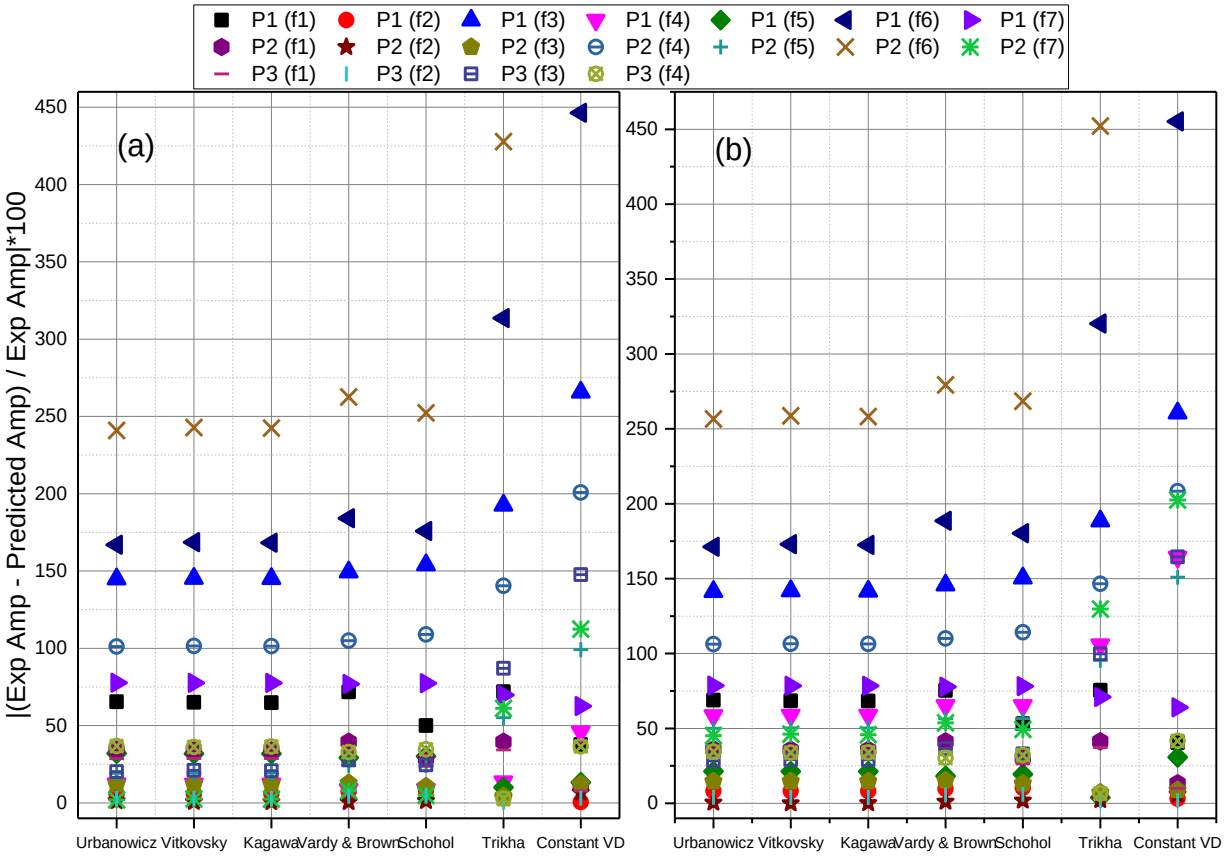

Figure 6.75: Resonant Amplitude Prediction Relative Errors a) Zero & b) Laminar Mean Flows

For zero mean flow, the first three resonant peaks at P_1 are predicted with less than 36% relative errors using the damping methodologies of UVK and Schohl (1993). This trend is also obtained with the constant VD method. For the following resonant peaks, the magnitudes of the relative errors are decreased with frequency-dependent damping methodologies, compared to the constant VD method. The magnitudes of the relative errors decrease to 50% and 45% for the 5th and the last resonant peaks, but they are still not deemed acceptable. For the laminar mean flow case, the relative error magnitudes at the 5th and the last resonant peaks decrease to less than 20% relative errors. It shows that for the laminar flow at P_1, using the damping methodologies of UVK and Schohl (1993) accurately predicts some resonant peaks at the higher frequencies. It

indicates an improvement for resonant amplitude prediction using frequency-dependent methods compared to the constant VD method. The better predictions for the 5th and the last resonant peaks of the laminar flow over the zero mean flow are attributed to the fact that the resonant amplitudes are over predicted with the assessed damping methods. Therefore, for the laminar flow case measured with the higher magnitude, the resonant amplitude peak is well predicted.

At P2, same as the constant VD method, only the 2nd and 5th resonant peaks of the zero mean flow case are predicted with less than 30% relative errors using the assessed frequency-dependent damping methodologies. For laminar flow, using the frequency-dependent damping methods improves the predictions for the 4th resonant peak to an acceptable value of relative error.

Table 6.19: Branch 1 m (P_2) Relative Errors (%) for Zero Flow

Peak Number	Urbanowicz	Schohl	Vitkovsky	Kagawa	Vardy & Brown	Trikha	Constant VD
1st	✗ 68.89	✗ 68.44	✗ 68.31	✗ 75.41	✗ 53.19	✗ 75.47	! 40.56
2nd	✓ 8.14	✓ 8.19	✓ 8.19	✓ 9.62	✓ 10.26	✓ 6.53	✓ 3.12
3rd	✗ 141.37	✗ 141.77	✗ 141.58	✗ 145.78	✗ 150.31	✗ 188.44	✗ 260.54
4th	✗ 58.66	✗ 58.89	✗ 58.89	✗ 65.30	✗ 65.37	✗ 105.94	✗ 164.40
5th	✓ 21.45	✓ 21.23	✓ 21.27	✓ 18.16	✓ 19.38	✓ 3.94	✓ 30.74
6th	✗ 171.26	✗ 172.93	✗ 172.52	✗ 188.65	✗ 180.25	✗ 320.25	✗ 455.21
7th	✗ 78.54	✗ 78.45	✗ 78.48	✗ 77.80	✗ 78.18	✗ 70.94	✗ 63.97

Table 6.20: Branch 1 m (P_2) Relative Errors (%) for Laminar Flow

Peak Number	Urbanowicz	Schohl	Vitkovsky	Kagawa	Vardy & Brown	Trikha	Constant VD
1st	✗ 65.43	✗ 64.99	✗ 64.86	✗ 71.81	✗ 50.05	✗ 71.88	! 37.68
2nd	✓ 5.68	✓ 5.73	✓ 5.73	✓ 7.19	✓ 7.85	✓ 4.02	✓ 0.52
3rd	✗ 144.80	✗ 145.21	✗ 145.01	✗ 149.27	✗ 153.87	✗ 192.53	✗ 265.66
4th	✓ 12.43	✓ 12.30	✓ 12.30	✓ 8.76	✓ 8.72	✓ 13.67	! 45.94
5th	✓ 31.96	✓ 31.78	✓ 31.82	✓ 29.12	✓ 30.17	✓ 9.98	✓ 13.24
6th	✗ 166.96	✗ 168.61	✗ 168.20	✗ 184.07	✗ 175.81	✗ 313.59	✗ 446.41
7th	✗ 77.67	✗ 77.59	✗ 77.61	✗ 76.91	✗ 77.30	✗ 69.77	✗ 62.52

At P_3, all four resonant peaks are predicted with relative errors less than 35% for both zero and laminar mean flows. It indicates the assessed frequency-dependent damping methods well predict the mainline outlet resonant amplitudes. For the same location and zero mean flow, constant VD prediction relative error for the last two peaks are obtained at about 164% and 41%.

Table 6.21: Mainline (P_3) Relative Errors (%) for Zero Flow

Peak Number	Urbanowicz	Schohl	Vitkovsky	Kagawa	Vardy & Brown	Trikha	Constant VD
1st	✓ 31.43	✓ 31.59	✓ 31.50	✓ 36.59	✓ 26.38	! 37.24	✓ 10.08
2nd	✓ 4.06	✓ 3.95	✓ 3.97	✓ 5.58	✓ 5.97	✓ 1.72	✓ 1.74
3rd	✓ 28.34	✓ 29.21	✓ 29.05	✓ 36.47	✓ 32.99	✗ 99.82	✗ 164.51
4th	✓ 34.40	✓ 33.84	✓ 33.98	✓ 30.29	✓ 32.19	✓ 6.54	! 41.61

Table 6.22: Mainline (P_3) Relative Errors (%) for Laminar Flow

Peak Number	Urbanowicz	Schohl	Vitkovsky	Kagawa	Vardy & Brown	Trikha	Constant VD
1st	✓ 28.59	✓ 28.75	✓ 28.66	✓ 33.64	✓ 23.65	✓ 34.28	✓ 7.70
2nd	✓ 2.81	✓ 2.70	✓ 2.73	✓ 4.35	✓ 4.74	✓ 0.44	✓ 3.06
3rd	✓ 20.14	✓ 20.96	✓ 20.82	✓ 27.76	✓ 24.50	✗ 87.06	✗ 147.63
4th	✓ 36.75	✓ 36.21	✓ 36.34	✓ 32.79	✓ 34.63	✓ 2.72	✓ 36.53

The predictions with the Trikha (1975) method give the highest values of relative errors among all the tested frequency-dependent damping methods. From constant VD, to the assessed frequency-dependent damping methods, the resonant amplitude predictions improve, but there is no frequency-dependent damping methodology that is able to predict the resonant amplitudes at all three locations accurately.

Figure 6.76 shows that at the P_3 the lowest RMSE value is obtained with UVK and Schohl (1993) damping methodologies. The constant VD RMSE value for the mainline is almost the same as the frequency-dependent damping methodologies' values. At P_1 and P_2, UVK and Schohl (1993) damping methodologies again show the lowest values of RMSE. The RMSE

values at P_1 for Branch 3 with close-ended mainline outlet are almost 30% higher than the open-ended case. It indicates better resonant amplitude predictions with the assessed damping methods for the open-ended case. The longer branch RMSE values are less than the shorter ones, but are considerably higher than mainline RMSE values. It indicates that the resonant amplitudes of the mainline are better predicted than that of the branches. The better predictions for the mainline can be attributed to the fact that the mainline outlet is open to the tank, and there is a long distance from the two consecutive junctions, with complex acoustic wave interactions, to the mainline line outlet.

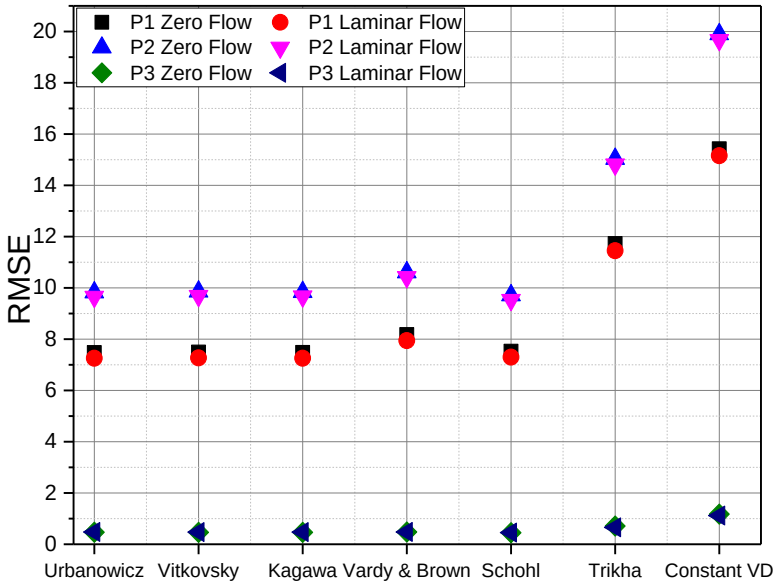

Figure 6.76: RMSE Values for Resonant Amplitude Predictions

6.2.4.1.6 Open-Ended Branch 3 (Turbulent Mean Flow)

The resonant amplitude relative errors for all the assessed methodologies are tabulated in Tables 6.23 and 6.24 for P_1, Tables 6.25 and 6.26 for P_2 and Tables 27 and 28 for P_3. Figure 6.77 shows

the resonant amplitude predictions relative errors at P_1, P_2 and P_3 for the two turbulent mean flow cases. The relative errors obtained using the constant VD method show that at P_1, except the 4th and 6th resonant peaks with the relative errors of more than 100%, the other peaks are predicted with less than 30% relative errors.

Table 6.23: Branch 2.07 m (P_1) Relative Errors (%) for Turbulent flow (Re = 8450)

Peak Number	Urbanowicz	Kagawa	Vitkovsky	Vardy & Brown	Schohl	Trikha	Constant VD
1st	✓ 25.81	✓ 25.47	✓ 25.37	✓ 30.66	✓ 20.67	✓ 30.71	✓ 4.71
2nd	✓ 4.86	✓ 5.33	✓ 5.43	✓ 6.39	✓ 7.05	✓ 3.18	✓ 0.41
3rd	✓ 22.01	✓ 22.03	✓ 22.06	✓ 22.52	✓ 20.67	✓ 15.13	✓ 0.51
4th	! 37.04	! 37.25	! 37.17	! 39.60	! 42.38	✗ 63.83	✗ 104.91
5th	✓ 24.15	✓ 24.01	✓ 24.01	✓ 20.92	✓ 20.87	✓ 1.18	✓ 26.81
6th	✗ 115.43	✗ 116.68	✗ 116.41	✗ 129.15	✗ 122.62	✗ 233.56	✗ 341.04
7th	! 48.03	! 47.70	! 47.80	! 45.00	! 46.55	✓ 17.81	✓ 8.28

Table 6.24: Branch 2.07 m (P_1) Relative Errors (%) for turbulent flow (Re = 20754)

Peak Number	Urbanowicz	Kagawa	Vitkovsky	Vardy & Brown	Schohl	Trikha	Constant VD
1st	✓ 19.01	✓ 18.69	✓ 18.59	✓ 23.60	✓ 14.14	✓ 23.64	✓ 0.95
2nd	✓ 6.48	✓ 6.94	✓ 7.05	✓ 7.99	✓ 8.63	✓ 4.83	✓ 1.30
3rd	✓ 25.52	✓ 25.54	✓ 25.57	✓ 26.01	✓ 24.24	✓ 18.95	✓ 4.99
4th	✓ 33.23	✓ 33.43	✓ 33.36	✓ 35.72	! 38.42	✗ 59.27	✗ 99.21
5th	✓ 35.02	✓ 34.90	✓ 34.90	✓ 32.25	✓ 32.21	✓ 15.34	✓ 8.64
6th	! 39.92	! 40.73	! 40.55	! 48.83	! 44.59	✗ 116.64	✗ 186.45
7th	✗ 66.28	✗ 66.07	✗ 66.13	✗ 64.32	✗ 65.32	! 46.67	✓ 29.75

At P_2, only the 1st, 2nd, 4th and 5th resonant peaks are predicted with less than 30% relative errors. The resonant amplitude predictions at P_3 show relative errors of less than 30% at the first three resonant peaks. It shows that the resonant amplitude prediction relative errors decrease from zero to turbulent mean flows. Those improvements in resonant amplitude prediction using constant VD are likely due to the fact that constant VD value employed in the current study was obtained from the turbulent flow experimental results. Indeed, the constant VD for different Re

values might report dissimilar magnitudes of relative errors. For instance, the 6th resonant peak at P_3 is only well predicted for the lower Re case.

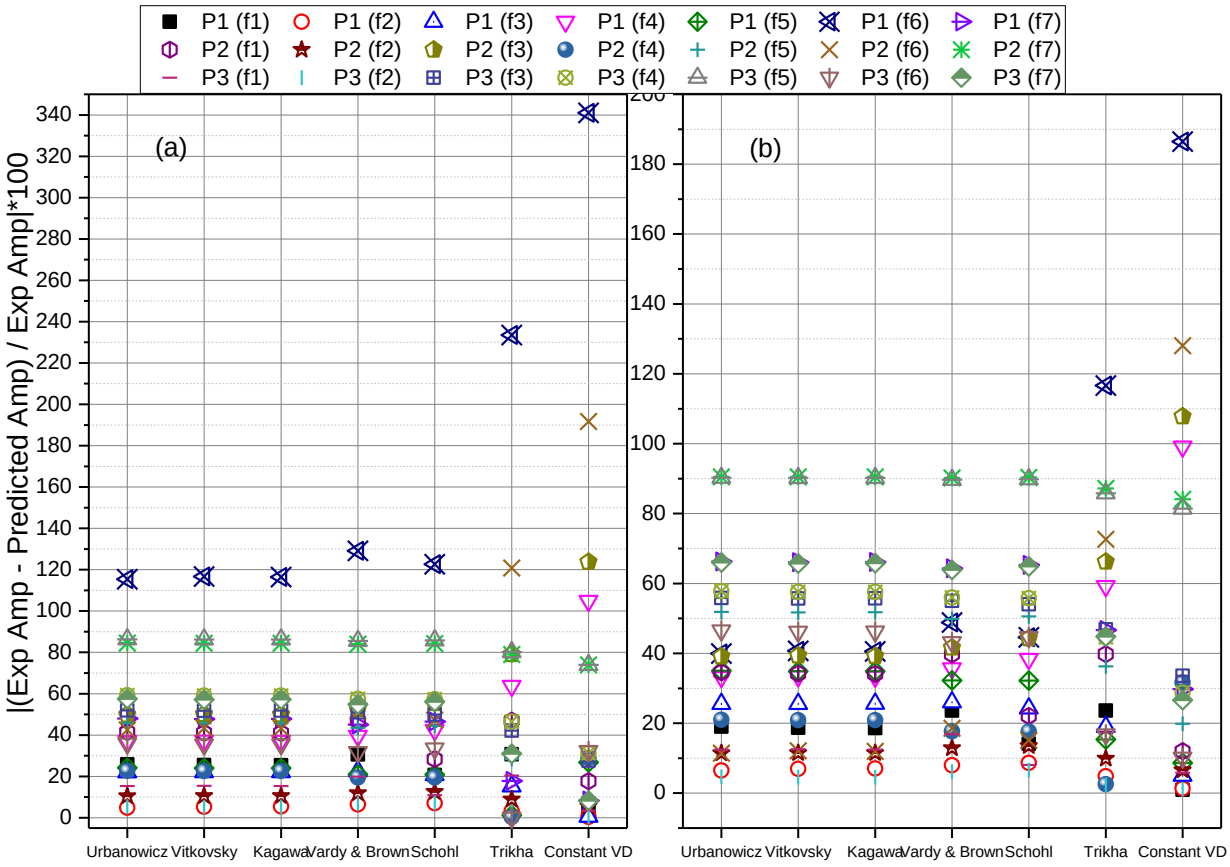

Figure 6.77: Resonant Amplitude Prediction Relative Errors a) Re =8450 & b) Re=20745

At P_1, using the UKV damping methodologies shows that the first five resonant peaks are predicted with less than 37% relative errors. Using UVK damping methodologies, compared to constant VD method, improves the resonant amplitude predictions at the 4th resonant peak to being less than 37% relative errors. It is an improvement over the constant VD method and indicates at P_1 for less than 300 Hz the resonant amplitude peaks are well predicted. At P_2, only the 2nd and 4th resonant peaks for Re = 8450, and the 1st, 2nd, 4th and 6th resonant peaks for Re =

20754, are properly predicted with the frequency-dependent damping methodologies. Although there are some peaks for less than 350 Hz that are not well predicted, the relative errors of those peaks are less than 50%. The resonant amplitude predictions at P_3 show that only the first two and the 6th resonant peaks are predicted with less than 35% relative errors. The relative errors indicate that at P_1 and P_2, a higher number of resonant peaks with the acceptable value of the relative errors are predicted the frequency-dependent damping methodologies.

Table 6.25: Branch 1 m (P_2) Relative Errors (%) for Turbulent Flow (Re = 8450)

Peak Number	Urbanowicz	Kagawa	Vitkovsky	Vardy & Brown	Schohl	Trikha	Constant VD
1st	! 41.46	! 41.09	! 40.97	! 46.92	✓ 28.32	! 46.98	✓ 17.74
2nd	✓ 10.48	✓ 10.53	✓ 10.53	✓ 11.92	✓ 12.54	✓ 8.90	✓ 5.58
3rd	! 49.83	✗ 50.08	! 49.96	✗ 52.57	✗ 55.38	✗ 79.04	✗ 123.80
4th	✓ 22.69	✓ 22.58	✓ 22.58	✓ 19.46	✓ 19.42	✓ 0.34	✓ 28.83
5th	! 45.85	! 45.70	! 45.73	! 43.59	! 44.42	✓ 28.35	✓ 9.87
6th	! 42.51	! 43.39	! 43.17	✗ 51.65	! 47.24	✗ 120.78	✗ 191.69
7th	✗ 84.47	✗ 84.41	✗ 84.43	✗ 83.94	✗ 84.21	✗ 78.98	✗ 73.93

Table 6.26: Branch 1 m (P_2) Relative Errors (%) for Turbulent Flow (Re = 20754)

Peak Number	Urbanowicz	Kagawa	Vitkovsky	Vardy & Brown	Schohl	Trikha	Constant VD
1st	✓ 34.56	✓ 34.21	✓ 34.10	! 39.76	✓ 22.06	! 39.81	✓ 11.99
2nd	✓ 11.44	✓ 11.50	✓ 11.49	✓ 12.87	✓ 13.48	✓ 9.89	✓ 6.60
3rd	! 39.13	! 39.36	! 39.25	! 41.67	! 44.28	✗ 66.25	✗ 107.82
4th	✓ 21.00	✓ 20.88	✓ 20.89	✓ 17.69	✓ 17.66	✓ 2.54	✓ 31.65
5th	✗ 51.85	✗ 51.72	✗ 51.75	! 49.84	✗ 50.59	✓ 36.30	✓ 19.87
6th	✓ 11.42	✓ 12.10	✓ 11.93	✓ 18.56	✓ 15.11	✗ 72.61	✗ 128.05
7th	✗ 90.53	✗ 90.49	✗ 90.50	✗ 90.20	✗ 90.37	✗ 87.18	✗ 84.10

Table 6.27: Mainline (P_3) Relative Errors (%) for Turbulent Flow (Re = 8450)

Peak Number	Urbanowicz	Kagawa	Vitkovsky	Vardy & Brown	Schohl	Trikha	Constant VD
1st	✓ 15.32	✓ 15.46	✓ 15.38	✓ 19.85	✓ 10.89	✓ 20.42	✓ 3.41
2nd	✓ 5.27	✓ 5.17	✓ 5.19	✓ 6.77	✓ 7.16	✓ 2.96	✓ 0.45
3rd	✗ 51.91	✗ 51.75	✗ 51.80	✗ 51.00	! 49.96	! 42.12	✓ 27.63
4th	✗ 59.26	✗ 59.08	✗ 59.10	✗ 57.51	✗ 57.35	! 46.53	! 41.12
5th	✗ 86.33	✗ 86.25	✗ 86.27	✗ 85.50	✗ 85.77	✗ 80.10	✗ 73.90
6th	✓ 35.83	✓ 35.40	✓ 35.47	✓ 31.77	✓ 33.50	✓ 30.21	✓ 36.04
7th	✗ 57.52	✗ 57.15	✗ 57.24	✗ 54.86	✗ 56.09	! 48.58	✗ 51.95

Table 6.28: Mainline (P_3) Relative Errors (%) for Turbulent Flow (Re = 20754)

Peak Number	Urbanowicz	Kagawa	Vitkovsky	Vardy & Brown	Schohl	Trikha	Constant VD
1st	✓ 12.42	✓ 12.56	✓ 12.48	✓ 16.83	✓ 8.10	✓ 17.39	✓ 5.84
2nd	✓ 4.67	✓ 4.56	✓ 4.58	✓ 6.18	✓ 6.56	✓ 2.34	✓ 1.09
3rd	✗ 55.86	✗ 55.71	✗ 55.75	✗ 55.03	✗ 54.06	! 46.87	✓ 33.57
4th	✗ 57.80	✗ 57.61	✗ 57.63	✗ 55.98	✗ 55.82	! 44.61	! 40.55
5th	✗ 90.26	✗ 90.20	✗ 90.21	✗ 89.67	✗ 89.86	✗ 85.81	✗ 81.39
6th	! 46.56	! 46.20	! 46.26	! 43.17	! 44.62	! 40.82	✗ 51.15
7th	✗ 66.01	✗ 65.72	✗ 65.79	✗ 63.89	✗ 64.87	✗ 51.59	✗ 50.73

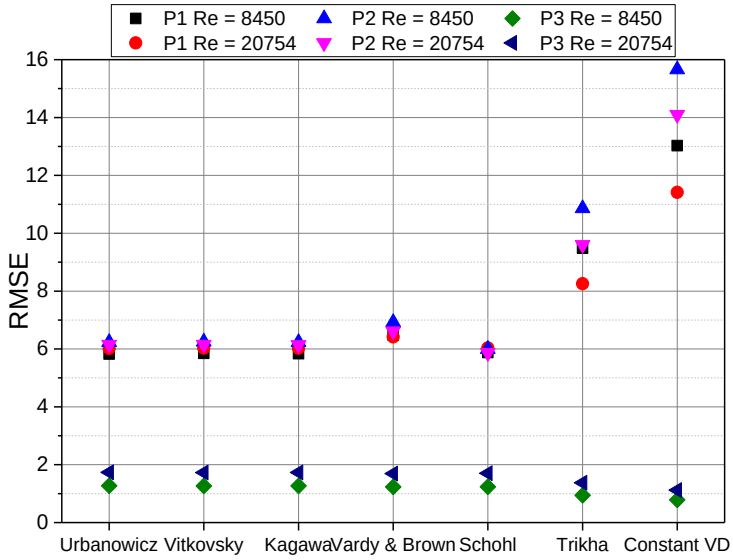

Figure 6.78: RMSE Values for Resonant Amplitude Predictions

Figure 6.78 shows that, same as the zero and laminar mean flows, the resonant amplitude RMSE values of the mainline outlets for the turbulent flows are less than that of the branches. The lowest RMSE values for the mainline outlets are obtained with constant VD and Trikha (1975) damping methodologies. The constant VD RMSE values for the mainline are almost 60% less than the highest RMSE value obtained with the frequency-dependent damping methodologies. At P_1 and P_2, the UVK and Schohl (1993) damping methodologies show the lowest magnitudes of the RMSE. The RMSE values at P_2 for the turbulent mean flows are almost

60% lower than zero and laminar mean flows. It represents better resonant amplitude predictions, with the assessed damping methods for the turbulent flow cases at P_1 and P_2. The RMSE values at the branches are very close together.

It is perceived that the resonant amplitude are changed from zero to turbulent flows. It is, however, difficult to decompose the amplified acoustic pressure into flowing fluid created eddies and explicit exciter, e.g., cylinder, due to the fact that the growth of the standing waves is based on the mix of flowing fluid created vortices and exciter frequency. These cases are investigated to have an overview that would allow a straightforward estimate of the important frequency ranges that the acoustic resonances are influenced by the flowing fluid created eddies; then, the prediction methods' accuracies are measured. The accurate realization of resonant peak amplitudes has been the criterion for identification of resonant frequencies. Based on the above discussion, the LWS using the assessed damping methods cannot always predict the acoustic resonances well.

6.2.4.1.7 Open-Ended Complex Experiment 2 (Zero and Laminar Mean Flows)

The resonant amplitude relative errors for all the assessed methodologies are tabulated in Tables 6.29 and 6.30 for P_1 and P_3, respectively. As the Figure 6.79 and Table 6.29 show, at P_1, the constant VD method only predicts the 1st resonant peak with 50% of relative error for the Complex Experiment 2 configuration. The other resonant peaks are predicted with relative errors of minimum 698%. At P_3, the 1st resonant peak is also predicted with 50% of relative error and the other peaks show a minimum 655% relative error. The resonant amplitude predictions for P_3 are better than P_1, but they are not considered acceptable. For the Complex Experiment 2

configuration with the open-ended outlet boundary condition, the predictions show higher values of relative errors compared to the mainline outlet of the Complex Experiment with close-ended boundary condition. The prediction relative errors indicate that the constant VD does not predict the resonant amplitudes for such a complex geometry well.

Table 6.29: Branch 2.07 m (P_1) Relative Errors (%) for Zero Flow, Complex Experiment 2

Peak Number	Urbanowicz	Kagawa	Vitkovsky	Vardy & Brown	Schohl	Trikha	Constant VD
1st	! 39.35096	! 38.62635	! 38.74548	✗ 51.63313	✓ 36.4999	✗ 52.66986	✗ 51.6024
2nd	✓ 21.18114	✓ 20.96648	✓ 20.92182	✓ 22.44659	✓ 16.00773	✓ 22.87943	✗ 68.05307
3rd	✗ 102.8607	✗ 102.6486	✗ 102.3029	✗ 99.63353	✗ 98.5159	✗ 105.987	✗ 227.1032
4th	✗ 67.8108	✗ 67.91533	✗ 68.75923	✗ 66.06829	✗ 68.91672	✗ 80.37247	✗ 220.1547
5th	✗ 69.95372	✗ 70.17025	✗ 70.12727	✗ 69.43099	✗ 72.67686	✗ 86.83306	✗ 237.9079
6th	✗ 104.1422	✗ 104.4072	✗ 102.9972	✗ 108.6369	✗ 111.7811	✗ 145.8224	✗ 375.3176
7th	✓ 12.20632	✓ 12.39684	✓ 12.34763	✓ 15.97923	✓ 17.56163	! 40.96027	✗ 177.121
8th	✗ 110.9182	✗ 111.2992	✗ 112.2355	✗ 120.0028	✗ 119.8571	✗ 174.653	✗ 443.1642
9th	✗ 129.8742	✗ 130.378	✗ 130.6423	✗ 141.3824	✗ 138.4835	✗ 213.3099	✗ 513.2412
10th	✓ 14.73654	✓ 15.11786	✓ 14.69986	✓ 21.46978	✓ 19.37898	✗ 64.10728	✗ 228.98
11th	✗ 73.02836	✗ 165.5632	✗ 168.2512	✗ 180.5667	✗ 173.0005	✗ 296.1134	✗ 698.9274
12th	✓ 16.25338	✓ 16.85304	✓ 16.89063	✓ 23.62762	✓ 19.92998	! 43.2924	✗ 268.0258

Table 6.30: Mainline (P_3) Relative Errors (%) for Zero Flow, Complex Experiment 2

Peak Number	Urbanowicz	Kagawa	Vitkovsky	Vardy & Brown	Schohl	Trikha	Constant VD
1st	! 38.44189	! 37.96	! 38.08899	✗ 50.58272	✓ 35.54107	✗ 51.92509	✗ 50.87503
2nd	✗ 77.94135	✗ 74.97594	✗ 77.57611	✗ 74.97594	✗ 73.6959	✗ 80.28289	✗ 187.6412
3rd	✗ 170.2426	✗ 170.0534	✗ 168.6418	✗ 168.8769	✗ 175.9379	✗ 198.4267	✗ 447.4904
4th	✗ 118.6407	✗ 118.9472	✗ 117.1028	✗ 123.5607	✗ 126.7708	✗ 163.3352	✗ 409.5042
5th	✓ 17.79429	✓ 17.62381	✓ 17.59762	✓ 15.04381	✓ 14.02095	✓ 2.59524	✗ 99.81762
6th	✓ 8.11855	✓ 8.46244	✓ 8.16059	✓ 14.65023	✓ 13.43663	✗ 55.44529	✗ 213.5737
7th	✗ 148.5736	✗ 149.6222	✗ 152.1479	✗ 163.8931	✗ 156.634	✗ 273.7049	✗ 655.4979
8th	✓ 7.83111	✓ 8.37836	✓ 8.33103	✓ 14.63291	✓ 11.28369	✗ 67.42215	✗ 241.0826

The 2^{nd}, 7^{th}, 10^{th}, and 12^{th} resonant peaks at P_1 are predicted with less than 23% relative errors using the damping methodologies of UVK and Schohl (1993). The same resonant peaks are poorly predicted using the constant VD method. The magnitudes of the relative error is about

39% for the 1st resonant peak, and they is not considered acceptable. For the other resonant peaks, the magnitudes of the relative errors are increased to a maximum of 180%, but they are still much less than the constant VD relative error magnitudes.

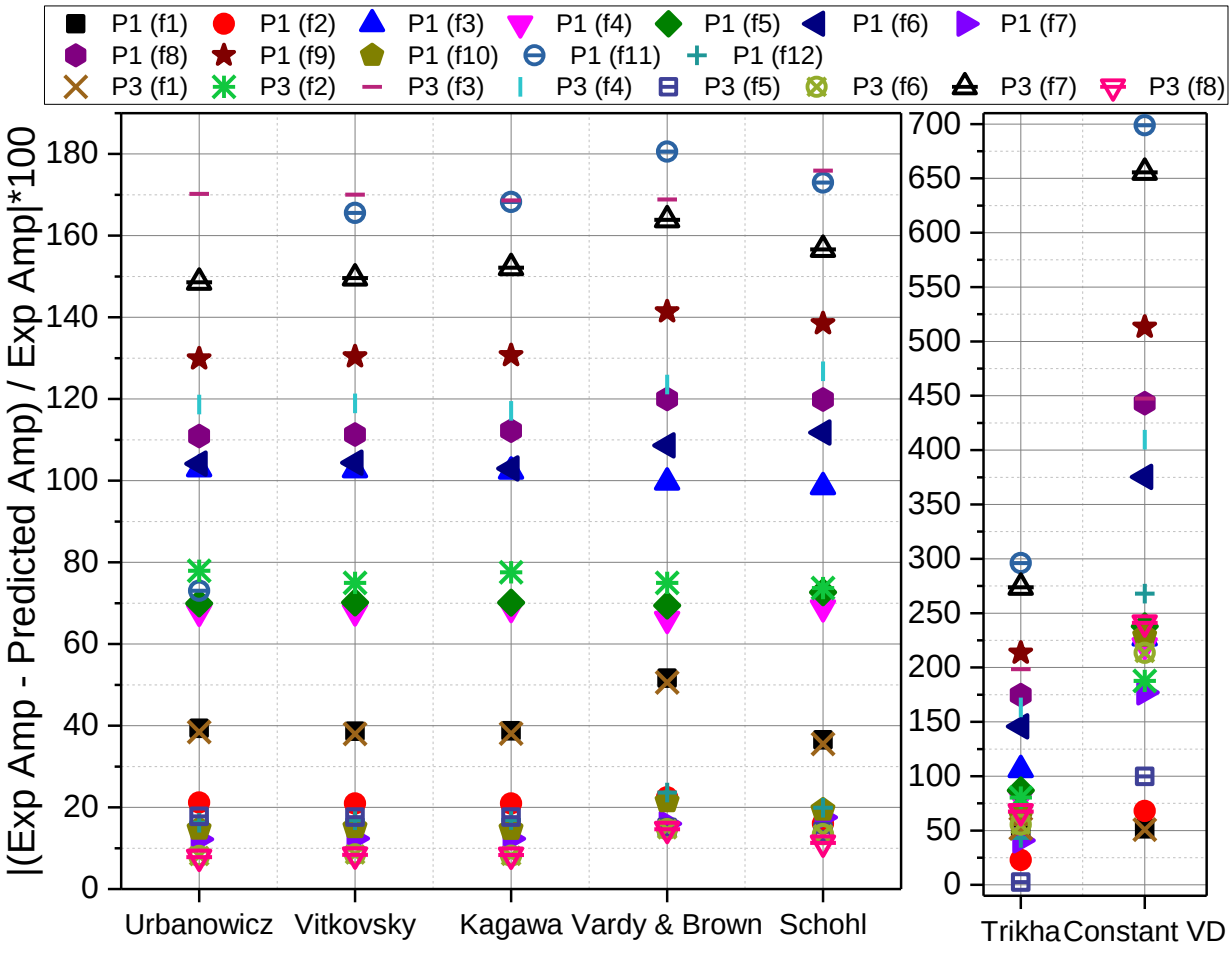

Figure 6.79: Resonant Amplitude Prediction Relative Errors for Zero Flow

At P_3, same as P_1, the 1st resonant peak is predicted with less than 39% relative errors using the damping methodologies of UVK and Schohl (1993). The 5th, 6th and the last resonant peaks are well predicted with less than 20% relative errors. Using the frequency-dependent methods improves the predictions at these resonant peaks to acceptable values of relative errors compared

to the constant VD method. From constant VD, to the frequency-dependent damping methods, the resonant amplitude predictions are improved, but there is no damping methodology that is able to predict the resonant amplitudes at all locations accurately. Specially, for the frequency range of 120 Hz to 280 Hz at the both locations, the assessed prediction methods show the high values of relative errors in term of resonant amplitude prediction.

Figure 6.80 shows that the constant VD RMSE values for the mainline and the branch are almost 4 times bigger than the minimum RMSE values of the frequency-dependent damping methodologies. At both the P_1 and P_3 locations, the lowest RMSE value is obtained with UVK and Schohl (1993) damping methodologies. These values in comparison to the Complex Experiment close-ended values decrease by almost 40% and 30% at P_1 and P_3, respectively. It denotes better resonant amplitude predictions with the assessed damping methods for the open-ended case than the close-ended one.

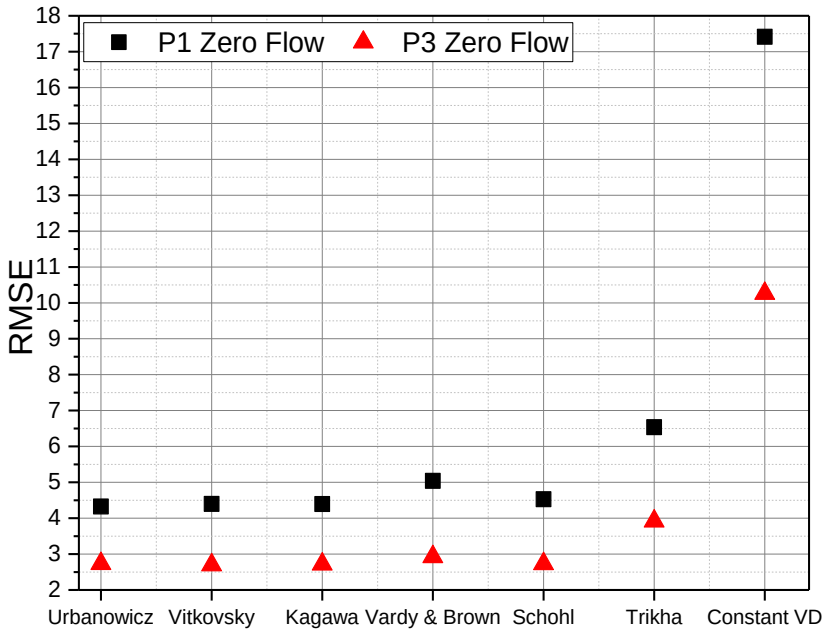

Figure 6.80: Resonant Amplitude Predictions RMSE

6.2.4.1.8 Open-Ended Complex Experiment 2 (Turbulent Mean Flows)

The resonant amplitude relative errors for all the assessed methodologies are tabulated in Tables 6.31 and 6.32 for P_1, Tables 6.33 and 6.34 for P_3. Figure 6.81 displays the resonant amplitude prediction relative errors at P_1 and P_3 for the two turbulent mean flow cases. The resonant amplitude predictions relative errors using the constant VD method show that at P_1, even the 1st resonant peaks, with the relative errors of minimum 45%, are not well predicted. The other peaks are predicted with more magnitude of relative errors than the first peaks. It indicates that the resonant amplitudes are poorly predicted with the constant VD method, at P_1.

Table 6.31: Branch 2.07 m (P_1) Relative Errors (%), Turbulent flow (Re= 16200), Complex Experiment 2

Peak Number	Urbanowicz	Kagawa	Vitkovsky	Vardy & Brown	Schohl	Trikha	Constant VD
1st	✓ 33.87991	✓ 33.18374	✓ 33.2982	! 45.67986	✓ 31.14079	! 46.67589	! 45.65035
2nd	✓ 20.3605	✓ 20.14729	✓ 20.10293	✓ 21.61738	✓ 15.22212	✓ 22.04729	✗ 66.91501
3rd	✗ 82.78594	✗ 82.59479	✗ 82.28333	✗ 79.87812	✗ 78.87109	✗ 85.60286	✗ 194.7336
4th	! 46.83445	! 46.92591	! 47.66433	! 45.30976	! 47.80213	✗ 57.82591	✗ 180.1354
5th	✓ 24.63273	✓ 24.79152	✓ 24.76	✓ 24.24939	✓ 26.6297	! 37.01091	✗ 147.7991
6th	✗ 67.2442	✗ 67.4613	✗ 66.30619	✗ 70.92652	✗ 73.50236	✗ 101.3909	✗ 289.4056
7th	✓ 32.18636	✓ 32.07121	✓ 32.10095	✓ 29.90614	✓ 28.9498	✓ 14.80846	✗ 67.4824
8th	✓ 23.65558	✓ 23.87893	✓ 24.42784	✓ 28.9816	✓ 28.89619	✗ 61.02154	✗ 218.4423
9th	! 41.82068	! 42.13153	! 42.29458	! 48.92068	! 47.1322	✗ 93.29627	✗ 278.3386
10th	✓ 30.73947	✓ 30.50929	✓ 30.76161	✓ 26.67496	✓ 27.93706	✓ 0.9369	✗ 98.58823
11th	✓ 2.85279	! 49.10112	✗ 50.61034	✗ 57.52486	✗ 53.27682	✗ 122.3989	✗ 348.5598
12th	✓ 6.61813	✓ 7.16809	✓ 7.20256	✓ 13.38118	✓ 9.99001	✓ 31.41611	✗ 237.5232

Table 6.32: Mainline (P_3) Relative Errors (%), Turbulent flow (Re= 16200), Complex Experiment 2

Peak Number	Urbanowicz	Kagawa	Vitkovsky	Vardy & Brown	Schohl	Trikha	Constant VD
1st	! 37.4658	✓ 36.98731	! 37.11539	! 49.52103	✓ 34.58543	✗ 50.85394	! 49.81128
2nd	✗ 55.97672	✗ 53.37734	✗ 55.65656	✗ 53.37734	✗ 52.25531	✗ 58.02922	✗ 152.1355
3rd	✗ 94.91638	✗ 94.77989	✗ 93.76178	✗ 93.93132	✗ 99.02414	✗ 115.2445	✗ 294.8853
4th	! 40.97433	! 41.17194	! 39.98269	! 44.14657	! 46.21642	✗ 69.79224	✗ 228.5161
5th	✗ 50.67657	✗ 50.57429	✗ 50.55857	! 49.02629	! 48.41257	! 38.44286	✓ 19.89057
6th	✓ 14.16847	✓ 13.89546	✓ 14.13509	✓ 8.98319	✓ 9.94663	✓ 23.40258	✗ 148.9352
7th	✓ 32.08339	✓ 32.64059	✓ 33.98266	! 40.22362	✓ 36.36642	✗ 98.5738	✗ 301.4454
8th	✓ 21.94184	✓ 21.54569	✓ 21.57995	✓ 17.01807	✓ 19.44254	✓ 21.19569	✗ 146.9072

At $P_{3,}$ only the 5th resonant peak is predicted with less than 20% of relative error. The other peaks show the relative errors from 45% to 300%. It shows that the resonant amplitudes are not properly predicted with constant VD for zero and turbulent mean flows. Indeed, the constant VD obtained from some experiments shows better agreement for the Branch 3 open-ended case than the Complex Experiment 2 case. It means that the resonant amplitude prediction accuracy of the constant VD method is influenced by changing the configuration.

Table 6.33: Branch 2.07 m (P_1) Relative Errors (%), Turbulent Flow (Re=28500), Complex Experiment 2

Peak Number	Urbanowicz	Kagawa	Vitkovsky	Vardy & Brown	Schohl	Trikha	Constant VD
1st	✓ 33.57143	✓ 32.87687	✓ 32.99106	! 45.34419	✓ 30.83862	! 46.33793	! 45.31475
2nd	✓ 17.57376	✓ 17.36549	✓ 17.32216	✓ 18.80154	✓ 12.55436	✓ 19.2215	✗ 63.05039
3rd	✗ 76.8005	✗ 76.61562	✗ 76.31436	✗ 73.98791	✗ 73.01385	✗ 79.52519	✗ 185.0824
4th	✓ 27.4119	✓ 27.49127	✓ 28.13201	✓ 26.08889	✓ 28.25159	✓ 36.94947	✗ 143.0804
5th	✓ 14.88492	✓ 15.03128	✓ 15.00223	✓ 14.53156	✓ 16.7257	✓ 26.29497	✗ 128.4182
6th	! 48.95416	! 49.14751	! 48.11872	✗ 52.23377	✗ 54.52791	✗ 79.36649	✗ 246.8197
7th	! 40.96508	! 40.86485	! 40.89074	! 38.98005	! 38.14751	✓ 25.83682	! 45.80119
8th	✓ 1.73129	✓ 1.55379	✓ 1.11758	✓ 2.50129	✓ 2.43341	✓ 27.96333	✗ 153.0652
9th	✓ 24.88687	✓ 25.1606	✓ 25.30418	✓ 31.1391	✓ 29.56418	✗ 70.21612	✗ 233.1639
10th	✓ 36.48046	✓ 36.26935	✓ 36.50076	✓ 32.75285	✓ 33.91034	✓ 9.14821	✗ 82.1273
11th	✓ 20.77745	✓ 21.59043	✓ 22.82118	✓ 28.45991	✓ 24.99567	✗ 81.36401	✗ 265.7959
12th	✓ 1.11782	✓ 0.60776	✓ 0.57579	✓ 5.15453	✓ 2.00941	✓ 21.88089	✗ 213.0334

Table 6.34: Mainline (P_3) Relative Errors (%), Turbulent Flow (Re=28500), Complex Experiment 2

Peak Number	Urbanowicz	Kagawa	Vitkovsky	Vardy & Brown	Schohl	Trikha	Constant VD
1st	✓ 35.7116	✓ 35.23921	✓ 35.36566	! 47.61299	✓ 32.86798	! 48.92889	! 47.89954
2nd	✗ 52.40473	! 49.86489	✗ 52.09191	! 49.86489	! 48.76855	✗ 54.41023	✗ 146.3614
3rd	✗ 80.40133	✗ 80.275	✗ 79.33271	✗ 79.48963	✗ 84.20319	✗ 99.21569	✗ 265.479
4th	✓ 29.03388	✓ 29.21475	✓ 28.12623	✓ 31.93743	✓ 33.83197	✗ 55.41093	✗ 200.691
5th	✗ 53.84171	✗ 53.74599	✗ 53.73128	✗ 52.29733	✗ 51.72299	! 42.39305	✓ 12.19706
6th	✓ 20.32722	✓ 20.0738	✓ 20.29624	✓ 15.51401	✓ 16.40831	✓ 14.54795	✗ 131.0731
7th	✓ 22.16587	✓ 22.68123	✓ 23.92253	✓ 29.69488	✓ 26.1273	✗ 83.66382	✗ 271.3027
8th	✓ 27.20228	✓ 26.83283	✓ 26.86478	✓ 22.61033	✓ 24.87141	✓ 13.02815	✗ 130.2678

The 1st, 2nd, 5th, 7th, 8th, 10th, 11th, and 12th resonant peaks at P_1 are predicted with less than 33% relative errors using the damping methodologies of UVK and Schohl (1993). Compared to the zero mean flow case, using these damping methodologies for turbulent flows improves the resonant amplitude predictions at the 5th, 8th, and 11th peaks to less than 33% relative errors. For the other resonant peaks, the magnitudes of the prediction relative errors increase to maximum 82%, and they are not accurately predicted. At P_3, the 6th, 7th and 8th resonant peaks for Re = 16200, and the 1st, 4th, 6th, 7th and 8th resonant peaks for Re = 28500, are well predicted with the frequency-dependent damping methodologies of UVK and Schohl (1993). For the zero mean flow case, only the 6th and 7th resonant peaks are correctly predicted. It shows using the frequency-dependent damping methods improve the predictions over constant VD considerably.

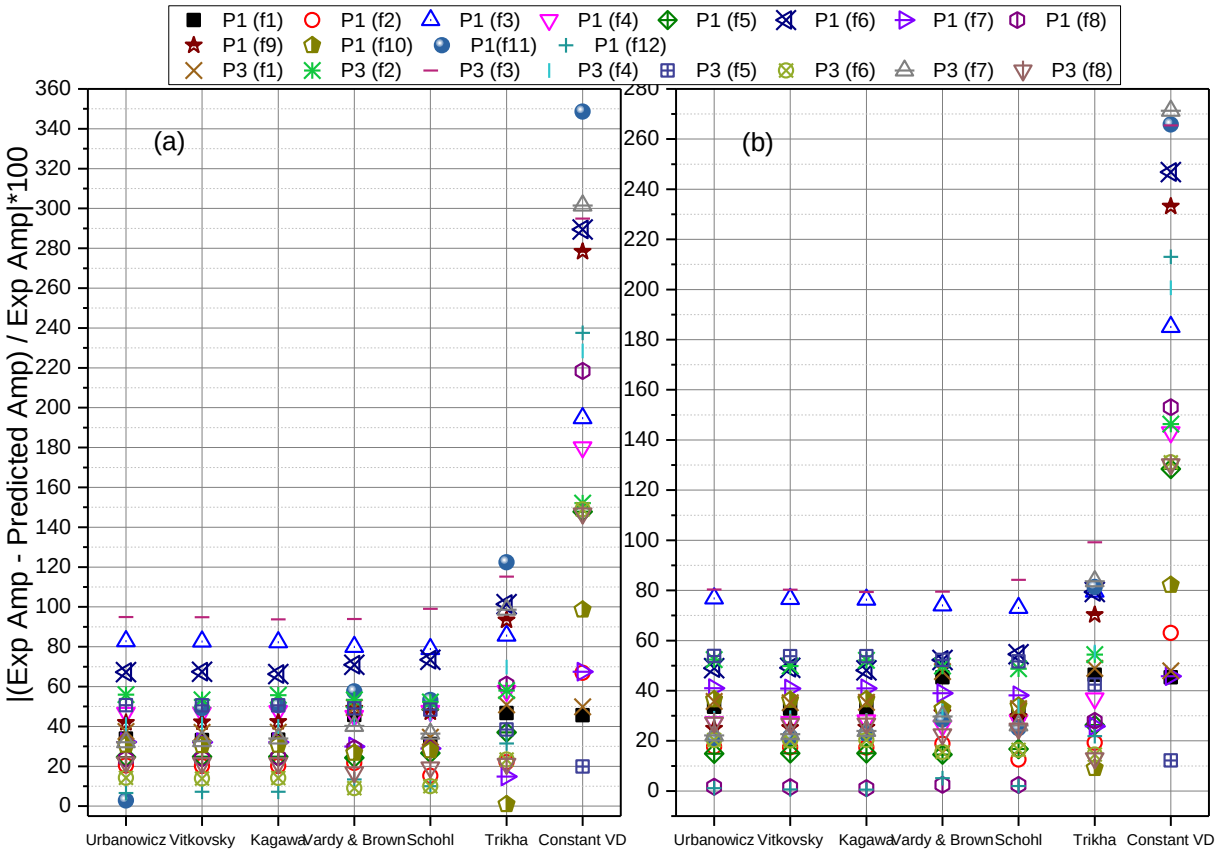

Figure 6.81: Resonant Amplitude Prediction Relative Errors a) Re =16200 & b) Re=28500

Figure 6.82 shows that, the highest RMSE value is obtained with constant VD and Trikha (1975) damping methodologies. The constant VD RMSE value for the branch is almost 70% higher than the mainline and almost 4 times bigger than the minimum RMSE values of the frequency-dependent damping methodologies. Same as the zero mean flow, at P_1 and P_3, the UVK and Schohl (1993) damping methodologies show the lowest magnitudes of the RMSE. The RMSE values for turbulent mean flows, at P_3, are almost the same as the zero mean flow RMSE values, but for P_1, they are less than zero mean flow values. For Re = 28500, RMSE values are lower than zero mean flow and the other turbulent mean flow. It represents better resonant predictions with the assessed damping methods of UVK and Schohl (1993) for the turbulent flow cases than the zero mean flow case. It is due to the fact that the resonant peaks are over predicted with the assessed methods, and for the turbulent flow cases the resonant amplitude measurements increase compared to the zero mean flows. Therefore, the turbulent mean flow cases are better predicted than the zero mean flow case.

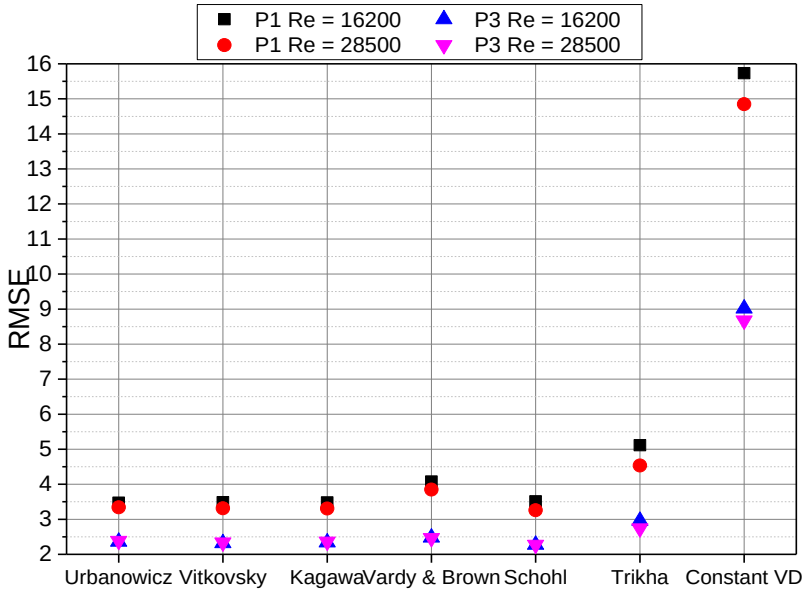

Figure 6.82: Resonant Amplitude Predictions RMSE

6.2.4.2 The CFD Solution

6.2.4.2.1 Close-Ended Straight Line

Figure 6.83 shows that all the four resonant peaks of both the straight line SS tubes are predicted with less than 23% of relative errors. It indicates that even for frequencies higher than 300 Hz, the CFD solution relative errors are acceptable for both the SS tubes. For frequencies higher than 300 Hz, the LWS using the UVK damping methods gives a minimum of 75% relative errors and the constant VD gives a minimum of 115% relative errors. The RMSE value of the CFD solution for the thinner SS tube is almost 1/5 of the RMSE values of the UVK damping methodologies and 1/10 of the RMSE value of the constant VD.

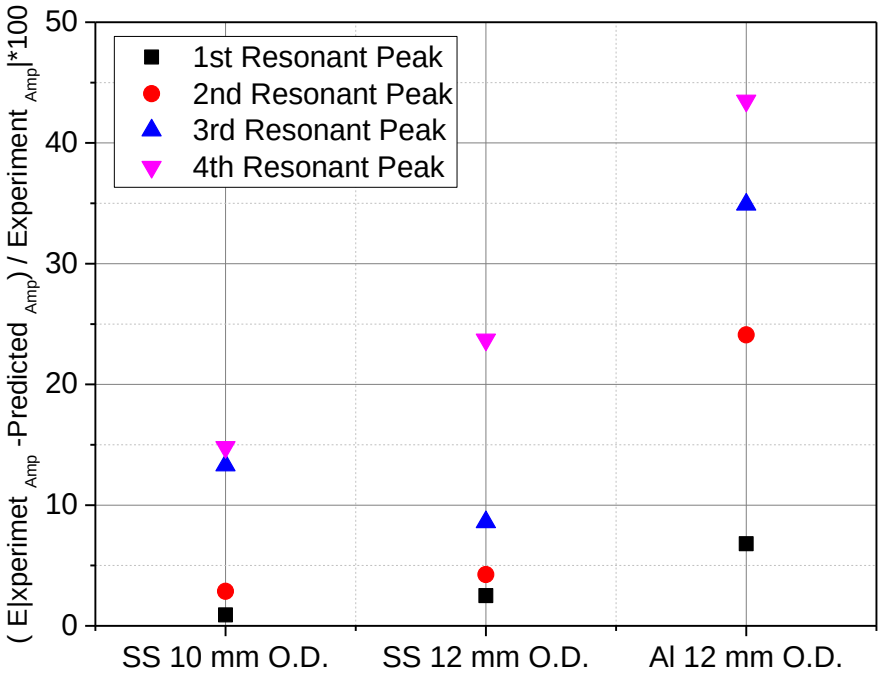

Figure 6.83: CFD Resonant Amplitude Prediction Relative Errors

For the Al tube, Figure 6.83 depicts that the CFD solution for the first three peaks gives the acceptable amount of relative errors (maximum 35%). For the 3rd resonant peak, LWS using the frequency-dependent damping methods shows a minimum relative error of 85%. Although CFD solution predicts the 4th resonant peak with 43% of relative error, this value is less than the relative errors obtained with LWS using the frequency-dependent damping methods and constant VD. The calculated RMSE value for the CFD solution is almost 1/2 the RMSE value of the UVK damping methods. It is also 1/3 of the RMSE value of the constant VD method. The RMSE value of the Al tube is 2.5 times bigger than the SS tube with the same wall thickness. It means that the CFD solution predicts the resonant amplitudes of the SS tubes better than the Al tube. The wall vibration of the Al tube is higher than the SS tube at higher resonant frequencies. Therefore, the wall vibration in the radial direction may need to be coupled with the CFD solution to improve the predictions. To do so, the fluid structure interaction methods can increase the accuracy of the predictions of the resonant amplitude of the Al tubes.

To show the deviation between the CFD-predicted velocities at different resonant frequencies, the predicted radial profiles of axial velocity at certain time duration are shown in Figure 6.84.

In Figure 6.84, the computed velocity profiles are shown by means of different data symbols and lines for the selected radial distances through the oscillation cycle. The six radial distances to the tube wall are selected to fully represent the variation of velocity profiles and phase differences through the cycles. The velocity profiles at the 2nd (167 Hz) and 4th (392 Hz) resonant peaks of the 12 mm O.D. Al tube displays some differences in magnitudes and phases. It means that 1D solutions that assumes constant velocity magnitude and phase in radial direction are not accurate.

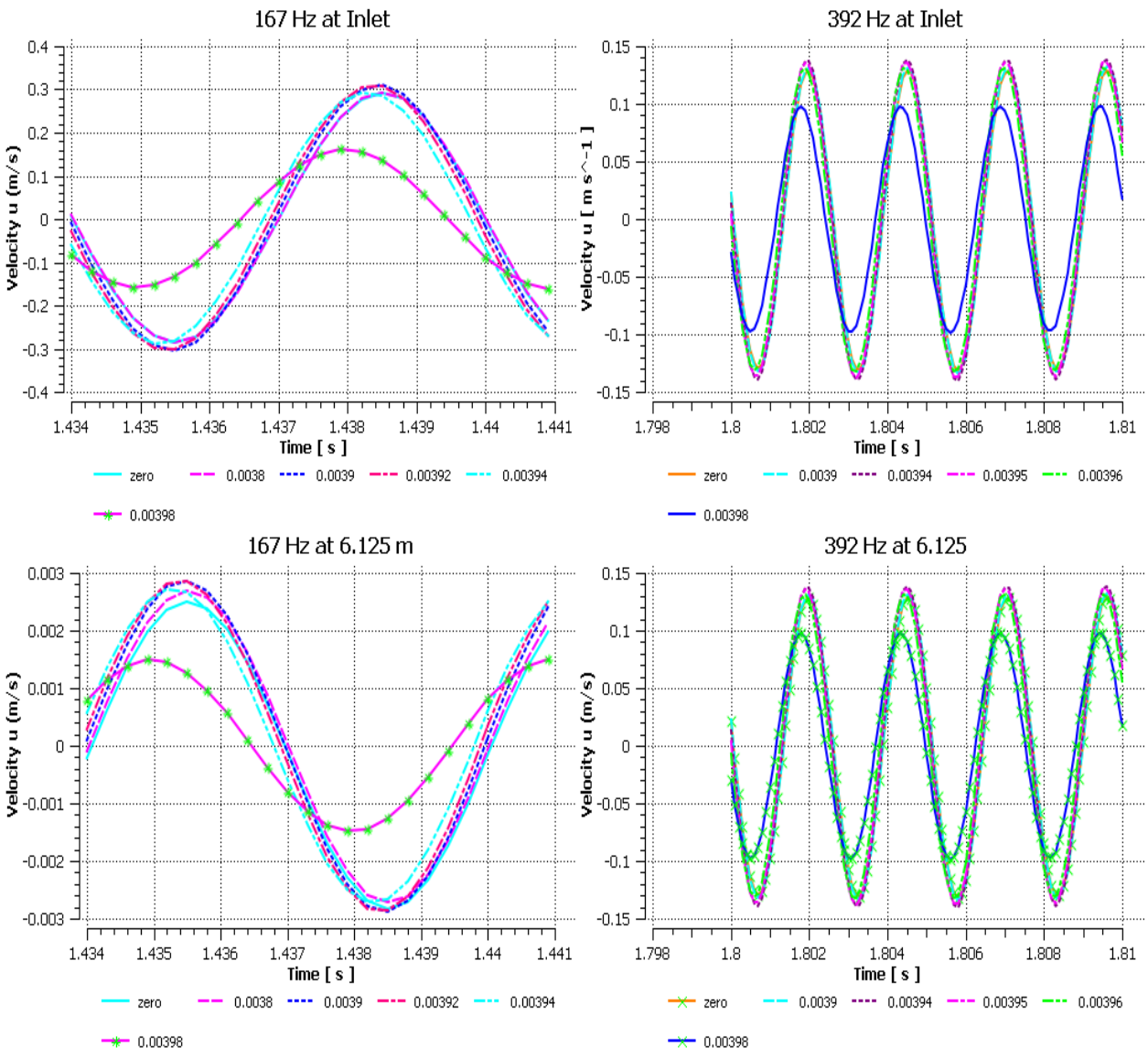

Figure 6.84: Radial Profiles of the Computed Axial Velocity with CFD at Two Different Resonant Frequencies, in Time Domain

For a better understanding of the resonant amplitude predictions using the CFD solution, the axial-predicted velocities for a period of time at two different resonant frequencies are plotted versus the radial distance in Figure 6.85.

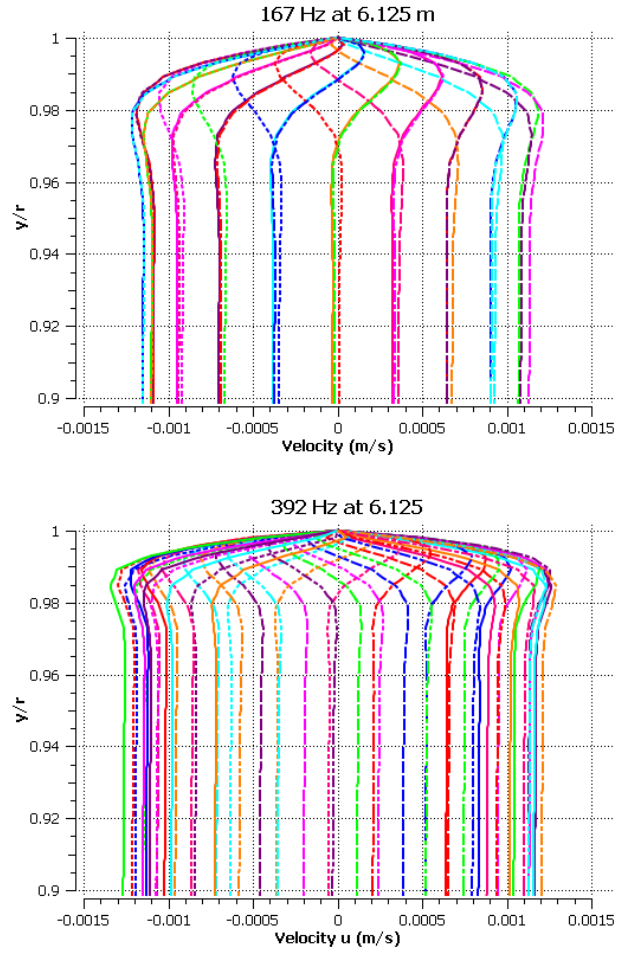

Figure 6.85: Radial Profiles of the Computed Axial Velocity with CFD at Two Different Resonant Frequencies, for a Period of Time

The peak of the velocity magnitudes are closer to the wall at 392 Hz (0.95<y/r<1) than 167 Hz (0.9<y/r<1). Based on the dimensionless frequency parameter $\sqrt{\omega'}$= r$\sqrt{\frac{\omega}{\nu}}$, some investigations were performed for $\sqrt{\omega'}$ <28 by Ohmi and Iguchi (1982). They show that when $\sqrt{\omega'}$ is large, the wall shear stress approaches a laminar value. Here, the velocity field of high $\sqrt{\omega'}$ numbers (>28) at two resonant peaks are investigated. It can be seen that the deviation in a parabolic shape and a maximum velocity are proportional to $\sqrt{\omega'}$. With increasing$\sqrt{\omega'}$, the velocity profiles reveal stronger gradients, lower maximum velocity, and closer reversal points to

the wall. Therefore, the viscous effects are narrowed to a thinner region close to the wall for the higher frequencies.

Besides the above shape of the velocity profiles, another important effect of the increasing frequency is the stronger velocity damping. It shows that acoustic resonance peaks have more features, such as a thinner viscous layer region close to the wall for higher resonant peaks, which cannot be captured with the one-dimensional LWS using simplified damping terms. The CFD solution does not assume the simplifications that are made by the assessed damping methodologies. Thus, the resonant amplitude predictions with the CFD solution are closer to the experimental data than the LWS with the assessed damping methodologies.

6.2.4.2.2 Open-Ended Straight Line for Zero Mean Flow

The relative errors of less than 17% are obtained at P_1, P_2, and P_3 with the CFD solution (See Figures 6.61-6.63). The 4^{th} resonant peaks are not well predicted with UVK damping methodologies. Also, the lowest RMSE values in amplitude predictions are obtained for the CFD solution. It can be concluded that the resonant amplitude predictions of the CFD solution are better than the LWS using UVK damping methodologies and the constant VD method.

6.2.4.2.3 CFD and LWS Solutions (Constant VD and Frequency-Dependent Damping Methods) for Turbulent Mean Flow

Figure 6.86 shows the resonant amplitude relative errors of the CFD solution using the SST turbulence model, the LWS using the constant VD method, and the LWS frequency-dependent damping methods of Kagawa et al. (1983), Schohl (1993), Trikha (1975), Urbanowicz and

Zarzycki (2012), Vardy and Brown (2004), and Vitkovsky et al. (2004) for a turbulent flow (Re = 16766.4) case, at P_1, P_2, and P_3.

Figure 6.86 shows that at P_1, P_2, and P_3, the resonant amplitude predictions with the SST turbulence model are obtained with less than 11% of the relative errors for the first three resonant peaks. For the 4th peak the relative errors are less than 16%. The results indicate that the resonant amplitudes at a turbulent flow with Re = 16766.4 are accurately predicted with the SST turbulent model.

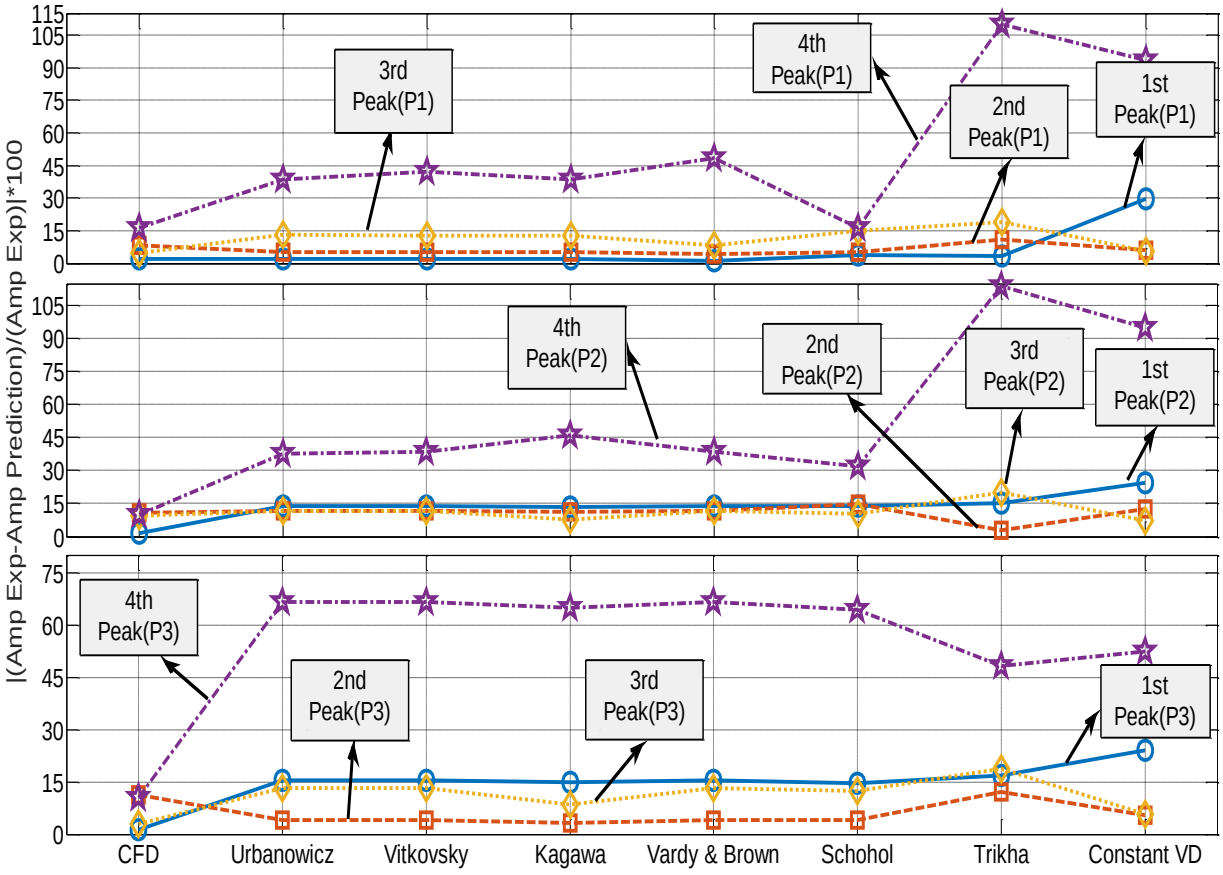

Figure 6.86: Resonant Amplitude Prediction Relative Errors for Turbulent flow

The first three peaks are predicted with less than 30% relative errors with constant VD, but for the 4th peak, the relative errors are increased to 95%. It shows that the first three resonant

peaks, just as the no flow case, are predicted well with constant VD. For the frequency-dependent methods, same as the constant VD method, the first three peaks are properly predicted with less than 20% of relative errors. The 4th resonant peaks are predicted with 41%, 37%, and 63% of relative errors at P_1, P_2, and P_3 using UVK and Vardy and Brown (2004) damping methodologies. The experimental results show the resonant amplitudes increase with increasing the flow rate. The Constant VD and frequency-dependent damping methods results are independent of flow velocity. It can be a reason why the resonant amplitude relative errors for the LWS using a constant VD and frequency-dependent methods increase at higher flow rates.

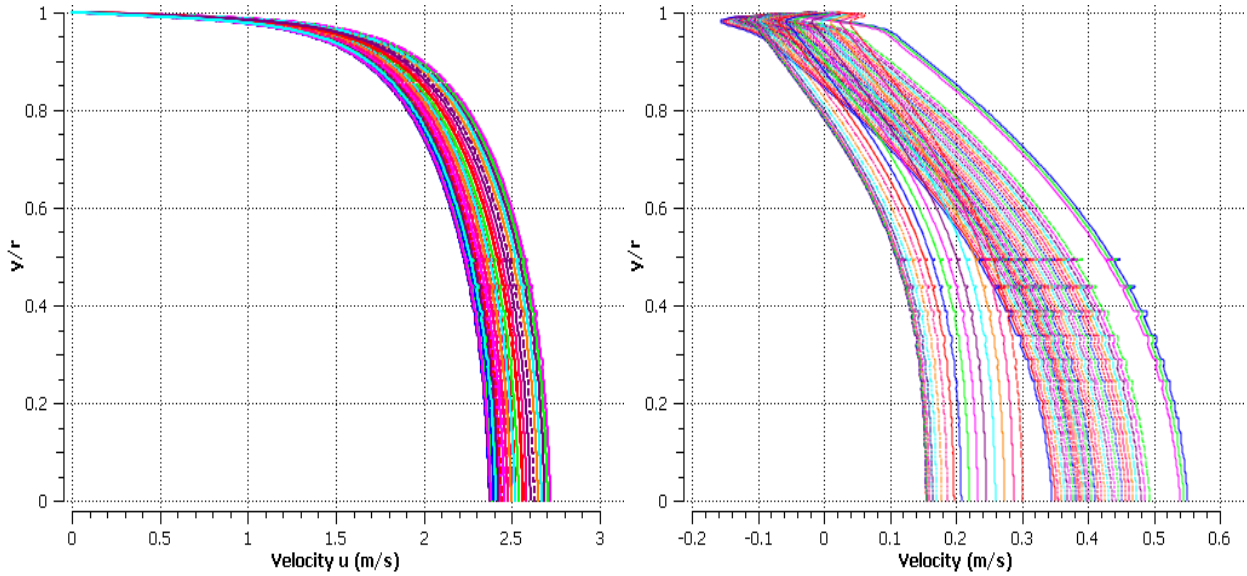

(a) (b)

Figure 6.87: Radial Profiles of the Computed Axial Velocity with CFD for the 4th Resonant Frequency, at P_3. a) Turbulent Flow b) Zero Mean Flow

The velocity profiles predicted using the CFD solution for the zero and turbulent mean flows at the 4th resonant peak of P_3 location are plotted in Figure 6.87. For the zero mean flow case, the shape of the velocity profile is not parabolic. In the turbulent flow case, at the same location and

the same resonant peak of zero flow case, there is no deviation from the parabolic shape and no back flow near the wall.

Figure 6.88(a) shows the turbulent kinetic energy at the 4th resonant peak of P_3 and the maximum value is visible close to the wall. The same trend for the turbulent eddy dissipation is shown in Figure 6.88(b). It shows the largest velocity gradient and the maximum dissipation in the area close to the wall. For higher frequencies with a higher number of reflected waves and shorter wave lengths, the turbulent flow field is affected with a large number of waves and more distributions than the lower frequencies with longer wave lengths. Therefore, for more accurate resonant amplitude predictions, the velocity profile close to the wall needs to be well simulated. The current predictions indicate that for the assessed cases, the SST turbulence method accurately models the velocity profile close to the wall.

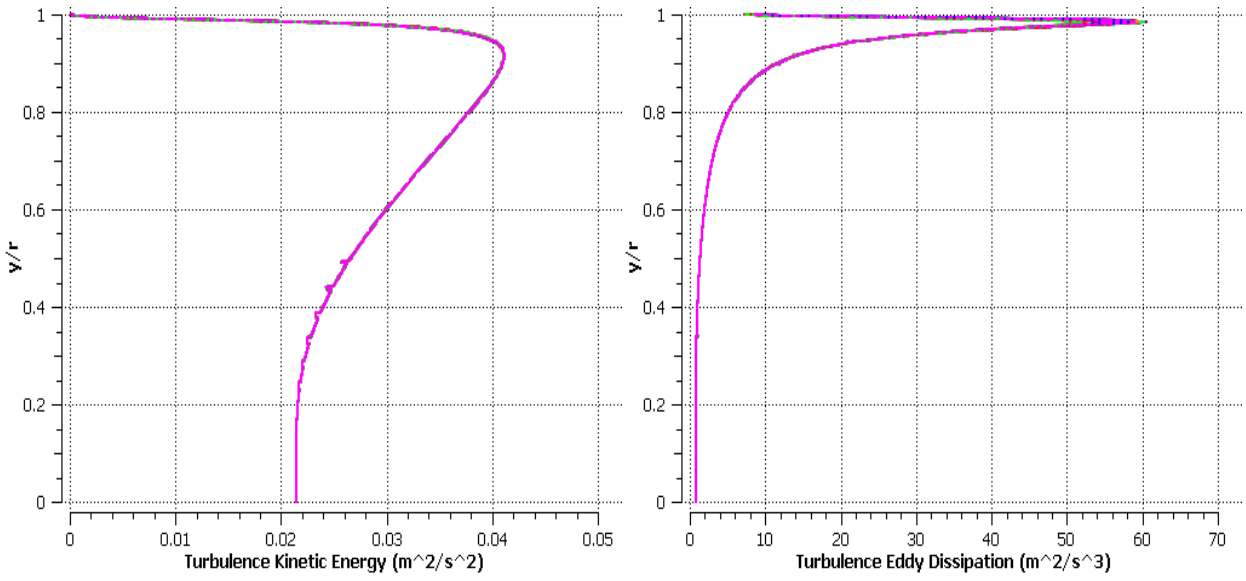

(a) (b)

Figure 6.88: Turbulent kinetic Energy and Turbulence Eddy Dissipation for the 4th Resonant Frequency, at P_3

6.3 Possible Experimental Errors

In the experiments, several factors may influence the accuracy of the results. They are measurement uncertainties, vibrations, shaker noises and oscillating pressures generated by the gear pump.

6.3.1 Measurement Uncertainties

The uncertainty analyses are conducted for every single experiment. To calculate measurement uncertainties, all the single uncertainties connected with the experiments are determined separately, and then combined to find an overall value. A summary of the estimating method and analysis are given here, and a complete set of results is given in Appendix C.

Type A and Type B approaches introduced by Bell (1999) are used to estimate the uncertainties. From the measured data sets with the adequate number of repeated readings, Type A estimation is evaluated. Since all measurement instruments in the study are new and include the calibration certificates, Type B is calculated from the instrument certifications.

To combine all the contributing uncertainties, they need to be expressed at the same level of confidence. To do so, they are converted to standard uncertainties. After collecting required sets of repeated readings at the resonant frequencies of each experiment in the frequency range of 20–500 Hz, the mean, $\bar{x}$, and estimated standard deviation, s, are calculated for the sets. The estimated standard uncertainty is calculated by dividing standard deviation over square root of the number of measurements in the set. This value is evaluated as Type A uncertainty in the calculations and shown as $u_A = \frac{s}{\sqrt{n}}$., where n is the number of readings in each data set.

To estimate Type B uncertainty value, the half distances between the upper and lower uncertainty levels of the measurement instruments (a) are divided over the magnitude of 2. The uncertainty values in the estimations are obtained from the calibration certificates. The calculations for Type B are based on the assumption that data is normally distributed. The Type B uncertainties are shown as $u_B = \frac{a}{2}$.

The individual standard uncertainties of u_A and u_B are calculated, then combined by 'summation in quadrature', and shown as $u_C = \sqrt{{u_A}^2 + {u_B}^2}$. At the straight line experiments, the final data are taken from dividing acoustic pressures of the outlet over the inlet. For the inlet acoustic pressure with uncertainty of $u_C(P_0)$, the relative uncertainty is $u_C(P_0)/P_0$. For the outlet acoustic pressure, the relative uncertainty is $u_C(P_0)/P_0$. Then, the relative combined uncertainty, $u_C(P)/P$, is given by

$$\frac{u_C(P)}{P} = \sqrt{\left(\frac{u_C(P_0)}{P_0}\right)^2 + \left(\frac{u_C(P_1)}{P_1}\right)^2} \tag{6.1}$$

The data is normally distributed and the estimated combined uncertainty only covers a level of confidence that is equal to 68%. To get expanded uncertainty, U, the combined standard uncertainty, u_C, is multiplied by a coverage factor, k. The expanded uncertainty is scaled by using the coverage factor $k = 2$, to give a level of confidence of approximately 95%. Uncertainty is estimated based on UKAS Publication M 3003. Since the PCB 482A16 charge amplifier, the NI PCI-4472 signal acquisition board, and the NI PCI-6731 analog output board are calibrated by the manufacturers, they are considered as Type B uncertainties.

The length measurement uncertainties are calculated within ±1 mm. Uncertainty of the acoustic pressure transducers, in the current experiments reported in the instrument specification, is ±0.64%. Also, from the turbine flowmeter calibration certificate, the flow velocity is measured with an accuracy of ±1.5%. The expanded uncertainty for the acoustic pressure, flow velocity, and temperature are calculated based on Type A and Type B standard uncertainty evaluations. For a case of 1 mm wall thickness straight line experiment with SS tube and zero mean flow, four resonant amplitude peaks are obtained. The relative measurement uncertainties from the first to the last peak are found to be within ±0.18%, ±0.35%, ±0.43% and ±0.71%, respectively. The relative uncertainty of measurements are estimated for the confidence level of 68% and multiplied by factor of 2 to cover the confidence level of 95%.

6.3.2 Effects of Vibration

The longitudinal vibration natural frequencies are shifted much above the experimental frequency, through using the cushioned clamps and positioning a short rubber hose between the test line and cylinder. Moreover, by fixing the close ends of the mainline, the axial vibrations are reduced to be as small as possible. Since no vibration sensors are mounted on the tube walls, the influences of vibration are not estimated.

6.3.3 Effects of Shaker Noises

During the experiments, the electromechanical shaker generates some noises in the systems. Since the P_0 pressure transducer is positioned at a distance of about 1.2 m away from the shaker,

these noises might have more influence on this transducer signals than the other pressure transducers. By detaching the shaker and cylinder from the system, the effects of shaker noises on the transducers are measured for all the configurations at the highest frequency (500 Hz). This is shown in Figure 6.89 for a close-ended SS straight line. It can be seen that the largest amplitude of the shaker noises is located in low frequencies which are filtered by the data acquisition system. Also, the largest amplitude at $P_{3,}$ is only 0.6 Pa, much smaller than the acoustic pressure signals which are larger than 100 Pa. Therefore, the effects of shaker noises on pressure transducers are small enough and are unable to produce large errors.

6.3.4 Effects of Gear Pump in Flow Experiments

In the experiments with flowing fluid, a gear pump is used to circulate water through the loop. It is known that the pump is able to create pressure pulsations at the vane-passing frequency. The pressure pulsations are produced by the pump and measured for the experiment without applying the frequency through the shaker. It is shown in Figure 6.90 that the vane-passing frequency for a straight line case is only 17 Hz, much lower than the natural resonant frequency of the test line. The resonant amplitude measurements of a straight line case at 200 Hz, is shown in Figure 6.91, and the largest magnitude of the pump vibrations is really small compared to the 200 Hz resonant amplitude values. It indicates that in the frequency range of 20–500 Hz, the gear pump vibration influences on the acoustic resonance results are negligible and do not cause large errors.

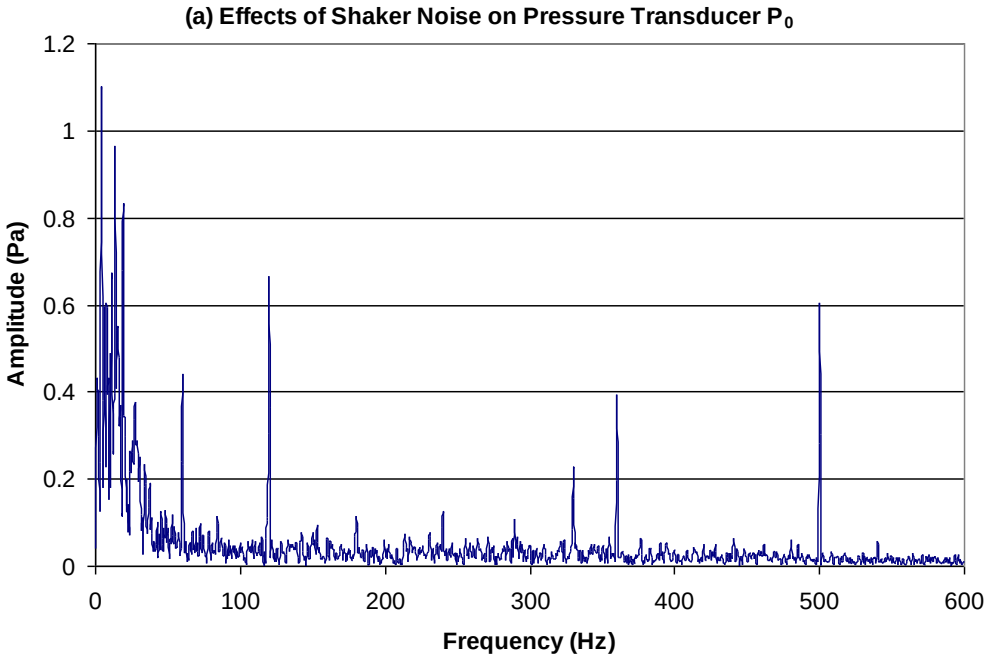

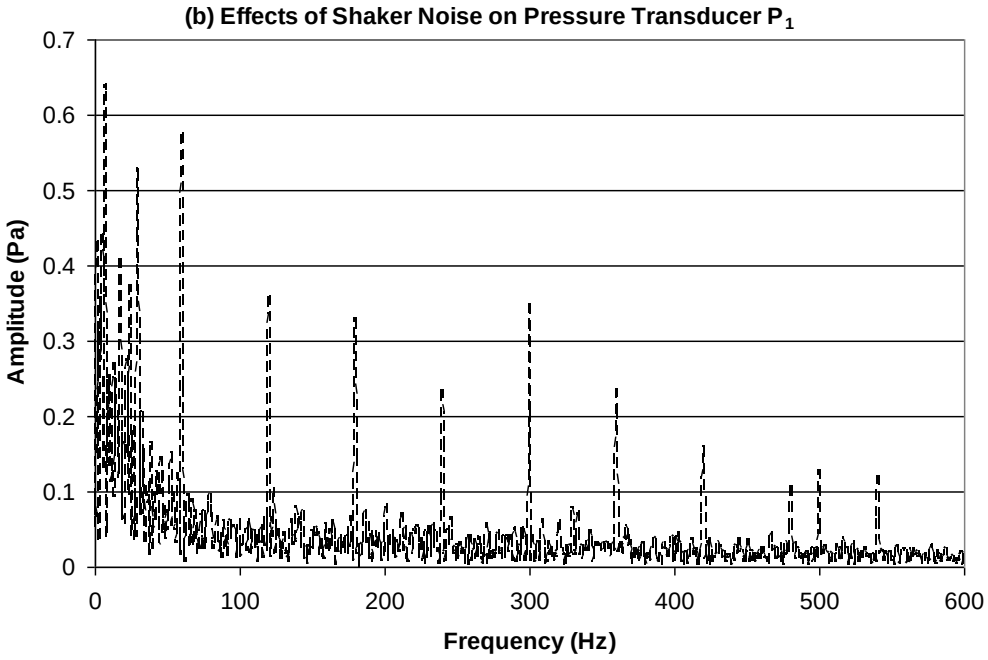

Figure 6.89: Effects of Shaker Noise on Pressure Transducers

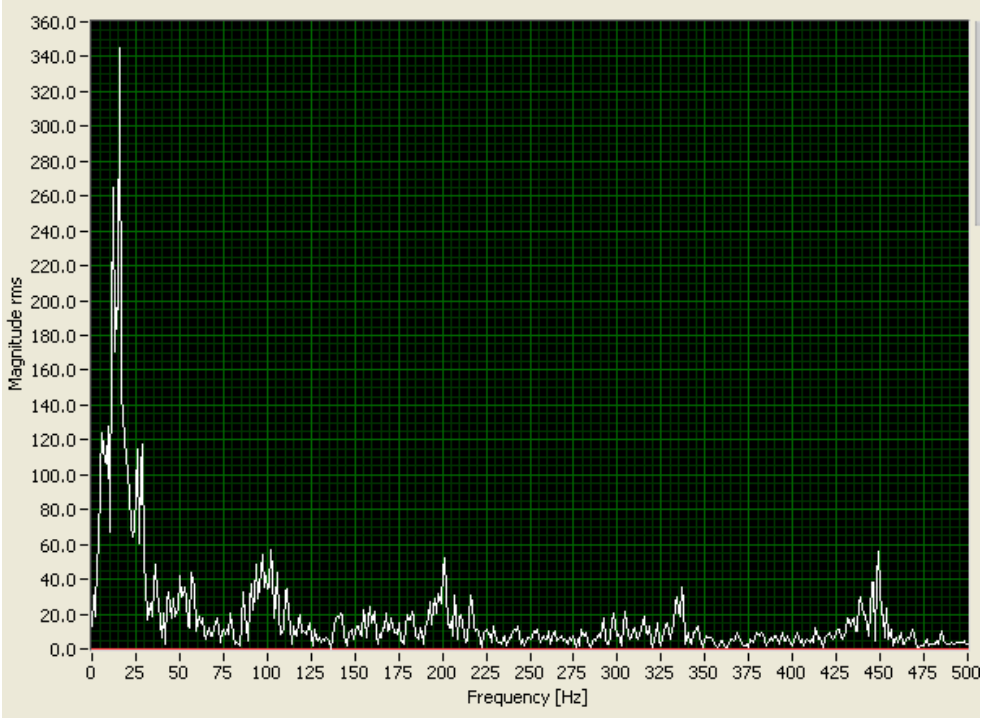

Figure 6.90: Pressure Pulsations Generated by Gear Pump

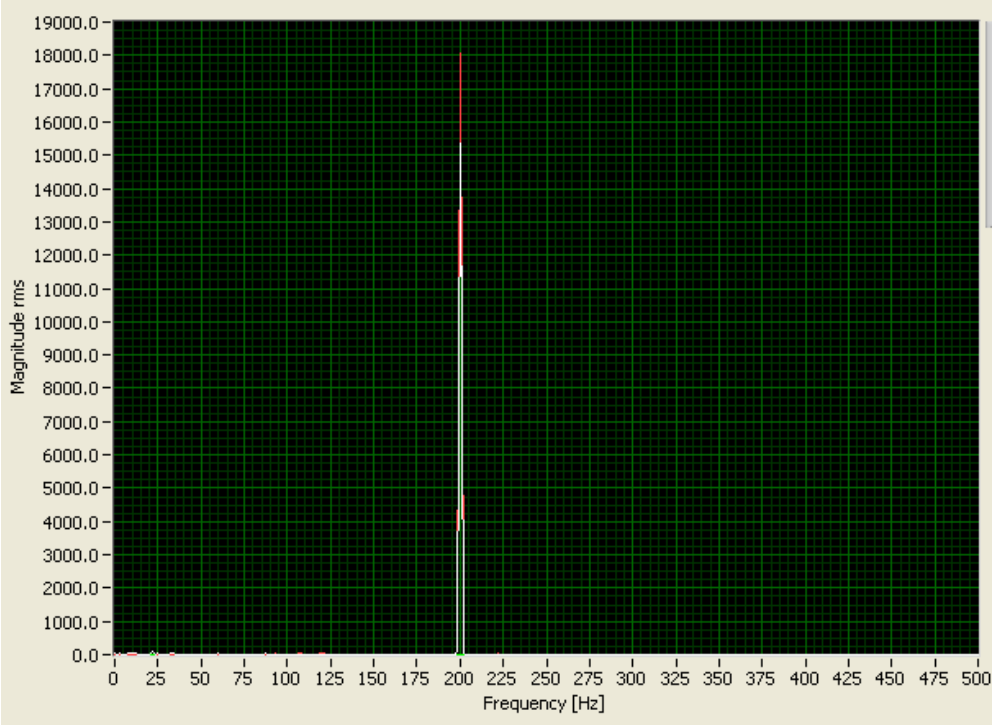

Figure 6.91: Pressure Pulsations Generated by shaker at P_1 and P_3

Chapter 7 Summary, Conclusions and Recommendations

7.1 Summary

Acoustic wave resonance in fluid-filled tubes for some selected straight lines and branched configurations are studied both experimentally and numerically. In the experimental investigations, data are collected for zero, laminar and turbulent mean flows. For all the 16 different experiments, the acoustic pressure measurements are taken at the inlet, outlet and the specific locations of the systems. Determining the best model for predicting such phenomena is an expected outcome of the numerical analysis.

The experiments presented here go beyond the range of frequencies and flow conditions reported by other investigators. While previous researchers go up to 100 Hz with laminar flow, these experiments go up to 500 Hz and include turbulent flow.

A frequency-dependent damping equation is developed for use in the ABAQUS software (nuclear industry evaluating software). It can be used by the nuclear industry to examine the acoustic resonance in the primary heat transport system. This is a most important contribution. It is noteworthy that the current prediction tools used by industry calculate damping with a constant VD.

This is the first in-depth use of a CFD code applied to acoustic resonance in fluid-filled piping within the frequency range 0-500 Hz. However, the CFD study is restricted to straight piping

only, as branched geometries took too much time and resources – hence, doing branched geometry with CFD is not practical.

7.2 Conclusions

The conclusions from the experimental and numerical studies on resonant frequency are summarized in the next section (7.1.1). Section 7.1.2 includes the conclusions obtained from the experimental and numerical studies on resonant amplitude.

7.2.1 Resonant Frequency

The finding here for the close-ended SS and Al straight line tubes is that the constant VD approach reasonably predicts the resonant frequencies. Using Urbanowicz and Zarzycki (2012) and Vardy and Brown (2004) methodologies improve the resonant frequency predictions compared to the constant VD method.

For the straight line open-ended case, using constant VD shows again an acceptable difference from the measurements for resonant frequency predictions. The highest differences are observed for frequencies higher than 350 Hz and those differences are acceptable in terms of percentage. Using the assessed frequency-dependent damping methods decreases the difference between the measurements and predictions and properly predicts the resonant frequency for the open-ended and zero mean flow cases.

For equal branched configurations there is a shift from the measurements at the last resonant peak, which is higher than 400 Hz. This can be attributed to the complexities of the unsteady

frictions at the junctions.

For the close-ended Branch 3, the LWS using the frequency-dependent and constant VD damping methods indicate disagreements between the resonant frequency predictions and measurements at frequencies higher than 250 Hz. For the Complex Experiment the disagreement between the predictions and measurement are obtained at frequencies higher than 240 Hz. For the equal branched configurations the unacceptable differences between the predicted and the measured resonant frequencies begin from 400 Hz. These differences are higher for the unequal branches and complex experiments. This demonstrates different branch lengths and configuration could influence the resonant frequencies.

The open-ended Branch 3 and Complex Experiment 2 experimental results indicate that the resonant frequency shifts from zero to turbulent flow are considerable for frequencies higher than 350 Hz. For the straight line experiments, the flow effect on the resonant frequency is not significant. It could be that, for increasing frequency, the created eddies of unequal branch configuration combined with turbulent flow eddies, shift the resonant frequencies.

7.2.2 Resonant Amplitude

The measurements on the close-ended straight line experiments show that the resonant amplitude slopes are lower for the Al tube with the lower Young's modulus and higher acoustic wave energy absorption than the SS tube. It means that, with increasing frequency, the Al material can damp the acoustic wave energy more effectively than the same SS tube, and the type of material influences the resonant amplitudes. Also, the minimum normalized amplitudes decreases to less than 1 for the frequencies higher than 200 Hz. The decrements in the minimum non-resonance

amplitudes with increasing frequency were also reported by Chatoorgoon and Li (2006).

For the open-ended straight line experiments and the employed tube size, measurements show that the resonant amplitudes are dependent on the flow rate, especially for frequencies higher than 350 Hz.

Due to the lack of resource to pump fluid in large diameter pipes (50 cm diameter), the current experimental study is limited to the small diameter tubes. Since the CFD solution on acoustic resonance of the large pipe requires long simulation time, some selected resonant frequency for zero and turbulent mean flow are simulated. From those CFD results, it seems the large diameter pipe would likely alter the 350 Hz value to make it a smaller amount.

The finding here for the close-ended SS and Al straight line tubes is that the constant VD approach reasonably predicts the resonant frequencies, but does a poor job of predicting the resonant amplitudes. The resonant amplitude predictions using constant VD have the same magnitudes for all the resonant peaks and cannot capture the feature of decrease in resonant amplitude with an increase in frequency. Therefore, it is not recommended for accurate resonant amplitude prediction for close-ended tubes.

Using the UVK as the best assessed methodology for the resonant amplitude predictions still shows high values of relative errors at the 4^{th} resonant peak. This means that they can only predict the first three peaks accurately. For the Al tube, only the first two peaks are accurately predicted. The UVK damping method is recommended for the ABAQUS instead of constant VD. It is relatively simple to include the UVK damping method.

Resonant amplitude predictions with CFD give better accuracy than the LWS using constant VD and the assessed damping methodologies for the straight line close-ended cases. This is because of the fact that the CFD solution solves the more complete Navier-Stokes equations and

it therefore included the terms pertinent to resonant damping. It is likely that fluid structure interaction can decrease the difference between the CFD predictions and the measurements from the Al fluid-filled tube.

Although for the first three peaks of the straight line open-ended case, the agreement between the constant VD resonant amplitude predictions and the measurements are good, this can be a coincidence. For the first three resonant peaks, the measured resonant amplitude peaks are almost the same and the constant VD predictions do not follow the trend of the decrease in the amplitude with an increase in the frequency, therefore, they are well predicted with the constant VD. For the higher frequencies (higher than 350 Hz), the measurements show a decrease in resonant amplitude for the last peak, where the constant VD does not accurately capture this decrease. For the first three peaks of the open-ended straight line, the resonant amplitudes are also accurately predicted by the LWS using UVK damping methodologies.

The LWS approach using the damping methodologies for both close-ended and open-ended straight line cases do not do a satisfactory job at the higher frequencies (> 350 Hz) for the Al and SS cases. Indeed, the assessed weighting functions cannot capture this effect for the higher frequencies and the lower acoustic wave periods throughout the entire cross section of the tube. The amplitude predictions with LWS using the assessed damping methodologies show that, when the frequencies satisfy $\frac{L}{\lambda} < 1$, the relative errors compared to the measurements are acceptable for the SS tubes. The improvement in acoustic resonance predictions of the straight line tubes using the UVK damping methodologies lead to the recommendation that they can be applied in ABAQUS instead of the constant VD for better resonant amplitude prediction.

The CFD simulations for the straight line open outlet end case with the turbulence mean flow show that the SST model results match the experiments with less than ~16% relative errors.

Hence, the SST turbulence model predicts the resonant amplitudes of the case with turbulent flow well. For the turbulent flow with Re = 16766.4 the constant VD and the assessed frequency-dependent methodologies only predicted the first three peaks accurately. Indeed, for the higher flow rate, the resonant amplitude prediction relative errors with LWS using the assessed damping methods increase at higher frequencies.

The measurements indicate that the trend of decreasing resonant amplitudes with increasing the frequency is only valid until the 4^{th} resonant peak of the equal branched configurations. Although the predictions with LWS using the assessed damping methodologies capture this trend, the 4^{th} resonant peak width is predicted to be narrower than the measurements. Also the resonant amplitude prediction relative errors, compared to the experiments for the equal branched configurations, are higher than SS and Al straight tubes values. Therefore, employing UVK damping methodologies for resonant amplitude prediction is not always accurate within the frequency range of 250 Hz to 400 Hz.

The resonant amplitude prediction with LWS using the damping methodologies are not always accurate for the unequal branch experiments. It should be noted that there is no frequency range where all the resonant peaks are accurately predicted. Although there are some dissimilarity between the measured and predicted values of the acoustic resonance on the test geometries, the employed UVK frequency-dependent methods in ABAQUS presents more accurate results than the constant VD.

The experimental results of the open-ended Branch 3 and Complex Experiment 2 also indicate that the higher Re turbulent flow increases the resonant amplitudes more than lower Re and laminar flows. This increment is more noticeable for the branches located close to the inlet. This is important for the nuclear reactor that includes several close-ended branches with highly

turbulent flows. It means that the turbulent flows eddies could combine with natural frequencies of some branches more significantly than the other branches.

There is still a need to extend experimental studies on more complex piping systems and larger diameter piping, as well as improve the numerical models on acoustic resonance predictions with frequencies higher than 250 Hz. Although the CFD solution improves the prediction accuracies in both resonant frequencies and amplitudes, it is not easily applied to complicated industrial cases with several branches and complexities. As long as there is no solid way in 1D to accurately predict resonant amplitudes in fluid-filled tubes, further attempts should be made to improve the mathematical models.

7.3 Recommendations

The following are the recommendations:

(1) Seek further ways to validate the recommended damping technology for a wider range of geometry and flow conditions.

(2) Conduct studies on larger diameter piping, since reactor piping is much larger than those used here.

(3) Further studies of branched geometries with flow in the branches are worth doing.

(4) Improve further the damping technology for 1D solutions.

(5) CFD studies should continue.

References

Allievi, L., 1902. General theory of the variable motion of water in pressure conduits. Annali della Società degli Ingegneri ed Architetti Italiani, 17(5), 285-325, Milan, Italy.

Arthurs, D., & Ziada, S., 2009. Flow Excited Acoustic Resonances of Co-Axial Side-Branches in an Annular Duct. Journal of Fluids and Structure, 25, pp. 42–59.

Baldwin, R.M., & Simmons, H.R., 1986. Flow-induced vibration in safety relief valves. ASME Journal of Pressure Vessel Technology, 108, pp. 267–272.

Bendat J.S., & Piersol, A.G., 2010. Random Data Analysis and Measurement Procedures. 4th Edition, John Wiley & Sons.

Bergant, A., Simpson, A.R., & Vitkowsky, J., 1999b. Review of unsteady friction models in transient pipe flow. IAHR, 9th Int. Meeting of the Work Group on the behaviour of hydraulic machinery under steady oscillatory conditions, Brno, Czech Republic.

Bergant, A., Simpson, A.R., and Vitkovský, J., 2001. Developments in unsteady pipe flow friction modelling. Journal of Hydraulic Research, Vol. 39(3), pp. 249–257.

Bergant, A., Vitkovsky, J., Simpson, A., & Lambert, M., 2002b. Behavior of unsteady pipe flow friction models in the case of valve opening. Proceedings of the 21stIAHR Symposium on Hydraulic Machinery and Systems, Lausanne.

Bratland, O., 1986. Frequency-Dependent Friction and Radial Kinetic Energy Variation in Transient Pipe Flow. 5th Int. Conf. on Pressure Surges, Hannover, F.R. Germany.

Brown, F.T., Morgolis, D.L., & Shah, P.P., 1969. Small amplitude frequency behaviour of fluid lines with turbulent flow. J. Basic Eng, Trans. ASME, Vol. 9(4), pp. 67-81.

Bruggeman, J.C., 1987. The propagation of low-frequency sound in a two-dimensional duct system with T-joints and right angle bends: theory and experiment. Journal of the Acoustical Society of America 82, pp. 1045–1051.

Bruggeman, J. C., Herschberg, A., Van Dongen, M. E. H., Wijnads, A. P. J., & Gorter, J., 1989. Flow-Induced Pulsations in Gas Transport Systems: Analysis of the Influence of Closed Side Branches. ASME J. Fluids Eng., 111, pp. 484–491.

Bruggeman, J.C., Hirschberg, A., Van Dongen, M.E.H., Wijnands, A.P.J., & Gorter, J., 1991. Self-sustained aero-acoustic pulsations in gas transport systems: experimental study of the influence of closed side branches. Journal of Sound and Vibration, 150, pp. 371–393.

Brunone, B., Golia, U.M., & Greco, M., 1991. Modeling of Fast Transients by Numerical Methods. Proc. 9th Round Table IAHR Group, Valentia, pp. 273-280.

Brunone, B., Karney, B.W., Mecarelli, M., & Ferrante, M., 2000. Velocity Profile and Unsteady Pipe Friction in Transient Flow. Journal of Water Resources Planning and Management, pp. 236-244.

Budny, D.D., Wiggert, D.C., & Hatfield, F.J., 1989. Energy Dissipation in Axially-Coupled Model for Transient Flow. Proceedings 6th International Conference on Pressure Surges, BHRA Fluid Engineering, pp. 15-26, Cranfield, England.

Budny, D.D., Wiggert, D.C., & Hatfield, F. J., 1991. The Influence of Structural Damping on Internal Pressure During a Transient Pipe Flow. J. of Fluids Engineering, TRANS. ASME, Vol. 113, pp. 424-429.

Bughazem, M.B., & Anderson, A., 1996. Problems with Simple Models for Damping in Unsteady Flow. Proc., Int. Conf. on Pressure Surges and Fluid Transients, BHR Group, pp. 537-548, Harrogate, England.

Carstens, M.R., & Roller, J.E., 1959. Boundary-Shear Stress in Unsteady Turbulent Pipe Flow. J. of Hydraulics Division, Proceedings of the American Society of Civil Engineers, pp. 67-81.

Chatoorgoon, V., & Li, Qizhao., 2009. A Study of Acoustic Wave Damping in Water-Filled Pipes with Zero Flow and Turbulent Flow. Nuclear Engineering and Design, 239, 2326–2332.

Chaudhry, M. H., & Hussaini, M.Y., 1985. Second-order accurate explicit finite difference schemes for water hammer analysis. J. Fluids Eng., 107, pp. 523-529.

Chaudhry, M.H., 1987. Applied Hydraulic Transients. Van Nostrand Reinhold, NewYork.

Chen, Y.N., & Florjancic, D., 1975. Vortex-induced resonance in a pipe system due to branching. In: Proceedings of International Conference on Vibration and Noise in Pump, Fan and Compressor Installations, pp. 79–86, University of Southampton, England.

Chen, Y.N., & Stuurchler, R., 1977. Flow-induced vibrations and noise in a pipe system with blind branches due to coupling of vortex shedding. Internoise 77, B189–B203, Zurich.

Chen, C., & Veshagh, A., 1993. A Wall Friction Model for One-Dimensional Unsteady Turbulent Pipe Flows. SAE Technical Paper 930610, doi: 10.4271/930610.

Daily, J.W., Hankey, W.L., Olive, R.W., & Jordaan, J.M., 1956. Resistance coefficients for accelerated and decelerated flows through smooth tubes and orifices. Trans. ASME, Vol. (78), pp.1071-1077.

DeBoo, G., Ramsden, K., Gesior, R., & Strub, B., 2007. Identification of Quad Cities Main Steam Line Acoustic Sources and Vibration Reduction. ASME 2007 Pressure Vessels and Piping Conference, San Antonio, Texas, USA.

Dequand, S., Hulshoff, S.J., & Hirschberg, A., 2003. Self-sustained oscillations in a closed side branch system. Journal of Sound and Vibration 265, pp. 359–386.

Docquier, N., & Candel, S., 2002. Combustion control and sensors: A review. Progress in Energy and Combustion Science, 28(2), pp. 107-150.

D'Souza, A.F., & Oldenburger, R. 1964. Dynamic Response of Fluid Lines. ASME Trans, J. of Basic Eng., Series D, Vol. 86, pp. 589-598.

Eichinger, P., & Lein, G., 1992. The influence of friction on unsteady pipe flow. Proc. Int. Conf. On Unsteady Flow and Fluid Transients, pp. 41–50, Durham, England.

Elansary, A.S., Silva, W., & Chaudhry, M.H., 1994. Numerical and Experimental Investigation of Transient Pipe Flow. J. of Hydraulic Research, Vol. 32, No. 5, pp. 689-706.

Foster, K., & Parker, G.A., 1964. Transmission of power by sinusoidal wave motion through hydraulic oil in a uniform pipe. Proceeding, Institution of Mechanical Engineers, Vol. 179: Pt. 1(19), pp. 599–612.

Frizell, J. P., 1898. Pressures Resulting from Changes of Velocity of Water in Pipes. Trans. Am. Soc. Civ. Eng. 39, pp. 1–18.

Geveci, M., Oshkai, P., Rockwell, D., Lin, J.-C., & Pollack, M., 2003. Imaging of the Self-Excited Oscillation of Flow Past a Shallow Cavity During Generation of a Flow Tone. Journal of Fluids and Structures 18(6), pp. 665–694.

Ghidaoui, M.S., & Karney, B.W., 1994. Equivalent differential equations in fixed grid characteristics method. J. Hydraul. Eng., 120(10), pp. 1159-1175.

Ghidaoui, M.S., 2001. Fundamental Theory of Waterhammer. Special Issue of the Urban Water J. (Special Issue on Transients, Guest Editor: B. W. Karney), 1(2), pp. 71–83.

Ghidaoui, M.S., Zhao, M., McInnis, D.A., & Axworthy, D.H., 2005. A review of water hammer theory and practice. Applied Mechanics Review, ASME, 58(1), pp. 49-76.

Goodson, R.E., & Leonard, R.G., 1972. A Survey of Modeling Techniques for Fluid Line Transients. Journal of Basic Engineering, ASME, pp. 474-482.

Gorter, J., Hirschberg, A., Wijnands, A., & Bruggeman, J.C., 1989. Flow induced pulsations in gas transport systems. International Gas Research Conference, Tokyo, Japan.

Graf, H. R. 1989. Experimental and Computational Investigation of the Flow Excited Acoustic Resonance in a Deep Cavity. Ph.D. thesis, Worcester Polytechnic Institute, Worcester, MA.

Graf, H.R., & Ziada, S., 1992. Flow induced acoustic resonance in closed side branches: an experimental determination of the excitation source. In: Proceedings of the Third International Symposium on Flow-Induced Vibration and Noise, vol. 7, ASME WAM, Anaheim, pp. 63–80.

Graf, H. R., & Ziada, S., 2010. Excitation Source of a Side-Branch Shear Layer. J. Sound Vib., 329, pp. 2825–2842.

Guinot, V., 2003. Godunov-type schemes. Elsevier Science B.V., Amsterdam, The Netherlands.

Hino, M., Sawamoto, M., & Takasu, S., 1977. Study on the Transition to Turbulence and Frictional Coefficient in an Oscillatory Pipe Flow. Transactions of JSCE, pp. 282-284.

Holmboe, E. L., & Rouleau, W. T., 1967. The Effect of Viscous Shear on Transients in Liquid Lines. J. Basic Eng, TRANS. ASME, Series D, Vol. 89, No. 1, pp. 174-180.

Iguchi, M., Ohmi, M., & Tanaka, S., 1985. Experimental Study of Turbulence in a Pulsatile Pipe Flow. Bulletin of JSME, Vol. 28, No. 246, pp. 2915-2922.

Janzen, V.P., Fisher, N.L., Smith, B.A.W. and Taylor, C.E., 1999. Investigations of Fuel-Bundle Motion and Fretting-Wear in the Chalk River Single-Channel Test-rig. Proceedings of the 6th International Conference on CANDU Fuel, Vol. I, Niagara Falls, Canada.

Joukowski, N. E., 1898. Memoirs of the Imperial Academy Society of St. Petersburg. 9(5) (Russian translated by O Simin 1904), Amer. Water Works Assoc. 24, pp. 341–424.

Kagawa, T., Lee, I., Kitagawa, A., & Takenaka, T., 1983. High Speed and Accurate Computing Method of Frequency-Dependent Friction in Laminar Pipe Flow for Characteristics Method. TRANS. JSME, Vol. 49, No. 447, pp. 2638-2644.

Kobori, T., Yokoyama, S., & Miyashiro, H., 1955. Propagation Velocity of Pressure Wave in Pipe Line. Hitachi Hyoron, Vol. 37, No.10, pp. 33-37.

Kirmse, R.E., 1979. Investigations of Pulsating Turbulent Pipe Flow. ASME Paper 79 WA/FE-1.

Kita, Y., Adachi, Y., & Hirose, K., 1980. Periodically Oscillating Turbulent Flow in a Pipe. Bull. JSME 23, pp. 656-664.

Kriesels, P.C., Peters, M.C.A.M., Hirschberg, A., Wijnands, A.P.J., Iafrati, A., Riccardi, Piva, G.R., & Bruggeman, J.C., 1995. High amplitude vortex-induced pulsations in a gas transport system. Journal of Sound and Vibration, 184, pp. 343–368.

Lafon, P., Caillaud , S., Devos, J.P., & Lambert, C., 2003. Aeroacoustical coupling in a ducted shallow cavity and fluid/structure effects on a steam line. Journal of Fluids and Structures, 18:695-713, 57, 102.

Margolis, D.L., & Brown, F.T., 1976. Measurement of the Propagation of Long-Wavelength Disturbances through Turbulent Flow in Tubes. J. of Fluid Engineering, Trans. of the ASME, pp. 70-78

Martınez-Lera, P., Schram, C., Feoller, S., Kaess, R., & Polifke, W., 2009. Identification of the Aeroacoustic Response of a Low Mach Number Flow Through a T-joint. Journal of Acoustical Soc. Am., 126, pp. 582–586.

Michalke, A., 1965. On spatially growing disturbances in an inviscid shear layer. J of Fluid Mechanics, 23, pp. 521–544

Misra, A., Pauls, R.E., Vijay, D.K., Teper, W., Liu, J. and Hemraj, R., 1994. Acoustic Modelling in Support of Fuel Failure Investigation in a CANDU Nuclear Generation Station. PVP-Vol, 279, Developments in a Progressing Technology ASME.

Mizushina, T., Maruyama, T., & Shiozaki, Y., 1973. Pulsating Turbulent Flow in a Tube. J. Chem. Engng Japan, pp. 487-494.

Mizushina, T., Maruyama, T., & Hirasawa, H., 1975. Structure of the Turbulence in Pulsating Pipe Flows. J. Chem. Engng Japan, pp. 210-216.

Morgentroh, M., & Weaver, D. S., 1993. Acoustic Pressure Pulsations of a Centrifugal Volute Pump in a Pipeline. 3rd International Conference, Czech Committee of the European Mechanics Society Conference, Engineering Aero-Hydroelasticity, Prague, pp. 111-116.

Morgentroh, M., & Weaver, D. S., 1998. Sound Generation by a Centrifugal Pump at Blade Passing Frequency. J. of Turbomachinery, TRANS. ASME, Vol. 120, pp. 736-743.

Nakiboglu, G., Belfroid, S., Golliard, J., & Hirschberg, A., 2011. On the Whistling Corrugated Pipes: Effect of Pipe Length and Flow Profile. J. Fluid Mech., 672, pp. 78–108.

Nakiboglu, G., Manders, H.B.M., & Hirschberg, A., 2012. Aeroacoustic Power Generated by a Compact Axisymmetric Cavity: Prediction of Self-Sustained Oscillation and Influence of the Depth. J. Fluid Mech., 703, pp.163–191.

Nelson, P.A., Halliwell, N.A., & Doak, P.E., 1983. Fluid dynamics of a flow excited resonance , Part II:flow acoustic interaction. Journal of Sound and Vibration 91 , 375–402.

NRC. Additional flow-induced vibration failures after a recent power uprate. NRC Information Notice 2002-26, Supplement 2, January 9, 2004, US Nuclear Regulatory Commission, Washington, D.C., United States. 1, 8, 102,187.

Ohmi, M., Usui, T., Tanaka, O., & Toyama, M., 1976. Pressure and velocity distributions in pulsating turbulent pipe flow, Part I: Theoretic treatments; Part II: Experimental investigations. Bull. of JSME, Vol. 19(129), pp. 307–313 (part I); Vol. 19(134), pp. 951–957 (part II).

Ohmi, M., Kyomen, S., & Usui, T., 1978. Analysis of velocity distribution in pulsating turbulent pipe flow with Time-dependent friction velocity. Bull. of JSME, Vol. 21(157), pp. 1137-1143.

Ohmi, M., Iguchi, M., Usui, T. & Minami, H., 1980. Flow pattern and frictional losses in pulsating pipe flow: Part 1 – 3. Bull. JSME, Vol. 23(186), pp. 2013-2036.

Ohmi, M., Iguchi, M. & Usui, T., 1981. Flow pattern and frictional losses in pulsating pipe flow: Part 4 – 6. Bull. JSME, Vol. 24(187), pp. 67 – 81, pp. 1756-1763.

Ohmi, M., Kyomen, S., & Usui, T., 1981. Numerical analysis of pressure and velocity distributions for a pulsating turbulent flow in a circular tube containing a slightly compressible fluid. Bull. of JSME, Vol. 24(187), pp. 60-66.

Ohmi, M. & Iguchi, M., 1982. Flow pattern and frictional losses in pulsating pipe flow: Part 7. Bull. JSME, Vol. 24(196), pp. 1537-1543.

Ohmi, M., Kyomen, S., & Usui, T., 1985. Numerical analysis of transient turbulent flow in a liquid line. Bull. of JSME, Vol. 28(239), pp. 799-806.

Okuyamaa, K., Tamuraa, A., Takahashia, S., Ohtsukaa, M., & Tsubakib, M., 2012. Flow-induced acoustic resonance at the mouth of one or two side branches. Nuclear Engineering and Design, 249, pp. 154–158.

Pezzinga, G., 1999. Quasi-2D model for unsteady flow in pipe networks. J. of Hydr. Eng., ASCE, Vol. 125(7), pp. 676–685.

Radavich, P.M., Selamet, A., & Novak, J.M., 2001. A Computational Approach for Flow-Acoustic Coupling in Closed Side Branches. J. Acoust. Soc. Am., 109, pp. 1343–1353.

Rich, G., 1945. Waterhammer Analysis by the Laplace-Mellin Transformations. Trans. ASME, 67(7) pp. 361–376.

Rockwell, D., & Schachenmann, A., 1983. The organized shear layer due to oscillations of a turbulent jet through an axisymmetric cavity. Journal of Sound and Vibration 87, pp. 371–382.

Rzentkowski, G., Forest, J.W., & Russel, J.H. 1993. Estimation of pump-generated pressure pulsations from instrument line measurements. Pump Noise and Vibrations, 1st International Symposium, Clamart, France.

Rzentkowski, G., & Zbroja, S., 2000. Experimental Characterization of Centrifugal Pumps as an Acoustic Source at the Blade-Passing Frequency. J. of Fluids and Structures, Vol. 14, pp. 529-558

Safwat, H.H., & Polder, J.V.D., 1973. Friction—Frequency Dependence For Oscillatory Flows In Circular Pipe. J. of The Hydraulics Division, ASCE, Vol. 99, No. HY11.

Sauer, R. E., 1969. Transient Viscous Losses during Turbulent Flow of a Liquid in a Pipe. MS thesis, Department of Mechanical Engineering, University of Kentucky.

Schohl, G.A., 1993. Improved approximation for simulating frequency-dependent friction in transient laminar flow. J. Fluids Eng., ASME, Vol. 115(3), pp. 420–424.

Svingen, B., 1997. Rayleigh Damping as An Approximate Model for Transient Hydraulic Pipe Friction. Proc., 8th Int. Meet. on the Behaviour of Hydraulic Machinery under Steady Oscillatory Conditions, IAHR, Chatou, France, Paper F-2

Shuy, E.B., 1995. Approximate wall shear equation for unsteady laminar pipe flows. J. Hydr. Res., Vol. (33) 4, pp. 457–469.

Silva-Araya, W.F., & Chaudhry, M.H., 1997. Computation of Energy Dissipation in Transient Flow. J. of Hydraulic Engineering, pp. 108-115.

Stirnemann, A., Eberl, J., Bolleter, U., & Pace, S., 1987. Experimental Determination of the Dynamic Transfer Matrix for a Pump. J. of Fluids Engineering, TRANS. ASME, Vol. 109, pp. 218-225.

Suzuki, K., Taketomi, T., & Sato, S. 1991. Improving Zielke's method of simulating frequency-dependent friction in laminar liquid pipe flow. J. Fluids Eng., ASME, Vol. 113(4), pp. 569–573.

Szymkiewicz, R., & Mitosek, M., 2004. Analysis of unsteady pipe flow using the modified finite element method. Commun. in Numer. Meth. in Eng., 21(4), pp. 183-199.

Takahashi, S., Ohtsuka, M., Okuyama, K., Ito, T., & Yoshikawa, K., 2008. Experimental study of acoustic and flow-induced vibrations in BWR main steam lines and steam dryers. ASME Pressure Vessels and Piping Division Conference, Chicago, Illinois, United States, 102.

Tonon, D., Hirschberg, A., Golliard, J., & Ziada, S., 2011. Aeroacoustics of pipe systems with closed branches. International Journal of Aeroacoustics Vol. 10, No. 2-3, pp. 201–276.

Tonon, D., Willems, J.F.H., & Hirschberg, A., 2011. Self-sustained oscillations in pipe systems with multiple deep side branches: prediction and reduction by detuning. Journal Of Sound And Vibration, Vol.330 (24), pp. 5894-5912.

Trikha, A.K., 1975. An efficient method for simulating frequency-dependent friction in transient liquid flow. J. Fluids Eng., Trans. ASME, 97(1), pp. 97-105.

Tu, S. W., & Ramaprian, B. R., 1983. Fully Developed Periodic Turbulent Pipe Flow.Part 1. Main Experimental Results and Comparison with Prediction. J. of Fluid Mech., Vol. 137, pp. 31-58.

Vardy, A.E., & Hwang, K.L., 1991. A characteristics model of transient friction in pipes. J. of Hydr. Res., IAHR, Vol. 29(5), pp. 669–684.

Vardy, A.E., 1992. Approximating unsteady friction at high Reynolds numbers. Pro., Int. Conf. On Unsteady Flow and Fluid Transients, Durham, England.

Vardy, A.E., Hwang, K.L., & Brown, J.M.B., 1993. A weighting function model of transient turbulent pipe flow. J. Hydr. Res., IAHR, Vol. 31(4), pp. 533–548.

Vardy, A.E., & Brown, J.M.B., 1995. Transient, turbulent, smooth pipe flow. J. Hydr. Res., IAHR, Vol. 33(4), pp. 435-456.

Vardy, A.E., & Brown, J.M.B., 1996. On turbulent, unsteady, smooth-pipe flow. Pro. Int. Conf. On Pressure Surges and Fluid Transients, BHR Group, pp. 289–311, Harrogate, England.

Vardy, A.E., & Brown, J.M.B., 2003. Transient turbulent friction in smooth pipe flows. J. of Sound and Vibration, Vol. 259(5), pp. 1011-1036.

Vardy, A.E., & Brown, J.M.B., 2004. Transient turbulent friction in fully rough pipe flows. J. of Sound and Vibration, Vol. 270, pp. 233-257.

Vardy, A., & Brown, J. 2004. Efficient Approximation of Unsteady Friction Weighting Functions. J. Hydraul. Eng., 10.1061/ (ASCE) 0733-9429(2004)130:11(1097), 1097-1107.

Vitkovsky, J., Stephens, M., Bergant, A., Lambert, M., & Simpson, A., 2004. Efficient and accurate calculation of Zielke and Vardy-Brown unsteady friction in pipe transients. Proc., 9th Int. conference on pressure surges, BHR Group.

Wilcox, D.C., 1986. Multiscale model for turbulent flows. In AIAA 24th Aerospace Sciences Meeting. American Institute of Aeronautics and Astronautics.

Wood, F. M., 1937. The Application of Heavisides Operational Calculus to the Solution of Problems in Waterhammer. Trans. ASME, 59, pp. 707–713.

Wood, D.J., Dorsch, R.G., & Lightner, C., 1966. Wave Plan Analysis of Unsteady Flow in Closed Conduits. Journal Hydraulic Div.-ASCE, 92:2:83.

Wood, D.J., & Funk, J.E., 1970. A boundary layer theory for transient viscous losses in turbulent flow. J. Basic Eng., Trans. ASME, pp. 865-873.

Wood, D.J., Lingireddy, S., Boulos, P.F., Karney, B.W., & McPherson, D.L., 2005. Numerical methods for modeling transient flow in distribution systems. Journal of the American Water Works Association, 97(7), pp. 104-115.

Wylie, E. B., & Streeter, V. L. 1993. Fluid Transient in Systems. Prentice-Hall, Englewood Cliffs.

Ziada, S., & Buhlmann, E.T., 1992. Self-excited resonances of two side-branches in close proximity. Journal of Fluids and Structures, 6, pp. 583–601.

Ziada, S., 1994. A flow visualisation study of flow-acoustic coupling at the mouth of a resonance side-branch. Journal of Fluids and Structures, 8, pp. 391–416.

Ziada, S., & Shine, S., 1999. Strouhal Numbers of Flow-Excited Acoustic Resonance in Side-Branches. Journal of Fluids and Structures, 13, pp. 127–142.

Ziada, S., Ng, H. & Blake, C. 2003. Flow-excited resonance of a confined shallow cavity in low Mach number flow and its control. Journal of Fluids and structures, 18, pp. 79-92.

Ziada, S., 2010. Flow-excited acoustic resonance in industry. Journal of Pressure Vessel Technology, TRANS. ASME, 132:1-9, 8, 65, 102.

Zielke, W., 1967. Frequency dependent friction in transient pipe flow. Trans. ASME, Journal of Basic Engineering, Vol. 90, pp. 109-115.

Zielke, W., Wylie, E. B., & Keller, R. B., 1969. Forced and Self-Excited Oscillations in Propellant Lines. Journal of Basic Engineering, TRANS. ASME, pp. 671-677.

Zhao, M., & Ghidaoui, M.S., 2004. Godunov-type solutions for water hammer flows. Journal of Hydraulic Engineering, 130(4), pp. 341-348

Appendix A

Adaptor and Sleeves Drawings

Drawings of the adaptor designed to align the shaker and cylinder and the sleeves designed to place the pressure transducers as flush as possible at the tubes are presented here. These drawings are made by the author and built at the university machine shop.

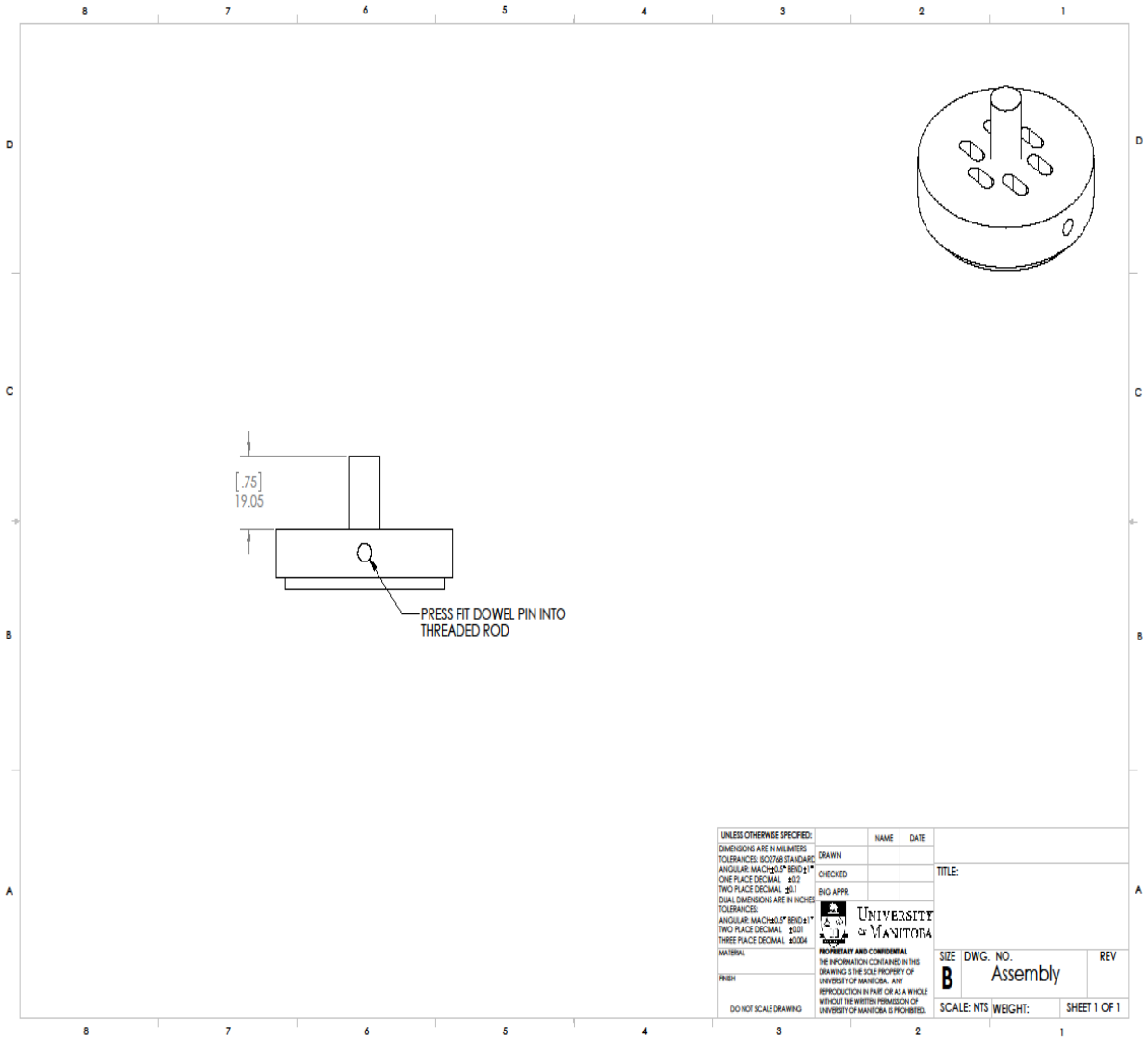

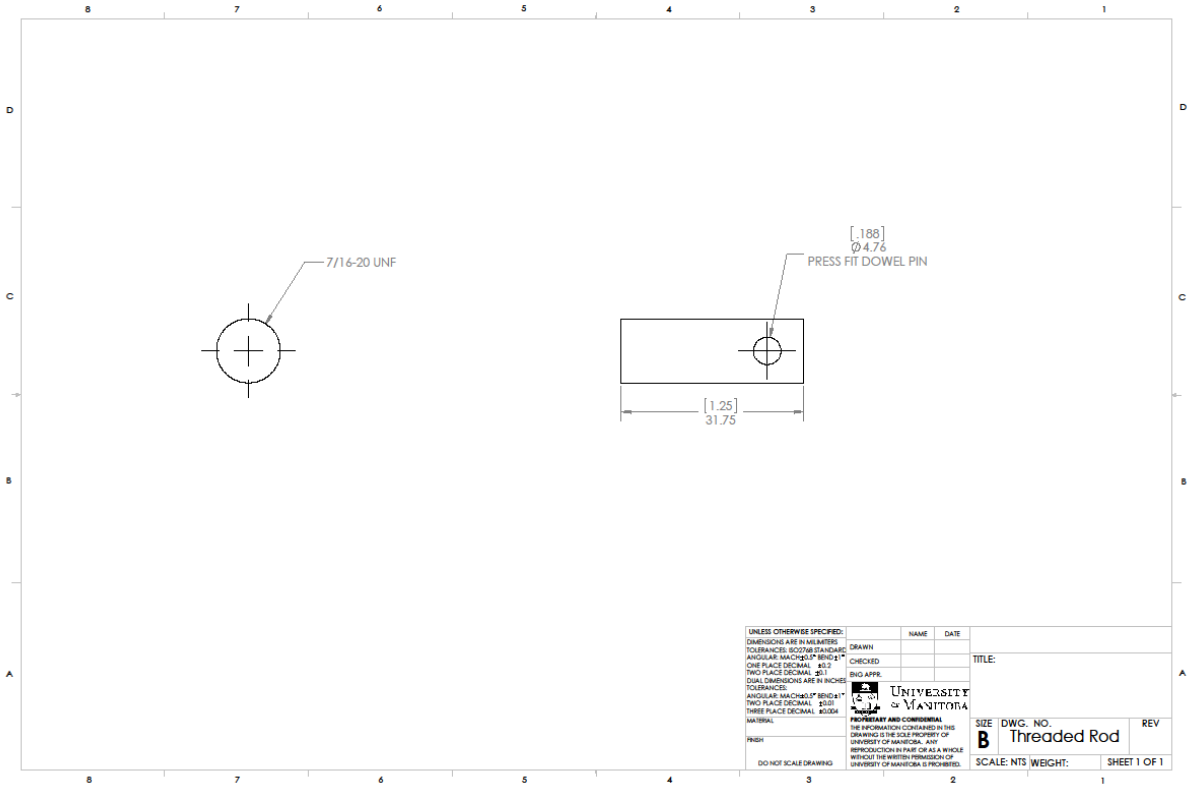
7/16-20 UNF
[.188]
Ø4.76
PRESS FIT DOWEL PIN
[1.25]
31.75
UNLESS OTHERWISE SPECIFIED:
DIMENSIONS ARE IN MILIMETERS
TOLERANCES: ISO2768 STANDARD
ANGULAR: MACH±0.5° BEND±1°
ONE PLACE DECIMAL ±0.2
TWO PLACE DECIMAL ±0.1
DUAL DIMENSIONS ARE IN INCHES
TOLERANCES:
ANGULAR: MACH±0.5° BEND±1°
TWO PLACE DECIMAL ±.01
THREE PLACE DECIMAL ±.004
MATERIAL
FINISH
DO NOT SCALE DRAWING
NAME
DATE
DRAWN
CHECKED
ENG APPR.
UNIVERSITY of MANITOBA
PROPRIETARY AND CONFIDENTIAL
THE INFORMATION CONTAINED IN THIS DRAWING IS THE SOLE PROPERTY OF UNIVERSITY OF MANITOBA. ANY REPRODUCTION IN PART OR AS A WHOLE WITHOUT THE WRITTEN PERMISSION OF UNIVERSITY OF MANITOBA IS PROHIBITED.
TITLE:
SIZE
B
DWG. NO.
Threaded Rod
REV
SCALE: NTS
WEIGHT:
SHEET 1 OF 1

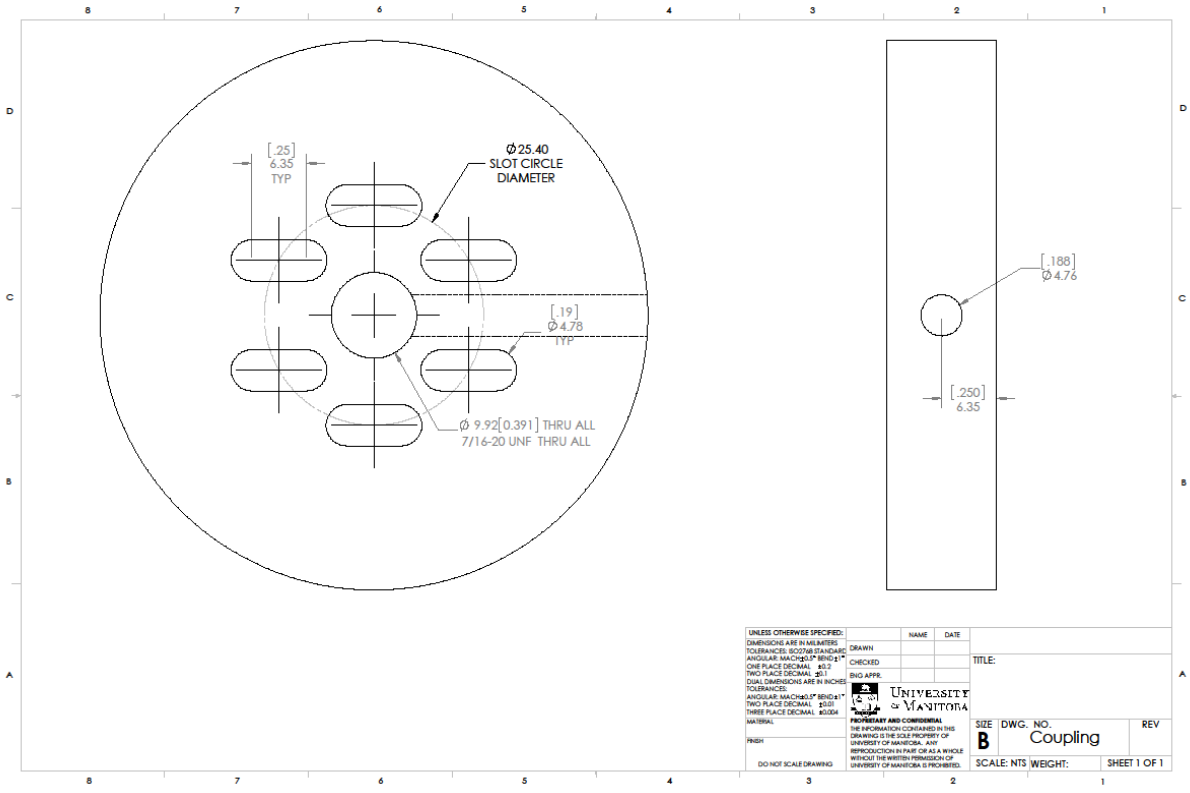
[.25]
6.35
TYP
Ø25.40
SLOT CIRCLE
DIAMETER
[.19]
Ø4.78
TYP
Ø 9.92[0.391] THRU ALL
7/16-20 UNF THRU ALL
[.188]
Ø4.76
[.250]
6.35
UNLESS OTHERWISE SPECIFIED:
DIMENSIONS ARE IN MILIMETERS
TOLERANCES: ISO2768 STANDARD
ANGULAR: MACH±0.5° BEND±1°
ONE PLACE DECIMAL ±0.2
TWO PLACE DECIMAL ±0.1
DUAL DIMENSIONS ARE IN INCHES
TOLERANCES:
ANGULAR: MACH±0.5° BEND±1°
TWO PLACE DECIMAL ±.01
THREE PLACE DECIMAL ±.004
MATERIAL
FINISH
DO NOT SCALE DRAWING
NAME
DATE
DRAWN
CHECKED
ENG APPR.
UNIVERSITY of MANITOBA
PROPRIETARY AND CONFIDENTIAL
THE INFORMATION CONTAINED IN THIS DRAWING IS THE SOLE PROPERTY OF UNIVERSITY OF MANITOBA. ANY REPRODUCTION IN PART OR AS A WHOLE WITHOUT THE WRITTEN PERMISSION OF UNIVERSITY OF MANITOBA IS PROHIBITED.
TITLE:
SIZE
B
DWG. NO.
Coupling
REV
SCALE: NTS
WEIGHT:
SHEET 1 OF 1

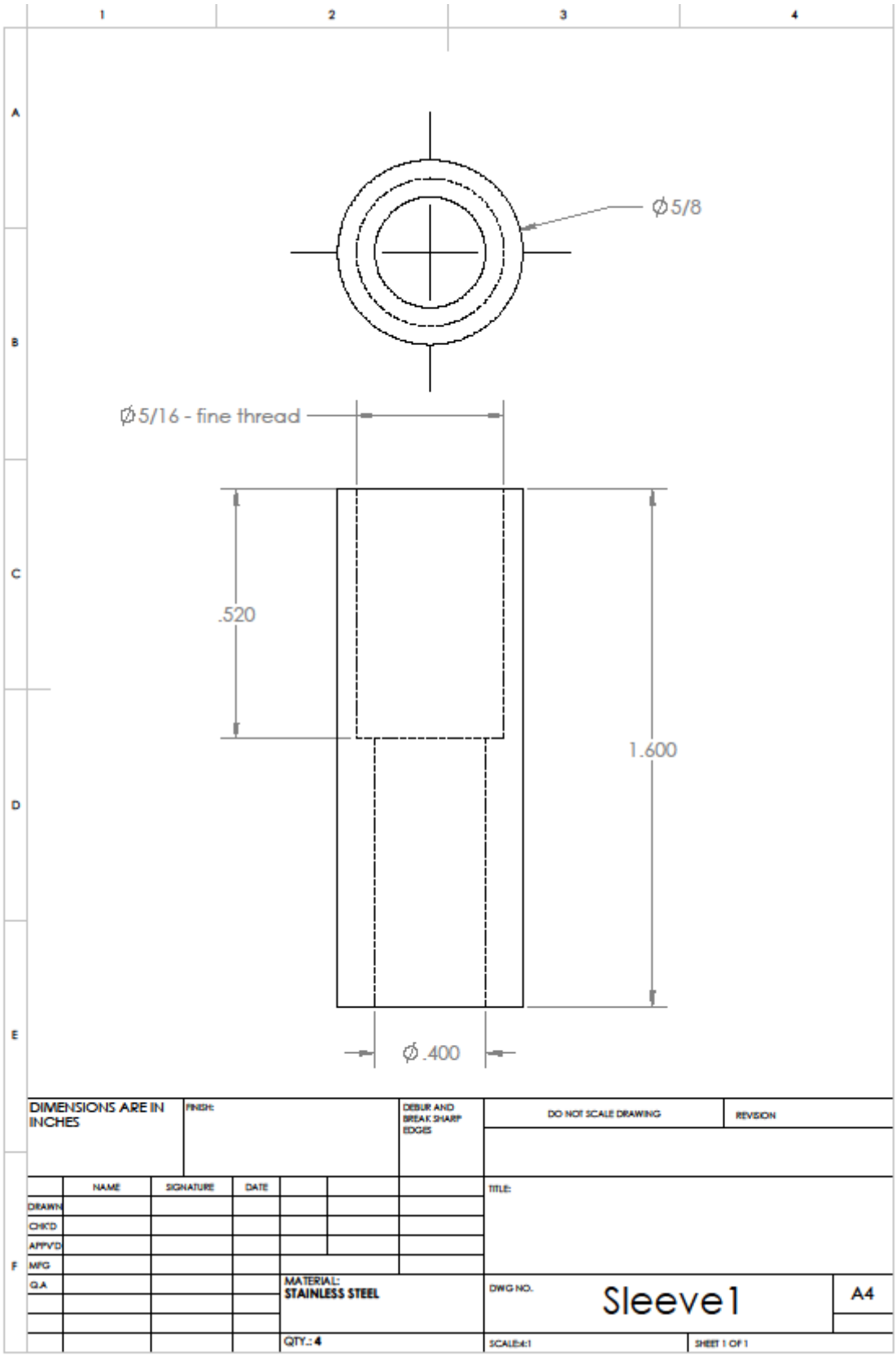
1
2
3
4
A
B
C
D
E
F
Ø5/8
Ø5/16 - fine thread
.520
1.600
Ø.400
DIMENSIONS ARE IN INCHES
FINISH:
DEBUR AND BREAK SHARP EDGES
DO NOT SCALE DRAWING
REVISION
NAME
SIGNATURE
DATE
DRAWN
CHK'D
APPV'D
MFG
Q.A
TITLE:
MATERIAL:
STAINLESS STEEL
DWG NO.
Sleeve1
A4
QTY.: 4
SCALE:4:1
SHEET 1 OF 1

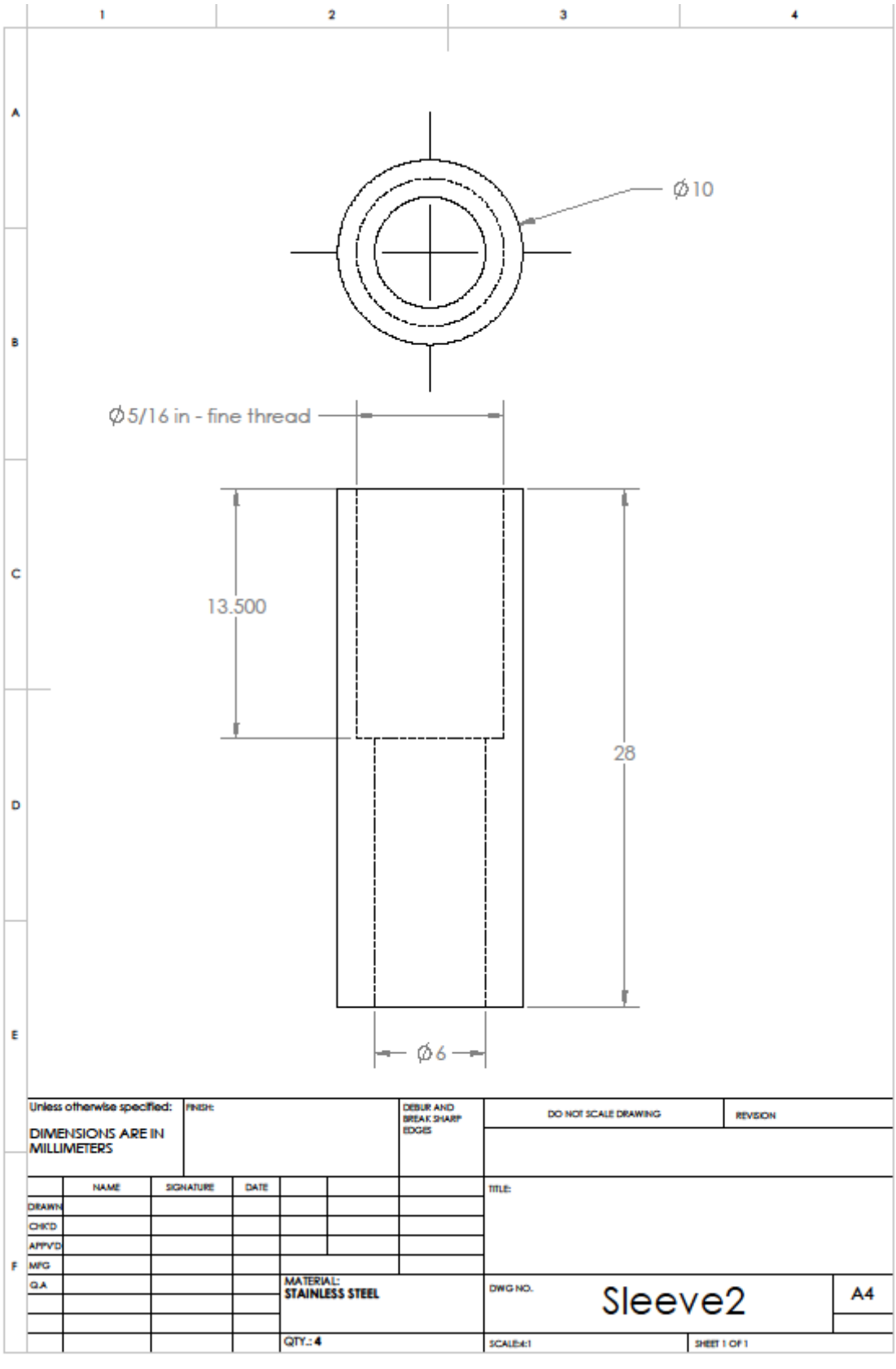
1
2
3
4
A
B
C
D
E
F
Ø10
Ø5/16 in - fine thread
13.500
28
Ø6
Unless otherwise specified:
DIMENSIONS ARE IN MILLIMETERS
FINISH:
DEBUR AND BREAK SHARP EDGES
DO NOT SCALE DRAWING
REVISION
NAME
SIGNATURE
DATE
DRAWN
CHK'D
APPV'D
MFG
Q.A
TITLE:
MATERIAL:
STAINLESS STEEL
DWG NO.
Sleeve2
A4
QTY.: 4
SCALE:4:1
SHEET 1 OF 1

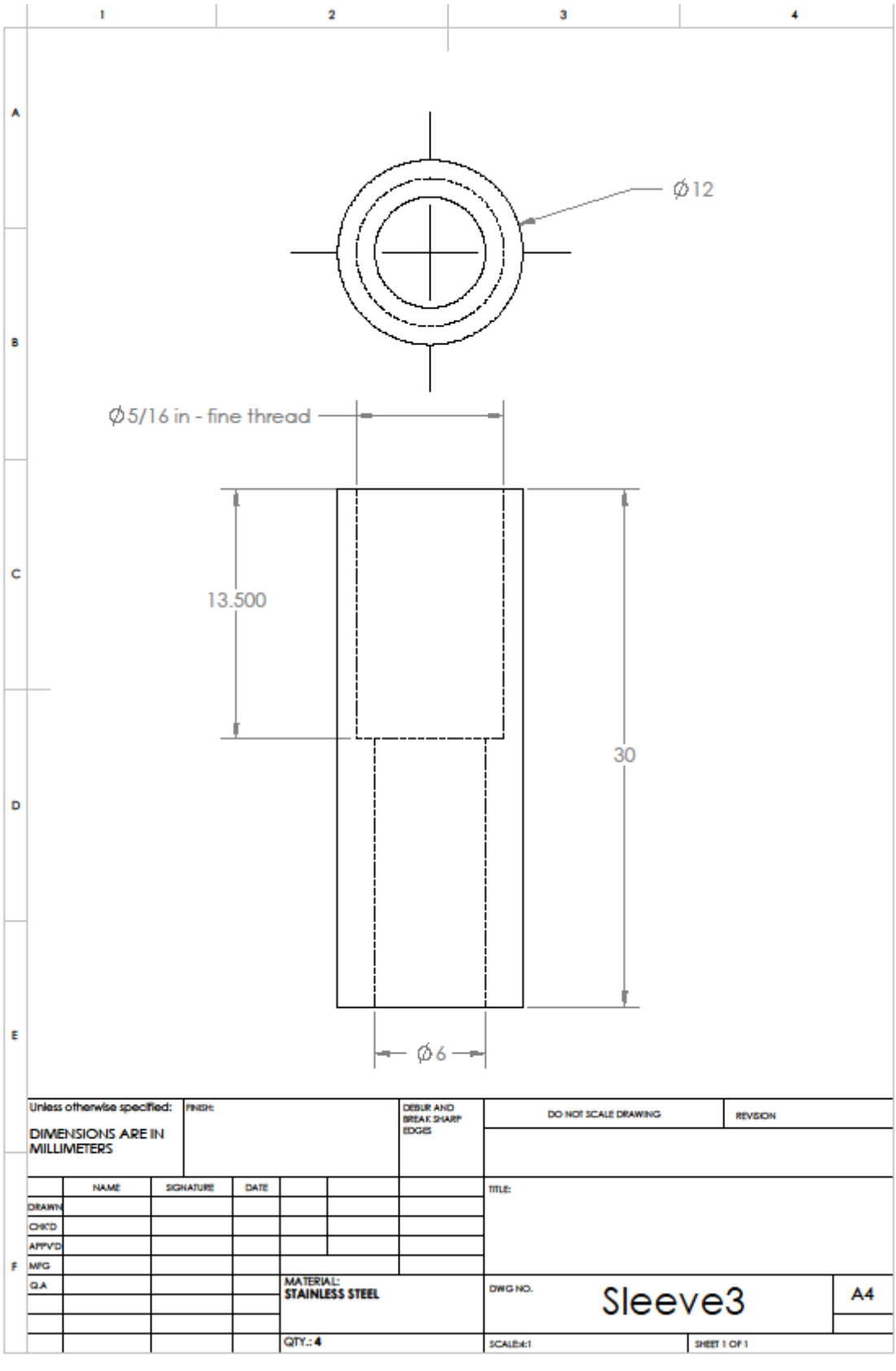
1
2
3
4
A
B
C
D
E
F
Ø12
Ø5/16 in - fine thread
13.500
30
Ø6
Unless otherwise specified:
DIMENSIONS ARE IN MILLIMETERS
FINISH:
DEBUR AND BREAK SHARP EDGES
DO NOT SCALE DRAWING
REVISION
NAME
SIGNATURE
DATE
DRAWN
CHK'D
APPV'D
MFG
Q.A
TITLE:
MATERIAL:
STAINLESS STEEL
DWG NO.
Sleeve3
A4
QTY.: 4
SCALE:4:1
SHEET 1 OF 1

Appendix B

ABAQUS General Formulation

The equation for small movement of a fluid with compressibility and velocity dependent losses is

$$\frac{\partial p}{\partial X}+\gamma(X,\theta_i)\,\dot{u}^f+\rho_f(X,\theta_i)\ddot{u}^f=0 \quad (4B.1)$$

where p is acoustic pressure, X is fluid lateral position; $\dot{u}^f$, $\ddot{u}^f$, ρ_f and γ are fluid particle velocity, acceleration, density and volumetric drag, respectively; θ_i is i independent field variable such as temperature on which ρ_f and γ may depend. Assuming no flowing fluid, the d'Alembert term has been written without convection, which is usually considered to be sufficiently accurate for steady fluid velocities up to Mach 0.1 (ABAQUS 6.12 User Manual).

The fluid is assumed to be inviscid, linear, and compressible, so

$$p=-K_f(X,\theta_i)\frac{\partial}{\partial X}.\dot{u}^f \quad (4B.2)$$

where K_f is the bulk modulus of the fluid.

In ABAQUS with respect to the volumetric drag value and changing the lateral position, the finite element formulations are to some extent different in direct integration transient and steady-state or modal analyses. For linear transient dynamic analysis, the modal technique can be used and is much more proficient.

To develop the partial differential equation used in direct integration transient analysis, Equation 4B.1 is divided by ρ_f, the gradient is taken with respect to $\mathbf{x}$, the gradient of $\frac{\gamma}{\rho_f}$ is ignored, and the result with the time derivatives of Equation 4B.2 is combined to obtain the equation of motion for the fluid in terms of the fluid pressure:

$$\frac{1}{K_f}\ddot{p}+\frac{\gamma}{\rho_f K_f}\dot{p}-\frac{\partial}{\partial X}.\left(\frac{1}{\rho_f}\frac{\partial p}{\partial X}\right)=0 \qquad (4B.3)$$

Dissipation of energy and attenuation of acoustic waves may occur in an acoustic medium due to a variety of factors. Such dissipation effects are considered in the frequency domain by the imaginary part of the propagation constant, which gives an exponential decay in amplitude as a function of distance. In ABAQUS the simplest way to model this effect is through a volumetric drag coefficient. In frequency-domain procedures, γ could be frequency-dependent. γ can be entered as a function of frequency $\gamma(f)$ in a steady-state dynamics procedure, where f is the frequency in cycles per time (usually Hz). If the acoustic medium is used in a direct-integration dynamic procedure, the volumetric drag coefficient is assumed to be independent of frequency and the first value entered for the current temperature and/or field variable is used.

To obtain acceptable results, the following requirements must be fulfilled. For the first order elements, the element sizes supposed to be taken in a way that the biggest one is at least six times smaller than the acoustic wavelength. For the second order elements, this requirement is twice smaller (ABAQUS 6.12 User Manual).

Appendix C

Experimental Data at the Resonant Points

Stainless steel 6.13 m length Closed End (10 mm O.D) 1st Resonant Peak	Frequency (Hz)	Amplitude	Temperature ^{o}C
Test #1	56.25	62.42	23.1
Test #2	56.25	62.5	23
Test #3	56.25	62.45	23
Test #4	56.25	62.39	23
Test #5	56.25	62.47	23.1
Test #6	56.25	62.61	23
Test #7	56.25	62.42	23
Test #8	56.25	62.5	23
Test #9	56.25	62.45	23
Test #10	56.25	62.5	23

Stainless steel 6.13 m length Closed End (10 mm O.D) 2nd Resonant Peak	Frequency (Hz)	Amplitude	Temperature ^{o}C
Test #1	173.25	34.25	23
Test #2	173.25	35.41	23
Test #3	173.25	35.3	23
Test #4	173	35.26	22.9
Test #5	173.25	35.34	23
Test #6	173.25	35.3	23
Test #7	173.25	35.38	23
Test #8	173	35.3	23.1
Test #9	173.25	35.27	23
Test #10	173.25	35..3	23

Stainless steel 6.13 m length Closed End (10 mm O.D) 3rd Resonant Peak	Frequency (Hz)	Amplitude	Temperature ^{o}C
Test #1	289	23.44	23
Test #2	289	23.51	23
Test #3	289	23.5	23
Test #4	289	23.5	23.1
Test #5	289	23.56	23
Test #6	289.25	23.39	23.2
Test #7	289	23.5	23
Test #8	289	23.41	23
Test #9	289.25	23.5	23
Test #10	289	23.5	23

Stainless steel 6.13 m length Closed End (10 mm O.D) 4th Resonant Peak	Frequency (Hz)	Amplitude	Temperature ^{o}C
Test #1	400.75	14.6	23
Test #2	400.75	14.61	23
Test #3	400.75	14.52	22.9
Test #4	400.5	14.6	23
Test #5	400.75	14.55	23
Test #6	400.75	14.49	23
Test #7	401	14.6	23.1
Test #8	400.75	14.51	23
Test #9	400.75	14.58	23
Test #10	400.5	14.6	23.1

Stainless steel 6.13 m length Closed End (12 mm O.D) 1st Resonant Peak	Frequency (Hz)	Amplitude	Temperature ^{o}C
Test #1	56.75	66.4	23
Test #2	56.75	66.38	23
Test #3	56.75	66.4	23
Test #4	56.75	66.4	23
Test #5	56.75	66.53	23
Test #6	56.75	66.43	23
Test #7	56.75	66.49	23.1
Test #8	56.75	66.4	23
Test #9	56.75	66.46	23
Test #10	56.75	66.4	23

Stainless steel 6.13 m length Closed End (12 mm O.D) 2nd Resonant Peak	Frequency (Hz)	Amplitude	Temperature ^{o}C
Test #1	175	37.5	23
Test #2	175	37.52	23
Test #3	175	37.47	23
Test #4	175	37.5	23
Test #5	175	37.49	23
Test #6	175.25	37.5	23
Test #7	175	37.5	23
Test #8	175	37.53	23
Test #9	175	37.48	23.1
Test #10	175	37.5	23.1

Stainless steel 6.13 m length Closed End (12 mm O.D) 3rd Resonant Peak	Frequency (Hz)	Amplitude	Temperature ^{o}C
Test #1	289.75	27.63	23.1
Test #2	289.5	27.58	23
Test #3	289.75	27.61	23
Test #4	289.75	27.6	23
Test #5	289.75	27.6	23
Test #6	289.75	27.64	23
Test #7	289.75	27.6	23
Test #8	289.5	27.59	23
Test #9	289.75	27.54	22.9
Test #10	289.75	27.6	23

Stainless steel 6.13 m length Closed End (12 mm O.D) 4th Resonant Peak	Frequency (Hz)	Amplitude	Temperature ^{o}C
Test #1	404	15.7	23
Test #2	404	15.75	23
Test #3	404	15.69	23
Test #4	404.25	15.7	23.1
Test #5	404	15.65	23
Test #6	404.25	15.68	23
Test #7	404	15.72	23
Test #8	404	15.7	22.9
Test #9	404	15.72	23.1
Test #10	404	15.74	23

Stainless steel 6.13 m length Closed End (12 mm O.D) 1st Resonant Peak	Frequency (Hz)	Amplitude	Temperature ^{o}C
Test #1	54.5	59.17	23
Test #2	54.5	59.2	23
Test #3	54.5	59.24	23
Test #4	54.5	59.19	23
Test #5	54.5	59.2	23
Test #6	54.5	59.21	23
Test #7	54.5	59.17	23
Test #8	54.5	59.23	23
Test #9	54.5	59.18	23
Test #10	54.5	59.2	23

Stainless steel 6.13 m length Closed End (12 mm O.D) 2nd Resonant Peak	Frequency (Hz)	Amplitude	Temperature ^{o}C
Test #1	165	29.8	23
Test #2	164.75	29.77	23
Test #3	164.75	29.8	23.1
Test #4	164.75	29.84	23
Test #5	164.75	29.76	23
Test #6	164.75	29.79	23
Test #7	164.75	29.81	23
Test #8	164.75	29.84	23
Test #9	164.75	29.8	23
Test #10	164.75	29.78	23

Stainless steel 6.13 m length Closed End (12 mm O.D) 3rd Resonant Peak	Frequency (Hz)	Amplitude	Temperature ^{o}C
Test #1	277.25	17.93	23
Test #2	277.25	17.91	23.1
Test #3	277	17.9	23
Test #4	277.25	17.86	23
Test #5	277.25	17.89	23
Test #6	277.5	17.9	23
Test #7	277.5	17.9	23
Test #8	277.25	17.88	23
Test #9	277.25	17.9	23
Test #10	277.25	17.91	23.1

Stainless steel 6.13 m length Closed End (12 mm O.D) 4th Resonant Peak	Frequency (Hz)	Amplitude	Temperature ^{o}C
Test #1	389.75	10.65	23
Test #2	389.75	10.62	23
Test #3	389.75	10.65	23
Test #4	389.75	10.6	23.1
Test #5	389.75	10.66	23.1
Test #6	389.75	10.64	23.1
Test #7	389.75	10.62	23
Test #8	389.5	10.65	23.1
Test #9	389.75	10.68	23
Test #10	389.75	10.59	23

Aluminum 8 m length Closed End (12mm & 16 mm O.D) 1st Resonant Peak	Frequency (Hz)	Amplitude	Temperature ^{o}C
Test #1	40.75	40.46	23
Test #2	40.75	40.5	23
Test #3	40.75	40.49	23
Test #4	40.75	40.5	23
Test #5	40.75	40.51	23
Test #6	40.75	40.5	23
Test #7	40.75	40.47	23
Test #8	40.75	40.5	23
Test #9	40.75	40.46	22.9
Test #10	40.75	40.5	23

Aluminum 8 m length Closed End (12mm & 16 mm O.D) 2nd Resonant Peak	Frequency (Hz)	Amplitude	Temperature ^{o}C
Test #1	132	25.03	23
Test #2	132	24.92	23
Test #3	132	25	23
Test #4	132	25	23
Test #5	132	25.08	23
Test #6	132	25.4	23
Test #7	132	25	23.1
Test #8	132	24.05	23
Test #9	132	25	23
Test #10	132	25.1	23.1

Aluminum 8 m length Closed End (12mm & 16 mm O.D) 3rd Resonant Peak	Frequency (Hz)	Amplitude	Temperature °C
Test #1	218	15.38	23
Test #2	218	15.4	23
Test #3	218	15.38	23
Test #4	218	15.41	23
Test #5	218	15.39	23.1
Test #6	218	15.42	23.1
Test #7	218	15.35	23
Test #8	218	15.38	23
Test #9	218	15.38	23
Test #10	218	15.42	23

Aluminum 8 m length Closed End (12mm & 16 mm O.D) 4th Resonant Peak	Frequency (Hz)	Amplitude	Temperature °C
Test #1	306.25	10.84	23
Test #2	306.25	10.88	23.1
Test #3	306.25	10.84	23
Test #4	306.25	10.86	23
Test #5	306.25	10.8	22.9
Test #6	306.25	10.86	23
Test #7	306.25	10.86	23
Test #8	306.25	10.92	23
Test #9	306.25	10.86	23
Test #10	306.25	10.89	23.1

Aluminum 8 m length Closed End (12mm & 16 mm O.D) 5th Resonant Peak	Frequency (Hz)	Amplitude	Temperature °C
Test #1	384	8	23
Test #2	384	7.99	23
Test #3	384	7.96	23
Test #4	384	8.04	23.1
Test #5	384	8.01	23.1
Test #6	384	7.99	23.1
Test #7	384	7.99	23
Test #8	384	8.02	23.1
Test #9	384	8	23
Test #10	384	7.99	23

Aluminum 8 m length Closed End (12mm & 16 mm O.D) 6th Resonant Peak	Frequency (Hz)	Amplitude	Temperature °C
Test #1	468.5	5.98	23
Test #2	468.5	5.96	23
Test #3	468.5	5.98	23.1
Test #4	468.5	5.96	23.1
Test #5	468.5	5.98	23
Test #6	468.5	5.97	23
Test #7	468.5	5.98	23
Test #8	468.5	5.91	22.9
Test #9	468.5	6.01	23.1
Test #10	468.5	6.03	23.1

7.18 m elbow Closed End (10 mm O.D) 1st Resonant Peak	**Frequency (Hz)**	**Amplitude**	**Temperature °C**
Test #1	48.75	64.25	23
Test #2	48.75	64.3	23
Test #3	48.75	64.32	23
Test #4	48.75	64.27	23
Test #5	48.75	64.3	23
Test #6	48.75	64.3	23
Test #7	48.75	64.28	23
Test #8	48.75	64.31	23
Test #9	48.75	64.3	23
Test #10	48.75	64.32	23

7.18 m elbow Closed End (10 mm O.D) 2nd Resonant Peak	Frequency (Hz)	Amplitude	Temperature °C
Test #1	143.50	40.37	23.1
Test #2	143.50	40.41	23
Test #3	143.50	40.4	23
Test #4	143.50	40.4	23
Test #5	143.50	40.4	23
Test #6	143.50	40.42	23
Test #7	143.25	40.38	23
Test #8	143.50	40.4	23
Test #9	143.50	40.4	23
Test #10	143.50	40.39	23

7.18 m elbow Closed End (10 mm O.D) 3rd Resonant Peak	Frequency (Hz)	Amplitude	Temperature °C
Test #1	244.75	26.53	23
Test #2	244.75	26.49	23
Test #3	244.75	26.5	23
Test #4	244.75	26.5	23
Test #5	245	26.5	23
Test #6	244.75	26.5	23
Test #7	244.75	26.52	23
Test #8	244.75	26.48	23
Test #9	244.75	26.5	23
Test #10	244.75	26.51	22.9

7.18 m elbow Closed End (10 mm O.D) 4th Resonant Peak	Frequency (Hz)	Amplitude	Temperature °C
Test #1	340.5	18.81	23
Test #2	340.25	18.8	23.1
Test #3	340.5	18.82	23
Test #4	340.5	18.8	23
Test #5	340.5	18.76	23
Test #6	340.5	18.78	23
Test #7	340.5	18.8	23
Test #8	340.5	18.79	23.1
Test #9	340.5	18.8	23
Test #10	340.5	18.82	23

7.18 m elbow Closed End (10 mm O.D) 5th Resonant Peak	Frequency (Hz)	Amplitude	Temperature °C
Test #1	440.25	10.3	23.1
Test #2	440.25	10.32	23
Test #3	440.25	10.3	23
Test #4	440.25	10.27	23
Test #5	440.25	10.31	23
Test #6	440.25	10.3	23
Test #7	440.25	10.3	23
Test #8	440.25	10.32	23
Test #9	440.25	10.3	23
Test #10	440.25	10.28	23.1

Branch 1 Closed End (10 mm O.D) 1st Resonant Peak	Frequency (Hz)	Amplitude	Temperature °C
Test #1	42.75	55.14	23
Test #2	42.75	55.1	23
Test #3	42.75	55.08	23
Test #4	42.75	55.1	23
Test #5	42.75	55.11	23
Test #6	42.75	55.1	23
Test #7	42.75	55.1	23
Test #8	42.75	55.12	23
Test #9	42.75	55.1	23
Test #10	42.75	55.11	23

Branch 1 Closed End (10 mm O.D) 2nd Resonant Peak	Frequency (Hz)	Amplitude	Temperature °C
Test #1	136.75	35.1	23
Test #2	136.75	35.12	23
Test #3	136.75	35.1	23
Test #4	136.75	35.09	23
Test #5	136.75	35.1	23
Test #6	136.75	35.11	23
Test #7	136.75	35.1	23
Test #8	136.75	35.07	23
Test #9	136.75	35.1	23
Test #10	136.5	35.12	23

Branch 1 Closed End (10 mm O.D) 3rd Resonant Peak	Frequency (Hz)	Amplitude	Temperature °C
Test #1	241.5	22.88	23
Test #2	241.5	22.93	23.1
Test #3	241.5	22.91	23.1
Test #4	241.5	22.9	23
Test #5	241.5	22.9	23
Test #6	241.5	22.89	23
Test #7	241.5	22.9	23
Test #8	241.5	22.9	23
Test #9	241.5	22.91	23
Test #10	241.5	22.9	23

Branch 1 Closed End (10 mm O.D) 4th Resonant Peak	Frequency (Hz)	Amplitude	Temperature °C
Test #1	345.75	9.11	23
Test #2	345.75	9.08	23
Test #3	345.5	9.1	23
Test #4	345.75	9.1	23
Test #5	345.75	9.12	23
Test #6	345.75	9.1	23
Test #7	345.75	9.1	23
Test #8	345.75	9.09	23
Test #9	345.75	9.1	23
Test #10	345.75	9.11	23

Branch 1 Closed End (10 mm O.D) 5th Resonant Peak	Frequency (Hz)	Amplitude	Temperature °C
Test #1	456	15.73	23
Test #2	456	15.7	23
Test #3	456	15.68	23
Test #4	456	15.7	23
Test #5	456	15.69	23
Test #6	456	15.7	23
Test #7	456	15.7	23
Test #8	456.25	15.72	23
Test #9	456	15.7	23
Test #10	456	15.72	23.1

Branch 2 Closed End (10 mm O.D) 1st Resonant Peak	Frequency (Hz)	Amplitude	Temperature °C
Test #1	43	48.52	23
Test #2	43	48.52	23
Test #3	43	48.49	23
Test #4	43	48.5	23
Test #5	43	48.51	23
Test #6	43	48.5	23
Test #7	43	48.5	23
Test #8	43	48.5	23
Test #9	43	48.48	23
Test #10	43	48.5	23

Branch 2 Closed End (10 mm O.D) 2nd Resonant Peak	Frequency (Hz)	Amplitude	Temperature °C
Test #1	136.25	29.2	23
Test #2	136.25	29.21	23
Test #3	136.25	29.22	23
Test #4	136.25	29.19	23
Test #5	136.25	29.2	23
Test #6	136.25	29.2	23
Test #7	136.25	29.21	23
Test #8	136.25	29.2	23
Test #9	136.25	29.21	23
Test #10	136.25	29.2	23

Branch 2 Closed End (10 mm O.D) 3rd Resonant Peak	Frequency (Hz)	Amplitude	Temperature °C
Test #1	241	18.82	23
Test #2	241	18.8	23
Test #3	241	18.79	23
Test #4	241	18.8	23
Test #5	241	18.8	23
Test #6	241	18.81	23.1
Test #7	241.25	18.8	23
Test #8	241	18.78	23
Test #9	241	18.79	23
Test #10	241	18.8	23

Branch 2 Closed End (10 mm O.D) 4th Resonant Peak	Frequency (Hz)	Amplitude	Temperature °C
Test #1	345.5	7.83	23
Test #2	345.5	7.85	23
Test #3	345.5	7.86	23
Test #4	345.5	7.85	23
Test #5	345.5	7.84	23
Test #6	345.5	7.85	23
Test #7	345.5	7.85	23
Test #8	345.5	7.85	23
Test #9	345.5	7.83	23
Test #10	345.5	7.86	23.1

Branch 2 Closed End (10 mm O.D) 5th Resonant Peak	Frequency (Hz)	Amplitude	Temperature °C
Test #1	455.5	11.82	23
Test #2	455.5	11.8	23
Test #3	455.5	11.8	23
Test #4	455.5	11.81	23
Test #5	455.5	11.8	23
Test #6	455.5	11.8	23
Test #7	455.5	11.8	23
Test #8	455.25	11.78	23
Test #9	455.5	11.81	23.1
Test #10	455.5	11.82	23.1

Branch 3, Main line, Closed End (10 mm O.D) 1st Resonant Peak	Frequency (Hz)	Amplitude	Temperature °C
Test #1	46	54	23
Test #2	46	53.96	23
Test #3	46	54.03	23
Test #4	46	54.05	23
Test #5	46	54	23
Test #6	46	54	23
Test #7	46	53.98	23
Test #8	46	54	23
Test #9	46	54	23
Test #10	46	54.02	23

Branch 3, Main line, Closed End (10 mm O.D) 2nd Resonant Peak	Frequency (Hz)	Amplitude	Temperature °C
Test #1	106.25	16.94	23
Test #2	106.25	16.88	23
Test #3	106.25	16.9	23
Test #4	106.25	16.9	23
Test #5	106.25	16.92	23
Test #6	106.25	16.9	23
Test #7	106.25	16.93	23.1
Test #8	106.25	16.9	23
Test #9	106.25	16.9	23
Test #10	106.25	16.87	23

Branch 3, Main line, Closed End (10 mm O.D) 3rd Resonant Peak	Frequency (Hz)	Amplitude	Temperature °C
Test #1	173	3.39	23
Test #2	173	3.36	23
Test #3	173	3.36	23
Test #4	173	3.33	23
Test #5	173	3.36	23
Test #6	173	3.38	23
Test #7	173	3.36	23
Test #8	172.75	3.36	23
Test #9	173	3.35	23
Test #10	173	3.41	23.1

Branch 3, Main line, Closed End (10 mm O.D) 4th Resonant Peak	Frequency (Hz)	Amplitude	Temperature °C
Test #1	235.75	11.9	23
Test #2	235.75	11.94	23
Test #3	235.75	11.92	23
Test #4	235.75	11.9	23
Test #5	235.75	11.9	23
Test #6	235.75	11.87	22.9
Test #7	235.75	11.9	23
Test #8	235.75	11.9	23
Test #9	235.75	11.91	23
Test #10	235.75	11.92	23

Branch 3, Main line, Closed End (10 mm O.D) 5th Resonant Peak	Frequency (Hz)	Amplitude	Temperature °C
Test #1	301	18.97	23
Test #2	301	18.94	23
Test #3	301	18.94	23
Test #4	301	18.92	23
Test #5	301	18.94	23
Test #6	301	18.98	23
Test #7	301	18.91	23
Test #8	301	18.94	23
Test #9	301	18.94	23
Test #10	301	18.92	23

Branch 3, Main line, Closed End (10 mm O.D) 6th Resonant Peak	Frequency (Hz)	Amplitude	Temperature °C
Test #1	379	7.44	23
Test #2	379	7.40	23
Test #3	379	7.44	23
Test #4	379	7.45	23
Test #5	379	7.47	23.1
Test #6	379	7.44	23
Test #7	379	7.44	23
Test #8	379	7.44	23
Test #9	379	7.48	23
Test #10	379	7.46	23

Branch 3, Main line, Closed End (10 mm O.D) 7th Resonant Peak	Frequency (Hz)	Amplitude	Temperature °C
Test #1	400.5	34.75	23.1
Test #2	400.5	34.72	23
Test #3	400.5	34.7	23
Test #4	400.5	34.7	23
Test #5	400.5	34.71	23
Test #6	400.5	34.7	23
Test #7	400.25	34.67	23
Test #8	400.5	34.7	23
Test #9	400.5	34.7	23
Test #10	400.5	34.7	23

Branch 3, Main line, Closed End (10 mm O.D) 8th Resonant Peak	Frequency (Hz)	Amplitude	Temperature °C
Test #1	455.5	4.93	23
Test #2	455.5	4.95	23
Test #3	455.5	4.95	23
Test #4	455.5	4.95	23
Test #5	455.5	4.98	23
Test #6	455.5	4.96	23
Test #7	455.5	4.97	23
Test #8	455.5	4.95	23
Test #9	455.5	4.95	23
Test #10	455.5	4.99	23.1

Branch 3, 2.07 m Branch, Closed End (10 mm O.D) 1st Resonant Peak	Frequency (Hz)	Amplitude	Temperature ^{o}C
Test #1	46	15.7	23
Test #2	46	15.72	23
Test #3	46	15.7	23
Test #4	46	15.74	23
Test #5	46	15.73	23
Test #6	46	15.7	23
Test #7	46	15.7	23
Test #8	46	15.7	23
Test #9	46	15.68	23
Test #10	46	15.7	23

Branch 3, 2.07 m Branch, Closed End (10 mm O.D) 2nd Resonant Peak	Frequency (Hz)	Amplitude	Temperature ^{o}C
Test #1	106.25	39.23	23
Test #2	106.25	39.22	23
Test #3	106.25	39.2	23
Test #4	106.25	39.2	23
Test #5	106.25	39.21	23
Test #6	106.25	39.2	23
Test #7	106.25	39.18	23
Test #8	106.25	39.2	23
Test #9	106.25	39.2	23
Test #10	106.25	39.2	23

Branch 3, 2.07 m Branch, Closed End (10 mm O.D) 3rd Resonant Peak	Frequency (Hz)	Amplitude	Temperature ^{o}C
Test #1	173.5	5.77	23
Test #2	173.5	5.75	23
Test #3	173.5	5.75	23
Test #4	173.5	5.74	23
Test #5	173.5	5.75	23
Test #6	173.5	5.78	23.1
Test #7	173.5	5.76	23
Test #8	173.5	5.75	23
Test #9	173.5	5.75	23
Test #10	173.5	5.75	23

Branch 3, 2.07 m Branch, Closed End (10 mm O.D) 4th Resonant Peak	Frequency (Hz)	Amplitude	Temperature °C
Test #1	235.25	16.8	23
Test #2	235.25	16.83	23
Test #3	235.25	16.81	23
Test #4	235.25	16.8	23
Test #5	235.25	16.78	23
Test #6	235.5	16.77	23
Test #7	235.25	16.8	23
Test #8	235.25	16.8	23
Test #9	235.25	16.8	23
Test #10	235.25	16.82	23

Branch 3, 2.07 m Branch, Closed End (10 mm O.D) 5th Resonant Peak	Frequency (Hz)	Amplitude	Temperature °C
Test #1	301.5	8.88	23
Test #2	301.5	8.87	23
Test #3	301.5	8.87	23
Test #4	301.5	8.84	23
Test #5	301.5	8.87	23
Test #6	301.5	8.86	23
Test #7	301.5	8.87	23
Test #8	301.5	8.87	23
Test #9	301.5	8.9	23
Test #10	301.5	8.87	23

Branch 3, 2.07 m Branch, Closed End (10 mm O.D) 6th Resonant Peak	Frequency (Hz)	Amplitude	Temperature °C
Test #1	378.75	4.36	23
Test #2	378.75	4.36	23
Test #3	378.75	4.41	23.1
Test #4	378.75	4.39	23
Test #5	378.75	4.36	23
Test #6	378.75	4.36	23
Test #7	378.75	4.35	23
Test #8	378.75	4.36	23
Test #9	378.75	4.37	23
Test #10	378.75	4.36	23

Branch 3, 2.07 m Branch, Closed End (10 mm O.D) 7th Resonant Peak	Frequency (Hz)	Amplitude	Temperature °C
Test #1	400.25	9.09	23
Test #2	400.25	9.11	23
Test #3	400.25	9.10	23
Test #4	400.25	9.09	23
Test #5	400.25	9.09	23
Test #6	400.25	9.06	23
Test #7	400.25	9.09	23
Test #8	400.25	9.08	23
Test #9	400.25	9.09	23
Test #10	400.25	9.09	23

Branch 3, 2.07 m Branch, Closed End (10 mm O.D) 8th Resonant Peak	Frequency (Hz)	Amplitude	Temperature °C
Test #1	455.75	14.88	23
Test #2	455.75	14.86	23
Test #3	455.75	14.86	23
Test #4	455.75	14.84	23
Test #5	455.75	14.86	23
Test #6	455.75	14.86	23
Test #7	455.75	14.89	23
Test #8	455.75	14.86	23
Test #9	455.75	14.83	23
Test #10	455.75	14.86	23

Complex Experiment, Main line, Closed End (10 & 12 mm O.D) 1st Resonant Peak	Frequency (Hz)	Amplitude	Temperature °C
Test #1	32.25	51.52	23
Test #2	32.25	51.51	23
Test #3	32.25	51.5	23
Test #4	32.25	51.5	23
Test #5	32.25	51.49	23
Test #6	32.25	51.5	23
Test #7	32.25	51.52	23
Test #8	32.25	51.53	23
Test #9	32.25	51.5	23
Test #10	32.25	51.5	23

Complex Experiment, Main line, Closed End (10 & 12 mm O.D) 2nd Resonant Peak	Frequency (Hz)	Amplitude	Temperature °C
Test #1	89.75	14.88	23
Test #2	89.75	14.86	23
Test #3	89.75	14.87	23
Test #4	89.75	14.88	23
Test #5	89.75	14.88	23
Test #6	89.75	14.91	23
Test #7	89.75	14.89	23
Test #8	89.75	14.88	23
Test #9	89.75	14.88	23
Test #10	89.75	14.88	23

Complex Experiment, Main line, Closed End (10 & 12 mm O.D) 3rd Resonant Peak	Frequency (Hz)	Amplitude	Temperature °C
Test #1	103	4.47	23
Test #2	103	4.47	23
Test #3	103	4.50	23
Test #4	103	4.49	23
Test #5	103	4.47	23
Test #6	103	4.47	23
Test #7	103	4.45	23
Test #8	103	4.47	23
Test #9	103	4.47	23
Test #10	103	4.46	23

Complex Experiment, Main line, Closed End (10 & 12 mm O.D) 4th Resonant Peak	Frequency (Hz)	Amplitude	Temperature °C
Test #1	148.25	4.12	23
Test #2	148.25	4.14	23
Test #3	148.25	4.1	23
Test #4	148.25	4.12	23
Test #5	148.25	4.1	23
Test #6	148.25	4.08	23
Test #7	148.25	4.1	23
Test #8	148.25	4.11	23
Test #9	148.25	4.1	23
Test #10	148.25	4.1	23

Complex Experiment, Main line, Closed End (10 & 12 mm O.D) 5th Resonant Peak	Frequency (Hz)	Amplitude	Temperature °C
Test #1	185.5	5.25	23
Test #2	185.5	5.27	23
Test #3	185.5	5.28	23
Test #4	185.5	5.25	23
Test #5	185.5	5.25	23
Test #6	185.5	5.24	23
Test #7	185.5	5.25	23
Test #8	185.5	5.27	23
Test #9	185.5	5.25	23
Test #10	185.5	5.25	23

Complex Experiment, Main line, Closed End (10 & 12 mm O.D) 6th Resonant Peak	Frequency (Hz)	Amplitude	Temperature °C
Test #1	231.25	2.96	23
Test #2	231.25	2.95	23
Test #3	231.25	2.97	23
Test #4	231.25	2.95	23
Test #5	231.25	2.95	23
Test #6	231.25	2.93	23
Test #7	231.25	2.95	23
Test #8	231.25	2.95	23
Test #9	231.25	2.96	23
Test #10	231.25	2.99	23.1

Complex Experiment, Main line, Closed End (10 & 12 mm O.D) 7th Resonant Peak	Frequency (Hz)	Amplitude	Temperature °C
Test #1	247.75	2.12	23
Test #2	247.75	2.10	23
Test #3	247.75	2.08	23
Test #4	247.75	2.12	23
Test #5	247.75	2.12	23
Test #6	247.75	2.12	23
Test #7	247.75	2.14	23
Test #8	247.75	2.12	23
Test #9	247.75	2.11	23
Test #10	247.75	2.12	23

Complex Experiment, Main line, Closed End (10 & 12 mm O.D) 8th Resonant Peak	Frequency (Hz)	Amplitude	Temperature °C
Test #1	280.25	1.56	23
Test #2	280.25	1.55	23
Test #3	280.25	1.54	23
Test #4	280.25	1.54	23
Test #5	280.25	1.54	23
Test #6	280.25	1.53	23
Test #7	280.25	1.54	23
Test #8	280.25	1.54	23
Test #9	280.25	1.57	23
Test #10	280.25	1.57	23

Complex Experiment, Main line, Closed End (10 & 12 mm O.D) 9th Resonant Peak	Frequency (Hz)	Amplitude	Temperature °C
Test #1	310.5	9.24	23
Test #2	310.5	9.22	23
Test #3	310.5	9.26	23
Test #4	310.5	9.25	23
Test #5	310.5	9.22	23
Test #6	310.5	9.22	23
Test #7	310.5	9.22	23
Test #8	310.5	9.20	23
Test #9	310.5	9.21	23
Test #10	310.5	9.22	23

Complex Experiment, Main line, Closed End (10 & 12 mm O.D) 10th Resonant Peak	Frequency (Hz)	Amplitude	Temperature °C
Test #1	351	15.08	23
Test #2	351	15.10	23
Test #3	351	15.10	23
Test #4	351	15.10	23
Test #5	351	15.12	23
Test #6	351	15.14	23
Test #7	351	15.11	23
Test #8	351	15.10	23
Test #9	351	15.10	23
Test #10	351	15.09	23

Complex Experiment, Main line, Closed End (10 & 12 mm O.D) 11th Resonant Peak	Frequency (Hz)	Amplitude	Temperature °C
Test #1	391.5	3.44	23
Test #2	391.5	3.45	23
Test #3	391.5	3.45	23
Test #4	391.5	3.43	23
Test #5	391.5	3.45	23
Test #6	391.5	3.45	23
Test #7	391.5	3.45	23
Test #8	391.5	3.48	23.1
Test #9	391.5	3.49	23.1
Test #10	391.5	3.46	23

Complex Experiment, Main line, Closed End (10 & 12 mm O.D) 12th Resonant Peak	Frequency (Hz)	Amplitude	Temperature °C
Test #1	428.25	3.90	23
Test #2	428.25	3.89	23
Test #3	428.25	3.89	23
Test #4	428.25	3.88	23
Test #5	428.25	3.89	23
Test #6	428.25	3.87	23
Test #7	428.25	3.89	23
Test #8	428.25	3.89	23
Test #9	428.25	3.91	23
Test #10	428.25	3.93	23

Complex Experiment, 2.07 m Branch Closed End, (10 & 12 mm O.D) 1st Resonant Peak	Frequency (Hz)	Amplitude	Temperature °C
Test #1	32.25	16.19	23
Test #2	32.25	16.2	23
Test #3	32.25	16.19	23
Test #4	32.25	16.2	23
Test #5	32.25	16.23	23
Test #6	32.25	16.21	23
Test #7	32.25	16.2	23
Test #8	32.25	16.2	23
Test #9	32.25	16.2	23
Test #10	32.25	16.2	23

Complex Experiment, 2.07 m Branch Closed End, (10 & 12 mm O.D) 2nd Resonant Peak	Frequency (Hz)	Amplitude	Temperature °C
Test #1	89.5	17.65	23
Test #2	89.5	17.67	23
Test #3	89.5	17.68	23
Test #4	89.5	17.65	23
Test #5	89.5	17.65	23
Test #6	89.5	17.66	23
Test #7	89.5	17.65	23
Test #8	89.5	17.63	23
Test #9	89.5	17.65	23
Test #10	89.5	17.65	23

Complex Experiment, 2.07 m Branch Closed End, (10 & 12 mm O.D) 3rd Resonant Peak	Frequency (Hz)	Amplitude	Temperature °C
Test #1	103	9.86	23
Test #2	103	9.89	23
Test #3	103	9.90	23.1
Test #4	103	9.86	23
Test #5	103	9.86	23
Test #6	103	9.85	23
Test #7	103	9.86	23
Test #8	103	9.87	23
Test #9	103	9.86	23
Test #10	103	9.86	23

Complex Experiment, 2.07 m Branch Closed End, (10 & 12 mm O.D) 4th Resonant Peak	Frequency (Hz)	Amplitude	Temperature °C
Test #1	148	10.52	23
Test #2	148	10.5	23
Test #3	148	10.54	23
Test #4	148	10.5	23
Test #5	148	10.5	23
Test #6	148	10.48	23
Test #7	148	10.47	23
Test #8	148	10.5	23
Test #9	148	10.5	23
Test #10	148	10.5	23

Complex Experiment, 2.07 m Branch Closed End, (10 & 12 mm O.D) 5th Resonant Peak	Frequency (Hz)	Amplitude	Temperature °C
Test #1	185.75	4.45	23
Test #2	185.75	4.45	23
Test #3	185.75	4.45	23
Test #4	185.75	4.44	23
Test #5	185.75	4.43	23
Test #6	185.75	4.45	23
Test #7	185.75	4.45	23
Test #8	185.75	4.46	23
Test #9	185.75	4.45	23
Test #10	185.75	4.48	23.1

Complex Experiment, 2.07 m Branch Closed End, (10 & 12 mm O.D) 6th Resonant Peak	Frequency (Hz)	Amplitude	Temperature °C
Test #1	212.5	5.34	23
Test #2	212.5	5.32	23
Test #3	212.5	5.33	23
Test #4	212.5	5.32	23
Test #5	212.5	5.32	23
Test #6	212.5	5.30	23
Test #7	212.5	5.32	23
Test #8	212.5	5.31	23
Test #9	212.5	5.32	23
Test #10	212.5	5.30	23

Complex Experiment, 2.07 m Branch Closed End, (10 & 12 mm O.D) 7th Resonant Peak	Frequency (Hz)	Amplitude	Temperature °C
Test #1	247.5	1.31	23
Test #2	247.5	1.32	23
Test #3	247.5	1.30	23
Test #4	247.5	1.32	23
Test #5	247.5	1.32	23
Test #6	247.5	1.34	23
Test #7	247.5	1.32	23
Test #8	247.5	1.31	23
Test #9	247.5	1.32	23
Test #10	247.5	1.32	23

Complex Experiment, 2.07 m Branch Closed End, (10 & 12 mm O.D) 8th Resonant Peak	Frequency (Hz)	Amplitude	Temperature °C
Test #1	280	3.57	23.1
Test #2	280	3.55	23
Test #3	280	3.54	23
Test #4	280	3.54	23
Test #5	280	3.53	23
Test #6	280	3.54	23
Test #7	280	3.54	23
Test #8	280	3.57	23
Test #9	280	3.54	23
Test #10	280	3.55	23

Complex Experiment, 2.07 m Branch Closed End, (10 & 12 mm O.D) 9th Resonant Peak	Frequency (Hz)	Amplitude	Temperature °C
Test #1	310.25	4.83	23
Test #2	310.25	4.84	23
Test #3	310.25	4.83	23
Test #4	310.25	4.82	23
Test #5	310.25	4.80	23
Test #6	310.25	4.83	23
Test #7	310.25	4.83	23
Test #8	310.25	4.83	23
Test #9	310.25	4.82	23
Test #10	310.25	4.83	23

Complex Experiment, 2.07 m Branch Closed End, (10 & 12 mm O.D) 10th Resonant Peak	Frequency (Hz)	Amplitude	Temperature °C
Test #1	350.75	15.90	23
Test #2	350.75	15.91	23
Test #3	350.75	15.93	23
Test #4	350.75	15.91	23
Test #5	350.75	15.91	23
Test #6	350.75	15.92	23
Test #7	350.75	15.91	23
Test #8	350.75	15.91	23
Test #9	350.75	15.90	23
Test #10	350.75	15.87	22.9

Complex Experiment, 2.07 m Branch Closed End, (10 & 12 mm O.D) 11th Resonant Peak	Frequency (Hz)	Amplitude	Temperature °C
Test #1	391.25	5.63	23
Test #2	391.25	5.65	23
Test #3	391.25	5.65	23
Test #4	391.25	5.64	23
Test #5	391.25	5.64	23
Test #6	391.25	5.65	23
Test #7	391.25	5.65	23
Test #8	391.25	5.63	23
Test #9	391.25	5.65	23
Test #10	391.25	5.66	23

Complex Experiment, 2.07 m Branch Closed End, (10 & 12 mm O.D) 12th Resonant Peak	Frequency (Hz)	Amplitude	Temperature °C
Test #1	428.5	2.47	23
Test #2	428.5	2.46	23
Test #3	428.5	2.47	23
Test #4	428.5	2.47	23
Test #5	428.5	2.45	23
Test #6	428.5	2.46	23
Test #7	428.5	2.47	23
Test #8	428.5	2.49	23
Test #9	428.5	2.47	23
Test #10	428.5	2.48	23

Complex Experiment, 2.07 m Branch Closed End, (10 & 12 mm O.D) 13th Resonant Peak	Frequency (Hz)	Amplitude	Temperature °C
Test #1	468.75	4.81	23
Test #2	468.75	4.82	23
Test #3	468.75	4.81	23
Test #4	468.75	4.81	23
Test #5	468.75	4.81	23
Test #6	468.75	4.79	22.9
Test #7	468.75	4.81	23
Test #8	468.75	4.83	23
Test #9	468.75	4.81	23
Test #10	468.75	4.80	23

Complex Experiment, 1 m Al Branch, Closed End (10 & 12 mm O.D) 1st Resonant Peak	Frequency (Hz)	Amplitude	Temperature ^{o}C
Test #1	32.25	55.72	23
Test #2	32.25	55.73	23
Test #3	32.25	55.7	23
Test #4	32.25	55.71	23
Test #5	32.25	55.7	23
Test #6	32.25	55.7	23
Test #7	32.25	55.68	23
Test #8	32.25	55.7	23
Test #9	32.25	55.69	23
Test #10	32.25	55.7	23

Complex Experiment, 1 m Al Branch, Closed End (10 & 12 mm O.D) 2nd Resonant Peak	Frequency (Hz)	Amplitude	Temperature ^{o}C
Test #1	89.5	13.42	23
Test #2	89.5	13.44	23
Test #3	89.5	13.42	23
Test #4	89.5	13.43	23
Test #5	89.5	13.42	23
Test #6	89.5	13.42	23
Test #7	89.5	13.40	23
Test #8	89.5	13.42	23
Test #9	89.5	13.39	23
Test #10	89.5	13.41	23

Complex Experiment, 1 m Al Branch, Closed End (10 & 12 mm O.D) 3rd Resonant Peak	Frequency (Hz)	Amplitude	Temperature ^{o}C
Test #1	102.75	4.65	23
Test #2	102.75	4.67	23
Test #3	102.75	4.68	23
Test #4	102.75	4.65	23
Test #5	102.75	4.65	23
Test #6	102.75	4.65	23
Test #7	103	4.67	23
Test #8	102.75	4.65	23
Test #9	102.75	4.63	23
Test #10	102.75	4.65	23

Complex Experiment, 1 m Al Branch, Closed End (10 & 12 mm O.D) 4th Resonant Peak	Frequency (Hz)	Amplitude	Temperature °C
Test #1	147.75	3.58	23
Test #2	147.75	3.56	23
Test #3	147.75	3.58	23
Test #4	147.75	3.58	23
Test #5	147.75	3.59	23
Test #6	147.75	3.58	23
Test #7	147.75	3.58	23
Test #8	147.75	3.61	23.1
Test #9	147.75	3.60	23
Test #10	147.75	3.58	23

Complex Experiment, 1 m Al Branch, Closed End (10 & 12 mm O.D) 5th Resonant Peak	Frequency (Hz)	Amplitude	Temperature °C
Test #1	212.25	3.98	23
Test #2	212.25	3.96	23
Test #3	212.25	3.95	23
Test #4	212.25	3.95	23
Test #5	212.25	3.95	23
Test #6	212.25	3.92	23
Test #7	212.25	3.94	23
Test #8	212.25	3.95	23
Test #9	212.25	3.95	23
Test #10	212.25	3.96	23

Complex Experiment, 1 m Al Branch, Closed End (10 & 12 mm O.D) 6th Resonant Peak	Frequency (Hz)	Amplitude	Temperature °C
Test #1	231.25	1.87	23
Test #2	231.25	1.88	23
Test #3	231.25	1.88	23
Test #4	231.25	1.85	23
Test #5	231.25	1.86	23
Test #6	231.25	1.88	23
Test #7	231.25	1.88	23
Test #8	231.25	1.88	23
Test #9	231.25	1.89	23
Test #10	231.25	1.91	23.1

Complex Experiment, 1 m Al Branch, Closed End (10 & 12 mm O.D) 7th Resonant Peak	Frequency (Hz)	Amplitude	Temperature °C
Test #1	280	6.83	22.9
Test #2	280	6.85	23
Test #3	280	6.86	23
Test #4	280	6.86	23
Test #5	280	6.86	23
Test #6	280.25	6.84	23
Test #7	280	6.86	23
Test #8	280	6.86	23
Test #9	280	6.88	23
Test #10	280	6.88	23

Complex Experiment, 1 m Al Branch, Closed End (10 & 12 mm O.D) 8th Resonant Peak	Frequency (Hz)	Amplitude	Temperature °C
Test #1	310	3.46	23
Test #2	310	3.48	23
Test #3	310	3.49	23
Test #4	310	3.46	23
Test #5	310	3.46	23
Test #6	310	3.44	23
Test #7	310	3.46	23
Test #8	310	3.46	23
Test #9	310	3.45	23
Test #10	310	3.46	23

Complex Experiment, 1 m Al Branch, Closed End (10 & 12 mm O.D) 9th Resonant Peak	Frequency (Hz)	Amplitude	Temperature °C
Test #1	351	31.23	23
Test #2	351	31.22	23
Test #3	351	31.2	23
Test #4	351	31.2	23
Test #5	351	31.18	23
Test #6	351	31.17	22.9
Test #7	351	31.19	23
Test #8	351	31.2	23
Test #9	351	31.2	23
Test #10	351	31.2	23

Complex Experiment, 1 m Al Branch, Closed End (10 & 12 mm O.D) 10th Resonant Peak	Frequency (Hz)	Amplitude	Temperature °C
Test #1	391.25	3.14	23
Test #2	391.25	3.14	23
Test #3	391.25	3.16	23
Test #4	391.25	3.16	23
Test #5	391.25	3.14	23
Test #6	391.25	3.17	23
Test #7	391.25	3.18	23
Test #8	391.25	3.14	23
Test #9	391.25	3.14	23
Test #10	391.25	3.15	23

Complex Experiment, 1 m Al Branch, Closed End (10 & 12 mm O.D) 11th Resonant Peak	Frequency (Hz)	Amplitude	Temperature °C
Test #1	428.25	3.43	23
Test #2	428.25	3.43	23
Test #3	428.25	3.42	23
Test #4	428.25	3.42	23
Test #5	428.25	3.42	23
Test #6	428.25	3.40	23
Test #7	428.25	3.42	23
Test #8	428.25	3.44	23
Test #9	428.25	3.42	23
Test #10	428.25	3.42	23

Complex Experiment, 1 m Al Branch, Closed End (10 & 12 mm O.D) 12th Resonant Peak	Frequency (Hz)	Amplitude	Temperature °C
Test #1	469	3.68	23.1
Test #2	469	3.67	23
Test #3	469	3.65	23
Test #4	469	3.66	23
Test #5	469	3.65	23
Test #6	469	3.65	23
Test #7	469	3.65	23
Test #8	469	3.63	23
Test #9	469	3.65	23
Test #10	469	3.64	23